UC San Diego
UC San Diego Electronic Theses and Dissertations

Title

Biophysical exploration of membrane-protein interactions in Alzheimer's Disease

Permalink

https://escholarship.org/uc/item/3n11802c

Author

Karkisaval Ganapati, Abhijith

Publication Date

2023

Peer reviewed|Thesis/dissertation

UNIVERSITY OF CALIFORNIA SAN DIEGO

Biophysical exploration of membrane-protein interactions in Alzheimer's Disease

A Dissertation submitted in partial satisfaction of the requirements for the degree
Doctor of Philosophy

in

Engineering Sciences (Engineering Physics)

by

Abhijith Karkisaval Ganapati

Committee in charge:

       Professor Ratnesh Lal, Chair

       Professor Javier Garay

       Professor Bruce Kagan

       Professor Zhaowei Liu

       Professor Padmini Rangamani

The Dissertation of Abhijith Karkisaval Ganapati is approved, and it is acceptable

in quality and form for publication on microfilm and electronically.

University of California San Diego

2023

DEDICATION

To my family, amazing friends, and good times!

TABLE OF CONTENTS

LIST OF FIGURES

LIST OF TABLES

ACKNOWLEDGEMENTS

First and foremost, I'd like to thank my advisor Prof. Ratnesh Lal for his involvement, advice and creative influence on the research work I performed during my M.S and Ph.D program. He let me pursue research questions that I was interested in without curtailing my freedom and supported me with constant encouragement. I'd also like to thank Prof. Bruce Kagan from the Department of Psychiatry at UCLA in providing critical feedback and expert opinions on work related to amyloid electrophysiology. As a co-author and a mentor, he has been instrumental in producing this body of research work.

I'd like to thank my committee members in their involvement in my work and their constant understanding and support. I'd like to thank Prof. Zhaowei Liu and his lab members for helping with concepts related to optics and also allowing me to work in his lab for a brief duration on a collaborative project. I'd like to especially thank Prof. Padmini Rangamani from the MAE Dept at UCSD. I got interested in membrane biophysics research work through one of the courses taught by Prof. Rangamani and since then my interest in the field has only increased. I'm highly grateful for her support throughout my Ph.D duration. I'd also like to thank Prof. Javier Garay for being highly encouraging and supportive. His classes in material science were always interesting and I gained significant understanding of basic material science from them. I worked as a teaching assistant for MAE170 under Prof. Garay for a quarter and he was nothing but caring and supportive. I'd like to thank Prof. Suren Tatulian from University of Central Florida for being a collaborator in some of the amyloid work I performed. His scientific rigour and research mindset

have had a profound impact on my outlook towards academic research and I'm truly grateful to him for providing me with an opportunity to work with him.

The members of the Lal lab have been instrumental in my development as a researcher and as the person I am today. Its safe to say the culmination of my work at UCSD would not have been possible without the involvement and encouragement of my lab mates and co-workers. Firstly, I'm deeply indebted to Dr. Deependra Ban, post-doctoral scholar in Lal lab who was my research mentor and a true source of inspiration for the major duration of my PhD. He taught me everything I needed to know to perform independently in a research field where I had very little experience and background to begin with. Our routine morning coffee conversations about research, ideas and everything under the sun, served as the bedrock for much of the work presented in this dissertation. He's a person that I've learned a lot from and moreover, a true friend. I'd like thank Dr. Vrinda Sant for her contribution in shaping the researcher I am today. Our constant interaction, bouncing ideas off of each other and discussions have played a major role in making my experience an overall, positive one. She has been the person I can count upon and she has supported me deeply as a lab-mate and as a great friend. I'd like to thank Dr. Nirav Patel for productive discussions and his AFM expertise which were crucial in making this work possible. I'd like to thank Dr. Srinivasan Ramachandran for his expertise in optical microscopy, AFM and cell biology. His preceding work in the lab and ideas propagated have served as critical points from which I was able to derive new directions. I am deeply grateful to the undergraduate student researchers in the lab who worked with me - Benjamin Balster, Andrew Nguyen, and William Livingston, without whom electrophysiology associated projects would be impossible. Their curiosity towards research, dedication and drive were major factors in realizing many of the

experiments presented in this work. I'd also like to thank current members of the lab, mainly Grace Jang, Tyler Bodily, Samuel Yauk, Rufu Gong, Omar Haroon, Anirudh Ramanathan, Armando Ramil, Thomas de Torsiac for creating a jovial environment in the lab, being curious researchers and in general making the experience a positive one for everyone involved. The lab dinners did really lift spirits in the lab since Covid-19 times and I'm happy I was a part of those. I'd also like to thank past members of the lab, Dr. Madhura Som, Dr. Qingqing Yang, Dr. Joon Lee, Dr. Michael Hwang, Dr. Brian Meckes, Dr. Fernando Terran Arce from whom I have learnt a lot of technical and interpersonal skills.

One of the aspects of my PhD training that has been crucial in my personal development was serving as a teaching assistant for MAE170 and MAE171A. The position also served as my main source of wages for the majority of my PhD, thus providing critical financial support. As such, I'm deeply indebted to the faculty and staff involved in MAE educational labs in believing my capacity to be a TA and helping me develop critical teaching skills. I'd especially like to thank Greg Specht, who is a wonderful mentor, a great friend and overall, a charming human being. His passion for technology, prototyping and all-things-cool have really brushed off on me and have led to some great times and conversations. I cannot discount the contribution of other staff members in MAE educational labs mainly, Edward Pogue, Steve Roberts, Ian Richardson, Paul Arcoleo who were instrumental in helping me understand practical electronics, prototyping methods and in general practical knowledge about a lot of experimental topics. They were such a pleasure to work with and I can confidently say I've amassed a lot of skills by being in their vicinity. In addition, I'm also highly grateful to Prof. Nicholas Boechler, Prof. Andrew Lucas, and Prof. Kalyanasundaram Seshadri - the professors teaching the courses, who believed in me

constantly and in my ability to teach students and other lead other TAs. They have been great sources of inspiration for me to learn how to communicate difficult topics and convey the meaning to a large body of students.

Last, but certainly not the least, I am deeply thankful to my family and friends in India who have unequivocally supported me and my decisions throughout this arduous journey. I'd like to especially thank my parents Ganapati Hegde, Sujata Hegde and my elder brother Abhishek Karkisaval for their unlimited patience, care and support. I'm also deeply thankful to my friends Suraj Sirsikar, Rakshit Manage, Darshan Vernekar and Swati Shahane who have played a major role in maintaining my sanity and have always supported me in good and tough times alike.

unmodified and pyroglutamylated Aβ peptides in lipid membranes'. The dissertation author was the primary author of the manuscript.

Chapter 5, in part, is a manuscript under preparation with *Karkisaval A.G., and Lal R.* titled 'Single molecule unfolding of Aβ$_{1-42}$ oligomers from lipid bilayers'. The dissertation author was the primary author of the manuscript.

Lastly, I want to thank publishing agencies such as Springer Nature Publishing and Elsevier Publications for granting me permission to use published images in my dissertation.

VITA

2015	B.Eng. in Mechanical Engineering, M.S. Ramaiah Institute of Technology, Bangalore, India
2018	M.S in Engineering Sciences (Engineering Physics), University of California San Diego
2023	Ph.D. in Engineering Sciences (Engineering Physics), University of California San Diego

PUBLICATIONS

Karkisaval, A.G.*, Ban, D.K.*, Nguyen, A., Balster, B., Lal, R. Amino acid sequence and readability dependence in Aβ-membrane interactions and relevance to Alzheimer's disease. 2023 (under preparation for submission)

Karkisaval, A.G.*, Balster, B., Nguyen, A., Abedin, F., Tatulian, S.A., Lal, R. Channel forming activities and structural features of unmodified and pyroglutamylated Aβ peptides in lipid membranes. 2023 (under preparation for submission)

Karkisaval, A.G., Patel, N., Lal, R. Single molecule unfolding of $Aβ_{1-42}$ oligomers from lipid bilayers. 2023 (under preparation for submission)

Ban, D.K.*, Bodily, T.*, **Karkisaval, A.G.***, Dong, Y., Natani, S., Ramanathan, A., Ramil, A., Srivastava, S., Bandaru, P., Glinsky, G., Lal, R. Rapid self-test of unprocessed viruses of SARS-CoV-2 and its variants in saliva by portable wireless graphene biosensor. *PNAS*, 2022, 119 (28) e2206521119, https://doi.org/10.1073/pnas.2206521119

Sant, V., Som, M., **Karkisaval, A.G.**, Carnahan, P., Lal, R. Scavenging amyloid oligomers from neurons with silica nanobowls: Implications for amyloid diseases. *Biophysical Journal*, 2021, 120, 3329–3340, https://doi.org/10.1016/j.bpj.2021.07.002

Karkisaval, A.G.*, Rostagno, A.*, Azimov, R.*, Ban, D.K., Ghiso, J., Kagan, B.L., Lal, R. Ion channel formation by N-terminally truncated Aβ (4-42); relevance for the pathogenesis of Alzheimer's disease. *Nanomedicine: Nanotechnology, Biology, and Medicine* 2020, 29(2020) 102235, https://doi.org/10.1016/j.nano.2020.102235

Ban, D.K., Liu, Y., Wang, Z., Ramachandran, S., Sarkar, N., Shi, Z., Liu, W., **Karkisaval, A.G.**, Martinez-Loran, E., Zhang, F., Glinksy, G., Bandaru, P.R., Fan, C., Lal, R. Direct DNA Methylation Profiling with an Electric Biosensor. *ACS Nano*. 2020;14(6):6743-6751. doi:10.1021/acsnano.9b10085

Kundanati, L., Chahare, N.R., Jaddivada., S., **Karkisaval, A.G.**, Sridhar, R., Pugno, N.M., Gundiah, N. Cutting mechanics of wood by beetle larval mandibles. Journal of the Mechanical Behavior of Biomedical Materials, 2020, 112, 104027. https://doi.org/10.1016/j.jmbbm.2020.104027

Hwang, M.T., Wang, Z., Ping, J., Ban, D.K., Shiah, Z.C., Antonschmidt, L., Lee, J., Liu, Y., **Karkisaval, A.G.**, Johnson, A.T.C., Fan, C., Glinsky, G., Lal, R. DNA Nano-tweezers and Graphene Transistor Enable Label-free Genotyping. *Advanced Materials*. 2018, 30, 1802440. DOI: 10.1002/adma.201802440

Arya, A.D., Hallur, P.M., **Karkisaval, A.G.**, Gudipati, A., Rajendiran, S., Dhavale, V., Ramachandran, B., Jayaprakash, A., Gundiah, N., Chaubey, A. Gelatin Methacrylate Hydrogels as Biomimetic Three-Dimensional Matrixes for Modeling Breast Cancer Invasion and Chemoresponse in Vitro. ACS Applied Material Interfaces, 2016, 8(34),22005-17, doi: 10.1021/acsami.6b06309.

Patent

Deependra Kumar Ban, Ratnesh Lal, Gennadi Glinskii, Prabhakar R Bandaru, Sunil Srivastava, Scott John, Tyler Bodily, **Abhijith Karkisaval Ganapati.** Methods and devices for detecting a pathogen and its molecular components, US Patent Application US 2022/0252584 (Patent pending)

*Denotes equal authorship

ABSTRACT OF THE DISSERTATION

Biophysical exploration of membrane-protein interactions in Alzheimer's Disease

By

Abhijith Karkisaval Ganapati

Doctor of Philosophy in Engineering Sciences (Engineering Physics)

University of California San Diego, 2023

Professor Ratnesh Lal, Chair

Alzheimer's disease (AD) is a devastating neurodegenerative disorder affecting millions of people worldwide and the number is projected to rapidly increase in the coming years. AD severely impairs an individual's memory, cognitive abilities leading to dementia and neuronal death. Although a large body of research work has gone into understanding AD in the past couple of decades, there is still no clear consensus on the molecular nature of the disease progression and thus, no cure or robust treatment methodologies have been found. The molecular hallmark of AD is the presence of extracellular, lesion-like deposits of a protein called Amyloid-β (Aβ).

The amyloid hypothesis argues that the presence of these extracellular deposits of Aβ triggers a neuropathological cascade of events which lead to the death of the neuron. The amyloid ion channel hypothesis suggests that Aβ is capable of forming high conductance, cation selective channels leading to calcium dyshomeostasis in neurons, leading to neuronal death. This dissertation investigates the biophysical, structural, and functional properties of full length Aβ and its various truncated and post translationally modified forms. We show that Aβ isoforms are also capable of causing ion flux in lipid bilayers, thus adding additional support to the amyloid channel-based neurotoxicity. As the exact structure and morphology of Aβ oligomers involved in the cytotoxicity are poorly characterized until now, we introduce single molecule force spectroscopy techniques that shed new light on the morphological characteristics of Aβ oligomeric species. The technique also helps uncover mechano-biological coupling involved in the process of protein-membrane structural organization. Finally, we describe the development and implementation of a combined atomic force microscopy and total internal reflection fluorescence (AFM-TIRF) microscopy system for high spatiotemporal and multiparametric studies of membrane-protein interactions. AD is a multifactorial disease and studies involving the convergence of bio -physical, -chemical, and -mechanical aspects of membrane-protein interactions and their structure-function relationships provides additional insights into the molecular nature of Aβ, and the probable mechanisms involved in the AD cascade. The understanding of molecular landscape of Aβ interactions is critical to the development of therapeutic interventions to arrest the progression of AD and reverse cognitive decline.

Chapter 1

Introduction

1.1 Alzheimer's Disease

Alzheimer's disease (AD) is a progressive neurodegenerative condition that leads to cognitive decline, dementia, neuronal death, and brain atrophy. According to CDC estimates, in 2020, worldwide there were approximately 50 million people with AD and 5.8 million Americans aged 65 years or older had AD or AD related dementia and the number is expected to grow by 3x by 2060 [1]. With growing life expectancy across the globe, AD or related dementia are regarded as the major mortality threats to the aging population. AD and related forms of dementia have been a major cause of concern to healthcare systems in developed countries and have also put a major strain in the management of the disease from a caregiver's perspective.

The first practical diagnosis and observation of AD was performed by the German psychiatrist Alois Alzheimer in 1901 [2], after whom the disease was named few years down the line. Since then, immense body of scientific literature has shed some light on the pathophysiology of the disease. However, till date there is no clear understanding about the molecular mechanism of disease causation, the exact timeline of disease progression, which has subsequently stunted the development of a definitive cure for the disease. To add to the complexity, it can take anywhere from 10-15 years for the disease to start at a molecular or cellular level and the apparent symptoms of the disease to occur. Until now, a definitive diagnosis of AD can only be made postmortem, while a 'probable' diagnosis can be made with a fair degree of certainty after

differentially excluding other forms of dementia via brain imaging techniques such as computed tomography (CT), positron emission tomography (PET) or magnetic resonance imaging (MRI) [3]. Additional behavioral and cognition tests can also help in tracking the progression of the disease.

The characteristic neuropathological hallmark of AD present in the form of extracellular deposits called 'senile plaques', intracellular tangles of a particular protein termed as 'neurofibrillary tangles', severe neuronal synaptic loss, and reduction in brain mass (Figure 1.1) [4]. Senile plaques are composed of fibrillar aggregates of proteinaceous material, in which a protein called 'Amyloid Beta' (Aβ) is the major constituent. Intracellular neurofibrillary tangles (NFTs) are composed of a hyperphosphorylated variant of a microtubule associated protein called 'Tau'. The Tau protein's main role is stabilization of the microtubule structure in healthy neurons [4]. These extra- and intracellular aggregates of proteins start forming in the regions of brain associated with memory recall, which over time worsens, leading to synaptic loss and impedes with other brain functions associated with cognition, communication, personality, reasoning etc. [5] [6]. Even though age matched controls of healthy individuals without AD also show extracellular amyloid beta plaques in the brain, their relative levels are comparatively lower and the same can be said about brain mass loss. Compared to healthy individuals, its also found that in individuals with AD, the blood brain barrier (BBB) is severely disrupted which results in higher extent of brain inflammation. It has also been proposed that sustained brain inflammation in the case of AD can create a negative feedback loop that can exacerbate amyloid beta and tau pathologies [7].
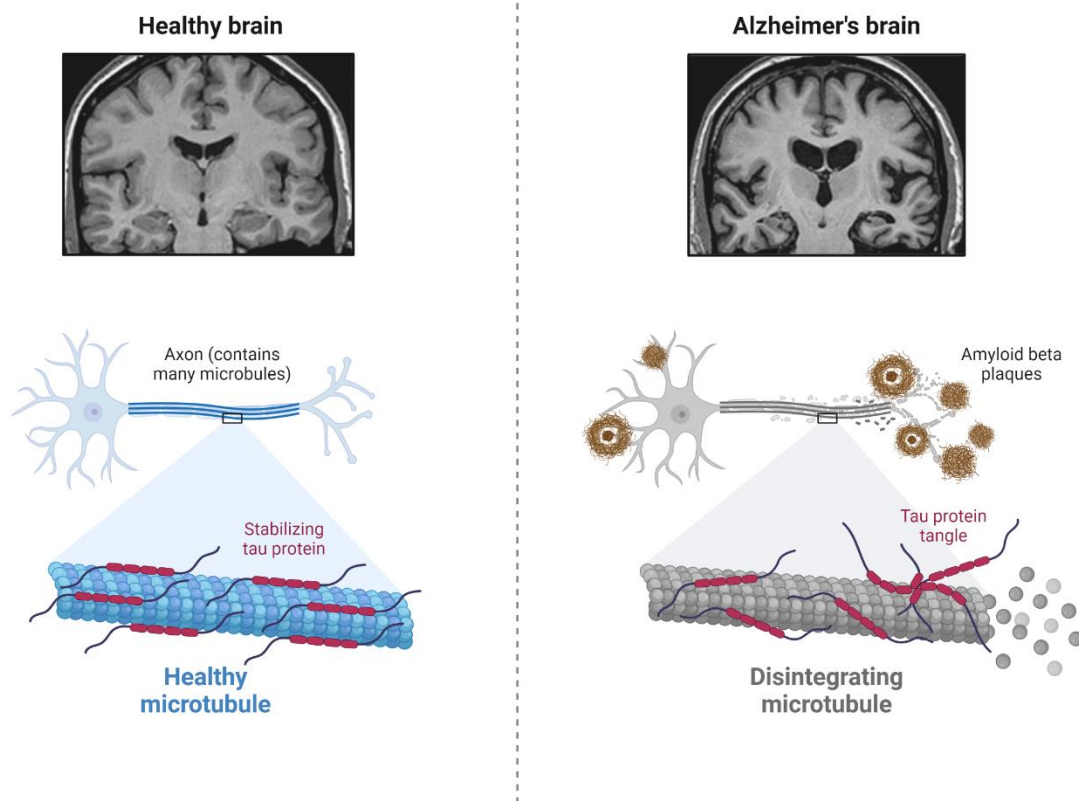
Figure 1.1 - Comparison of healthy brain vs AD affected brain and their underlying neuropathological hallmarks (neurofibrillary Tau tangles, Amyloid β plaques). Reprinted from "Pathology of Alzheimer's Disease 2", by BioRender.com (2023). Retrieved from https://app.biorender.com

Some of the early population specific research on AD hinted towards genetic changes or abnormalities as the main risk factor of the disease. Indeed, it was found that in a minority of cases where people aged lesser than 60 years showed symptoms of AD that were strikingly similar to people above the age of 65 who were living with AD. Abnormalities in an allele (ε4) of a gene called Apolipoprotein E (APOE), which is normally involved in cholesterol processing in the brain, was found to be involved in the cascade of AD in these cases. Two other genes called Presenilin 1 & 2 (P1, P2) and Amyloid Precursor Protein (APP) were also implicated as the risk factors for AD [4]. This led to a unique classification of pathology into early onset AD (EOAD) and

3

late onset AD (LOAD). A small percentage of EOAD cases where mutations in the P1 & P2 gene and APP gene lead to a sub-class of AD known as familial AD (FAD) where the disease progression begins in mid-30s – mid-40s and the disease fully develops by age 60 with full severity. In the case of late onset AD (LOAD), also known as sporadic AD which major symptoms begin after age 60, the progression of the disease can be comparatively slower. Its now known that in the overall population of AD, ~95% of the cases are of LOAD (sporadic) nature and the remaining ~5% can be ascribed to EOAD (or FAD) [8]. Interestingly, whatever maybe the classification of the disease (EOAD vs LOAD), the type of pathophysiological events and the nature of disease unfolding has been found to be similar in both cases.

1.2 Hypotheses for AD

1.2.1 Cholinergic hypothesis

Acetylcholine (ACh) is one of the important neurotransmitters required for optimal functioning of neurons and cognitive functions of the brain. The cholinergic hypothesis of AD states that a reduction in the production of acetylcholine in the brain is the causative mechanism of AD. The rationale for this hypothesis comes from the fact that examined brains of patients with AD had significantly lower levels of the enzyme acetyltransferase (ChAT) which is responsible for the production of the neurotransmitter ACh. Further reports suggested lower levels of choline (an essential nutrient) and the degeneration of cholinergic neurons in the brain of AD patients. It was thus proposed that a combination of the above-mentioned factors lead to AD pathogenesis [4] [9]. The cholinergic hypothesis was proposed around 1970s and a few drugs which were designed with the hypothesis as the main driving factor were tested. However, none

of these drugs showed any improvements in the pathology of AD and were often plagued by extreme side effects. More recent studies suggest that ACh depletion may accompany AD pathology, but they may not be the causative factors of the disease [9].

1.2.2 Amyloid Hypothesis

One of the dominant and critically analyzed hypothesis put forward in the AD field is the Amyloid hypothesis. The amyloid hypothesis suggests that the deposition of plaques of the protein amyloid-β (Aβ) , formed after the proteolytic cleavage of amyloid precursor protein (APP) is the central event and thus the causative factor of the disease [10] [11]. Irregular clearance of these extracellular plaques from the brain progressively worsens the condition, leading to neurotoxicity. The rationale of the amyloid hypothesis stems from the fact that, in Down's syndrome (another type of genetic dementia) which is caused by an extra chromosome at location 21, also leads to deposition of extracellular plaques. After FAD cases of AD were recognized and their gene sequenced, it was found that mutations linked to APP gene expression are also in the same gene region as Down's syndrome and also lead to deposition of plaques made of the protein amyloid-β, a typical characteristic in AD pathology [10] [12]. Its also well known that, the pathology of patients diagnosed with Down's syndrome converges with AD pathology as they age. The amyloid hypothesis also suggests that other parts of the pathology (neurofibrillary tangles, synaptic loss etc) are a direct consequence of the plaque deposition, however exact molecular mechanism of how Aβ goes about causing these effects is still unknown [12] [13].

Since the first proposal of amyloid cascade hypothesis in 1991, intense investigations by multiple groups found that the fibrillar plaque cores of Aβ and their relative concentrations did not correlate well with neurotoxicity [14] [15]. It was later argued that plaques, mainly composed of insoluble fibrillar aggregates of Aβ may not be directly involved in the disease cascade, but smaller, soluble aggregates called 'oligomers' (n-mer stands for 'n' associations of a peptide or protein monomer molecule) may be more neurotoxically active [14] [16] [17]. In-vitro and in-vivo studies with soluble, lower order aggregates also bolstered the idea that Aβ oligomers and their interaction with cellular membranes are the main causative factors of the disease [18], [19]. It is now generally accepted in the AD field, that lower order soluble oligomers are responsible, however, the exact configuration of the oligomer, its structural features and the exact mechanism of oligomer induced toxicity is not well understood.

1.2.3 Tau Hypothesis

Even though the amyloid hypothesis explains some of the pathophysiological aspects of AD, exact mechanism by which the amyloid peptide (Aβ) affects the downstream pathophysiology is unclear. Clinical data has suggested that the timeline of progression and cognition decline is more in line with the appearance and burden of NFTs of Tau protein [20] [21]. This is also supported by the fact that in all cases of AD, the presence of Tau pathology correlates strongly with diseased conditions and in some cases may also precede Aβ associated pathology [22] [23]. There is some evidence to suggest that the presence of Aβ plaques (absence of Tau NFTs) may not correlate strongly with dementia [23]. Tau is a microtubule associated protein (Figure 1.1). Its role is understood to be stabilizing the structure of microtubules, thus indirectly stabilizing the axonal compartment of the neuron. Hyperphosphorylation (a type of protein post-

translational modification) of Tau protein, causes them to unbind from microtubules and aggregate forming NFTs [24]. Considering the above ideas, the Tau hypothesis suggests that formation of NFTs causes a cascade of events which leads to neuronal dyshomeostasis and death [25] [26] [27]. In support of Tau hypothesis, it was found in the case of Fronto-Temporal Dementia (FTD, another prevalent form of dementia) mutations in the Tau gene were mainly responsible for the observed pathology. FTD shares many aspects of the pathology with AD, hence the Tau hypothesis seems to hold promising ground in unraveling the mechanism of AD progression. As stated with the amyloid hypothesis, the tau hypothesis also faces similar problems; not every aspect of the disease cascade is explained by the hypothesis and the exact interplay between Tau, Aβ and neuronal death is also unclear.

1.2.4 Other Hypotheses

In addition to the two major hypotheses analyzed in the AD field, there have been a few other hypotheses put forward to explain some aspects of AD. The inflammatory hypothesis posits that microglia, astrocytes and to a relatively lesser extent, neurons are involved in a continuous state of neuroinflammation in the case of AD, which may or may not be caused due to levels of Aβ and Tau. This creates negative feedback of continuous inflammation, which in turn develops into more advanced cascade of AD [28]. The oxidative stress hypothesis suggests that in cases of AD, reactive oxygen species (ROS) are generated in cellular compartments at abnormal levels due to mitochondrial dysfunction. AD affected brains are known to have lesser antioxidants compared to normal brains and the progressive buildup of ROS and incomplete reduction of ROS causes the formation of toxic radicals which eventually cause neuronal death [29]. The infectious disease hypothesis of AD puts forward the idea that certain bacterial or viral infections may have

7

been the starting points of the AD cascade. The support for this hypothesis comes from the fact that in patients with AD, certain bacterial infections (ex. Herpesvirus) were commonly found. This hypothesis is also partially supported by the inflammatory hypothesis as inflammation would be a common response to any bacterial infection [28] [30]. The transition metal ion theory of AD proposes that dyshomeostasis of transition metal ions in the brain as a major causative event in the AD cascade. There is some evidence that claims the ability of the brain to maintain transition metal (Zn, Cu) homeostasis is severely impaired in AD brains and as a consequence, protein aggregation catalyzed by metal ions could be accelerated [31] [32].

1.3 Amyloid-β – production and biomolecular properties

The peptide at the heart of the amyloid cascade hypothesis for AD is the Amyloid-β peptide. It is formed by the sequential proteolytic cleavage of a bigger, transmembrane protein, the Amyloid Precursor Protein (APP). APP is a 100-140 kDa transmembrane protein that is broadly involved in important neuronal functions such as synaptic formation, neuronal repair and neuronal transport. Its exact molecular involvement in AD, other than production of Aβ is not well understood [33].

Amyloid- β and its various isoforms are produced by the proteolytic cleavage of APP at 2 sites [33]. The cleavage site and the specificity of the enzymes lead to 2 main pathways of Aβ generation termed as the amyloidogenic pathway and the non-amyloidogenic pathway (Figure 1.2). In the non-amyloidogenic pathway (Figure 1.2, right), the first APP cleavage is mediated by a membrane associated enzyme called α-secretase on the N-terminal side, which leads to

secretion of sAPPα into the extracellular space. The remaining, membrane inserted fragment of

APP (termed C99) gets cleaved the second time, this time on the C-terminal side via a membrane

embedded enzyme complex γ-secretase, which releases a fragment $A\beta_{17-42}$ (also termed p3) and

a cytoplasmic fragment termed Amyloid Intracellular Domain (AICD). In the amyloidogenic

pathway (Figure 2, left), APP is cleaved first by plasma membrane associated enzyme β-secretase

(BACE 1), releasing the N-terminal fragment sAPPβ into the extracellular space. The membrane

inserted portion of APP (termed C83 in this case) gets cleaved once more via the membrane

embedded enzyme complex γ-secretase, which leads to production of a 37-43 amino acid peptide

fragment Aβ, the most abundant of which are $A\beta_{1-40}$ (40 amino acids long) and $A\beta_{1-42}$ (42 amino

acids long). In both pathways, the second cleavage by γ-secretase and release of AICD into the

cytoplasm are common mechanisms. In the case of non-amyloidogenic pathway, the extracellular

secreted fragment sAPPα is shown to have neurotrophic behavior. In both cases, the AICD

fragment is shown to bind to different proteins inside the cytoplasm modulating cytoskeletal

dynamics and also control gene expression [34] [35] [36].
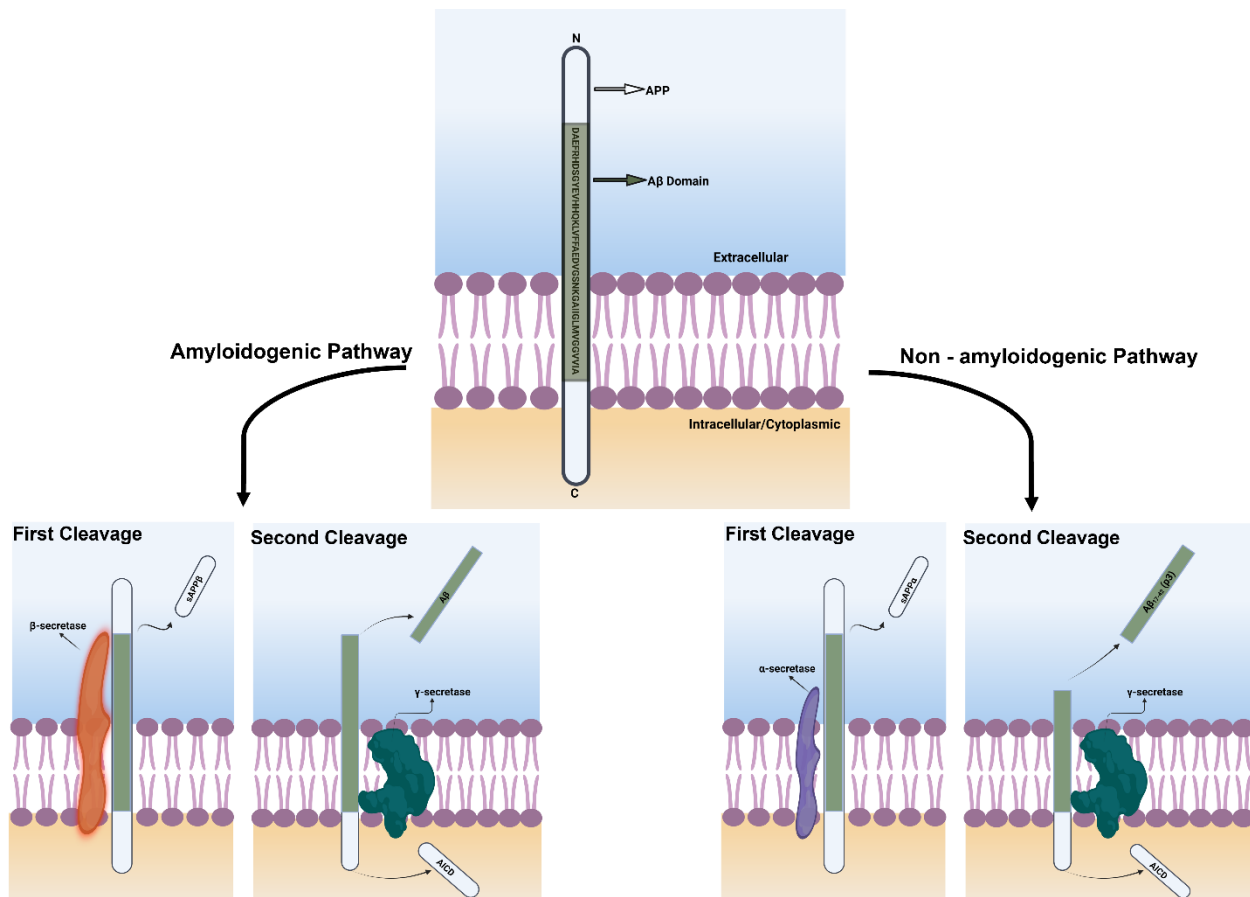
Figure 1.2 - Schematic depicting Amyloid precursor protein (APP) processing via amyloidogenic (left side) and non-amyloidogenic (right side) pathways to generate Aβ peptides (not to scale). The Aβ domain is shown in green color with 42 amino acids marked.

The 40-42 amino acids long generated Aβ peptides have interesting biochemical and biophysical properties. The $Aβ_{1-42}$ peptide has a molecular weight of 4514.10 g/mol (4.5kDa) and has a net negative charge at pH 7.4. The amino acid makeup and properties of individual amino acids are shown in Figure 1.3. Overall, the 42 amino acid sequence can be divided into 3 sections, N-terminal segment (amino acids 1-14), central segment (amino acids 15-28) and the C-terminal fragment (amino acids 29-42). The N-terminal segment contains a significant amount of charged amino acids. The central segment contains higher proportion of hydrophobic amino acids, and the C-terminal fragment is almost completely dominated by hydrophobic residues [33].

NH₂- D A E F R H D S G Y E V H H Q K L V F F A E D V G S N K G A I I G L M V G G V V I A - COOH

Negatively charged   **Positively charged**   **Polar Uncharged**   **Hydrophobic**   **Special cases (ambivalent)**
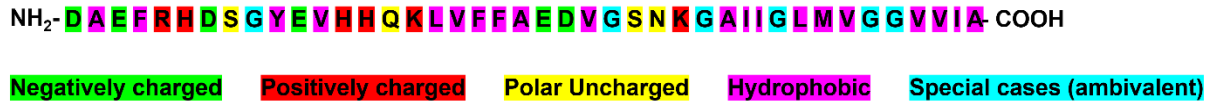
Figure 1.3 - Amino acid composition of Aβ$_{1-42}$ peptide with residues assigned from electrical charge, polarity and hydropathicity standpoint.

The other commonly found Aβ peptide in the brain is Aβ$_{1-40}$, has 2 lesser amino acids in the C-terminal (residue 41 and 42 from full length Aβ$_{1-42}$) which makes it less hydrophobic (more hydrophilic) compared full length Aβ$_{1-42}$. Although Aβ$_{1-42}$ and Aβ$_{1-40}$ are the most abundant Aβ species found in patient brains, several N-terminal and C-terminal truncated forms of Aβ have also been reported. Among N-terminal truncations, Aβ$_{2-x}$ (missing the first amino acid of Aβ$_{1-42}$), AβpE_{3-x} (missing the first 2 residues, plus subsequent pyroglutamylation of the 3rd residue), Aβ$_{4-x}$ (missing the first 3 residues) , Aβ$_{11-x}$ (missing first 10 residues) are the predominant fractions. The x- notation indicates that these truncations can occur in both Aβ$_{1-42}$ and Aβ$_{1-40}$. Aβ$_{4-42}$ and AβpE_{3-42}, especially are found in large quantities in patients with advanced progression of AD. N-terminal truncations mainly lose the charged amino acids in the N-terminal segment of the full length Aβ$_{1-42}$ which changes the biophysical properties of Aβ peptides, which can indirectly affect aggregation propensity and cytotoxic properties of the peptide.

Among the C-terminal truncations, Aβ$_{1-34,}$ Aβ$_{1-24,}$ Aβ$_{1-37}$, Aβ$_{1-38}$ are the commonly found variants. As with N-terminal truncations, peptides truncated at the C-terminal lose mainly hydrophobic amino acids in the C-terminal segment. This can have major consequences in terms of the biophysical characteristics due to the loss of hydrophobic residues at the C-terminal. The C-terminal segment with a high concentration of hydrophobic residues is widely known to accelerate the aggregation process of the peptides [33]. It comes as no surprise that the initial therapeutics developed in the AD field targeted the regulation (secretase inhibitors) of cellular

proteolytic enzymes that are involved in the truncation of peptides, indirectly controlling the relative population pools of the peptides that tend to aggregate and form amyloid plaques [37] [38].

1.4 Amyloid-β – oligomerization & fibrillization

As stated in section 1.1, one of the hallmarks of AD is the presence of insoluble aggregates of Aβ proteins called plaques. At the microscale, these aggregates consist of regular, stacked arrangement of Aβ protein forming highly stable fibrillar structures. These structures are formed by hydrophobicity mediated protein-protein interactions [39]. Evidence from multiple lines of studies have implicated the C-terminal hydrophobic segment as the aggregation driving domain of the peptide [33] [40]. In the case of Aβ, monomers which are intrinsically disordered (lacking particular secondary structures) or partially folded, self-associate to form transient, heterogenous structures called oligomers. These oligomers can range in heterogeneity from a dimer (containing 2 monomers) to few tens of monomers ('n'-mer) and they can spontaneously transition from one form to another in response to changes in environmental factors [38]. Its also possible that the secondary and tertiary structure of the oligomeric species formed may be non-uniform. These lower order oligomers can further associate to form nanoscopic linearized structures called protofibrils. At some point during the lifecycle of oligomerization, some lower order oligomers and protofibrils serve as nucleation substrates (Figure 1.4). These nuclei are highly energetic, unstable states that allow rapid association of monomers and growth of the initially formed protofibrils into elongated, regular and energetically equilibrated structures called amyloid fibrils [41] (Figure 1.4).
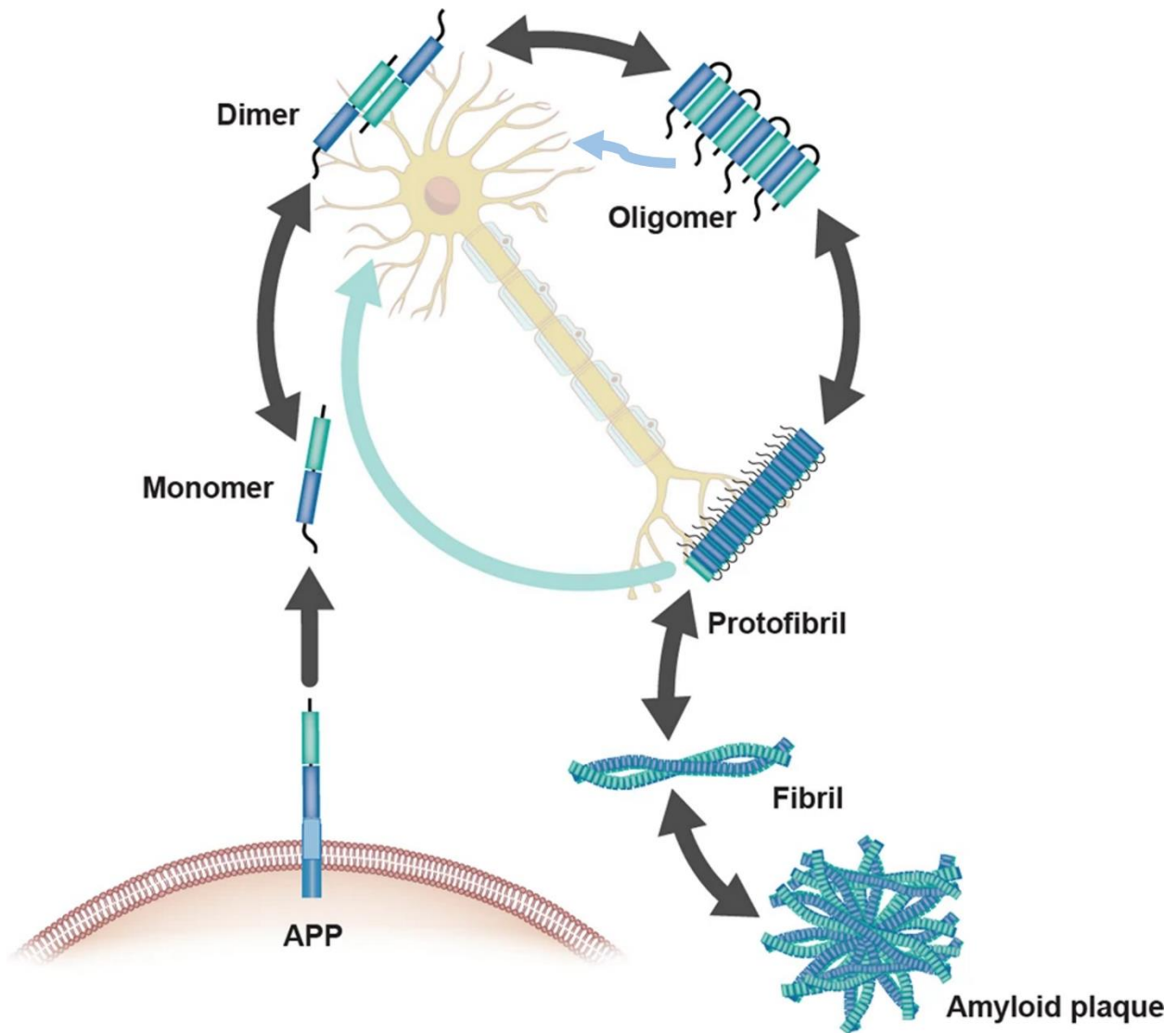
Figure 1.4 - Amyloid beta oligomerization pathways and interconvertible states. Adapted from *[41]*, under creative commons license.

In some cases, the parts of the fibril or the surfaces of fibrils can serve as secondary nucleation sites which allows branching out of the fibrils and further depletion of monomers [41] [42]. Macroscale clustering of amyloid fibrils with other biomolecules (lipids, cellular debris etc) forms amyloid plaques. In the case of Aβ, the monomer is known to be partially disordered[33]. As the monomer traverses further in the oligomerization cascade, it acquires a β-strand rich

secondary structure. This β-strand structure further morphs into a hydrogen bonded, parallel/antiparallel cross-β folded tertiary structure found at the core of amyloid fibrils [43].

1.4.1 Structure of amyloid-β fibrils

The parallel/antiparallel cross-β sheet molecular structure of amyloid- β fibrils is shared by many proteins/peptides implicated in other amyloid associated conditions such as Parkinson's disease (α-synuclein protein), Type 2 diabetes (islet amyloid polypeptide IAPP), Prion disorders (HET-S, PrP[Sc] Prion protein), Tau protein(AD, FTD and other tauopathys) etc. This has led to the coining of the term 'amyloid fold' which describes the common structural features of the fibrils formed by these proteins which don't share a strong sequence homology (Figure 1.5). The amyloid fold structure of the fibril consists of a linear stack of the planar cross-β sheet motif oriented perpendicular to the fibril growth axis [44]. X-ray diffraction, High resolution TEM, and cryo-EM imaging have revealed a 4.7 – 4.8 Å inter-plane spacing arising from hydrogen bonding of one cross - β subunit plane to another. Intra-strand spacing between the β -strands is about 10-11 Å. On a larger length scale, amyloid fibrils also show hierarchical organization and similarities in the form of helical twists along the length of the fiber with regular periodicity, which can vary from one protein amyloid type to another [44] [45].

The fibrillar core of $A\beta_{1-42}$ and $A\beta_{1-40}$ show a dimeric unit as the structure that repeats through the fibril axis. In the case of $A\beta_{1-40}$, approximately, amino acid residues 17-40 of each monomer of the dimeric unit adopts a U-shaped conformation with 2 beta sheets forming the
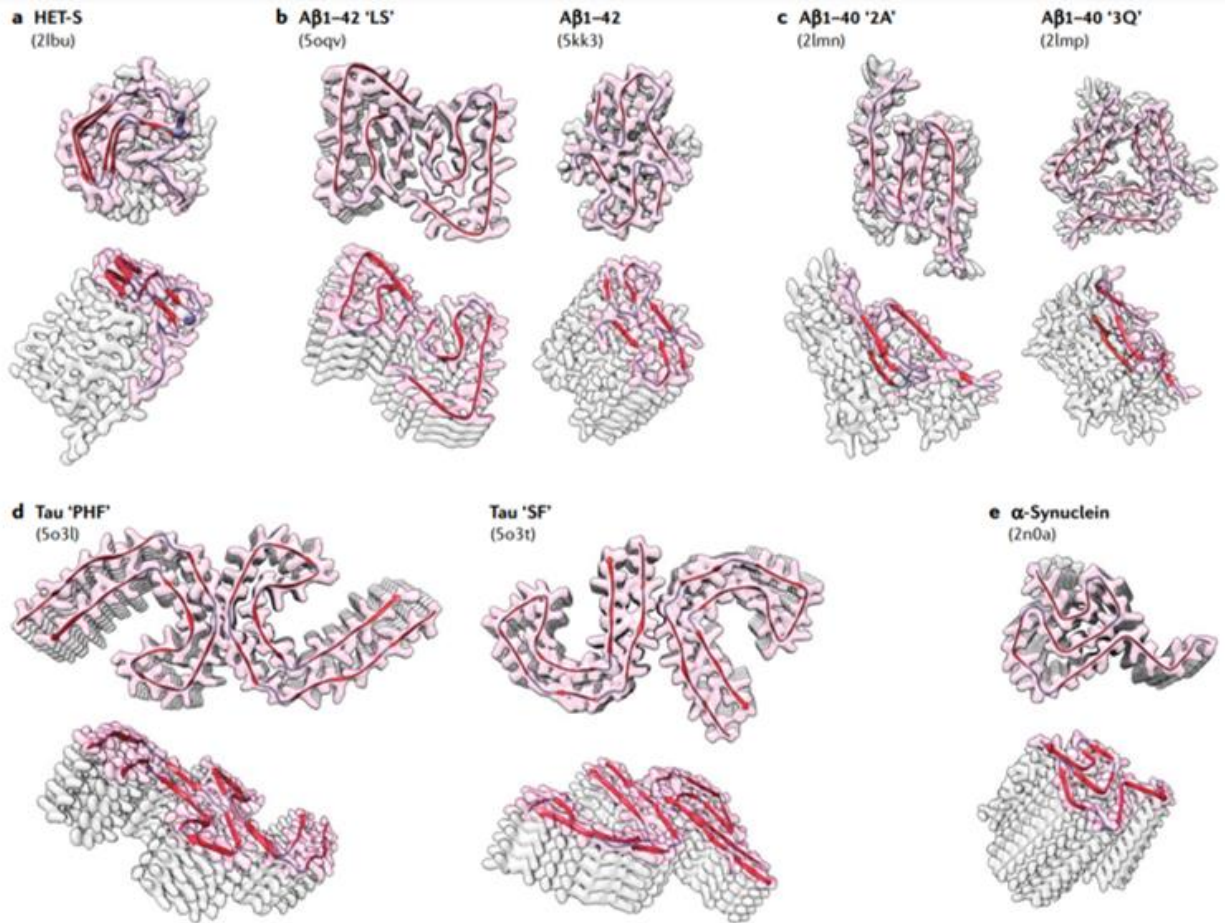
Figure 1.5 - Space filling representation of near-atomically resolved amyloid fibril structures formed by different amyloidogenic proteins. a) HET-S, b) Two polymorphs of $A\beta_{1-42}$ formed under different growth conditions, c) Two polymorphic structures of $A\beta_{1-40}$ formed under different seeding conditions, d) Two polymorphic structures of Tau and e) structure of α-synuclein. Reprinted with permission from [45]

arms of the U-shape and residues in between form the loop or turn (Figure 1.5c). This is commonly referred to as β-strand-turn-β-strand motif [46] [47]. In the case of $A\beta_{1-42}$, similar dimeric association at the core of the fibril can be found, however instead of a U-shaped motif, a characteristic S-shaped motif is resolvable (Figure 1.5b). Due to the 2 extra hydrophobic residues in $A\beta_{1-42}$, a greater degree of core stabilization is evident in the high resolution atomic structure [48] [49]. Other hierarchical organizations common to amyloid fibrils is maintained, albeit with different helix periodicity over the length of the fibril. One of the major characteristics exhibited

by Aβ fibrillar structures is structural polymorphism [50]. With the same amyloid core (cross-β sheet stacking), variable hierarchical organization has been reported, mainly a trimeric core instead of a dimeric one [50]. Variability in the number of protofibril filaments making up a larger fibril is also not uncommon and has been reported in multiple high resolution structural characterization studies [51] [52]. Amyloid polymorphs are highly susceptible to even minute changes in sourcing of the sample, processing conditions (temperature, pH, ionic strength etc) and cross-seeding based fibril growth. Even though recent studies and the overall consensus in the AD field have implicated lower order oligomers as the neurotoxic species (originally fibrils were thought to be the neurotoxic species), understanding the molecular structure of the amyloid core can provide useful insights in further elucidating the core structure of oligomeric species [53] [54] [55].

1.5 Amyloid- β pathology as a membrane-protein interaction disorder

With the emergence of studies implicating Aβ oligomers as the major species that induce neurotoxicity, the next question that naturally arises – what is the exact mechanism by which these oligomers cause the cascade of activities that eventually lead to neuronal death? Multiple lines of thought have proposed that after the formation of Aβ by the proteolytic cleavage of APP, in the early stages of oligomerization, dynamic, energetically metastable nuclei formed interact with cellular membranes through a myriad of mechanisms (intermolecular forces mediated, hydrophobicity interactions mediated or active mechanisms involving molecular chaperone machineries, cell surface receptors etc). These Aβ-membrane interactions are not just happening

at the plasma membrane interface, but also with membranes of intracellular compartments such as mitochondria, endosomal membranes, lysosomal compartments etc.
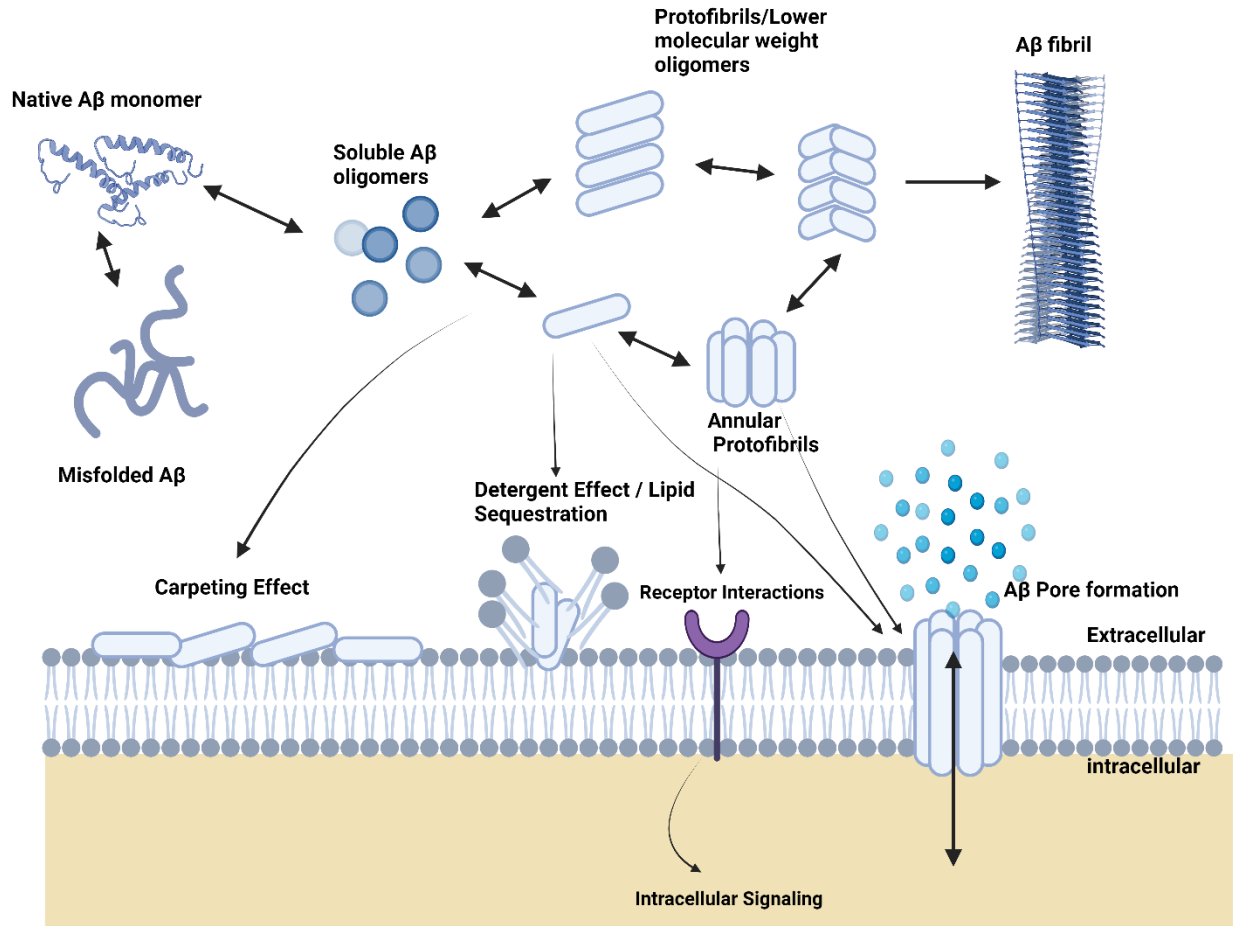
Figure 1.6 - Possible modes of Aβ-Membrane interactions

Monomers and oligomers of Aβ can interact with membranes via multiple mechanisms and pathways. The interactions are further modulated by lipid specificity in the membrane, membrane properties (such as membrane ordering, packing density, curvature) cholesterol content, environmental factors such as temperature, pH etc. Aβ – membrane interactions can also differ based on the type, structural features, and relative concentration of the oligomeric

species. Among the type of Aβ-membrane interactions studied in the AD field, some of the commonly reported ones include (Figure 1.6) i) carpeting effect, where in the oligomeric species of Aβ form a 2-D planar layer on lipid membranes and exert indirect localized stress on the membrane [56], ii) detergent effect, analogous to a surfactant's behavior, the oligomeric Aβ species sequester lipid molecules from the membranes, thereby destabilizing the membrane which in turn could trigger other modes of cell death [57], iii) amyloid pore/ion channel formation – preformed oligomeric complexes resembling annular pore like structures or membrane assisted oligomerization of Aβ can form pore like structures in the membrane that act as unregulated ion flux conduits disturbing the ionic homeostasis of cells and cause cell death [58] [59], iv) monomers and oligomers of Aβ can act as ligands to cell surface receptors which can activate/deactivate important cellular functions served by the receptors or the ligand-receptor interaction can activate signaling mechanisms inside the cell, causing an indirect cascade of events that lead to cell death [60].

As with amyloid fibrils, the oligomeric species of Aβ show structural (atomic level secondary and tertiary structures for lower order oligomeric species are not yet fully resolved) and morphological polymorphism. It's not uncommon in biophysical and structural studies of Aβ-membrane interactions, the same starting peptide can form a wide variety of structures ranging from few n-mer linear, annular, and primitive protofibrils to large amorphous aggregate assemblies. The complexity is increased even more when all of these polymorphic structures also show a concentration, micro-environment, and membrane specificity-based dependencies (Figure 1.6). From a thermodynamic standpoint, these polymorphic structures and aggregates can be thought of as the native protein traversing through all possible conformations down the

protein folding energy well [61]. The oligomeric and structural intermediates (along the pathway

of an Aβ oligomer forming a fibril structure) are thus thought to be local energy minima in the
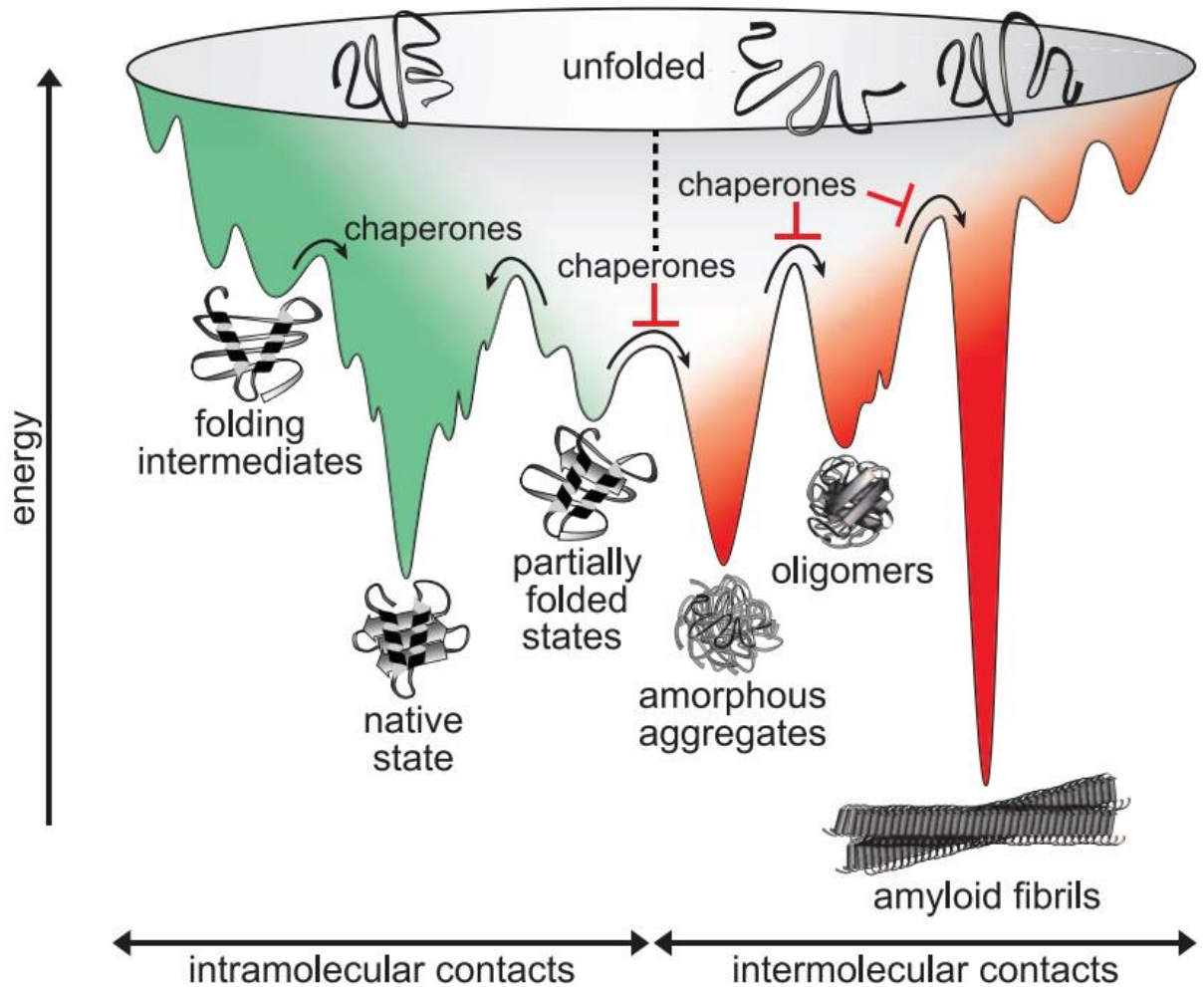
Figure 1.7 - Protein folding energy landscape and its relevance in amyloid formation. Adapted from [61]. Reprinted with permission from AAAS.

protein folding energy landscape (Figure 1.7). Amyloid fibrils are stable structures that form as

the end point of the folding cascade and thus found at the global minima of the energy landscape.

Thus, oligomers and some folding intermediates can be thought of as kinetically trapped

structures which are different than the native conformation of the protein [44]. This has also led

to AD and Aβ pathology being labeled as a 'protein misfolding' disorder. Hence, understanding

the structural features of the cytotoxic oligomeric intermediate and its interaction with the membrane seems to be the key to understanding Aβ pathology.

1.6 Amyloid Ion Channel/Pore Hypothesis

With the oligomer hypothesis gaining ground over the years, the focus is now to pinpoint which oligomeric type, conformation and mechanism is actually involved in pathological cascade of AD. The amyloid ion channel/pore hypothesis proposes that Aβ, either through direct interaction of pre-formed oligomeric complex with the membrane or oligomerization in the membrane environment, leads to the formation of structures which behave as ion channels/pores. These ion channels/pores are unregulated in nature, weakly cation selective and induce unregulated Ca^{2+} ionic flux into neurons leading to Calcium dyshomeostasis and putting the cell in the path of death. The evidence for this hypothesis mainly stems from electrophysiological studies of Aβ peptides in planar bilayers and patch clamp recordings, atomic force microscopy (AFM) imaging and Electron Microscopy (EM) of Aβ structures in synthetic and natural cell membranes alike. Arispe et al, in 1993, were the first to show that $Aβ_{1-42}$ forms cation selective, multi-conductance level channels in membrane-mimetic environments [59] [62]. Interestingly, this conductance could be blocked by Zn^{2+} ions and dyes such as Congo red. Subsequent, similar studies by multiple groups have also confirmed the ionic flux created by $Aβ_{1-42}$ can be due to some form of oligomeric structure in the membrane that can behave as an unregulated ion pore [63] [64] [65]. Morphological imaging data from AFM and EM confirmed the presence of annular donut like structures in the membrane with a central pore that resembles an ion-channel structure with a tetrameric or hexameric subunit morphology[58] [66] [67]. The

sizes of these annular channel-like morphologies were reported to be in the range of 6-15nm, with the central pore 0.8 – 2nm in size. Molecular Dynamics (MD) simulations have also shown the possibility of a stable 4 - 6 subunit morphologies in the membrane which can contain between 16 – 36 monomers of Aβ [68] [69] [70].

1.7 Biomechanical aspects of membrane-protein interactions

With a multitude of biological and biochemical factors directly involved in modulating membrane-protein interactions, new lines of studies have also shown the possibilities of biomechanical factors directly affecting the process. Cell membranes with their underlying cytoskeleton and biomimetic lipid bilayers on flat substrates serve as mechano-biological matrices which tightly modulate protein function at the nanoscale [71]. One of the widely understood systems in this category are mechanosensitive ion channels whose activity is precisely controlled by stress experienced by the membrane environment they are in. Macro scale factors such as touch, vibration etc can act to cause mechanical stress on the membranes of the cells involved and the resultant mechanical stress can activate/deactivate some on the ion channels present on the membrane. Most commonly, membrane tension is known to directly influence the electrophysiological activity of MscM, MscS and MscL ion channels (mechano-sensitive ion channels of mini, small and large conductance activity) which in-turn can regulate osmotic pressure difference between the inside and the outside of the cell [72] [73]. These regulatory functions can also be controlled by the lipidic makeup of the membrane, modifications to lipids, cholesterol content and degree of membrane crowding [74] [75]. Notably, lipid phase separated domains on the cell membrane (called lipid rafts) are known to sequester certain

proteins into localized domains and thereby regulate functions of proteins [76] [77]. Lipidic

factors such as chemical nature of lipids, charge and mechanical properties of the membranes

formed also control protein-protein interactions happening on or in the membrane environment.

In the case of Aβ, it has been extensively reported that membrane factors can affect the

probability of a particular polymorph being favored and the concentration and type of oligomers

being formed [56][68]. The amyloid ion channel hypothesis doesn't directly suggest any mode of

ion channel regulation activity via membrane factors, however the possibility of lipidic factors

affecting channel properties such as conductance, gating and kinetics should be a part of future

experimental designs to validate the ion channel hypothesis. The amphiphilic membrane

environment is quintessential for proper folding of membrane proteins. Thus, any changes to

membrane mechanics can also alter protein-folding behavior and indirectly the function of the

protein [61].

Cell membranes specifically, and their biomechanical properties control large scale

cellular functions such as cell division, motility, cell-cell adhesion, nutrient and foreign material

uptake and expulsion via processes such as endo- and exocytosis etc., [78] [79] [80] Particularly

in endo and exocytosis mechanisms, special proteins are recruited at the membrane interface

which actively help in remodeling of the plasma membrane to engulf the incoming cargo and

transport it further into or out of the cell respectively. This process is energy intensive and

membrane specific factors such as membrane tension, curvature, membrane fluidity etc.,[80]

[81] can heavily influence the outcome of these processes. The role of mechanobiological factors

in etiology and progression of few diseases have been well documented and, in some cases,

forms the molecular basis of disease causation [82]. Hence, a high degree of mechano-biological

22

coupling has to be considered in understanding the overall landscape of membrane-protein interactions.

1.8 Atomic Force Microscopy

Atomic Force Microscopy (AFM) is a high-resolution, extremely sensitive, scanning probe-based surface imaging and force measurement technique, widely used for imaging at the micro- and nanoscale. After the invention and demonstration of Scanning Tunneling Microscopy (STM) in 1982-1986 by Gerd Binnig and Heinrich Rohrer [83] [84], it was quickly realized that STM was severely limited to the study of conductive samples in vacuum conditions. As all biological samples do not meet this requirement, AFM was born out of the necessity for observing biological molecules and processes in their native environments [85]. For a long time and to this day, fluorescence microscopy has been the go-to method for the visualization of the biological world, offering a wide range of specific fluorescent probes which can be bound/tagged to the biological molecule of interest. However, in conventional fluorescence microscopy, the resolution is limited by the diffraction limit (~200nm). Even though very detailed images could be gathered for large feature sizes, most of the active biomolecules of interest such as proteins, DNA, intracellular compartments etc are well within the 200nm limit and cannot be observed with fine details through fluorescence microscopy. Additionally, there is always an uncertainty of the behavior and dynamics of the biological system being disturbed from its native configuration due to sample preparation requirements and in some cases chemical cross-linking of fluorophore molecules. Electron Microscopy (EM) such as Scanning Electron Microscopy (SEM) and Transmission Electron Microscopy (TEM) offer X-Y resolution of ~10nm and ~1nm respectively,

however are severely limited by the vacuum conditions used for imaging. AFM overcomes all of these difficulties and offers the flexibility of imaging biomolecules in their native environment without any modifications to the sample. The X-Y resolution in AFM is limited by the probe shape, but in special cases, resolutions of ~1nm have been demonstrated (typical resolution of 10nm can be expected in routine imaging). One of the most attractive features of AFM is the z-resolution, which can reach up to 100pm (limited by thermal noise) [85] [86].
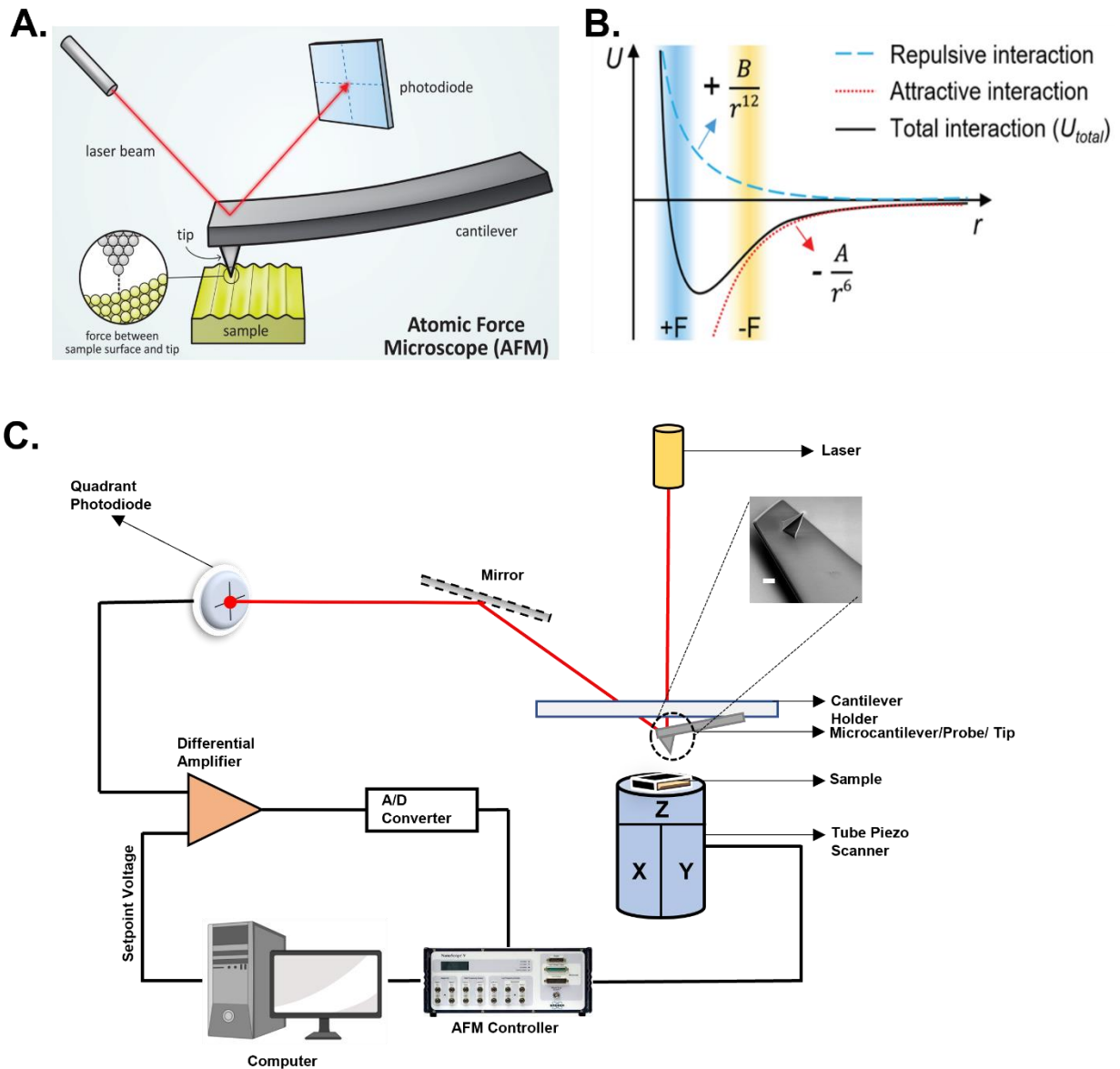
Figure 1.8 - Concepts in AFM. A) Schematic describing the mechanism of AFM imaging, B) AFM probe-sample interaction force dependence on distance, C) Practical implementation of AFM machinery and electronics. The schematic displays 'sample scanning' type of AFM, wherein the probe is held stationary, and the sample is moved.

In AFM, a sharp microcantilever probe vertically deflects from its equilibrium position when its brought into close proximity to the sample (Figure 1.8A). Under the influence of intermolecular Van der Waals attractive force and repulsive forces due to coulombic and exclusion forces, the cantilever undergoes vertical deflection at each point of the scanned area

(Figure 1.8, B). As the probe is scanned on the surface of the sample in a raster pattern, the deflection of the probe at each point on the sample is monitored using a laser beam reflected from the back face of the cantilever (Figure 1.8, A and C). With the deflection of the probe proportional to surface topography, a one-to-one topographic height map of the surface can be reconstructed. AFM can be operated in air or native fluid/buffered environments with minimal force applied, making sure the morphology is undisturbed.

Figure 1.8C shows the schematic of a commercially available AFM instrumentation setup. Sample movement in X,Y and Z is controlled by piezoelectric crystals (tube piezo in this case). The cantilever is mounted onto a holder and a laser light bounces off the back of the cantilever, which responds to changes in deflection by vertical translation of the reflected laser beam spot on the quadrant photodiode (Optical Beam Deflection (OBD) method). The signal from the photodiode is compared against a 'setpoint' voltage input by the user (the setpoint value controls the magnitude of force imparted by the probe to the sample) and a control signal is generated by the controller that modulates the Z-piezo behavior in response to changes in surface topography. Monitoring the Z-piezo modulation voltage also gives a one-to-one signal which is proportional to the surface height changes. This is the basis of working of most modern AFMs. The very first AFMs worked in a type of AFM imaging mode called the contact mode, in which the probe comes into contact with the sample. However, in some situations, such as soft biological materials, this can be problematic due to sample damage and as such advanced non-contact modes of AFM were developed. One such mode is called Tapping mode in which the cantilever is vibrated at its resonance frequency. When the vibrating probe is brought closer to the sample surface, the probe-sample force modulates the amplitude of vibration of the cantilever and this change in

amplitude is also proportional to surface topography. Thus, sample damage is minimal to non-existent as the probe doesn't come into contact with the sample [87].

AFM started out as a sensitive imaging technique. However, the principle of working of AFM is from a surface force measurement standpoint, which makes it an ideal tool to measure very small forces which are involved in nanoscale interactions of biological molecules. AFM has a force sensitivity in the ~1-10pN range and thus is ideally suited in measurement of forces involved in ligand-receptor binding kinetics, energetics of surfaces, forces that hold a protein in a 3D conformation etc [84] [88]. As AFM is a probe-based technique, it's also capable of applying pico-Newtons to micro-Newtons levels of forces to deform the sample and quantify the mechanical properties of samples. All of these are collectively put under the category of 'AFM Force Spectroscopy' [89]. AFM has also been used as a 'nanomanipulator' to precisely construct and manipulate features at nanoscale (dip-pen lithography), thus acting as an alternate nanolithography approach for bottom-up design of nanoscale structures [90].

Although AFM is an ideal technique to study biological interfaces at nanoscale, the technique does suffer from a few drawbacks, one of the major being the speed of acquisition of frames. As it's a raster technique and used with tube piezos, limitations on the speed of acquisitions are placed due to mechanical constraints on the piezo scanners. Another major issue with AFM is that the lateral resolution is limited by the shape and radius of curvature of the probe. When trying to image a feature smaller than the radius of curvature of the probe, the dimensions of the feature in the lateral direction tend to be overestimated. This is called tip-broadening or tip-convolution effect. However, recent developments in AFM electronics have led to high-speed AFM (HS-AFM) which can acquire 10s or 100s of frames per second, enabling

dynamic processes to be monitored by AFM [91]. Algorithms that account for the tip broadening effect have been developed, which can improve the accuracy of measurements [92].

1.9 Voltage Clamp Electrophysiology and Black lipid membranes

One of the widely used techniques to understand the electrical behavior of biological systems is the patch clamp current recording [93] [94]. Pioneered by Neher and Sakmann, the technique consists of creating a gigaOhm seal with the plasma membrane of cells using micropipettes, forming a small area ('the patch') which can contain ion channels expressed on the surface of cells. Two electrodes, one through the micropipette and another submerged in the bath electrolyte solution containing the cells, can be used to provide a voltage bias to the patch and the resulting currents from the applied voltage can be recorded. From the recorded currents, the kinetic behavior and electrical characteristics of the ion channel can be deduced.

As an extension and simplification of the original patch clamp technique, planar lipid bilayer recordings can be performed [95], wherein a lipid bilayer is formed on a circular aperture (typical diameter of the aperture can range from 50µm to 300µm) created on the vertical wall of a cuvette chamber (typically made of inert low energy materials such as Teflon, Delrin etc). Another cuvette chamber is mechanically connected to the first chamber, forming a 2-cell recording system (Figure 1.9). Ag/AgCl reference electrodes are positioned in each of the cuvettes that can record currents passing from one chamber to another, depending on the voltage bias provided. The electrode system is connected via a head stage (operational amplifier

circuit) to the high gain voltage clamp amplifier which can measure currents in the 10s of fA

(femtoampere) to nA (nanoampere) range [96].
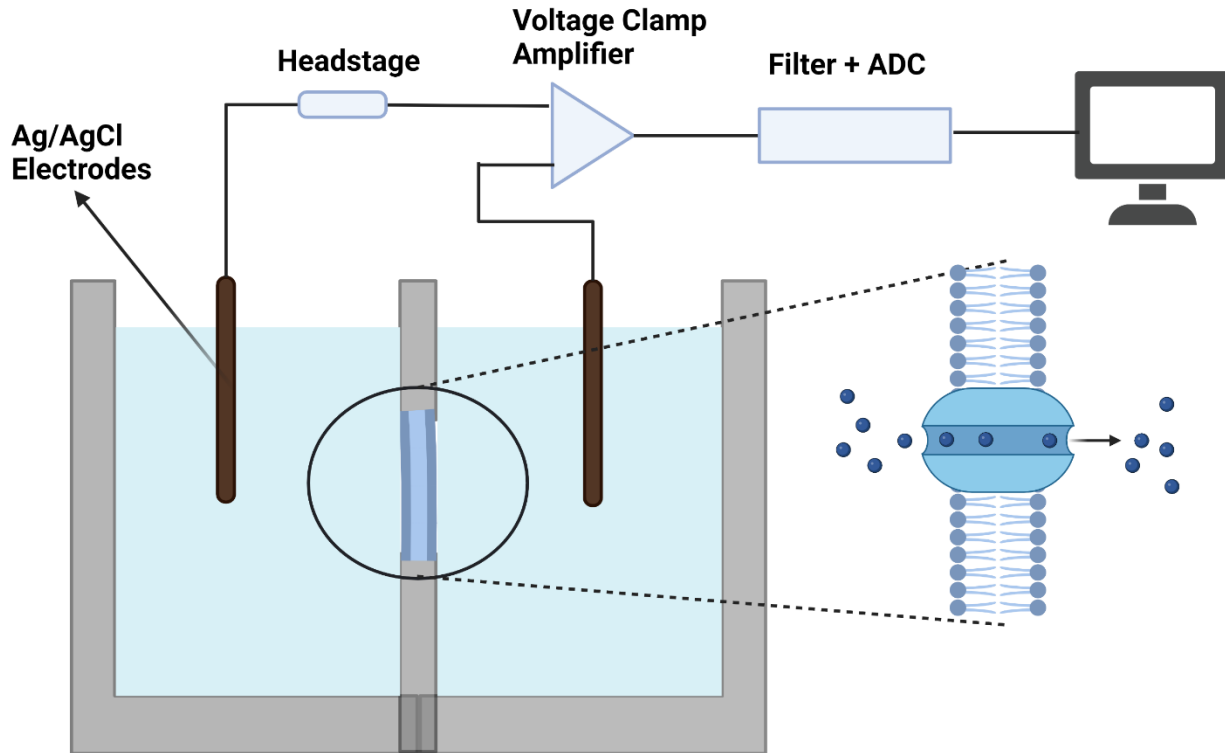
Figure 1.9 - Experimental setup of voltage clamp electrophysiology of ion channels in planar lipid bilayers. The inset to the right shows one ion channel molecule embedded in the lipid bilayer formed on the aperture, which is submerged in a buffered electrolyte solution (commonly a buffer + KCl).

In a typical planar lipid bilayer electrophysiology experiment the lipid bilayer is formed by

via one of 2 methods – i) 'painting' method, wherein lipids dissolved in organic solvents such as

heptane, decane or squalene are painted on the aperture using a paint brush and bilayer

formation is spontaneously induced by adding a high ion strength recording solution (also known

as black lipid membranes due to their optical opacity in the apertures, ii) Montal-Mueller method,

wherein lipids dissolved in organic solvent is added to each of the cuvette which have small

amounts of recording solution whose levels are initially below the aperture height. As the organic

solvent starts evaporating, a fluid perfusion setup starts raising the level of the solution in

cuvettes above the aperture level, which causes individual leaflet of lipids to fuse in the aperture forming a bilayer. The lipid bilayers formed have capacitances of 0.8-1uF/cm^2 and resistances of 1-10 GΩ. Once a bilayer is formed, ion channel peptides/proteins can be directly added to the cuvettes or a proteoliposomes containing the protein can be fused with the formed bilayer, incorporating the ion channel into the planar bilayer. Any kind of molecules (agonists and antagonists) that can have an effect on the behavior of the ion channel, environmental factors can also be changed and the kinetics of the ion channel under these conditions can also be studied. One of the major advantages of using this approach lies in its sensitivity and dynamic range of the experimental setup. These voltage clamp amplifiers can measure currents even from an individual ion channel (displaying currents in the lower pA range) [96].

2.0 Summary of the Dissertation

This dissertation can be divided mainly into three sections. The first part focuses on the biophysical and biochemical characterization of distinct Aβ peptide species in lipid bilayer and cell membrane environments through a combination of biophysical techniques such Spectroscopy, AFM imaging and voltage clamp electrophysiology. These studies help shed some light on the prospective mechanisms of AD progression. The second part focuses on understanding the structural features and unfolding behavior of Aβ oligomers via AFM based single molecule force spectroscopy. The third part consists of design and implementation of a combined AFM and TIRF microscopy system for future studies of membrane-interaction at high spatio-temporal resolution. In chapter 2, we show the dependence of amino acid sequence and readability dependence on amyloid formation from a fundamental biophysical and biochemical

standpoint. In chapter 3, we show the structural characteristics and functional behaviors of N- and C-terminally truncated Aβ species. In chapter 4, we focus on an in-depth structural and functional characterization of full length Aβ$_{1-42}$, Aβ$_{1-40}$ and their pyroglutamylated variants AβpE$_{3-42}$ and AβpE$_{3-40}$ in biologically relevant membrane systems to elucidate the role of post-translational modifications in AD progression. In chapter 5, we focus on characterizing the protein unfolding behavior of Aβ$_{1-42}$ oligomers in different membrane environments. In chapter 6, we show the development of AFM-TIRF combined microscopy modality for high spatiotemporal resolution structure and function imaging.

Chapter 2

Amino acid sequence and readability dependence in Aβ-membrane interactions

2.1 Introduction

Neurodegenerative diseases are a group of conditions that involve the progressive loss of neurons in the brain and spinal cord, cognitive and motor function decline, dementia, and death. One of the major modes of neurodegeneration of interest is due to the accumulation of misfolded proteins, which can lead to the formation of aggregates known as amyloids [4][5]. Amyloid beta (Aβ) is one such protein that has been implicated in Alzheimer's Disease (AD) [33]. Aβ peptide is produced by cellular membrane metabolic processes which involve cleavage of amyloid precursor protein (APP) by successive activity of β-secretase and γ-secretase [11]. In Alzheimer's disease and other neurodegenerative diseases, Aβ aggregates and accumulates in the brain, leading to the formation of extracellular amyloid plaques [4]. This forms the basis of the amyloid hypothesis of AD, which states that the deposition of Aβ as plaques, triggers a series of events, some of which ultimately lead to synaptic loss and neuronal death [12] [41].

Of the different variants of Aβ, $Aβ_{1-42}$, a 42 amino acid long peptide, and $Aβ_{1-40}$ are the predominant isoforms found in the amyloid plaques that are characteristic of AD [97]. Multiple research studies and clinical trials have focused on developing therapeutics targeting clearance of amyloid plaques from brain matter [98] [99] [100]. Oligopeptides, small molecule Aβ moderators such as Anle-138B [101], AmyP53 [102] and , monoclonal antibody [100] based immunotherapies are being continuously investigated in the AD field to find the best possible

therapeutic solution to halt AD progression and reverse the cognitive decline. Success of these therapeutics rely on interaction of these molecules with different conformational states of Aβ, or Aβ aggregates, and its complex with the lipid membrane. It is well known that the amino acid sequence of a protein/peptide plays a critical role in determining its structure and function. Although, only the primary structure of a protein is genetically encoded, the functional tertiary and quaternary structures of proteins are formed from the amino acid sequence in conjunction with environmental variables such as pH, ionic strength, temperature etc. To a degree, the sequence of the protein determines its interfacial interactions with other molecules and surfaces and these interactions in turn decide the final folded structure of the protein. This would naturally imply that disturbing the native sequence should lead to changes in interfacial interactions and the final structure, sometimes even leading to loss of a definitive structure. Amyloids, which are highly organized and regular aggregates of proteins, are thermodynamically stable species formed by self-association of the peptides. Initial understanding of the biochemical properties of amyloid forming proteins held the notion that only certain proteins/peptides are capable of forming amyloids and amyloid formation is mainly driven by reserved sequences of amino acids with high propensity for aggregation [103]. However, this understanding has now evolved and it's the consensus that almost >90% of known proteins or some domains in those proteins are capable of forming amyloids, with atleast 50 proteins directly linked to diseases [45]. Hence, there seem to be universal principles governing the amyloid formation and the mechanism maybe evolutionarily conserved. Therefore, it is highly essential to understand the role of amino acid sequence, the relative content of hydrophobic amino acids in the evolution of Aβ structures, its interaction with membrane, cellular toxicity, and how changes in its amino acid

sequence can affect its propensity to form amyloid fibrils and its toxicity to neurons. These fundamental studies might further lead us to better understand the interaction of therapeutic molecules and explore the rationale behind its success or plausible failure. Most of the research in the field have majorly focused on understanding amyloid fibrillation and aggregate mediated neural toxicity, with more recent studies focusing on oligomeric species of Aβ as neurotoxic agents. Even then, a clear molecular understanding of the mechanism of Aβ mediated cascade of neurotoxic effects has not fully emerged. Systematic studies exploring the link between amino acid sequence, hydrophobic amino acid levels, and their interaction with the membrane under a single framework have been very limited [104] [105]. This is why it is interesting to study the effects of changes to Aβ$_{1-42}$ from an amino acid sequence perspective. Modifications such as reversing the amino acid sequences and scrambling of the sequence can provide valuable insights into the role of the amino acid sequence, its arrangement and global amino acid content (within the sequence) in amyloid formation. Comparing the properties of these Aβ variants with the normal sequence of Aβ$_{1-42}$, can provide a better understanding of the specific amino acids and structural features that are critical for amyloid formation and toxicity.

To understand the role of amino acid sequence and readability in Aβ$_{1-42}$ structure, and function, we performed computational analysis to predict amyloid forming propensity using web server for prediction of amyloid structural aggregation, PASTA 2.0 [106]. The amyloid growth kinetic analysis was performed by Thioflavin-T assay and evolution of sequence specific protein hydrophobicity using ANS binding mediated fluorescence. The sequence specific variation in protein secondary structure was analyzed by circular dichroism analysis. Morphology of amyloids were observed by atomic force microscopy. Further, we also analyzed the structural changes

mediated propensity of peptide toward proteinase-K digestion by SDS-PAGE analysis. Voltage clamp electrophysiology was performed to analyze the interaction of peptides with lipid membrane both in presence and absence of Zinc ion, an amyloid ion channel blocker. Finally, we also performed cell viability studies and fluorescence imaging-based quantification of calcium uptake by B103 neuroblastoma cells to elucidate the role of aa-sequence in cellular toxicity and membrane interaction.

2.2 Materials and Methods

2.2.1 Materials: $A\beta_{1-42}$ - normal, reverse and scrambled variants were purchased from Anaspec, Inc. 1,2-dioleoyl-sn-glycero-3-phosphocholine (DOPC),1,2-diphytanoyl-sn-glycero-3-phosphocholine (DPhPC) lipids were purchased from Avanti Polar Lipids. 1-Anilinonaphthalene-8-Sulfonic Acid (ANS) was purchased from Cayman Chemicals. 4-20% TGX Mini-Protean precast polyacrylamide gels and Precision Plus Dual Xtra protein standards were purchased from BioRad Laboratories. ProteinaseK was purchased from New England Biolabs. 3-(4,5-dimethylthiazol-2-yl)-2,5-diphenyl-2H-tetrazolium bromide (MTT) was purchased from Biotium and Fluo4-AM calcium detection dye was purchased from Invitrogen. Throughout the manuscript, we have adopted the following naming convention for the peptides - $A\beta_{1-42}$ is referred to as Aβ-N, the reverse variant $A\beta_{42-1}$ is referred to as Aβ-R and the scrambled variant is referred to as Aβ-S. Their respective sequences are as follows:

Table 1.1 : Amino acid sequence of the 3 Aβ peptides

Peptide	Sequence
Aβ-N	DAEFRHDSGYEVHHQKLVFFAEDVGSNKGAIIGLMVGGVVIA
Aβ-R	AIVVGGVMLGIIAGKNSGVDEAFFVLKQHHVEYGSDHRFEAD
Aβ-S	AIAEGDSHVLKEGAYMEIFDVQGHVFGGKIFRVVDLGSHNVA

Methods

2.2.2 Amyloid Propensity Prediction using PASTA 2.0 web server

In order to predict the aggregation propensity, disorder and the supposed secondary structure acquired by the 3 different variants of the Aβ$_{1-42}$ purely on sequence-based properties, we used the PASTA 2.0 web server (http://old.protein.bio.unipd.it/pasta2/about.html, [106]). PASTA 2.0 uses segment pairwise statistical energy function minimization approach to predict amyloidogenic regions (regions of the sequence with high propensity to aggregate). The algorithm has also been trained using available PDB data to predict secondary structure and intrinsic disorder in the peptides. We used default parameters to run the predictions - energy threshold of -5.96 Kcal/mol, TPR (sensitivity) of 43.6% and FPR(1-specificity) of 5.1%.

2.2.3 8-Anilinonapthalene-1-sulfonic acid (ANS) hydrophobicity assay

In order to assess how exposed the hydrophobic cores of the 3 peptides were in solution, we performed ANS exclusion assay at 0 hrs (freshly solubilized) and after 24hrs in fibrillization

conditions. Stock solution of ANS was prepared by dissolving ANS at a concentration of 20 mg/ml in DMSO and thereafter diluted in 1xPBS to 1 mg/ml. The diluted ANS solution was mixed with 10 uM of peptide solution and incubated for 30 min at room temperature. Fluorescence emission intensity was scanned between 400-700 nm with excitation at 350 nm in a spectrofluorometer (Tecan Infinite M200 Pro, Tecan Instruments, Belgium). From the recorded spectra, we evaluated the amplitude of fluorescence emission and wavelength blue shift of the peptide spectra with respect to ANS only emission peak (approximately at 535 nm).

2.2.4 Circular Dichroism Spectroscopy

Circular Dichroism spectroscopy was performed to assess the secondary structure of the 3 peptides at 2 time points: freshly solubilized and after 24 hrs under fibrillization conditions (incubated at 37C in PBS 1X buffer) according to standard procedure [107]. The peptide concentration used was 10uM. Aviv 202 spectropolarimeter (Aviv Biomedical, Lakewood, NJ) was used in the wavelength scan range of 200-300 nm (bandwidth of 1 nm), at a temperature setpoint of 25°C. Three scans were performed for each peptide and the data were averaged. The raw data were then converted and expressed in mean residue ellipticity $[\theta]_{mrw}$

2.2.5 Amyloid stability assay & gel electrophoresis

In order to probe the biochemical stability of the 3 peptides and their relative resistance to degradation by proteolytic cleavage, we performed a ProteinaseK digestion assay on the freshly solubilized peptides. The products of proteolytic cleavage were analyzed by SDS-PAGE gel electrophoresis. The peptides were divided into 2 groups: control (no ProteinaseK added) and test (ProteinaseK added). Briefly, test group peptides at concentrations of 100uM were mixed

with 170uM of ProteinaseK solution and incubated at 37°C for 10 minutes. To stop the proteolysis reaction, the mixture was placed in a boiling water bath for 60 seconds. Next, the control and test groups were mixed with 5% SDS solution and incubated for 5 minutes at room temperature. The peptide mixture with SDS was then loaded onto individual lanes of a 4-20% gradient polyacrylamide gel at 10ug peptide per lane (TGX Mini-Protean precast polyacrylamide gels) with Precision plus protein molecular weight standards in 2 separate lanes. The loaded gel plates were then assembled in an electrophoresis system (Mini Protean tetra cell, BioRad) with a gel loading buffer (SDS-Glycine). Electrophoresis was performed at a constant voltage of 80V (20-30mA current) until the peptide products were fully resolved.

2.2.6 ThioflavinT (ThT) fibrillization assay

In order to assess the hydrophobicity driven aggregation (fibrillization) of the 3 peptides, we performed a ThioflavinT kinetics assay using standard techniques [108]. Briefly, peptides were mixed at a final concentration of 10uM, 20uM ThT (stock solution prepared in 1X PBS) and PBS 1X to a final volume of 100ul. Triplicate samples were aliquoted in 96-well plate and fibrillization kinetics were monitored over 24 hours at 37C in a spectrofluorometer (Tecan Infinite M200 Pro). Fluorescence intensity readings were taken every 5 minutes (excitation - 440 nm, emission-488 nm) with 1s shaking before taking fluorescent intensity reading. Data are expressed in normalized fluorescence units. In order to calculate the kinetic constant (k) and lag time, the data (after buffer subtraction) were fit using the following equation 2.1:

$$F(t) \; = \; F_0 + \frac{a}{(1+e^{-k(t-t_{1/2})})} \qquad\qquad (2.1)$$

Where, F is the fluorescence intensity at time t, F_0 is the fluorescence intensity at t=0, a is the maximum fluorescence intensity, $t_{1/2}$ is the time taken to reach half maximal fluorescence and k is the rate constant (units = hr^{-1}). After fitting the data with the above equation, the lag time (t_{lag}) was calculated with equation 2.2:

$$t_{lag} = t_{1/2} - \frac{2}{k} \qquad\qquad (2.2)$$

2.2.7 Voltage Clamp Electrophysiology

The electrophysiological activity of the 3 peptides were probed using voltage clamp bilayer electrophysiology setup [66] [108]. Bilayers were formed by the lipid painting method on 250um diameter apertures carved out in Delrin cuvettes [109]. Briefly, dried lipids were dissolved in decane to a final concentration of 25-35 mg/ml. The lipids in decane solution were then painted (priming) on the apertures using the fine bristles of a paint brush. The painted apertures were then left to dry for >4 hours. After drying the cuvettes were assembled in a conventional 2-well set up. Recording buffer (10mM Hepes, 1M KCl, pH 7.4) was then added to each of the wells to submerge the aperture. To aid in spontaneous bilayer formation via thinning, a glass blob terminated pasteur pipette was gently brushed on the aperture and bilayer formation was monitored by real-time capacitance changes. We set a threshold of >90pF for optimal bilayer formation. In all the experiments, the typical capacitance of the bilayer was 110-180pF. The voltage clamp setup consisted of a high gain electrophysiology amplifier (Warner Instruments BC-535) connected to a resistive feedback headstage with telegraphed gain connections. All the data were collected at a sampling frequency of 10kHz and passed through an integrated 8-pole Bessel filter in the amplifier, with a cutoff frequency of 1kHz. All the data were digitized through

an analog-to-digital converter (Digidata 1440A, Axon Instruments) which was in turn connected to a workstation computer running the Clampex data acquisition software (v10.6, Axon Instruments). All subsequent data analysis was carried out in Clampfit software (v10.6, Axon Instruments). The data collection protocol consisted of applying a hold potential (voltage clamp) from -100mV to 100mV in 50mV increments. Data was collected for 2-3 minutes at each of the hold potential. Bilayer capacitance was monitored every few minutes for the whole duration of the recording to ensure bilayer stability. After bilayer stability was ensured, peptides were directly added to the trans side of the setup at final concentration of 1uM and stirred using micro stirbars (total volume in each well was 1ml). For zinc blocking experiments, after electrophysiological activity was visually apparent at a particular clamp voltage, zinc chloride solution was added to one of the recording chambers (trans side) in increments of 5mM, until the activity visually subsided and the current returned to I=0pA baseline (wherever applicable).

Electrophysiology Data Analysis

All the raw traces collected were transferred to the Clampfit analysis environment. First, offset correction was performed by subtracting the current at 0mV applied potential from the whole trace (typically 2-3pA of current offset). Then, a manual baseline correction was performed in the cases where a baseline drift was apparent. In order to remove 60Hz noise from the traces, a digital low pass filter with a cutoff frequency of 50Hz was applied on the traces. For visualization purposes, we chose snippets of the recording of time duration 150-300s and histograms of these traces were also generated.

2.2.8 Atomic Force Microscopy (AFM) Imaging

The size distributions of the peptides devoid of membrane and their morphologies in the membrane were investigated by AFM imaging. Freshly solubilized peptides and peptides that were put under fibrillization conditions were imaged directly on mica. Briefly, peptides were diluted to 1uM final concentration and deposited and incubated on a freshly cleaved piece of mica for 5 mins and washed 3x with imaging buffer (10mM HEPES, 300mM KCl, pH 7.4). For imaging peptide interactions with membranes, we chose to image only freshly solubilized peptides. Briefly, dried lipids were hydrated for 20 mins at room temperature in imaging buffer containing 3mM $CaCl_2$ and sonicated in a bath sonicator for 20 minutes to form small unilamellar vesicles (SUVs). Aβ peptides were then added to the vesicle solution at a final concentration of 1-2uM (lipid:peptide relative concentration of 500:1 molar ratio) and further sonicated for 2 mins to form proteoliposomes. A 20ul solution of the proteoliposome solution was then drop casted on a freshly cleaved piece of mica and incubated for 15 minutes at room temperature and washed 3x with the imaging buffer. In all cases, the imaging was performed under fluid conditions in imaging buffer.

AFM imaging was performed with a Multimode V AFM connected to a Nanoscope V controller in ScanAsyst or PFQNM mode (Bruker, Billerica, MA). The cantilevers used had a spring constant of 0.1-0.3 N/m (SNL-10, Bruker). New cantilevers were used for each peptide to avoid cross contamination. All collected images were analyzed in Nanoscope Analysis software (v1.5, Bruker) or Gwyddion. All images were line flattened (1st or 2nd order) and an in-built particle counting feature was used for particle distributions (wherever applicable).

2.2.9 MTT Cell viability

In order to assess the relative cytotoxicities of the Aβ peptides, we performed a MTT cell viability assay. Briefly, B103 cells were cultured in DMEM culture media with 10% FBS and 0.5% Penicillin/Streptomycin. After the cells reached 80% confluence, we transferred the cells to 96-well plates at 10000 cells/well density (100ul well volume). After 6 hours of transferring, we added Aβ peptides at concentrations of 100nm, 1uM and 10uM (diluted in 1X PBS) in triplicates for each of the peptides. A similar volume of 1X PBS without any peptide added was used as the control. Cells were incubated with the peptides for 20 hours in a 37C, 5% CO2 incubator. Next, 10ul of MTT solution (diluted in 1X PBS) was added to the wells and incubated for 3 hours at 37C. After 3 hours of incubation with MTT, 180ul of DMSO was added to each of the wells and mixed thoroughly to dissolve the formazan crystals formed (with 10 minute shaking on an orbital shaker) after the metabolic breakdown of MTT by cells. MTT absorbance was measured at 570nm with 630nm background absorbance subtracted (Tecan Infinite M200 Pro spectrofluorometer). Cell viability is expressed as the ratio of MTT absorbance of test wells (with peptide added) to control wells (no peptide added).

2.2.10 Fluo-4 Calcium uptake assay

We also analyzed the ability of Aβ peptides to induce intracellular calcium flux in B103 cells, with the procedure developed in [66]. Cells were plated on a 35mm coverslip bottom petri dish (MatTek) at 20,000 cells and grown overnight. Fluo-4 AM calcium sensitive dye (Excitation - 488nm, Emission - 517nm) was pre dissolved in DMSO and diluted to 5uM final concentration in culture media. The media in the petri dish were replaced with Fluo-4 containing media and

incubated for 35-40 mins at 37C and 10 minutes at room temperature. The cells were washed

with Fluo-4 imaging buffer (1X HBSS, 20mM HEPES, 5mM CaCl2) and resuspended in the same

buffer. The petri dishes were placed in a 37C imaging incubator mounted on an inverted widefield

fluorescence microscope (Olympus IX71, Hamamatsu ImageEM EMCCD camera). Images were

acquired in a time-lapse fashion for 15 minutes (2 images per minute) after the addition of the

peptide, with a 40X objective lens. The acquired images were background subtracted and regions

of interest were drawn on cells displaying healthy morphology. The mean grayscale intensity of

the ROIs was tracked for the imaging duration.

2.3 Results and Discussion

2.3.1 Computational analysis of Amyloid formation propensity

The full length $A\beta_{1-42}$ can be segmented into 3 parts (Residues: NH_2- 1-14, 15-29 and 30-42-COOH). The C-terminal 1/3rd of the residue is highly hydrophobic in nature and is the aggregation driving domain.
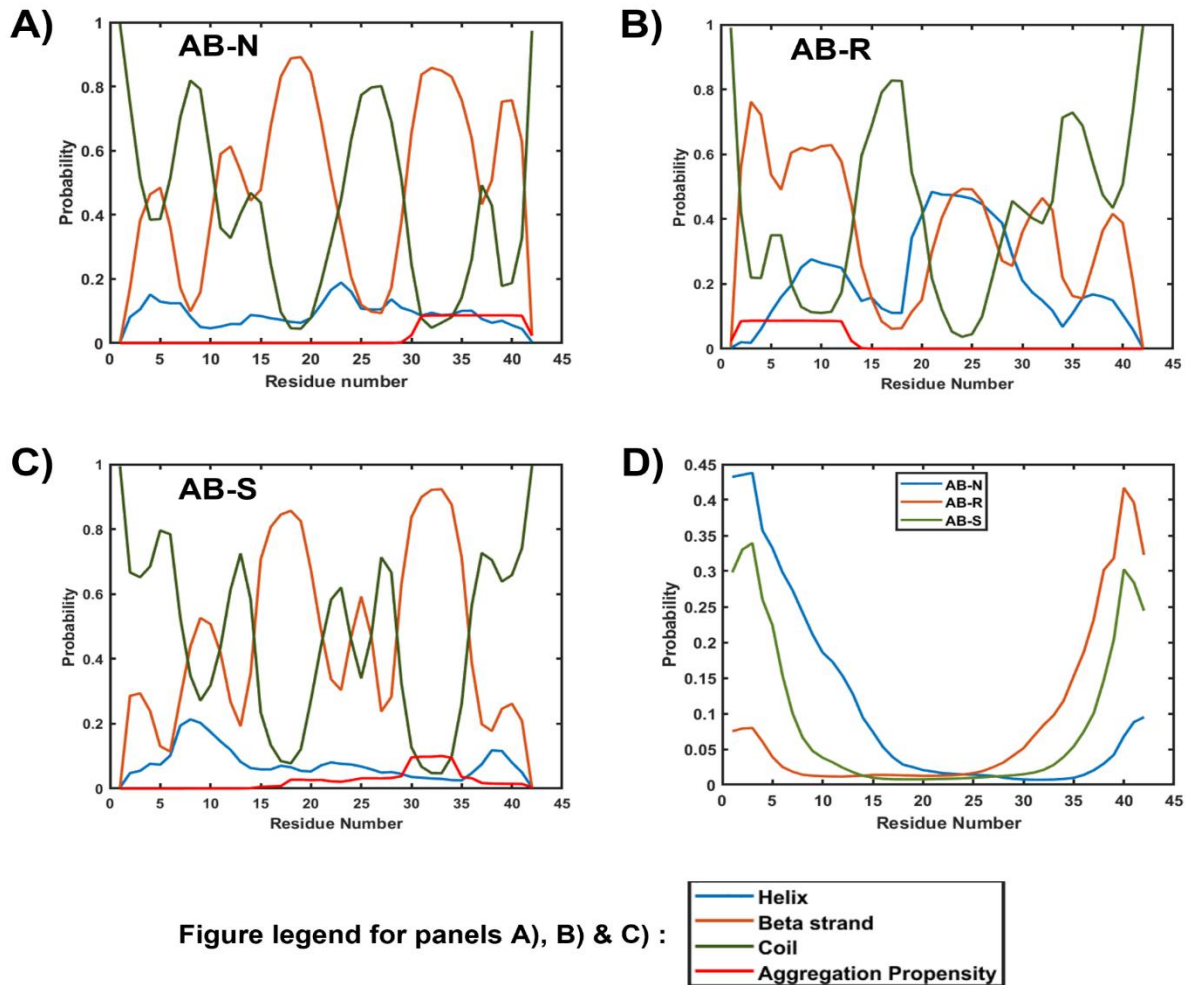
Figure 2.1 - Secondary structure, aggregation propensity and disorder prediction of Aβ peptides using PASTA 2.0: A) Aβ-N, B) Aβ-R, C) Aβ-S and D) peptide intrinsic structural disorder probability (all 3 peptides shown in the same plot)

Secondary structure prediction using PASTA 2.0 server suggests that Aβ-N (normal peptide) shows high propensity to form amyloids driven by residues 31-41 (Figure 2.1, A, red curve). In the case of Aβ-R (reverse peptide), we observed similar aggregation propensity as the normal peptide, but with the trend reversed (residues 2-12 showing higher propensity for aggregation), corresponding to N and C terminal switching of the peptide (Figure 2.1, B). Interestingly, in the case of the scrambled variant, even though the scrambling is pseudo-random

in nature, we observed non-zero aggregation propensity in the 18-34 residue range with residues 30-34 exhibiting propensities that are comparable to the normal and reverse variants (Figure 2.1, C).

Table 1.2: Secondary structure data extracted from PASTA 2.0

Peptide	%α-helix	%β-strand	%coil
Aβ-N	0	57.14	42.86
Aβ-R	11.9	40.48	47.62
Aβ-S	0	47.62	52.38

Next, we looked at the secondary structure of the peptides predicted by PASTA 2.0. Table 1.2 shows the relative percentages of α-helix, β strand and random coil conformations of the peptides in solution. In case of Aβ-N a high percentage of beta strand conformations is observed with the remaining designated as random coil structures. Figure 2.1A also shows this trend in a residue specific manner. According to the prediction algorithm, alpha helix conformation had very low probabilities throughout the peptide length.

In the case of Aβ-R, the relative percentage of beta strand was comparatively lower, and a small percentage of the residues show alpha helix content, and the remaining residues display random coil structures similar to Aβ-N (Figure 2.1B). Interestingly, Aβ-S also displays a significant percentage of beta strand content while the majority of the residues are predicted to be in random coil conformation (Figure 2.1C). The algorithm also predicted intrinsic disorder of

28.57%, 19.04% and 26.19% for Aβ-N, Aβ-R and Aβ-S respectively. Residue specific assignment of intrinsic disorder is shown in Figure 2.1D.

For Aβ-N, the intrinsic disorder is localized to the first 1/3rd of the sequence and for Aβ-R, a mirror image trend of Aβ-N is visible. Aβ-S however exhibits intrinsic disorder on both the N- and C-terminal sides, with the center region of the sequence displaying little to no intrinsic disorder. These further warrants verification by experimental methods such as Thioflavin-T assay to quantify amyloid, secondary structure analysis methods such as circular dichroism.

2.3.2 ThioflavinT fibrillation assay

ThioflavinT is an amyloid β-sheet backbone binding dye that indicates the relative fibrillization levels of Aβ peptides [110]. We performed ThT kinetics assay over 24 hours under fibrillization conditions. Fibril growth via primary nucleation and monomer addition follows sigmoidal growth kinetics. In sigmoidal growth, there is a 'lag phase' where monomers and oligomeric species formed are under the critical nucleation barrier limit. Once the critical barrier is reached, fibril elongation starts via monomer addition and the kinetics enters the 'log phase' of exponential growth [110]. After remaining monomers have been added to the fibril, an equilibrium is reached (saturation phase). All three peptides showed a sigmoidal growth trend over the period of 24 hours, characteristics of primary nucleation-based fibril growth, however with different kinetic behavior (Figure 2.2 and Table 1.3).
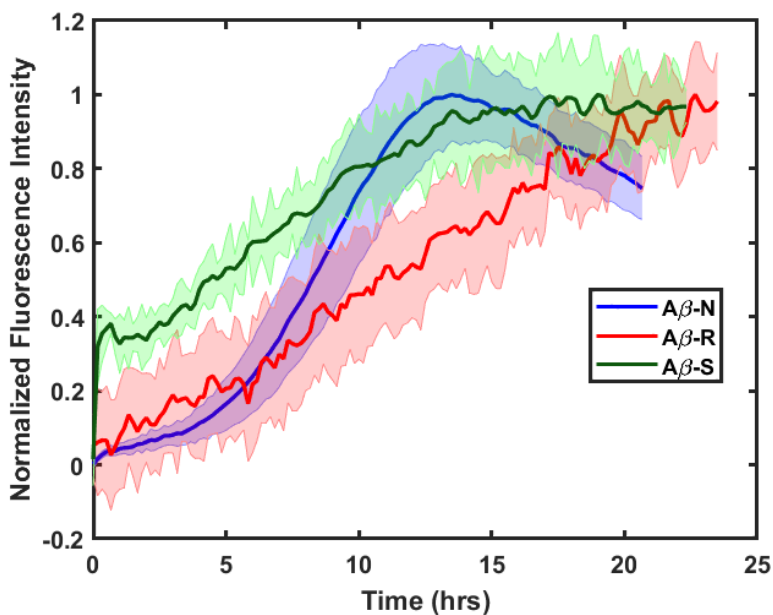
Figure 2.2 - Normalized ThioflavinT fluorescence intensity tracked over 24 hours under fibrillization conditions. Blue - Aβ-N, Red - Aβ-R and Green - Aβ-S. The shaded bands above and below the mean curve represent the standard deviation of the triplicate samples.

Table 1.3: Kinetic parameters derived from ThT curve fitting.

Peptide	T_lag (hrs)	k (hr^{-1})
Aβ-N	4.09±0.37	0.488
Aβ-R	1.81±0.48	0.203
Aβ-S	2.90±0.66	0.464

The lag phase for Aβ-N was the highest, followed by Aβ-S and Aβ-R. The rate constant (k) also followed a similar trend (Table 1.3). Aβ-N and Aβ-S readily form amyloid fibrils, with Aβ-R displaying mostly higher order oligomeric structures (AFM imaging section). ThT dye-binding based kinetic analysis showed comparative propensity of all the tested Aβ sequences to form

amyloid with variable lag phase, which might be due to evolution of sequence specific different

nucleation structure in the initial state of the amyloid formation.

2.3.3 Secondary Structure Analysis by Circular Dichroism

In order to understand the secondary structure of the peptides under freshly solubilized

and fibrillization conditions, we performed circular dichroism measurements in the far-UV range.

The measured spectra for freshly solubilized Aβ-N displays a negative peak in the 216nm range

(Figure 2.3A).
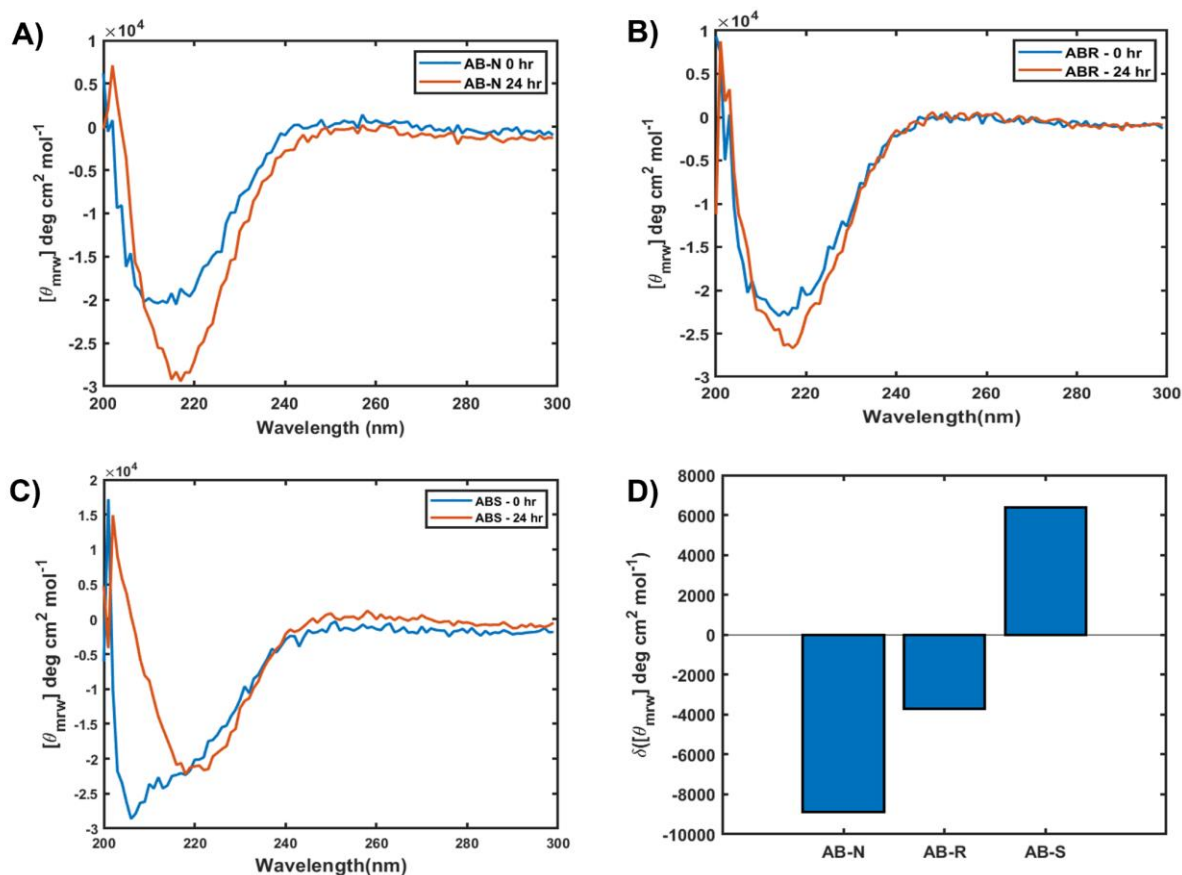
Figure 2.3 - Circular Dichroism spectra of the peptides at 0 hr and after 24 hrs under fibrillization conditions: A) Aβ-N, B) Aβ-R and C) Aβ-S. The blue curves indicate spectra at 0hr and the orange curve indicates spectra at 24hrs. D) Relative shift in mean residue residue ellipticity calculated with respect to the 24hr sample. The spectra are expressed as mean residue ellipticity $[\theta]_{mrw}$ deg cm^2 mol^{-1}

Under fibrillization conditions (24 hrs) the negative peak of the spectra is found at 217nm (Figure 2.3A). The peaks in the spectra around the 218nm range are typically ascribed to β-sheet dominated secondary structures. In the case of Aβ-R, the measured CD spectra shows similar behavior wherein, under freshly solubilized conditions, the negative minima peak is observed at 214nm, and under fibrillization conditions, the minima is found to be at 217nm (Figure 2.3B). Interestingly, in the case of Aβ-S, the negative peak is found at 206nm and 218nm under similar conditions, respectively (Figure 2.3C).

The magnitude of the characteristic negative peak at ~218nm is directly proportional to the β-sheet content in the peptides. Thus, the shift in the magnitude of the negative peak of the spectra can be ascribed to changes in the secondary structure of the peptides subject to different environmental conditions (ex. fibrillization). Figure 2.3D shows the relative change in magnitude of the spectra for the 3 peptides. Aβ-N displays highest change in ellipticity followed by Aβ-R, both displaying an increase in the β-sheet content under fibrillization conditions. In contrast, Aβ-S displays a decrease in the β-sheet content under similar change in conditions.

In the case of Aβ-N and Aβ-R, the 0hr spectra shows β-sheet characteristic peaks close to 215nm indicating the presence of oligomeric entities with β-sheet content. Under fibrillization conditions, both spectra indicate a red shift to 218nm and the β-sheet content increases in both peptides (Aβ-N = 47.90% increase and Aβ-R = 18.09% increase). This is consistent with the understanding that as oligomeric intermediates form fibrils over time, the β-sheet content increases as the amyloid fibril core is majorly composed of parallel/antiparallel β-sheets stacked along the fibril axis [43] [52]. However, Aβ-S does not show a characteristic negative peak in the 218nm range (the peak is found at 206nm which can be loosely ascribed to unordered state) at

0 hours and tends to move towards a negative peak at 218nm after 24 hours of incubation in fibrillization conditions. This indicates that Aβ-S transitions from an unordered state to a β-sheet rich state under fibrillization conditions. Our 0h and 24h analysis of secondary structure further verifies the variable lag phase in amyloid formation is caused by variability initial starting structure of Aβ species. It is highly interesting to further analyze, how the initial variability in the structure influence the evolution of different amyloid morphologies.

2.3.4 ANS Hydrophobicity Assay

It is well established that levels of hydrophobic amino acids of peptides play an important role in peptide aggregation and peptide-peptide assembly [111]. To investigate how hydrophobicity evolves during aggregation, we analyzed this using ANS assay.
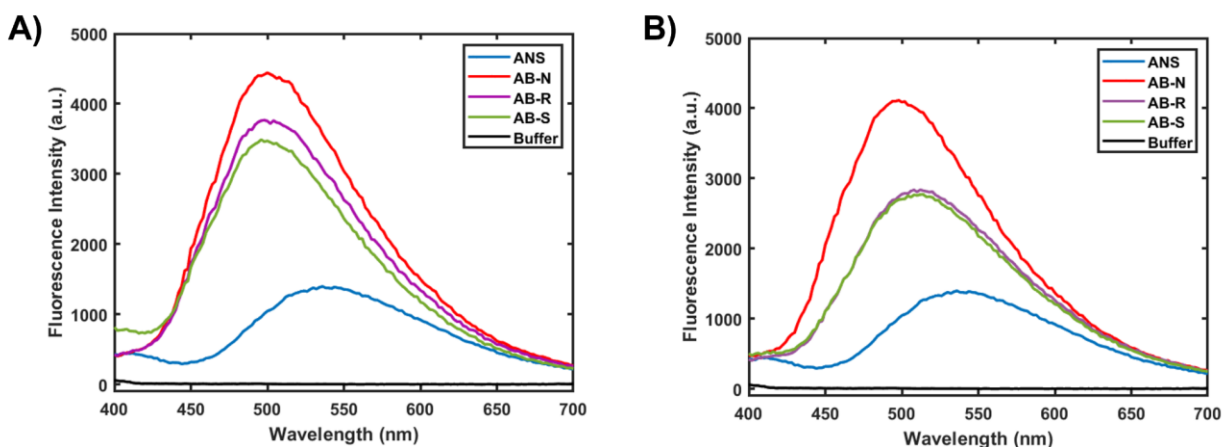
Figure 2.4 - Fluorescence Intensity spectra of the peptides incubated with ANS dye A) Freshly solubilized peptides (0hr) mixed with ANS, B) peptides after fibrillization (24 hrs) mixed with ANS. All the data were collected in the 400-700nm visible wavelength range with excitation wavelength of 350nm.

ANS is a fluorescent molecular probe which is composed of an aniline ring, a naphthalene group and a sulfonate moiety that is negatively charged. Due to the aromatic groups, the dye is

hydrophobic and tends to localize itself in pockets/clefts of protein residues which are hydrophobic in nature. Interestingly, due to the negative charge on the sulfonate group, the dye has also been shown to bind to positively charged amino acids [112]. Thus, the localization of the dye is very high in regions where positively charged amino acids and hydrophobic amino acids are in close proximity, which is generally the case in folded proteins (as compared to unstructured or denatured proteins). Upon strong binding to the peptide/protein, the peak fluorescence intensity of ANS increases drastically (proportional to the extent of strong binding) and the fluorescence spectra also undergoes a blue shift, which can indicate the relative levels of hydrophobicities [112] [113]. We performed ANS exclusion assay to understand how the 3 peptides would differ in terms of their dye binding capability, which would in turn hint at their relative hydrophobicities. In the case of freshly solubilized peptides (0 hrs, Figure 2.4A), Aβ-N shows the highest increase in peak fluorescence intensity (3.17x), followed by Aβ-R (2.69x) and AB-S (2.49x). Their blue shifts in wavelength of free ANS vs peptide bound ANS in the case of the 3 peptides were 36nm, 38nm and 40nm respectively. Relative increase in peak fluorescence intensity in the case of Aβ-N being the highest suggests that the dye was more strongly bound to regions of the peptide which contained both hydrophobic and charged amino acid residues in the core. This effect of the dye binding was observed to a lesser degree in the case of Aβ-R and Aβ-S. This further indicates that amino acid sequence; directionality of amino acid sequence and neighboring amino acid play important role in variable initial structure and subsequent ANS binding.

In the case of peptides that were incubated for 24 hours in fibrillization conditions, (Figure 2.4B), similar trends were observed, with some interesting characteristics. Aβ-N showed a 2.94x

increase in peak fluorescence intensity, followed by 2.03x for Aβ-R and 1.98x for Aβ-S. The blue shift in wavelength however changed significantly with AB-N showing a 38nm shift, followed by a 24nm shift for Aβ-R and 22nm shift for Aβ-S respectively. This suggests that Aβ-N contains fibrillation products which are more hydrophobic in nature compared to Aβ-R and Aβ-S.

2.3.5 Morphology analysis by AFM Imaging

We performed AFM imaging to quantify the morphological variation among these Aβ peptides. First, we imaged only the peptides immobilized on mica at two different time points – freshly solubilized condition and after incubating the peptides under amyloidogenic fibril forming conditions (24 hours at 37°C in 10mM HEPES, 300mM KCl buffer). Under freshly solubilized conditions, we observed mostly globular oligomeric structures. Aβ-N mostly displayed lower order oligomers in the 1-3nm height range (average 1.65±1.22nm, section profile below Figure 2.5A), with small percentage of population showing aggregates bigger in size (>5nm height). Aβ-R shows oligomeric species in 2-4nm range (average 2.87±1.03nm, section profile below Figure 2.5B). Interestingly, Aβ-S also displayed globular morphology, with heights in the range of 1-5nm

(average 2.77±2.35nm, section profile below Figure 2.5C). The number density of aggregates with bigger diameters were also observed to be higher in the case of Aβ-S.
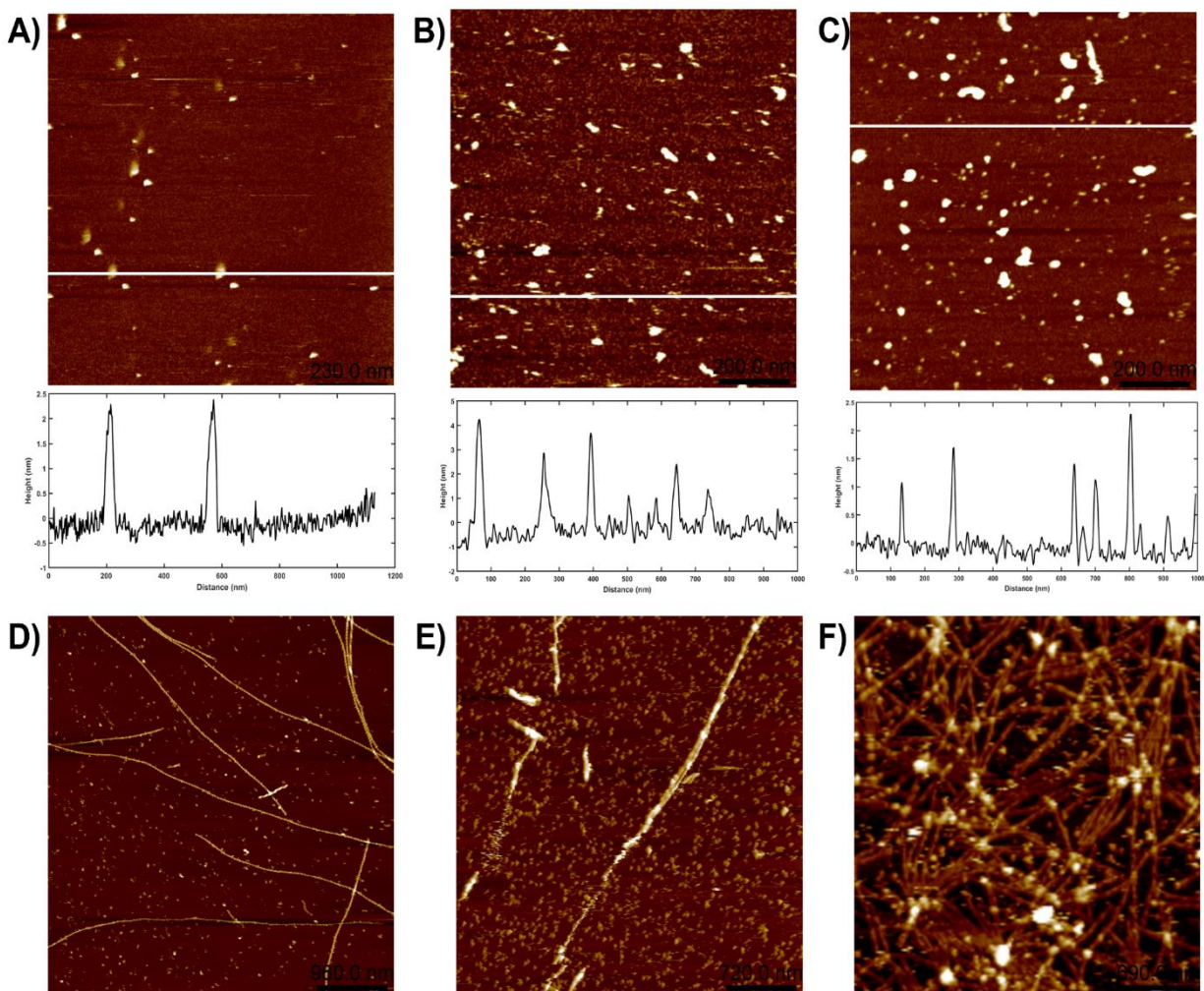
Figure 2.5 - AFM Height images of Aβ peptides at two time points - freshly solubilized (0 hrs) - A)Aβ-N, B)Aβ-R, C)Aβ-S (Scan sizes for panels A, B and C are 1um X 1um, z-scale = 0-5nm) and under fibrillization conditions (24 hrs) - D) Aβ-N, E) Aβ-R, F) Aβ-S (Scan sizes for panel D is 4.5um X 4.5um, E and F are 3.5um X 3.5um, z- scale for all panels is 0-20nm). For panels A, B and C the height section profile (white horizontal line) is displayed below the image.

The results observed for peptides under fibrillation conditions were slightly more interesting. As expected, Aβ-N showed linear elongated, untangled fibril structures (Figure 2.5D). In some imaging areas, the fibrils were found to be loosely associated with each other in a parallel

fibril-like morphology i.e., the fibrils are aligned through fibril-to-fibril interactions through the side chains. We did not observe fibril branching and growth from preformed fibrils, thus the fibril growth could be happening from a primary nucleation behavior. The section profile of Aβ-N fibrils showed a height of 9.76±1.36nm. Aβ-R also displayed fibril-like morphology, however, the density of fibrils seen on the surface of mica were much lower compared to Aβ-N (Figure 2.5E). The Aβ-R fibrils show a section height of 10.23±1.78nm. In the case of Aβ-R, the fibrils observed show a paired morphology where atleast 2-3 fibrils were found to be tightly linked to each other through side chain interactions and the fibrils were not as well separated as in the case of Aβ-N. The most perplexing observation was made in the case of Aβ-S, which also displayed high density of fibril morphology (Figure 2.5F). Aβ-S displayed highly tangled, branched fibril morphology with sectional height of fibrils ranging from 5.64nm to 8.43nm. The fibrils were also observed to be growing in random fashion with some imaging areas showing highly parallel arrangement of fibrils, some areas showing a crisscross arrangement and some areas showing densely packed amorphous aggregates of fibrils. We also measured the periodicity (helical turn-to-turn distance) of the fibril units along the direction of fibril growth. In the case of Aβ-N we found a periodicity of ~45nm between one resolvable unit of the fibril to another. In the case of Aβ-R, we were able to resolve a fibril unit-to-unit periodicity of ~100nm. In Aβ-S, as the fibril density was very high, we measured the periodicity in a small region of the fiber and found a periodicity of ~110 to ~130nm.

Next, we analyzed the distribution of these peptides in lipid bilayers. Aβ peptides were reconstituted in DOPC lipid bilayers at 1000:1 or 500:1 (lipid:peptide) molar ratios. Height images from Aβ-N show that Aβ-N is fairly uniformly distributed across the bilayer area (Figure 2.6A).

The structures found had a wide distribution in terms of the height and diameter. Excluding the obviously large aggregates, the heights of the intermediate or small oligomeric structures above the bilayer plane ranged from 0.8nm to 2.1nm in some cases. The diameter of these structures were found to be fairly uniform ranging from 11nm to 35nm. A small population of oligomeric structures in the <20nm outer diameter range exhibited globular topology with some of them showing a subunit like topography. However, we could not fully resolve the subunit organization due to imaging issues. It was also noticed that some of the oligomers appear to exclusively localize into the edges of the lipid bilayer or even in the defects found in the bilayer. This maybe due to higher energies created by line tension near the edges. In the case of Aβ-R, the distribution of the oligomers was found to be clustered with small pocketed areas showing higher distribution (Figure 2.6B). The height of the oligomers above the bilayer plane was found to be ranging from 1.67nm to 5.34nm, considerable higher than the ones found for Aβ-N. The diameter of these oligomeric complexes were also found to be significantly higher (ranging from 15nm to 50nm). The oligomer edge localization effect could be observed in the case of Aβ-R as well, however not as strongly as Aβ-N.
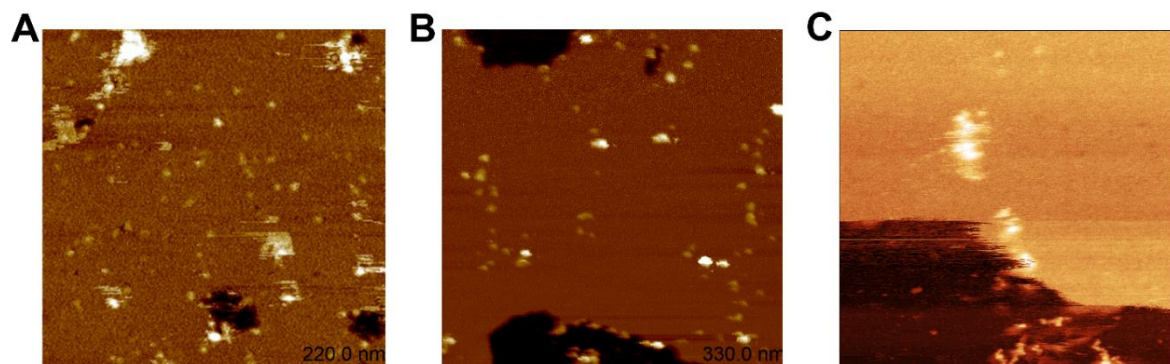
Figure 2.6 - AFM height images of Aβ peptides reconstituted in DOPC lipid bilayers at 1000:1 or 500:1 (lipid:peptide molar ratio). A) Aβ-N (scan size 1.1um X 1.1um, z-scale=0-5nm), B) Aβ-R (scan size 1.6um X 1.6um, z-scale=0-10nm), C) Aβ-S (scan size 900nm X 900nm, z-scale=0-18nm). In all images, the darkest color-coded part of the image corresponds to the plane of mica support.

In the case of Aβ-S, the oligomer distribution was highly irregular and in a lot of cases, even after careful imaging, globular structures were hard to observe (Figure 2.6C). Aβ-S mostly showed structures of a highly irregular nature, with irregular distribution throughout the samples. The heights of these structures were in the 5-10nm range with large aggregates/clusters of the peptide visible in all conditions. The dimensions of the Aβ oligomers reported here in all cases are very similar to the ones reported in literature [107] [108].

2.3.6 Proteinase-K Amyloid Stability Assay
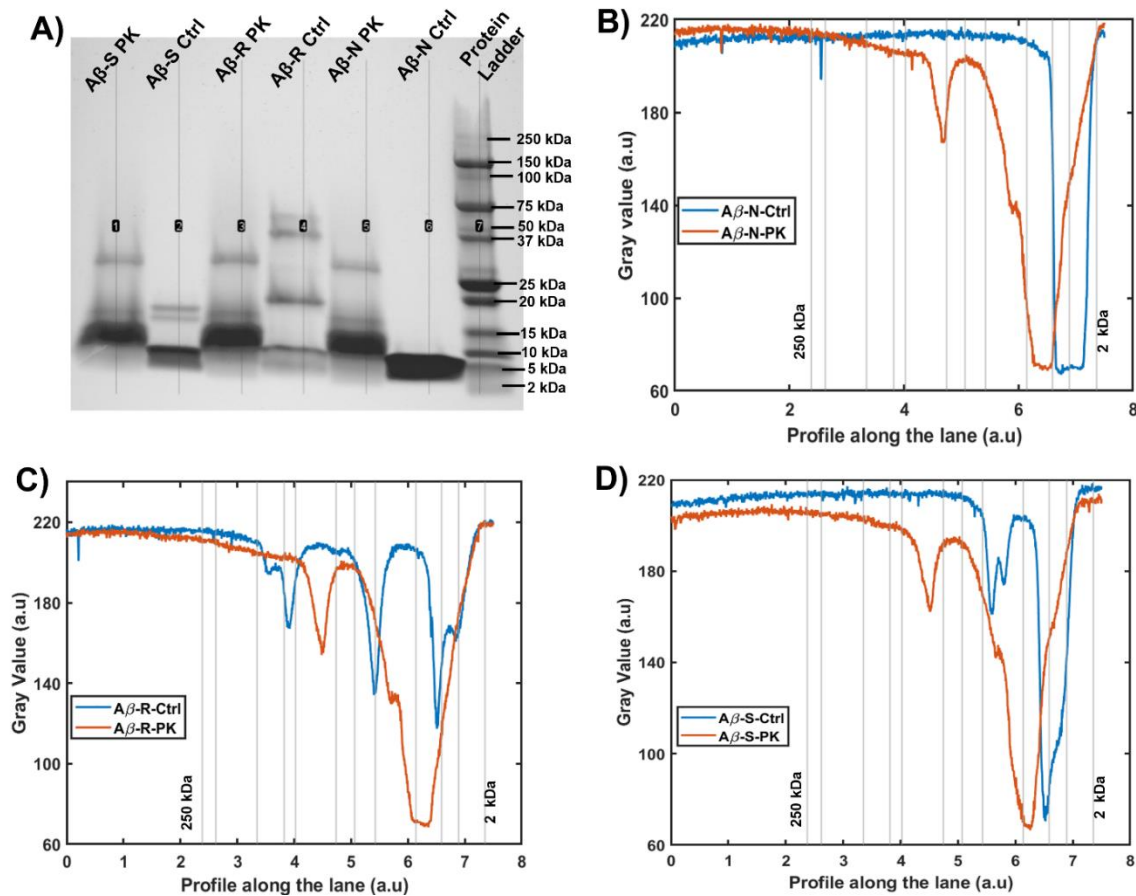
Figure 2.7 - Gel Electrophoresis intensity analysis of proteolytic digestion products of freshly solubilized peptides A) Snapshot of the gel(lane 1 – Aβ-S-PK, 2- Aβ-S-Ctrl, 3-Aβ-R-PK, 4-Aβ-R-Ctrl, 5-Aβ-N-PK, 6-Aβ-N-Ctrl, 7-Protein ladder standards), B) Aβ-N, C) Aβ-R, D) Aβ-S - grayscale intensity distribution of the respective lane plotted against the lane length (For all the plots, the legend is as follows - blue - Control (no PK added), orange-test(PK added), grey – vertical lines - protein ladder standards)

Amyloid aggregates of proteins are considered to be highly stable structures from a thermodynamic standpoint. They could be thought of as the structures lying in the global energy minima of a protein's folding pathway. Thus, understanding the stability of oligomeric intermediates which are involved in the amyloidogenic pathway could shed light into the nature of Aβ oligomer landscape. One of the major biochemical aspects of amyloids is resistance to protease degradation [114]. As such, we performed ProteinaseK (PK) proteolysis assay to understand the relative propensities of the three peptides to degradation and formation of other structural intermediates. PK is a broad-spectrum serine protease enzyme that cleaves peptide bonds next to the carboxyl group of either aromatic or aliphatic amino acid residues [115]. However, recent reports have claimed that PK's specificity may not be restricted to hydrophobic amino acids, and it may include other amino acids as well, with the exception of amino acid Proline.

After incubating peptides with PK, we probed the products of proteolysis reaction using SDS-PAGE gel electrophoresis (Figure 2.7A). In all the gel lanes used for peptides treated with PK (lanes with PK indicated next to the peptide's name), a common band can be seen just above the 25kDa band, which corresponds to the signature of PK, whose molecular weight is ~29kDa. Aβ-N control (not treated with PK) shows a very strong band in the 2kDa - ~7kDa band which means Aβ-N starts out predominantly as monomers or dimers. After treatment with PK, the products of proteolysis lie mainly in the 2-18kDa range, with a high intensity band spanning 8-13kDa (Figure 2.7B). Aβ-R control shows a slightly complex behavior with intensity bands observed at ~4kDa, ~9kDa, ~18kDa, ~37kDa and ~50kDa. This indicates that Aβ-R approximately starts out as a mixture of monomers, dimers, tetramers, 9-mers and 12-mers. After treatment with PK, these

higher order structures seem to be broken down into products in the ~3kDa to ~17kDa, with an strong intensity band observed in 8-15kDa region. Aβ-S control, interestingly, starts out as a mixture of monomers, dimers, tetramers and pentamers with bands observed in the 3-8kDa range, and 2 clear bands observed near ~14kDa and ~17kDa. After treatment with PK, this distribution predominantly shifts into an intense band near 8-14kDa range, with an additional less intense band at ~16kDa (Figure 2.7C).

2.3.7 Electrophysiology of Aβ peptides

In order to understand the biophysical behavior of the Aβ peptides in membranes, we probed the electrophysiological currents induced by the peptides through DPhPC bilayers. Voltage clamp electrophysiology data indicate that all 3 peptides induced currents through the lipid bilayer suggesting a pore formation or membrane destabilization activity, albeit with different characteristics. When 100mV potential was applied to the experimental system, in the case of Aβ-N we observed that the current would jump to a macro-conductance level, and at that macro- conductance level, we observed ion conductance currents with a combination of step-like and quick transitioning burst-like behavior (Figure 2.8A). With time, we often observed that the baseline would change to a different macro-conductance level and electrical activity (combination of step and burst) would resume in that state. This behavior was consistent throughout the duration of the recording at all tested hold voltages (~60mins). Due to the heterogeneity in the conductance behavior, in combination with the effect of changing baseline with time, the conductance spanned a range 0-230pS (Figure 2.8D).
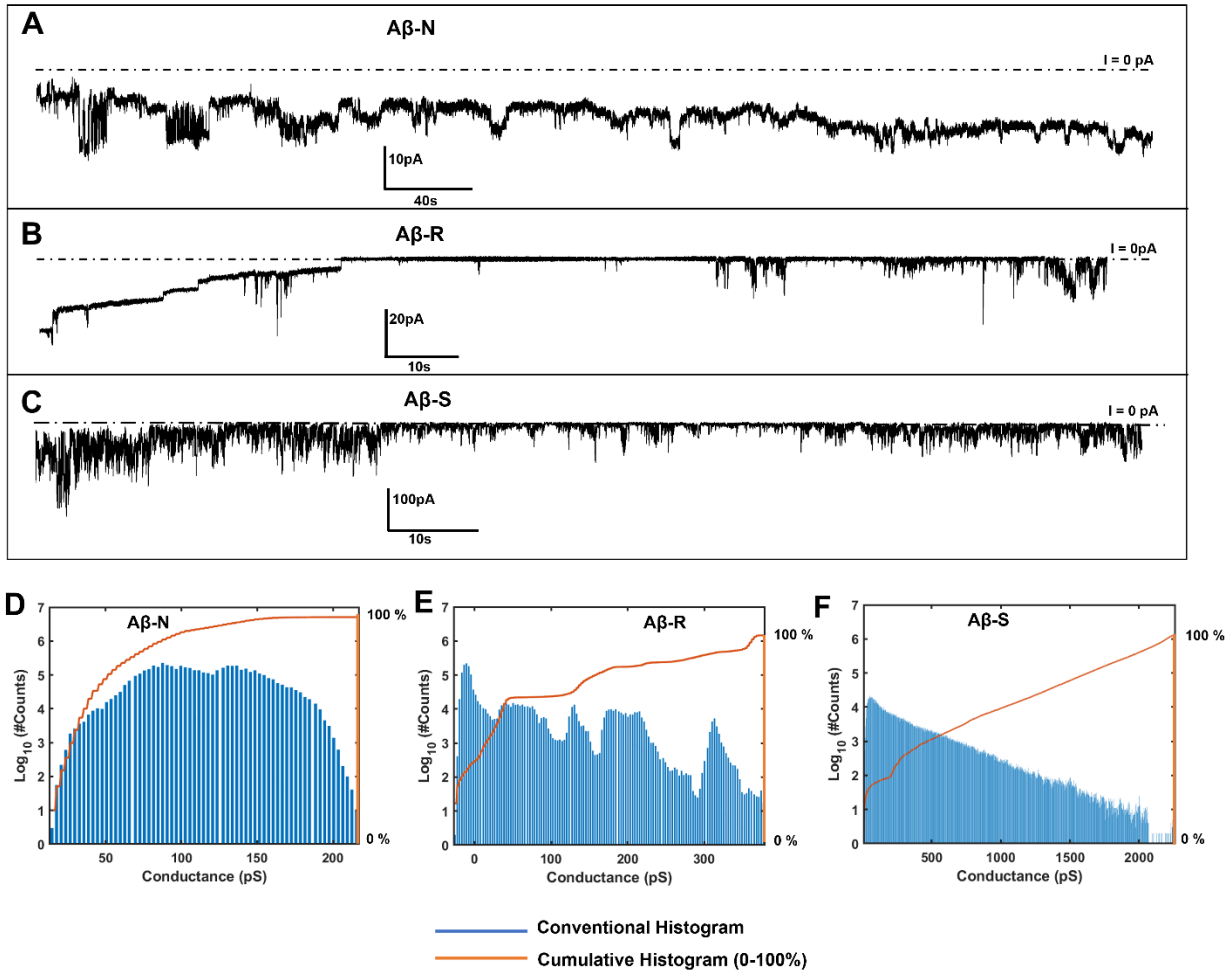
Figure 2.8 - Voltage clamp electrophysiology current traces of the Aβ peptides in DPhPC bilayers at 100mV hold voltage. A) Aβ-N, B) Aβ-R and C) Aβ-S. D), E) and F) display the same data in A, B and C converted to a conductance histogram plot (blue bars - conventional histogram, orange curve - cumulative histogram (0-100%)). The conductance was calculated by dividing each point of the current trace with the applied voltage.

The currents induced by Aβ-R were intermittent, separated by long periods of zero conductance and infrequent bursts (Figure 2.8B). Occasionally, upon applying 100mV hold voltage, the conductance was observed to jump to a macro conductance level in a step-like fashion, which persisted for 20-30s (initial part of Figure 2.8B) and the type of activity further at the same hold voltage would revert to mostly burst-like. The conductance spanned in the range of 0-370pS, with 'levels' that are clearly distinguishable from each other (Figure 2.8E, peaks in the histogram). Figure 2.8C shows the currents induced by Aβ-S under similar conditions. The

trend of currents induced are fully dominated by high-frequency, burst-like events throughout the duration of the recording. Unlike Aβ-N and Aβ-R, no step-like transitions in currents were observed for Aβ-S. Due to the nature of continuously induced currents, the conductance spanned over a wide range from 0-2200pS, with no clear specificity towards any conductance level (Figure 2.8F).

Even though some of the electrophysiological characteristics may have been common among the three peptides (quick transitioning, burst-like events), there seem to be a few contrasting differences as well. Firstly, as observed for Aβ-N, upon application of voltage, a macro-conductance level was achieved and sustained throughout the duration of the recording (~12pA mean at 100mV, this effect was observed in 3 out of 5 independent recordings). This could possibly indicate that after the application of voltage, multiple pores/ion channels may open, leading to establishment of a macro-conductance level and transitions seen at that level are from other channel-like structures in the membrane, exhibiting conformational transitions, which are evident as high frequency burst-like events. This behavior was absent for the remaining 2 peptides. For Aβ-R, after the application of voltage, a small duration of the curve shows a macro-conductance level, which quickly returns back to I=0pA baseline conductance and only shows infrequent burst-like behavior thereon. Aβ-S however, never seems to jump to any macro-conductance level, but only shows variable, quick transitioning, burst-like events with respect to the I=0pA baseline. In all cases, for all peptides, a voltage dependence could not be firmly established.

Among the 3 peptides, Aβ-N seems to have a stable conductance behavior with a combination of step-like and burst-like events, followed by Aβ-R and the least stable behavior is

60

shown by Aβ-S. It is possible that Aβ-N and Aβ-R may insert into the bilayer and adopt comparatively stable conformations (although the possibility of these conformations changing over time cannot be fully ruled out due to dynamic oligomeric states). This is also supported by the fact that between Aβ-N and Aβ-R, only the readability of the sequence has been reversed, but the hydrophobic amyloidogenic region is still preserved, which may insert into the lipid bilayer and achieve a relatively stable configuration when compared to Aβ-S. The nature of the currents induced by Aβ-S hints at an unstable conformation which may be associated with the membrane and damage the membrane through non-specific membrane damage mechanisms. This can explain the wide range of conductance seen in the case of Aβ-S, without a bias towards any particular conductance level.

2.3.8 Zinc Blocking of Aβ ion channels

Aβ channels/pores formed in the membrane are conventionally known to be blocked by Zn^{2+} ions in the recording solution. We tested the ability of Zn^{2+} ions to block the conductance activity under these conditions [65]. We added Zinc chloride solution (in increments of 5mM) directly to the trans chamber and recorded currents at 100mV hold voltage. When Zn^{2+} ions were added to Aβ-N, the current was fully blocked after ~120s (Figure 2.9A). Similar behavior was observed for Aβ-R, wherein the conductance fully reverted to I=0pA baseline roughly ~60s after the addition of Zinc chloride (Figure 2.9B). Interestingly, in the case of Aβ-S, the conductance could not be blocked even after double addition of zinc (final concentration of ZnCl2 = 10mM, additions are spaced ~180s apart, Figure 2.9C).
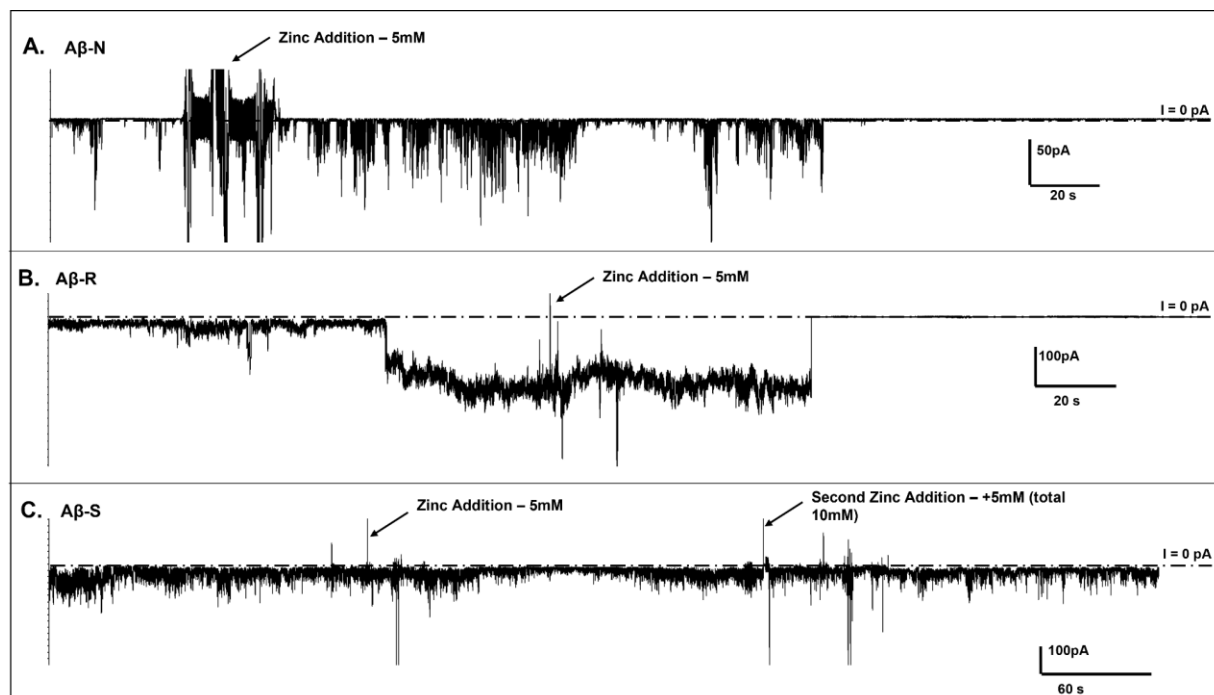
Figure 2.9 - Zn2+ ion blocking of Aβ peptides at 100mV hold voltage: A) Aβ-N, B) Aβ-R and C) Aβ-S. Zinc Chloride was added to the trans chamber at time points indicated by arrows. Each Zinc addition was done in 5mM increments.

It has been theorized and supported by experimental and molecular models that Aβ channels/pores formed in the membrane (via direct oligomeric conformation insertion or through monomer insertion and further oligomerization in the membrane) have histidine amino acid residues lining the mouth of the pore. Zn^{2+} ions have high binding affinity towards histidine residues, which has been proposed as the mode of conductance blocking in Aβ pores [116]. In our studies, this effect seems to be very pronounced, wherein the conductance can be fully blocked for Aβ-N and Aβ-R, but not for Aβ-S. This indicates that Aβ-N and Aβ-R may have formed ion channels/pores with a similar conformational makeup, exposing the pore mouth lining histidine residues to the recording solution where Zn^{2+} ions could easily bind and block the conductance. Aβ-S, however, seems to have a different conformational makeup or is exhibiting

non-specific membrane damage/permeabilization effects which could not be blocked even after dual addition of Zinc.

2.3.9 MTT Cell viability assay and Calcium uptake
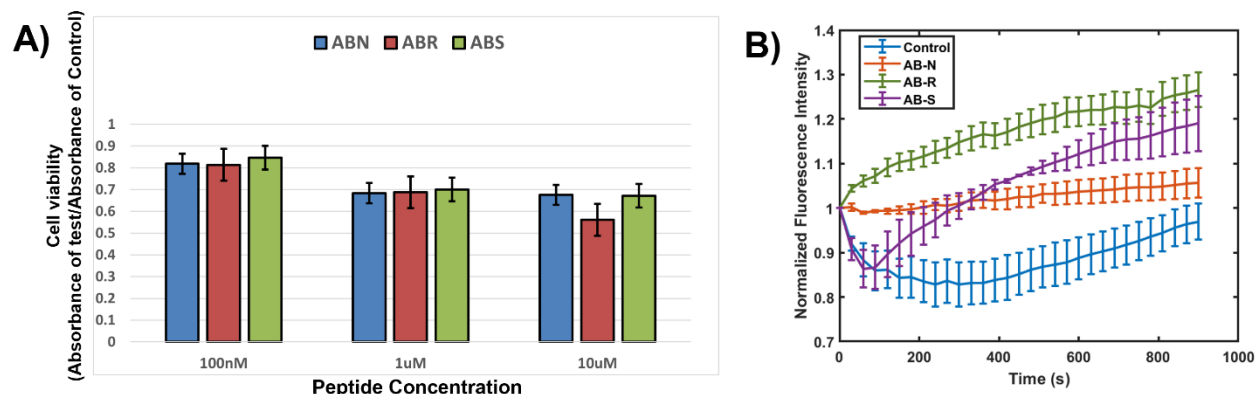
Figure 2.10 - A) MTT cell viability analysis of B103 cells exposed to different concentrations (100nM, 1uM, 10uM) of Aβ peptides. Data are expressed as the ratio of MTT absorbance of test (peptides added to media) to absorbance of control (10ul of 1X PBS added, without peptides). Error bars represent the standard deviation of the absorbance intensity of triplicate wells. B) Fluo-4 calcium uptake analysis of B103 cells exposed to 10uM Aβ peptides. The error bars represent standard deviations of the fluorescence intensity of the regions of interest selected in fluorescence images of cells (Fluo4 - excitation 488nm, emission 515nm)

In order to assess the relative cytotoxicities of the Aβ peptides, we performed a MTT cytotoxicity assay by adding 3 different concentrations of the peptides into the culture media. B103 neuroblastoma cells devoid of endogenously expressed APP (Amyloid Precursor Protein) were used such that the cytotoxic effects are majorly from exogenously added Aβ peptides. Figure 2.10A displays the relative toxicities of the Aβ peptides in a dose dependent manner. Higher concentrations (10uM) of the peptides show the highest cytotoxicity, with Aβ-R displaying slightly higher toxicity than Aβ-N and Aβ-S. A significant difference in toxicity at a particular concentration could not be established.

Next, we analyzed the calcium uptake behavior of B103 cells upon exposure to Aβ peptides. The ion channel hypothesis of AD proposes that Aβ peptides form cation permeable ion channels. Multiple studies have shown that in cell cultures, these Aβ ion channels cause unregulated calcium flux into the cells, leading to calcium dyshomeostasis, which triggers a cascade of events that put the cells in the pathway of death [66] [117] . With this hypothesis in mind, we tested the possibility of the Aβ peptides in this study to create calcium flux in B103 cells. Fluo-4 is a calcium sensitive fluorescent dye that is commonly used to quantify calcium uptake in cell studies. Through fluorescence microscopy, we quantified the intensity of fluorescence over a time period of 15 minutes after exposure of the cells to the peptides. Over the 15-minute time period of observation, Aβ-N showed an approximate 8.5% increase in fluorescence. In contrast Aβ-R showed an increase in fluorescence of ~22% and Aβ-S showed an increase of ~17% from the baseline reading at time zero (Figure 2.10 B).

The results of calcium uptake are surprising, but somewhat in line with results from electrophysiology studies. Aβ-N shows the least increase in calcium uptake in cells and in electrophysiological studies, the conductance levels exhibited by Aβ-N is confined to a small range. In the case of Aβ-R which displays the highest calcium uptake in B103 cells, the electrophysiological current traces indicate that Aβ-R is capable of causing sudden increase in conductance by jumping to various macro conductance levels. Finally, in the case of Aβ-S, through electrophysiology we found that Aβ-S is capable of causing large ionic conductances through non-specific mechanisms, and possibly not through ion channel formation.

Most of the biochemical and biophysical studies focusing on Aβ behavior have been performed under certain experimental conditions through which experimental variability could

be introduced. Studies which analyze the structural, functional, and cytotoxic behavior of peptides through the lens of multiple, parallel, biophysical, and biochemical experiments have been only handful. Although some of these studies have probed the sequence and readability dependence in amyloid formation from a structural analysis standpoint, studies focusing on the interaction of Aβ peptides with biological membranes from a functional standpoint, under the same comparative framework is lacking [104][105]. Given the lack of fundamental molecular understanding of the behavior of Aβ, we found it fruitful to perform these studies to uncover universal mechanisms in amyloid formation and their functional effects in relevant systems. The fundamental question of whether the sequence of amino acids in Aβ, or their readability, or just the presence of particular amino acids in close vicinity of each other is the deciding factor, has far reaching consequences in terms of understanding the molecular mechanism of pathophysiology and subsequent therapeutics development.

Computational analyses of amyloid formation using protein structure prediction algorithms is a useful way of de novo analysis of peptide-peptide interactions and can also help in designing/modifying peptides which do not go into the amyloid pathway. In this study, the amyloid prediction algorithm PASTA 2.0 indicated that Aβ-N and Aβ-R have high propensity for amyloid formation, particularly the C-terminal segment of the peptide (reversed in the case of Aβ-R). To PASTA 2.0's credit, Aβ-S was shown to have non-zero aggregation propensity and amyloid formation capacity, mostly due to the arrangement of amino acids in the central segment of Aβ-S. In one of the similar studies on Aβ$_{1-42}$, the scrambled variant's amyloid propensity was shown to be non-existent [105]. However, in our studies the prediction agreed well with the observations. ThioflavinT fibrillation assay and secondary structure analysis via

Circular Dichroism proved that in addition to Aβ-N and Aβ-R forming β-sheet secondary structure enriched fibrils under physiological conditions, Aβ-S also seems to follow a similar pattern and forms amyloidogenic fibrillar structures. AFM imaging confirmed these observations, although strong morphological differences in the makeup of these fibrils are evident. This hints at the possibility that amyloid formation maybe driven favorably by the presence and relative percentages of hydrophobic amino acids in the sequence and the readability of the sequence maybe a second order effect. An important point that has to be emphasized is that the Aβ-S used in our study, coincidentally, may also have been uniquely suited to amyloid formation, even though the sequence is generated from pseudorandom scrambling of the original Aβ sequence.

Further, functional studies using voltage clamp bilayer electrophysiology, MTT cell viability and calcium uptake assays suggest that all Aβ peptides in the study are capable of causing ionic conductance in bilayers and calcium flux in cells. Interestingly, Aβ-S shows relatively high degree of ionic conductance in both bilayer system and cell cultures, although with mechanisms that seem to be significantly different than the ones by Aβ-N and Aβ-R. In the case of Aβ-N and Aβ-R, step like conductance changes, which are conventionally characteristics of well-formed ion channels seem to be the major mode of interaction with the membrane, in good agreement with previous studies of ionic conductance behavior of Aβ [58][108]. In the case of Aβ-S, the ionic flux is highly variable and burst-like, which could indicate that Aβ-S may not form ion channels directly but may induce ionic flux through non-specific mechanisms (applying local stress on the membranes causing them to deform or a membrane-thinning effect). This is also substantiated by CD spectroscopy findings which indicate high β-sheet content for Aβ-N and Aβ-R under freshly solubilized conditions (which are akin to the conditions used in electrophysiology) and

comparatively lower for Aβ-S, although Aβ-S transitions to high β-sheet content over time. Amyloid pores are known to have high β-sheet content [33][50], which can explain the different behaviors of ionic conductivity observed in our studies, coupled with the fact that Aβ-S conductivity could not be blocked by zinc ions. The cell viability changes with concentration of the peptides; however, it does not show significant specificity towards the type of the peptide. Calcium uptake data suggest that Aβ-R and Aβ-S display higher calcium influx compared to Aβ-N. Although Aβ-R and Aβ-S are not naturally found in cells or bodies of animals, this mode of calcium influx further supports the notion that the particular pool of amino acids, through multiple cooperative, molecular mechanisms acquire some structural conformation that leads to cytotoxicity. We also note that cellular uptake of peptides or interaction of the peptides with cells could involve multiple other factors, with the possibility of these peptides acting as ligands to cell surface receptors and triggering intracellular signaling cascades [60]. From a cytotoxicity standpoint, studies which probe the mode and mechanism of cytotoxity have to be carefully considered and especially with Aβ system, the exact oligomeric intermediates interacting with cells have to be tightly controlled [118]. Thus, combination studies presented above can gather critical sequence specific information which can help in advancing our thinking about therapeutic interventions focusing on disrupting the cooperative mechanisms that lead to amyloid formation.

Conclusion

In Chapter 2, we discuss the propensity of amyloid formation from the fundamental standpoint of primary sequence of the peptide, its readability and overall amino acid content-based modulation of amyloid-membrane interactions. Understanding the core ideas about what

drives amyloid formation can offer deep insights into the development of alternate and efficient therapeutic measures.

Chapter 2, in part, is a manuscript in preparation with *Karkisaval A.G.; Ban D.K.; Nguyen A, Balster B.; and Lal R.*; titled 'Amino acid sequence and readability dependence in Aβ-membrane interactions and relevance to Alzheimer's disease'. The dissertation author was the primary author of the manuscript.

Chapter 3

Ion channel formation by N-terminally truncated Aβ (4–42): relevance for the pathogenesis of Alzheimer's disease

3.1 Abstract

Aβ deposition is a pathological hallmark of Alzheimer's disease (AD). Besides the full-length amyloid forming peptides (Aβ$_{1-40}$ and Aβ$_{1-42}$), biochemical analyses of brain deposits have identified a variety of N- and C-terminally truncated Aβ variants in sporadic and familial AD patients. However, their relevance for AD pathogenesis remains largely understudied. We demonstrate that Aβ$_{4-42}$ exhibits a high tendency to form β-sheet structures leading to fast self-aggregation and formation of oligomeric assemblies. Atomic force microscopy and electrophysiological studies reveal that Aβ$_{4-42}$ forms highly stable ion channels in lipid membranes. These channels are blocked by monoclonal antibodies specifically recognizing the N-terminus of Aβ$_{4-42}$. An Aβ variant with a double truncation at phenylalanine-4 and leucine 34, (Aβ$_{4-34}$), exhibits unstable channel formation capability. Taken together the results presented herein highlight the potential benefit of C-terminal proteolytic cleavage and further support an important pathogenic role for N-truncated Aβ species in AD pathophysiology.

3.2 Introduction

Alzheimer's disease (AD), the most common form of dementia in the world, is a progressive neurodegenerative disorder neuropathologically characterized by the presence of extracellular parenchymal and vascular Aβ amyloid deposits as well as intracellular neurofibrillary

tangles composed of hyperphosphorylated versions of tau, a microtubule accessory protein. Parenchymal amyloid lesions adopt different morphological characteristics presenting as dense core neuritic plaques or diffuse deposits [119]. Irrespective of their dissimilar morphology, both lesions are populated by relatively short Aβ peptides cleaved from the much larger membrane spanning amyloid precursor protein (APP) [120]. Whereas compact plaques and vascular deposits are rich in β-sheet structures responsible for their characteristic green birefringence under polarized light after Congo red staining, and exhibit fibrillar appearance under electron microscopy (EM), diffuse plaques are non-fibrillar and Congo red negative, likely representing early phases in the development of compact plaques [121]. Multiple lines of investigation implicate amyloid peptides in the pathogenesis of Alzheimer's disease. Individuals with Down's syndrome – trisomy 21 harbor similar lesions and develop early AD-like pathology, typically by middle age [121]. Furthermore, familial mutations in the APP gene in the long arm of chromosome 21 are associated with early onset hereditary forms of AD. In addition, animal models overexpressing human APP or transgenic for familial APP mutations exhibit progressive AD-like Aβ amyloid pathology associated with cognitive deficits [120]. Amyloid peptides are known to be produced by the sequential processing of APP through the action of β- and γ-secretases which result in the generation of Aβ peptides starting at the aspartate residue at position 1 and ending at amino acids 38/ 40 / 42 [122]. Although, $A\beta_{1-40}$ and $A\beta_{1-42}$ have been the most frequently studied species, a wide variety of post-translational modifications – including isomerization and racemization of aspartate residues, cyclization of N- terminal glutamate, and oxidation of methionine, among others – have also been documented.

The post translationally modified peptides also include different N- and C-terminally10 truncated Aβ species that have been identified in animal models and AD patients [123] [124] .and are likely generated by a number of Aβ-degrading enzymes among them neprilysin, insulin degrading- and endothelin converting enzymes, plasmin and matrix metalloproteases [125] [126]. In this sense, biochemical and mass spectrometry analyses have revealed the presence of a variety of C- terminally truncated Aβ species in human brain interstitial fluid (ISF) and cerebrospinal fluid (CSF), among them $Aβ_{1–16}$, $Aβ_{1–30}$, $Aβ_{1–34}$, and $Aβ_{1–37}$ [127] [128] [129] [130]. likely representing the proteolytic action of local resident enzymes. Similarly, an assortment of Aβ peptides truncated at the N-terminus have been reported, among them $Aβ_{2–42}$, $Aβ_{3–42}$, $AβpE_{3-42}$, $Aβ_{4–42}$, $Aβ_{9–42}$, and $Aβ_{17–42}$ [131]. Aβ truncations severely alter the biophysical properties of the molecule. While C-terminal cleavage of Aβ generates peptides that are soluble and normal components of body fluids, N-terminal truncated forms, due to their propensity for adopting β-sheet conformations, are prone to self-aggregation, are poorly soluble, and typically exhibit exacerbated cytotoxicity [119][131] [132]. One of the most relevant N-terminal truncated forms, $Aβ_{4–42}$ was first reported over three decades ago [121]. This peptide, preferentially found in dense core plaques and cerebrovascular deposits in AD cases and transgenic animal models [119][121] [133], is also highly prevalent in patients with trisomy-21, and vascular dementia [134]. Recent studies indicate that the N-terminal truncation at Phe4 of Aβ results in greater hydrophobicity and higher β-sheet content of the molecule compared to $Aβ_{1–42}$ leading to an augmented ability to oligomerize [119]. These biophysical properties of $Aβ_{4-x}$ forms contrast with those of C-terminally cleaved Aβ species, generally found in aqueous-based biological fluids, which typically exhibit higher solubility and less aggregation propensity than the parent full-length peptides.

Mounting evidence indicate a critical role of the lipid microenvironment in the molecular pathways affecting amyloid aggregation. In this sense, the composition of the different cellular membranes including the type of lipid molecules and cholesterol content [135] [136] are known to play important roles in the oligomerization and aggregation fates of amyloid peptides. Particularly, the presence of GM1 gangliosides has been shown to increase amyloid aggregation by forming ganglioside-peptide complexes with capacity to act as amyloid seeds [137] [138]. Recent NMR based studies have also explored geometric factors such as bilayer thickness in modulating binding affinity of $A\beta_{1-40}$ with the membrane and propensity of oligomerization by folding into an intermediate, partially folded helical filament, which maybe a crucial step in the aggregation cascade [139] [140]. Notably, in-vitro NMR studies of $A\beta_{1-40}$ with lipid nanodiscs have reported an inhibition of fibrillation as a consequence of the trapping of aggregation intermediates, indicative of a potential use for future therapeutic avenues [141] [142].

In spite of extensive studies focusing on Aβ, the relevance of the N- and C-terminal truncated species for AD pathogenesis as well as their contribution to the complex cellular mechanisms affected during the disease remain largely understudied. Among the most relevant pathogenic pathways under investigation, the insertion of channel structures in cellular and intracellular membranes, a two-step insertion mechanism, is certain to cause alterations in membrane potential and leakage of critical cellular ions such as calcium and potassium, ultimately damaging cellular homeostasis and survival [68] [143] [144] [145]. The present work examines the ability of $A\beta_{4-42}$ to form ion channels in lipid membranes using both electrophysiology and AFM approaches, further demonstrating that additional C-terminal truncation of Phe4 starting peptides results in highly unstable pore structures. Overall, the

current studies provide insight into the detrimental pathogenic mechanisms of N-terminally truncated Aβ proteoforms, contribute to a more comprehensive understanding of the three dimensional structure of Aβ aggregates – both in solution and in the membrane environment– and expand existing knowledge on the significance of Aβ heterogeneity for disease pathophysiology. All these features provide new and unique ways to design and develop therapeutic molecules targeting the aggregation and oligomerization pathways and/or blocking channel activity [101] [146].

3.3 Materials and methods

Aβ peptides: synthesis and structural changes Peptides $Aβ_{4-42}$ (FRHDSGYEVHHQKLVFFAEDVGSNKGAIIGLMVGGVVIA) and $Aβ_{4-34}$ (FRHDSGYEVHHQKLVFFAEDVGSNKGAIIGL) were synthesized at ERI Amyloid Laboratory (Oxford, CT) using N-tert-butyloxycarbonyl chemistry. Peptides were purified by reverse phase high performance liquid chromatography using a Vydac C4 column (Western Analytical, Murrieta, CA). Molecular masses and purity of the synthetic peptides were corroborated by matrix assisted laser desorption ionization time of flight (MALDI-TOF) mass spectrometry, as previously reported [147]. Monodisperse amyloid subunit of both peptides were obtained by dissolving 1 mg/ml of peptides in 1,1,1,3,3,3, hexafluoroisopropanol (HFIP; Sigma Chemical Co., St. Louis, MO) and subsequent incubation for 4 days, which breaks down β-sheet structures and disrupts hydrophobic forces, promoting the formation of stable α-helical secondary structures [148] [149] [150]. HFIP-pretreated peptides were lyophilized and maintained frozen at -80 °C, storage conditions that in our hands preserved the same unaggregated structures for up to 1 month, as

verified by the predominance of monomeric components in Western blots and negligible fluorescence signal after thioflavin T binding.

3.3.1 Atomic force microscopy: sample preparation and imaging conditions

Proteoliposome preparation has been included in supplementary information. For AFM sample preparation, 10-20 µl of sonicated proteoliposome solution was added to a freshly cleaved muscovite mica disk and further diluted to 50 µl by adding HEPES/ KCl/MgCl2 buffer. The solution was incubated for 10–15 min at room temperature on the mica disk, washed thrice, and rehydrated to 50ul using imaging buffer (HEPES, pH 7.4). A Bruker Multimode equipped with Nanoscope V controller, EV scanner and fluid cell was used for all AFM imaging studies (Bruker, Santa Barbara, CA). Bruker SNL-20 (silicon nitride cantilever, Al coated, k = 0.08 N/m, fr ~ 8 kHz in buffer or 0.24 N/m, fr ~ 32 kHz in buffer) or Mikromasch XNC12 (silicon nitride tip, Au coated, k = 0.08 N/m, fr ~ 7 kHz in buffer) were used (Mikromasch, USA). Contact and Tapping (according to convenience and imaging stability) mode imaging was performed in 10 mM HEPES at scan rates of 1–2 Hz. Scanning was usually started with a larger scan size (10 µm × 10 µm) and then gradually reduced to smaller sizes depending upon area of interest (1 µm×1 µm, 500 nm × 500 nm etc.). Setpoint voltage and feedback gains were optimized, and height and phase images collected. The resulting images were processed with the Nanoscope Analysis 1.9 software provided by Bruker. The height images were first flattened (0th, 1st or 2nd order) and section analysis feature was used to extract cross sections of different regions feature heights.

3.3.2 Electrophysiology

POPE (1-palmitoyl-2-oleoyl-sn-glycero-3-phosphoethanolamine), and POPG (1-palmitoyl-2-oleoyl-sn-glycero-3-phospho1'-rac-glycerol), purchased from Avanti Polar Lipids and stored at −20 °C, were dissolved in n-heptane to a final concentration of 1.5%. Aβ peptides were reconstituted in deionized water to the concentrations illustrated in Figure 3.4 whereas anti-Aβ$_{4-x}$ monoclonal antibody 18H61 was diluted to the desired concentration in deionized water and stored at −20 °C. Phospholipid bilayer membranes were prepared as previously described [151]. Briefly, bilayer membranes were prepared by placing a bubble of lipid dissolved in solvent onto the end of the Teflon tube of approximately 300 μm in diameter. The chamber design allows rapid introduction of solution into immediate proximity with the membrane in a volume of 50 μl. One percent agar salt bridges with 1 M KCl were used to connect the Ag/AgCl electrodes (E-207, Warner Instruments) to the solutions. Voltage clamp conditions were employed in all experiments. The side where peptides were added (cis side) was taken as ground. All voltages given in Figure 3.4 refer to the voltage of the trans side. Current was recorded with an "Axopatch C1" amplifier and stored by "DataTrax" system for later analysis. Membrane capacitance and resistance were monitored regularly to ensure the integrity of the membranes.

3.4 Results

3.4.1 Structural properties of Aβ$_{4–42}$ and Aβ$_{4–34}$ truncated peptides: Figure 3.1A illustrates the purity of the synthetic peptides used in our studies. In each case, MALDI-TOF analysis revealed the presence of a single component with a m/z value well within the range of the expected theoretical mass. The structural changes of the Aβ$_{4–42}$ and Aβ$_{4–34}$ synthetic homologues, pretreated, solubilized, and aggregated as described in Methods, was analyzed by

CD spectroscopy, thioflavin T-binding, and electron microscopy analysis over a time-lapse of 2 h. Consistent with previous findings [119], the highly fibrillogenic Aβ$_{4-42}$ (Figure 3.1, B), showed upon 2 hr incubation under physiological salt concentrations, a CD spectrum with a typical minimum at 218 nm, indicative of β-sheet secondary structures. In contrast, Aβ$_{4-34}$, bearing an additional C-terminal truncation display a primarily random conformation in the experimental timeframe. Thioflavin T binding, largely associated with the presence of cross β-sheet structures and typically correlating with the existence of fibrillar and/or protofibrillar components [152], also varied between both peptides. In accordance with its tendency to form β-sheet structures, Aβ$_{4-42}$ exhibited much higher fluorescence values than the freshly solubilized peptide after 2 h incubation (Figure 3.1, C). Further C-terminal truncation at position 34 completely abolished the fluorescence signal, in agreement with the absence of changes in the CD profile. Figure 3.1, D and E, illustrates the characteristics of the Aβ$_{4-x}$ truncated species visualized by EM after uranyl acetate negative staining. The formation of oligomeric structures defined as elements of b100 nm in length with longer assemblies classified as protofibrils was evident for the 2 h incubated Aβ$_{4-42}$ (Figure 3.1, D). The C-terminally truncated Aβ$_{4-34}$, displayed a lower capacity to form oligomeric species within the same time frame (Figure 3.1, E). The above data clearly indicates that the N-terminal truncation at position 4 induces formation of high β-sheet content elements and concomitant generation of oligomeric assemblies, all characteristics associated with pro-amyloidogenic properties. In contrast, the additional C-terminal truncation at position 34 leads to the generation of peptides less prone to oligomerization, suggestive of molecules with more accelerated clearance potential, in agreement with the reported tissue retrieval of C-terminally cleaved derivatives in water-based buffers and their presence in biological fluids [119].
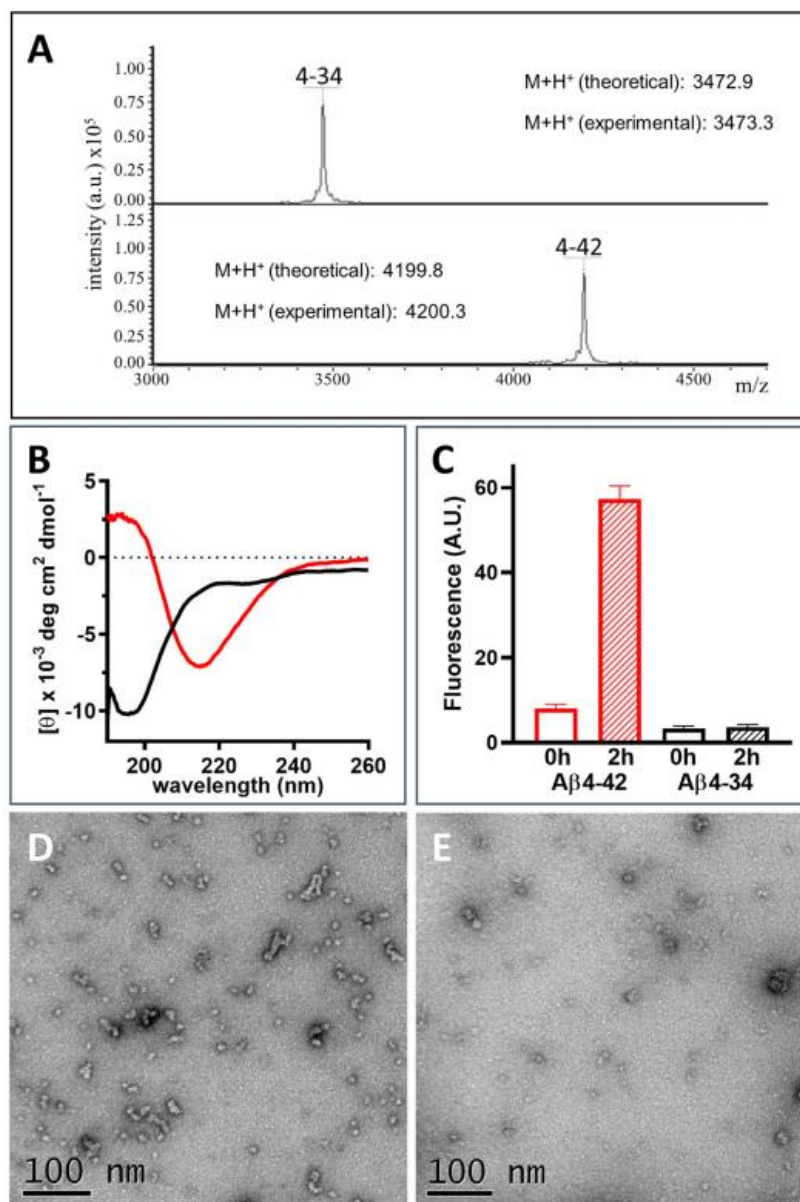
Figure 3.1 - Biophysical and structural analysis of Aβ₄₋₄₂ and Aβ₄₋₃₄ truncated peptides. The purity of the peptides was assessed via MALDI-TOF (A) performed in a Bruker Daltonics Autoflex MALDI-TOF mass spectrometer (Bremen, Germany) in linear mode using standard instrument settings at the New York University Mass Spectrometry Core for Neuroscience. External calibration was performed using human adrenocorticotropic hormone peptide 18–39 (average mass = 2465.68 Da) and insulin (average mass = 5733.49 Da). In all cases MS spectra were processed and analyzed by FlexAnalysis (Bruker Daltonics). The different Aβ homologues, pre-treated in HFIP and reconstituted in physiologic salt concentration containing buffer, were incubated at 37 °C for up to 2 hours. (B) CD spectra of Aβ4–42 (red line) and Aβ4–34 (black line) incubated 2 h under physiological salt concentrations. Graph is representative of three independent experiments; (C) Fluorescence evaluation of Thioflavin T binding to the respective synthetic homologues (50 μM) either freshly reconstituted (open bars) or after 2 h incubation (patterned bars). Results are expressed in arbitrary units (A.U.) and represent the mean ± SEM of three independent experiments after subtraction of blank levels. (D) Structural assessment of Aβ₄₋₄₂ 2 h oligomerization visualized by EM after negative staining. (E) EM analysis of Aβ₄₋₃₄ oligomerization after 2 h incubation. In both (D) and (E), bar represents 100 nm.

3.4.2 Aβ$_{4-42}$ and Aβ$_{4-34}$ show pore-like structures in lipid bilayer - AFM images of different concentrations of freshly prepared Aβ$_{4-42}$ and Aβ$_{4-34}$ (outlined in methods) on mica showed densely populated clusters of different diameter distributions; ~5 nm for smaller oligomeric structures, ~5 nm–20 nm for intermediate aggregates and > 20 nm for larger irregular aggregates (Figure 3.2, A and B). Significantly, Aβ$_{4-34}$ formed oligomers at a higher propensity (Figure 3.2, B), and the peptides were closely packed compared to Aβ$_{4-42}$ (Figure 3.2, A). This is consistent with the difference in the number of membrane-spanning amino acids (8 amino acids for Aβ$_{4-34}$ vs 16 amino acids for Aβ$_{4-42}$). In general, the size of the globular Aβ$_{4-42}$ (Figure 3.2, A) was larger than the size of the globular Aβ$_{4-34}$ (Figure 3.2, B). AFM images of Aβ$_{4-42}$ and Aβ$_{4-34}$ when reconstituted in a DOPC bilayer show multiple different forms of oligomeric species of different
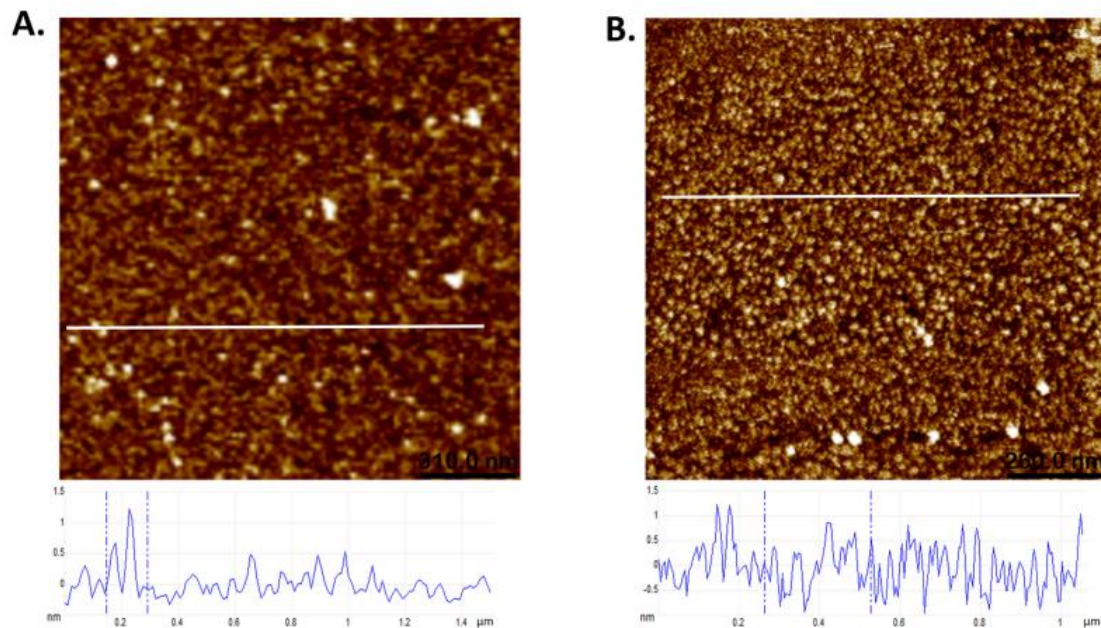
Figure 3.2 - AFM images (height and amplitude error) of Aβ4–42 and Aβ4–34 interaction with DOPC bilayer. A) Aβ4–42 and B) Aβ4–34 incubated on plane mica surface show distribution of monomers and oligomers. The white horizontal line depicts a section through the scanned area whose corresponding profile is shown below the image (A: scan size = 1.4um, height scale = 1.9 nm; B: scan size = 1.4um, height scale = 3.2 nm).

sizes present in the bilayer membrane as well as some clustered together around membrane edges and defects (Figure 3.3, A for $A\beta_{4-42}$ and 3.3, B for $A\beta_{4-34}$). At a lower molar ratio (1:1000) of $A\beta_{4-42}$:DOPC, much lesser membrane disruption was observed, and oligomeric species were easier to detect and differentiate from DOPC bilayer over the mica substrate. High resolution AFM images of $A\beta_{4-42}$ oligomers interacting with DOPC membrane reveal annular pore-like structures with outer diameter 12–16 nm (±2.3 nm, accounting for tip convolution) with a central dip, indicative of a peptide pore in the membrane. These are very similar to $A\beta pE_{3-42}$ porelike structures reported previously [153] [154] (Figure 3.3, C and inset attached with C). Similar
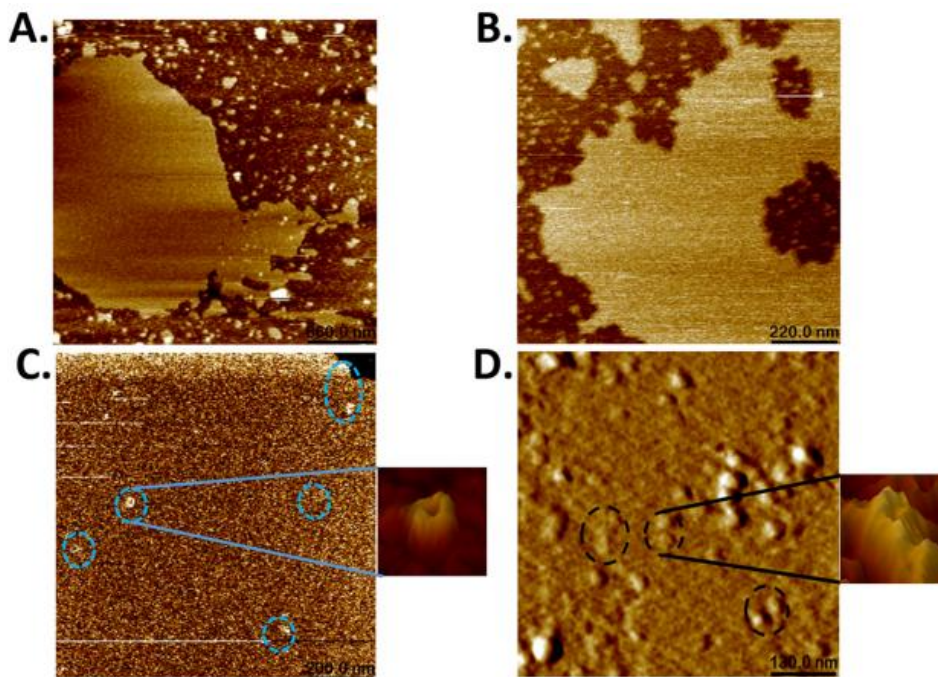
Figure 3.3 - AFM images of amyloid beta ion channels when reconstituted in lipid bilayer.A) Aβ4–42 reconstituted DOPC bilayer showing clusters of protein distributed (scan size = 3.5um, height scale = 9.5 nm). B) $A\beta_{4-34}$ reconstituted DOPC bilayer showing clusters of protein distributed (scan size = 1.2um, height scale = 5.6 nm). C.) $A\beta_{4-42}$ reconstituted DOPC bilayer at low peptide concentration (1:1000) shows intact bilayer with oligomeric peptides (blue dotted circles) in pore-like morphology. The inset in C) shows the pore-like structure in isometric view (scan sizes – 1 μm, inset scan size 50 nm, height scale 2.3 nm). D) Amplitude error (which is proportional to the feedback signal and very sensitive to height changes on the surface) image of Aβ4–34 reconstituted DOPC bilayer at low peptide concentration (1:1000) shows intact bilayer with oligomeric peptides (black dotted circles) in pore-like morphology. The inset in D) shows the porelike structure in isometric view. (scan sizes = 650 nm, inset scan size = 60 nm; height scale = 4.6 mV).

structural clusters of diameter 14–18.5 nm with a pore-like morphology are observed for $A\beta_{4-34}$ reconstituted with DOPC bilayer, although a clear dip in the pore structure was not resolvable (Figure 3.3, D and inset attached with D). The height protrusion of these pore-like structures above the DOPC planar surface is found to be about 0.9 ~ 1.2 nm. These pore-like structures were found to be distributed throughout the sample with varying spatial and number density.

3.4.3 $A\beta_{4-42}$ forms a stable and long-lived ion channel in lipid bilayer: Figure 3.4A shows the results of an experiment where $A\beta_{4-42}$ was added to the aqueous phase bordering a phospholipid membrane. The horizontal traces represent current passing through the membrane as a function of time under voltage clamp conditions. The current was extremely close to zero prior to the addition of peptide. After the addition of peptide (first arrow), there is a lag phase, and then the current begins to rise in a stepwise manner ultimately resulting in a large (negative) and stable current through the membrane representing the insertion of multiple ion channels in the membrane. The current increase is represented by a downward deflection of the current trace, indicating that the current is in the negative direction, as a negative voltage was applied to the membrane. When the voltage is reversed to a positive voltage, the current direction reverses, but is approximately equal in magnitude, indicating the channels do not turn on or off with voltage. These channels appear to have significant stability over time and relatively long lifetimes comparable to those exhibited by $A\beta_{1-42}$ [155]. At the point indicated by the second arrow, zinc chloride was added to the solution. A short time later the magnitude of the negative current was reduced by the addition of zinc, similar to the previous findings of zinc blockade of $A\beta_{1-42}$ [156].

3.4.4 Aβ₄₋₃₄ forms unstable and short-lived ion channels - Figure 3.4B shows the results

of a lipid bilayer experiment where peptide Aβ4–34 was added to the solution bathing the

membrane on one side. In the initial phase of the experiment the current passing through the

membrane is close to zero reflecting the very low permeability to ions of the unmodified

phospholipid
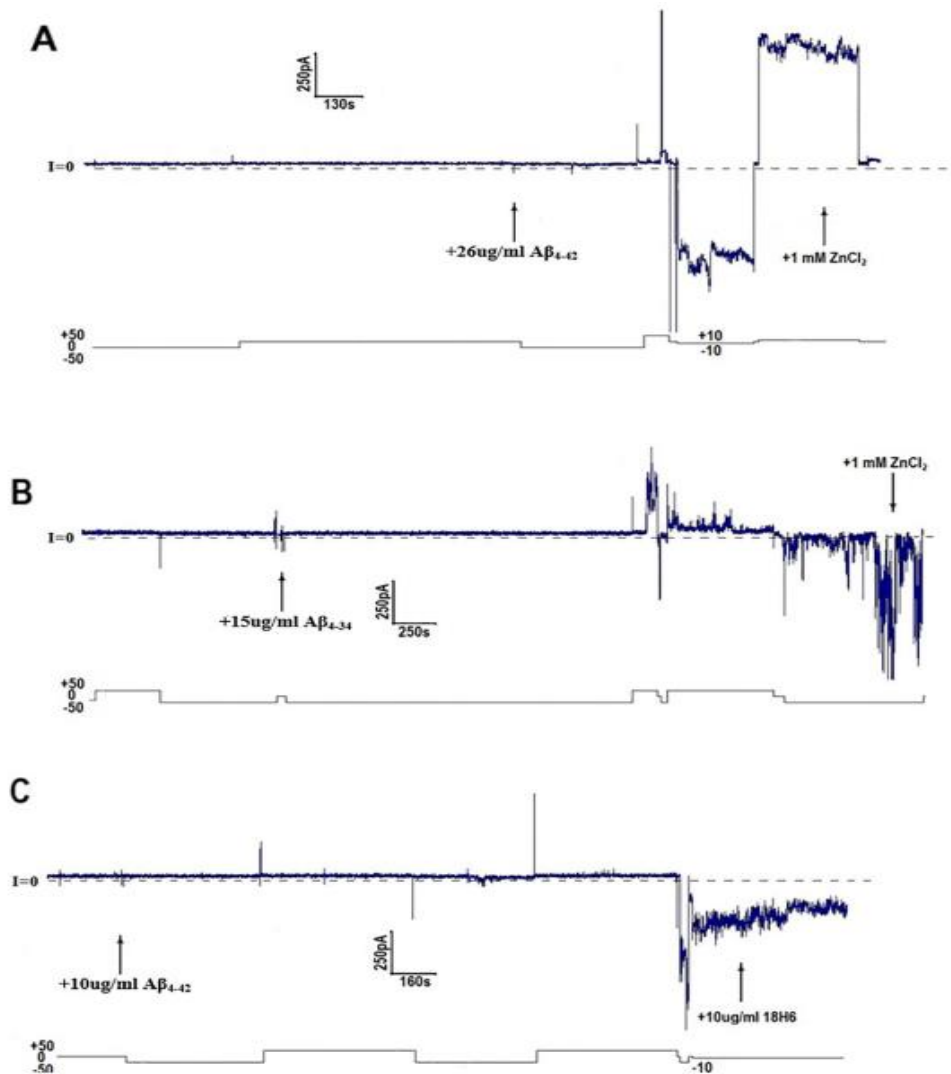
Figure 3.4 - Lipid bilayer membrane conductivity initiated by truncated Aβ peptides. A) Conductivity initiated by Aβ4–42 peptide. B) Conductivity initiated by Aβ4–34 peptide. C) Aβ4–42 conductivity inhibition by monoclonal antibody 18H6. In all cases: chamber solution contains 100 mM NaCl, 20 mM Tris-Citrate buffer pH 7.4. Membrane formed from POPE/POPG 2:1 w/w, final concentration of lipids 1.5% in n-heptane. Top lines represent transmembrane currents; bottom lines, holding potential.

membrane. After the addition of Aβ$_{4-34}$, there is a lag phase followed by the appearance of spontaneous fluctuations in the current. These fluctuations represent the insertion and opening of ion channels in the membrane. These channels appear to have very poor stability and short lifetimes (~1 sec). The channels flicker rapidly open and closed, and do not exhibit the more typical stability of full length Aβ peptides (1–40 and 1–42) [157].

3.4.5 Monoclonal 18H6, specific to the N-terminal truncation at Aβ Phe4, blocks activity of Aβ$_{4-42}$ ion channels - Figure 3.4, C shows an experiment where Aβ$_{4-42}$ was added to the solution bounding the membrane. After a lag there is a significant increase in the membrane current represented by a downward deflection as the voltage at that time across the membrane was a negative voltage therefore resulting in a negative or downward current. Monoclonal antibody 18H6, specific for N-terminal truncated peptides, was added to the solution bounding the membrane (arrow). This resulted in a rapid reduction of the magnitude of the negative current indicating partial blockade of the channel by the antibody. This suggests not only that the current induced in the membrane was specific to Aβ$_{4-42}$, but also that the N-terminal epitope that recognized the antibody was still accessible to the side of the membrane to which the peptide was added. That is, Aβ$_{4-42}$ is oriented in the membrane with its N-terminus facing the side to which it has been added.

3.5 Discussion

N-terminally truncated peptide Aβ$_{4-42}$, a major fibrillar component of parenchymal plaques and vascular deposits, has a high tendency to adopt β-sheet conformations and lead to the rapid formation of oligomeric assemblies, structures that are considered today the most

pathogenic amyloid species associated with the development and progression of AD. Indeed, previous work indicates that this truncated form exhibits even higher aggregation/oligomerization tendency than the parent full-length Aβ$_{1-42}$ molecule itself and is an invariable component of the plaque cores [119][121]. Also consistent with previous reports demonstrating the protective effect of C-terminal cleavages for Aβ oligomerization and toxicity, Aβ$_{4-34}$ lacking the C-terminal portion of Aβ$_{4-42}$ exhibits a random-coil conformation and very little oligomerization propensity in the current experimental timeframe. The results presented herein clearly indicate that both Aβ$_{4-42}$ and Aβ$_{4-34}$ can differentially form ion permeable channels in phospholipid bilayer membranes. The results are not totally surprising given previous reports of channel formation by peptides containing the full length Aβ$_{1-42}$ sequence [158] [159] or its N-terminal truncated species AβpE$_{3-42}$ 38 and Aβ$_{17-42}$ [160] [161] as well as smaller fragments such as Aβ$_{25-35}$ [162], [163] all of which are capable of forming ion permeable channels, albeit with varying electrophysiological characteristics. What is striking about the results presented here is the marked difference in physiologic properties between the two ion channels tested. Aβ$_{4-42}$ exhibits channels that appear quite stable in the timeframe of our experiments with lifetimes lasting many seconds to minutes. The conductance induced by these channels is quite large and stable over the time course of our experiments. The conductance also appears to be independent of voltage which is a typical characteristic of full length Aβ$_{1-42}$ and Aβ$_{1-40}$ [164][62]. Moreover, Aβ$_{4-42}$ is blocked by zinc added from the same side as the peptide, sharing this property with Aβ$_{1-42}$ [164]. In contrast Aβ$_{4-34}$ forms channels that appear to be unstable during the time course of our experiments and rapidly flicker open and shut. This instability is consistent with the less hydrophobic nature of the C-terminal truncated peptide Aβ$_{4-34}$. It seems to be less comfortable

in the hydrophobic environment of the membrane and less stable, therefore. Because the insertion of small numbers of ion channels in a planar lipid bilayer membrane is an inherently variable process, we cannot make firm conclusions about the relative channel forming activity of both peptides from the present data. Many factors including lipid and ionic composition, temperature, and molecular crowding, among others, can affect channel activity. Still, the contrast between the two $A\beta$ variants examined here is striking. This physiologic evidence is consistent with the AFM images presented here in which $A\beta_{4-42}$ clearly shows multimeric aggregates in the membrane, clustered around a central pore implying that the receptor site in the pore for zinc is similar in both peptides. Notably, the $A\beta_{4-42}$ channel activity can be specifically blocked by the antibody 18H6 which is specific for $A\beta$ peptides N-truncated at position 4. This demonstrates that the N-terminus of this peptide is clearly accessible to the aqueous solution surrounding the membrane on the side that the peptide was added to, providing valuable information about the orientation of the $A\beta$ N- terminus in the functional channel structure. This finding will be extremely useful for further molecular modeling of potential ion channel structures in the lipid membrane. The results presented here give further weight to the idea that N-terminal truncated peptides that are more prone to aggregation and more toxic to neurons than comparable full length $A\beta$ species may play a key role in the pathogenesis of Alzheimer's disease. This idea may be critical in the formulation of therapeutic approaches to inhibiting or reducing amyloid deposition in the brain using antibodies or small molecule inhibitors targeted toward N- terminal truncated peptides. We have previously reported on the channels formed by $A\beta_{9-42}$ and $A\beta_{17-42}$ [160][161]. These N-terminally truncated peptides do not form amyloid, but are toxic to neurons, allow calcium ions to enter cells, and do aggregate in the presence of

membranes, forming ion channels. These features are all inhibited by millimolar zinc ion, indicating that calcium entry and neurotoxicity directly result from ion channel formation, leading us to propose this pathway as an alternative mechanism for AD. Similarly, we have also studied the structure and biological activity of $A\beta pE_{3-42}$, an N-terminal truncated amyloid peptide where after the loss of the first 2 amino acids, the third position glutamate is converted to pyroglutamate via intramolecular dehydration by the enzyme glutamyl cyclase, creating a lactam ring. While glutamate is a charged polar group and typically seeks an aqueous environment, the pyroglutamate is more nonpolar and seeks the hydrophobic environment of the membrane. Pyroglutamate-modified Aβ represents a dominant fraction of Aβ oligomers found in AD brains, while control brains show much lower concentrations of pE Aβ [165]. Plaques formed with pE Aβ appear earlier in the course of the AD-like illness due to trisomy 21 (Down's syndrome) and transgenic $A\beta pE_{3-42}$ mice develop an earlier and more severe illness than those with $A\beta_{1-42}$[165]. Lipid bilayer experiments showed that $A\beta pE_{3-42}$ formed channels more rapidly and exhibited a larger fraction of high conductance (100–200 picoSiemens) channels compared to $A\beta_{1-42}$[154]. The precise mechanisms leading to the development and progression of AD are complex and multifactorial involving crosstalk among different cellular pathways. Over the years, different lines of investigation have provided support for a central role of Aβ in the disease pathogenesis [166]. It is now clear that the conformational transition from soluble to fibrillar material is a highly complex process modulated by a variety of factors, among them the presence of post translational modifications in the Aβ molecule including N- and C-terminal truncations as studied in the current work. The interlinked cellular pathways compromised by Aβ – many of them shared by those elicited by non-Aβ oligomeric conformations associated with other forms of cerebral

amyloidosis[148][152], – are currently under active investigation. Among the most studied pathways, induction of apoptotic/cell death mechanisms, oxidative stress, metabolic/mitochondrial dysfunction, and the ability of amyloid subunits to assemble into functional ion channel-like structures in lipidic environments are the most relevant [167] [168]. Insertion of channel structures in cellular and intracellular membranes has the potential to alter homeostasis and metabolism since cells depend on intact membrane structures for a wide variety of functions. Beta sheet conformers are well-suited to forming pore-like structures in a hydrophobic environment which may account for their widespread presence in three-dimensional amyloid and non-amyloid pores. Cells depend on intact membrane structures for a wider variety of cellular functions. Non-specific ion channels, such as those described by us and other laboratories, insert leakage pathways into membranes that interfere with their biological function causing dissipation of membrane potential and leakage of critical calcium and potassium ions [144]. Ultimately, cells are forced to work harder and use up their energy stores. Ion channel formation and its potential modulation carry vast potential for the development of novel therapeutic strategies. Indeed, in spite of extensive research efforts, disease-modifying therapies that may prevent or slow the rate of AD progression are still lacking. While biochemical, genetic, and longitudinal imaging analyses provide strong support to the role of Aβ aggregation in initiating disease pathogenesis, the clinical trials conducted so far have not panned out. Current consensus in the research community indicates that Aβ-modifying therapies are not beneficial for symptomatic patients and those in the late stage of disease when Aβ fibrillogenesis and brain deposition is extensive [169]. Targeting ion channel formation and its deleterious effects on cellular function either independently or as part of future combinatorial therapies is certainly a

promising alternative to address the crosstalk mechanistic paths involved in the disease. A better understanding of the relevance of $A\beta_{4-42}$ and other N-terminal truncated fragments will certainly provide insight into the role of $A\beta$ heterogeneity in the complex mechanisms of Alzheimer's pathophysiology and open new avenues for translational opportunities.

3.6 Conclusion

In chapter 3, we show that N-terminally truncated $A\beta_{4-42}$ is uniquely capable of forming stable ion channels in lipid bilayers compared to C-terminally truncated $A\beta_{4-34}$ which forms unstable, short lived ion channels. Combination of CD spectroscopy, fibrillation kinetics assay, EM and AFM imaging and voltage clamp electrophysiology studies offer viewpoints of understanding pathological agents and mechanisms involved in the progression of AD pathology.

Chapter 3, in part, is a reprint of the material as it appears in Karkisaval A.G.; Rostagno A; Azimov R; Ban D.K; Ghiso J; Kagan B.L; and Lal.R. Ion channel formation by N-terminally truncated $A\beta$ (4–42): relevance for the pathogenesis of Alzheimer's disease. Nanomedicine: Nanotechnology, Biology and Medicine, 2020;29:102235. The article has been reprinted with permission from Elsevier Inc. The dissertation author was the primary author of this paper.

Chapter 4

Channel forming activities and structural features of unmodified and pyroglutamylated Aβ peptides in lipid membranes.

4.1 Abstract

Alzheimer's Disease (AD) is a progressive neurodegenerative disorder characterized by dementia, cognitive decline, and neuronal death. The amyloid β (Aβ) peptide forms soluble oligomers, which play a key role in the etiology of AD. N-terminal truncation and pyroglutamylation of Aβ significantly affects its biophysical/biochemical properties and enhances cytotoxicity. One of the mechanisms of neurotoxicity of Aβ is membrane destabilization or pore formation and dysregulation of cellular ionic homeostasis. Here, the structural features and ion-conducting channel formation in lipid bilayers by four Aβ variants ($A\beta_{1-42}$, $A\beta_{1-40}$, $A\beta pE_{3-42}$, $A\beta pE_{3-40}$) are reported. Voltage clamp bilayer electrophysiology studies indicate that all variants except $A\beta_{1-40}$ exhibit stable ion channel activity in phosphatidylcholine/phosphatidylglycerol/cholesterol bilayers with distinct conductance behaviors. $A\beta_{1-42}$ and $A\beta pE_{3-42}$ show majorly step-like conductance changes with well-defined open-close states whereas $A\beta pE_{3-40}$ show high-frequency burst-like activity with multi-state conductance. $A\beta_{1-40}$ exhibits infrequent burst-like activity. Structural data from infrared spectroscopy identify significant β-sheet content for the peptides in lipid membranes. In all cases, the channel activity could be blocked by Zn^{2+} ions to varying degrees. Overall, these results suggest that pyroglutamylated variants of Aβ, like unmodified Aβ, are capable of forming ion channels in cell membranes. Characterization of the molecular structure and ion channel

formation activities of the most abundant and toxic Aβ species may help in rational drug design for AD.

4.2 Introduction

Alzheimer's disease (AD) is a progressive neurodegenerative disorder that leads to dementia, cognitive decline, synaptic loss and neuronal death. The disease affects elderly individuals above the age of 65 and has turned out to be a major stressor on healthcare systems all over the world. Even though a large body of research has been dedicated to understanding the causal mechanisms and progression of Alzheimer's pathology, a definitive cure or treatment modalities have not been found. The main hallmark of the disease is the presence of extracellular lesion like deposits called amyloid plaques and intracellular aggregates called neurofibrillary tangles (NFTs) [6]. At the core of these extracellular plaques lies aggregates of a protein called Amyloid-β (Aβ), which is formed by the proteolytic cleavage of the amyloid precursor protein (APP) [36]. $Aβ_{1-42}$, a partially transmembrane peptide comprised of 42 amino acids (also called full length Aβ), is implicated in the cascade of events leading to Alzheimer's pathology. This has led to the proposal of the 'amyloid hypothesis', which argues that the aggregates of Aβ peptides are the main causative factors which trigger a cascade of events affecting different regions of the brain associated with cognitive tasks and thus causing a decline in the mental faculties of the individual [10][12]. The extracellular aggregates are comprised of highly ordered fibrillar assemblies of the Aβ peptide in conjunction with other extracellular material. Recent atomic resolution structural studies (ssNMR, cryoEM) of these fibrillar assemblies, in conjunction with in-vitro and ex-vivo studies have reached a consensus that small, soluble oligomeric form of the

Aβ (which maybe precursors to Aβ fibrillar assemblies) are the agents responsible for neurotoxicity [46][47][52]. Irrespective of the causal modality (oligomer induced vs fibrillar aggregate induced) the amyloid cascade hypothesis still offers plausible explanation on some aspects of the pathophysiology.

Although $A\beta_{1-42}$ seems to be the major component of amyloid plaques, multiple studies have also found significant presence of $A\beta_{1-40}$ (2 amino acids lesser in the C-terminus side compared to full length $A\beta_{1-42}$), N-terminal truncated variants of $A\beta_{1-42}$ (denoted by $A\beta_{1-x}$) such as $A\beta_{4-42}$ and pyroglutamylated $A\beta pE_{1-x}$ in histological examination of postmortem brain slices of patients with AD [170] [171] [172]. These studies have also posited that the presence of pyroglutamylated Aβ variants correlates strongly with neurotoxicity and their absence in age matched controls of individuals without AD further supports the notion of these variants being central to the toxicity cascade. Pyroglutamylated variants of Aβ are formed by enzyme mediated (by Meprin-β or DPP4) cleavage of full length Aβ ($A\beta_{1-42}$ or $A\beta_{1-40}$) between Ala-2 and Glu-3 residues. DPP4 catalyzed by another enzyme glutaminyl cyclase (QC) leads the conversion of N-terminal truncated Aβ peptides to their pyroglutamylated variants by intramolecular dehydration of the exposed glutamate residue in position 3 and subsequent post-translational conversion into a lactam ring [173]. These posttranslational modifications increase the stability and aggregation propensity of the pyroglutamylated variants. Due to their abundant presence in patients with AD, pyroglutamylated variants have emerged to be prime drug development targets for inhibition of aggregation [173]. Thus, it is important to understand the molecular properties of these peptides in a comparative framework with their full-length counterparts. In this study, we characterized the structural properties and functional behavior of four Aβ peptides – $A\beta_{1-42}$, $A\beta_{1-40}$ and their

pyroglutamylated variants AβpE$_{3-42}$ and AβpE$_{3-40}$. A combination of fluorescence spectroscopy, Circular dichroism spectroscopy (CD), Attenuated Total Reflection – Fourier Transform Infrared spectroscopy (ATR-FTIR) show that the pyroglutamylated variants and full length Aβ display relatively high β-sheet secondary structure content in POPC:POPG:Cholesterol bilayers which are characteristic structural features of amyloid peptides. Voltage clamp electrophysiological studies of these peptides reveal the propensities of these peptides to exhibit pore like/ion channel like function in these lipid bilayers, albeit with different signatures. Atomic force microscopy (AFM) imaging revealed the presence of pore like structures in lipid bilayers. These structural studies in combination with functional studies under homogenous circumstances can pave the way towards developing robust therapeutics to counter the cascade of AD.

4.3 Materials and Methods

POPC (1-palmitoyl-2-oleoyl-glycero-3-phosphocholine), POPG(1-palmitoyl-2-oleoyl-sn-glycero-3-phospho-(1'-rac-glycerol)) and cholesterol (stock solutions in Chloroform) were purchased from Avanti Polar Lipids(Alabaster, AL). Amyloid beta variants (Aβ$_{1-42}$, pEAβ$_{3-42}$, Aβ$_{1-40}$, pEAβ$_{3-40}$) were purchased from Innovagen(Sweden). HEPES buffer, PBS 1X buffer were purchased from Gibco.

4.3.1 Lipid preparation: POPC, POPG and Cholesterol were aliquoted at 6:3:1 mol% into glass vials (total dry mass of lipids adding up to 1 mg). The glass vials were stored in vacuum to evaporate the chloroform while forming lipid cakes on the walls of the glass vials.

4.3.2 Peptide preparation - Lyophilized peptides were dissolved in 1% ammonium hydroxide, divided into aliquots and stored in -80C until further use. For all the experimental studies, the frozen aliquots were thawed in an ice bath and buffer solution was added to dilute the aliquots to the required concentration. For voltage clamp bilayer electrophysiology experiments, 10mM HEPES with 1M KCl buffer was used. For AFM and other experiments, 10mM HEPES with 300mM KCl buffer was used (also called as imaging buffer). All buffers were freshly prepared and filtered with 0.22uM PTFE filters before usage.

4.3.3 Voltage Clamp Electrophysiology - Electrophysiological characterization of peptide activity in bilayer membranes were performed with voltage clamp experiments. The bilayers were formed in 250um diameter circular apertures (formed on Delrin cuvettes) using the lipid painting method [96]. Briefly, the dried lipids were dissolved in decane to final concentrations of 40-50mg/ml. The lipid solution in decane was then painted on the apertures using a fine paint brush. The apertures were left to dry for about 4 hrs. After drying, the cuvettes were assembled in a conventional 2-well setup. Buffer solution was added slowly (1 ml in each side of the cuvette) and the bilayer was allowed to form for about 5-10 minutes. To induce optimal bilayer formation by thinning, a glass-blob terminated pasteur pipette was used to gently brush over the aperture. Spontaneous bilayer thinning and formation was monitored using real-time capacitance measurements. For all the experiments a 90pF capacitance was set as the minimum threshold to ensure optimal bilayer formation and stability. Generally, the capacitance of the bilayers formed varied between 100-180pF. The voltage clamp setup consisted of a high gain electrophysiology amplifier with a resistive feedback headstage (Warner Instruments BC-535) connected to a digitizer (Digidata 1440A) which in turn was connected to a workstation computer. All data were

recorded with a sampling frequency of 10kHz. An integrated 8-pole low pass Bessel filter was used to filter the data at 1kHz bandwidth. For further filtering and noise reduction, the data were also collected in parallel with another Bessel filter (Warner Instruments, LPF-8) at a cutoff frequency of 60Hz. For controlling and visualization of the signals in real-time, Clampex software was used (v10.6, Axon Instruments) and all the subsequent data analysis was carried out in Clampfit (v10.6, Axon Instruments, San Jose, CA).

In a typical electrophysiology experiment, after the bilayer was formed in the aperture, the stability was tested using a combination of intermittent capacitance measurements and linear voltage ramp in the -150mV to +150mV range. After bilayer stability was ensured, solubilized peptide was added to one of the wells (trans side) at the required final concentration. In most cases electrophysiological activity was assessed at peptide final concentration of 100nM. After about 5 min of peptide addition, bilayer hold voltages were ramped in 50mV increments from -100mV to +100mV

4.3.4 Electrophysiology data analysis – The recorded data files were transferred into the pClamp analysis environment, and a manual baseline correction was performed in conjunction with offset removal. For analysis and visualization of the electrophysiological activity of the peptides at each of the holding voltages, 120-180s snippets were selected, where the electrical activity was visually clear. Amplitude histograms of these snippets were generated to visualize the distribution of conductances.

4.3.5 Attenuated Total Internal Reflection-Fourier Transform Infrared Spectroscopy (ATR-FTIR)

A mixture of POPC, POPG, cholesterol dissolved in chloroform, and peptide dissolved in HFIP were combined in a vial at a peptide/total lipid molar ratio 1:50, spread onto a Ge plate, and dried via desiccation for 1 h to allow the peptide-lipid sample to make a multilayer on the Ge plate. Buffer was then injected and FTIR spectra were measured using plane-polarized infrared light, at parallel and perpendicular polarizations with respect to the plane of incidence (Figure a). These measurements have allowed determination of peptide structure and orientation in lipid membranes by peak-fitting of the amide I absorbance bands and from linear dichroism, respectively.

4.3.6 Atomic Force Microscopy (AFM) Imaging – In order to probe the membrane organization and morphology of the 4 different peptides, we performed Atomic Force Microscopy Imaging. AFM imaging was performed on peptides directly incubated on mica and reconstituted in lipid bilayer. For AFM imaging on mica, the peptide stocks were diluted to 1uM final concentration, vortexed for 30s and ~20ul of 1uM peptide solution was added to a freshly cleaved mica disk. The sample was incubated at room temperature for ~10 minutes, washed 3x in an imaging buffer (10mM Hepes, 300mM KCl, pH 7.4) and imaged. For AFM imaging with lipids, dried lipids were hydrated with the imaging buffer containing 3mM CaCl2 at room temperature for about 20 minutes. The hydrated lipid sample was then bath sonicated for 15 mins to form unilamellar vesicles. After formation of vesicles, the peptide was added to the vial at final concentration of 1:1000 or 1:500 (molar ratio, peptide:lipid) and incubated for 10 minutes at room temperature. For better incorporation of peptides into vesicles, the incubated sample was briefly bath sonicated (60-75s). The sample consisting of proteoliposomes was then drop casted on freshly

cleaved mica surface and incubated for 20 minutes at room temperature, washed 3x in imaging

buffer and the formed supported lipid bilayers were imaged in the same imaging buffer.

All AFM imaging was performed on a Multimode AFM (Bruker) controlled by a Nanoscope V

controller. All images were collected in PeakForce Tapping mode with SNL-10 cantilevers (Bruker)

of spring constant in the range of 0.1-0.3N/m. Fresh cantilevers were used in every imaging

session and among different peptides.

AFM Data analysis – All collected images were analyzed using Nanoscope Analysis v1.5 software

or the SPM analysis package Gwyddion. Briefly, images were line flattened and color scale

adjusted. For generating particle height histograms, we used the 'Particle Analysis' feature in

Nanoscope Analysis which categorizes particles based on height thresholding.

4.3.7 CD and Fluorescence Spectroscopy: For CD and fluorescence experiments, the lyophilized

lipids were dissolved in chloroform at 2.00 mM concentration and the peptides were dissolved

in hexafluoroisopropanol (HFIP) at 200 μM concentration as stock solutions. Peptide samples

were prepared by placing 50 μL of 200 μM peptide solution in HFIP in a glass vial, drying by 1-h

desiccation, adding 500 μL of the buffer and vortexing for 5 minutes. To prepare the

proteoliposomes, a mixture of 150 μL of 2 mM POPC, 75 μL of 2 mM POPG, 25 μL of 2 mM

cholesterol, and 50 μL of 200 μM peptide were combined in a glass vial and desiccated for 1 hour.

Then 500 μL of buffer was added and vortexed for 5 minutes, resulting in total lipid concentration

of 1.00 mM at POPC:POPG:cholesterol molar ratio of 6:3:1 + 20 ⊠M peptide, corresponding

to1:50 peptide-to-total lipid molar ratio. The buffer was either 25 mM NaCl + 25 mM Na,K-

phosphate (pH 7.2) or 25 mM NaCl + 25 mM Tris-HCl (pH 7.2). The buffer solutions were filtered

with 0.22 μm filter-syringes and were kept at 4°C. When needed, the peptide or proteoliposome samples were vortexed through 100 nm pore-size polycarbonate membranes (15 passages) using an Avanti Polar Lipids mini extruder.

CD and fluorescence spectra were measured using a J-810 spectropolarimeter equipped with a fluorescence attachment and a temperature controller (Jasco, Tokyo, Japan) at 20°C and 37°C. Then scans were averaged for the CD spectra and 3 scans for the fluorescence spectra.

4.4 Results

4.4.1 Membrane Channel Forming Activities of the Peptides. Voltage clamp experiments have been conducted at selected hold voltages between +100 mV and -100 mV (the sign corresponds to the trans side, where the peptide was added). Current recordings for over 2 minutes at +50 mV transmembrane voltage showed that at ~5 min following addition of Aβ$_{1-42}$, the current reached a baseline level of ~40 pA, featuring stepwise transitions between discrete conductance levels (Figure 4.1A). The stability of the conductance pattern and the consistent amplitude of the transitions suggest that Aβ$_{1-42}$ inserts into the membrane and forms ion-conducting channels that are able to switch between on/off states [59][108].
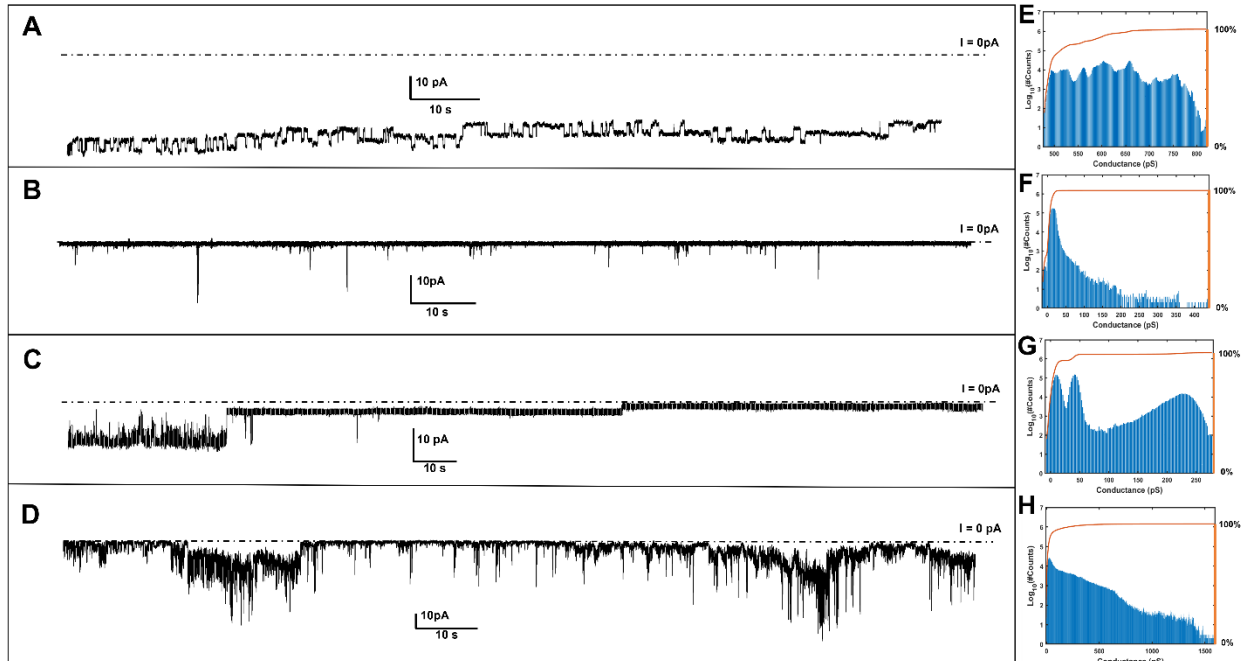
Figure 4.1 Voltage clamp current traces of Aβ$_{1-42}$ (A), Aβ$_{1-40}$ (B) AβpE$_{3-42}$ (C) AβpE$_{3-40}$ (D) at 50 mV membrane-hold potential. The dotted horizontal line indicates the zero current baseline level. Conductance histograms for Aβ$_{1-42}$, Aβ$_{1-40}$, AβpE$_{3-42}$, and AβpE$_{3-40}$ are shown in panels E, F, G, H, respectively, where the total counts/bin are expressed in log scale in the left y-axis (blue bars) and the cumulative counts (0-100%) per conductance level are indicated in the right y-axis (red line)

A similar behavior of stepwise current fluctuations was observed for Aβ$_{1-42}$ at other voltages, although in these traces the step-like pattern was superimposed with gradual changes of the total conductance level, possibly indicating the presence of a heterogeneous set of ion-conducting structures such as assemblies of different oligomeric numbers (Figure 4.2). This is consistent with the histogram, which indicates a distribution of Aβ$_{1-42}$-induced conductance in a range of values (Fig. 4.1E and Figure 4.2 D, E and F)
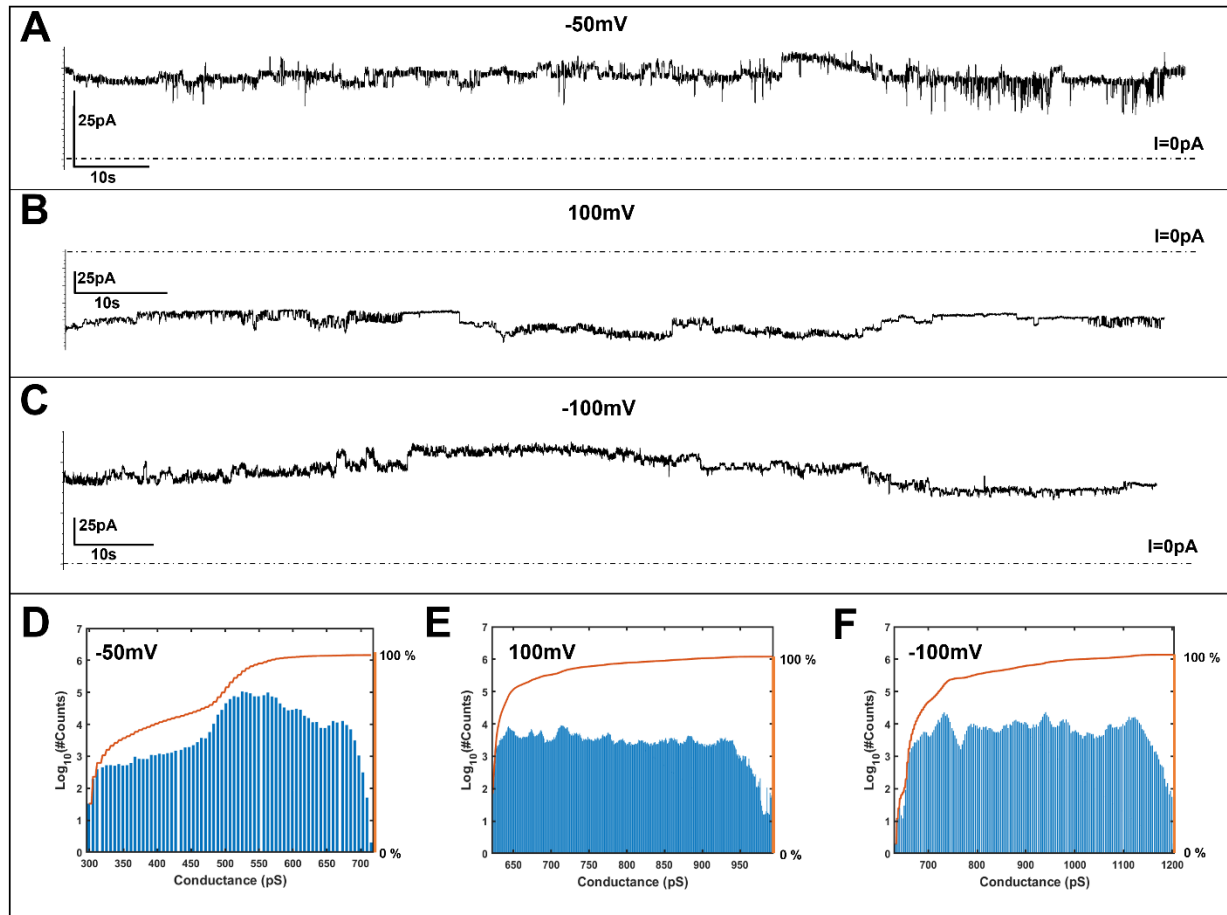
Figure 4.2 - Voltage clamp current recordings (A, B and C) and conductance histograms of Aβ$_{1-42}$ at hold voltages of -50mV, +100mV and -100mV (D, E and F) respectively.

Aβ$_{1-40}$ displayed a different behavior; infrequent burst-like current spikes with <50 ms duration were detected that were superimposed on a zero current level (Fig. 4.1B). The amplitude, duration, and the frequency of current spikes were significantly higher at 100 mV and -100 mV applied voltages, more frequent at -100 mV than +100 mV, and their magnitude exceeded severalfold the current steps induced by Aβ$_{1-42}$ (Figure 4.3). Non-zero macro current was not observed for this peptide. The conductance histogram of Aβ$_{1-40}$ featured a peak around the zero level and a relatively wide range for conductance distribution (Figure 4.1F) without favoring any particular conductance level.
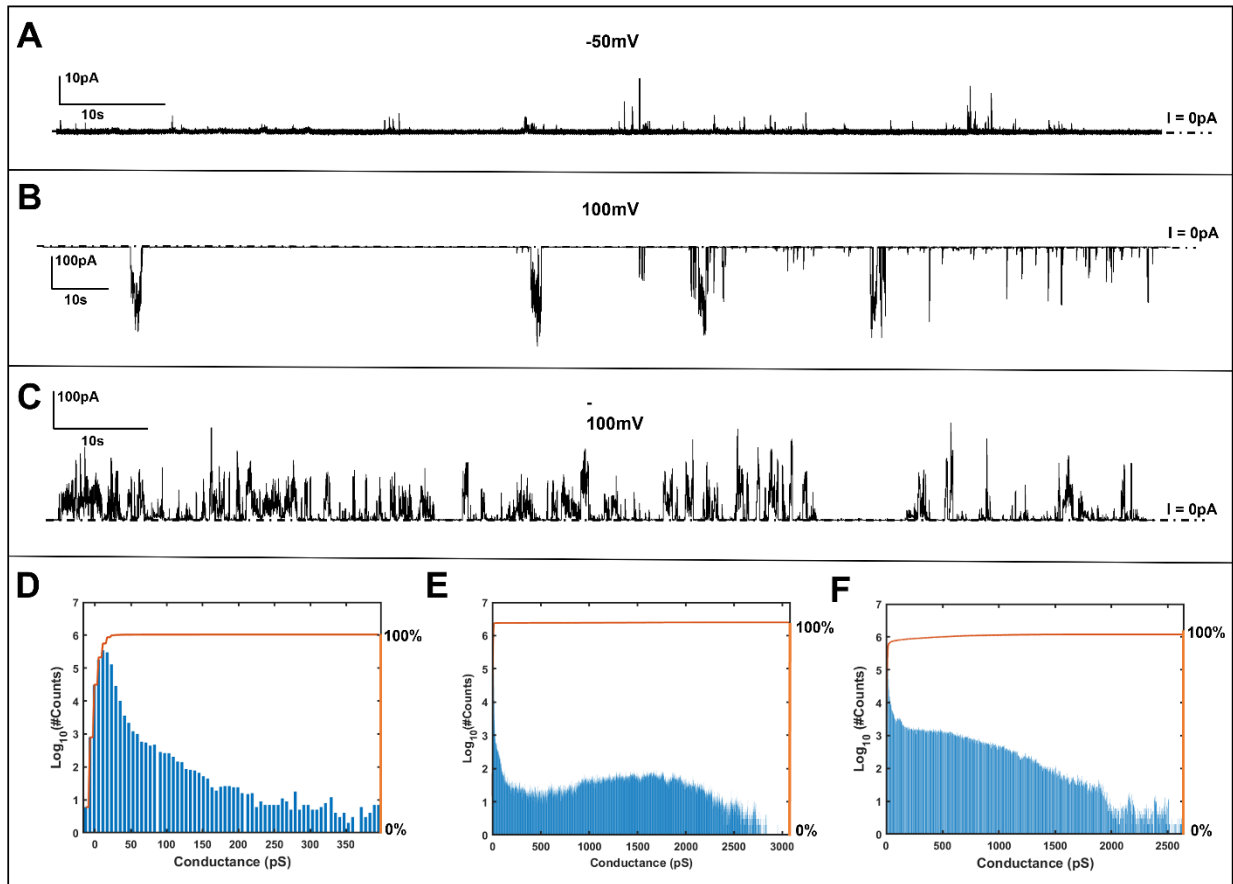
Figure 4.3 - Voltage clamp current recordings (A, B and C) and conductance histograms of Aβ1-40 at hold voltages of -50mV, +100mV and -100mV (D, E and F) respectively.

Membrane conductance induced by AβpE$_{3-42}$ involved both stepwise and high frequency burst-like patterns (Figure 4.1 C; Figure 4.4). In addition, events of sudden jump between different macro conductance levels occurred, which might result from cooperative opening/closing of multiple channels (Figure 4.4) [154]. Some clear patterns of AβpE$_{3-42}$ as compared to Aβ$_{1-42}$ were the presence of constant macro conductance levels for long dwell time (~1 min) as well as shifts to zero current level, both of which could be overlayed with short bursts of current. This behavior is reflected in the histogram of these peptides, displaying a bimodal conductance distribution (Figure 4.1G, Figure 4.4).
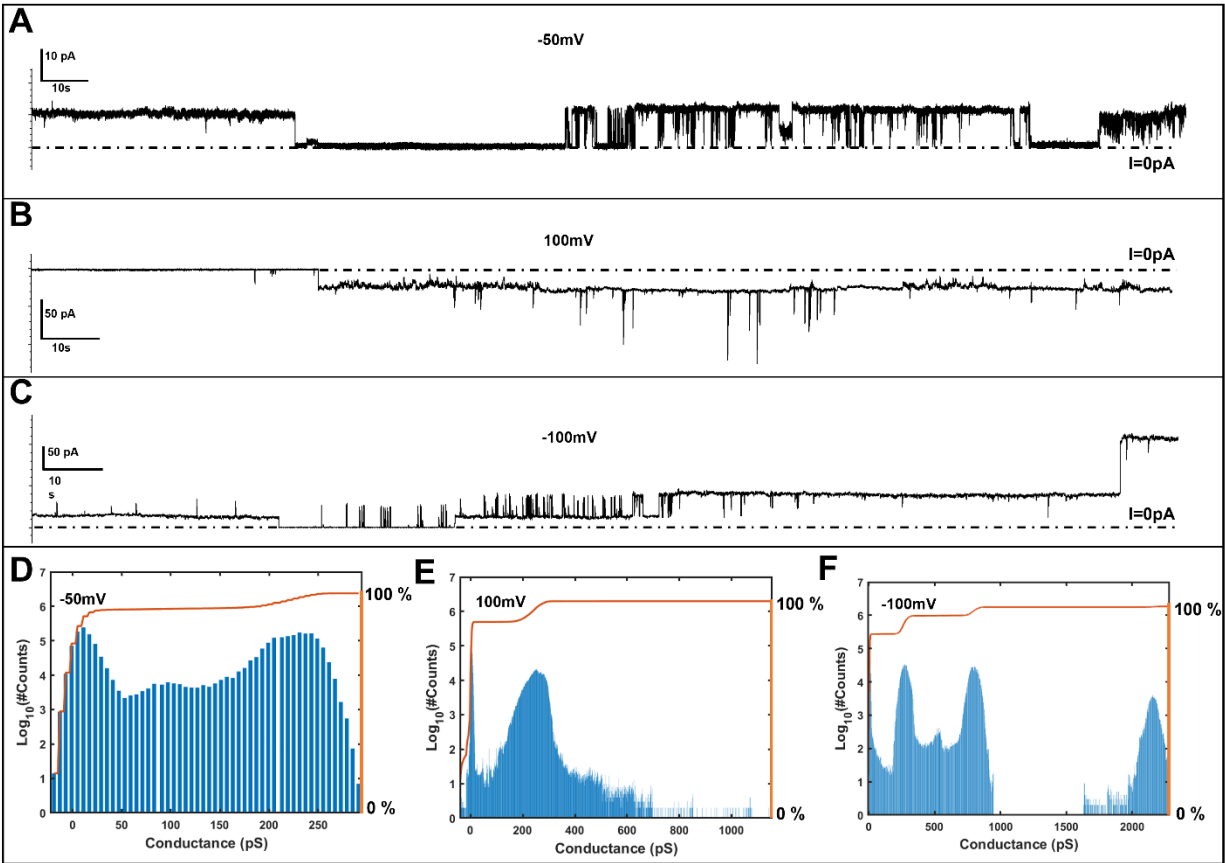
Figure 4.4 - Voltage clamp current recordings (A, B and C) and conductance histograms of AβpE$_{3-42}$ at hold voltages of -50 mV, +100 mV and -100 mV (D, E and F) respectively.

AβpE$_{3-40}$ also exhibited a combination of step-like and burst-like activities, with a higher frequency and conductance magnitude of burst-like events compared to Aβ$_{1-40}$ and AβpE$_{3-42}$ (Figure 4.1D). The burst-like activities AβpE$_{3-40}$ were continuous throughout the recording and showed similar behavior at all tested voltages. The conductance histogram of AβpE$_{3-40}$ was spread over a range of values, with no clearly discernible peaks (Figure 4.1H, Figure 4.5). Even though clear step-like transitions in the conductance were observed for some holding voltages, rapid switching between sub-states of intermittent conductance were also observed. The change in voltage did not influence the kinetic behavior of the channels, with the frequency of current transition events remaining approximately constant.
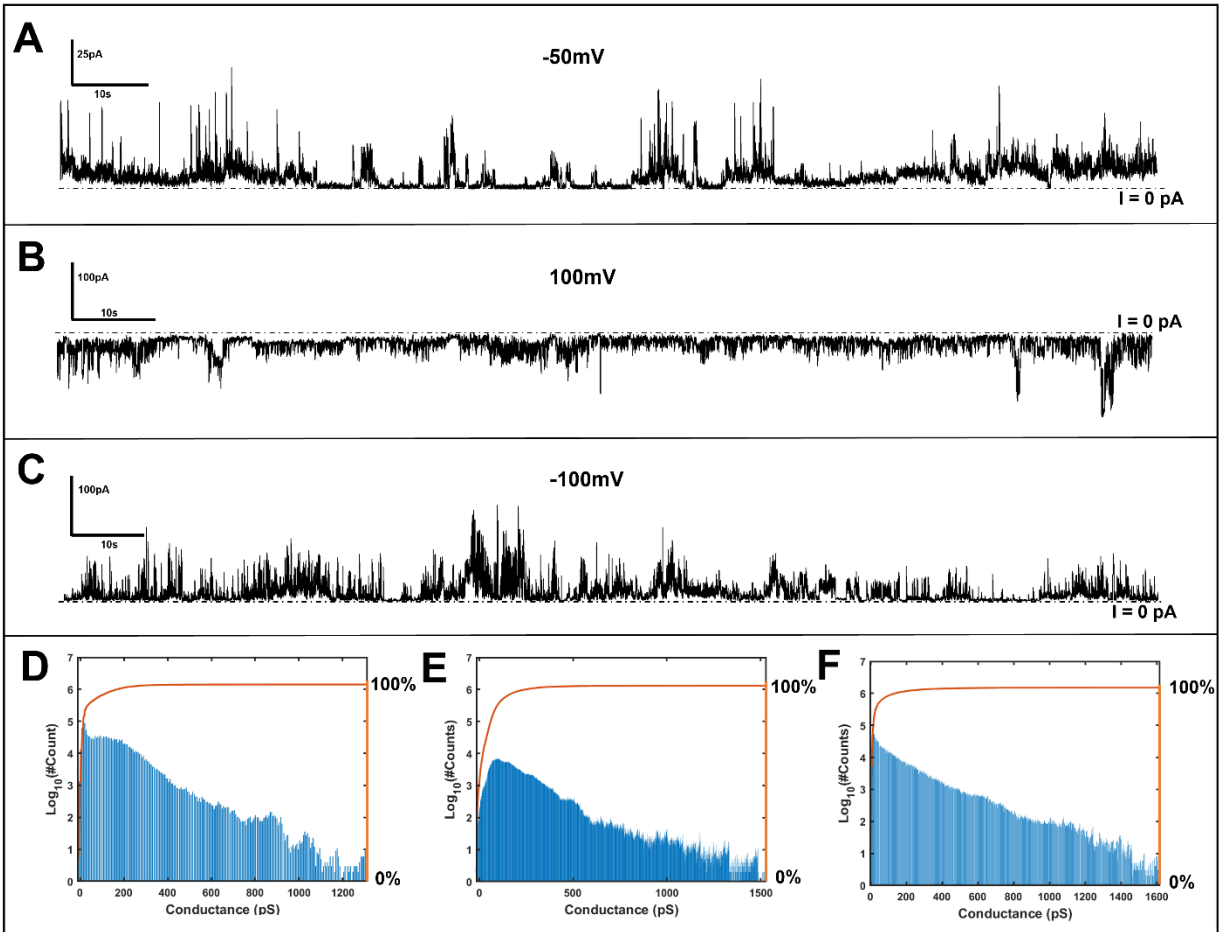
Figure 4.5 - Voltage clamp current recordings (A, B and C) and conductance histograms of AβpE$_{3-40}$ at hold voltages of -50 mV, +100 mV and -100 mV (D, E and F) respectively.

4.4.2 Single Channel Properties. More detailed analysis of current traces revealed the single channel properties. Aβ$_{1-42}$ channels switched between closed and open states, designated L$_c$ and L$_o$, respectively, with channel conductance of ~100 pS (Figure 4.6A). The open state dwell time varied in a wide range, from <100 ms to >1 s, indicating slow on/off kinetics. The other peptides displayed more than one open sub-state, designated L$_{o1}$, L$_{o2}$, etc. (Figure 4.6 B, C and D). Aβ$_{1-40}$ mostly exhibited burst-like activity, i.e. jumps from L$_c$ to a short-lived L$_{o1}$ state (80-100 pS) and

101

back, although other states of larger conductance (~340 pS) are possible (Figure 4.6 B). Thus, $A\beta_{1-40}$ does not form stable channels with significant open state dwell time under these conditions.
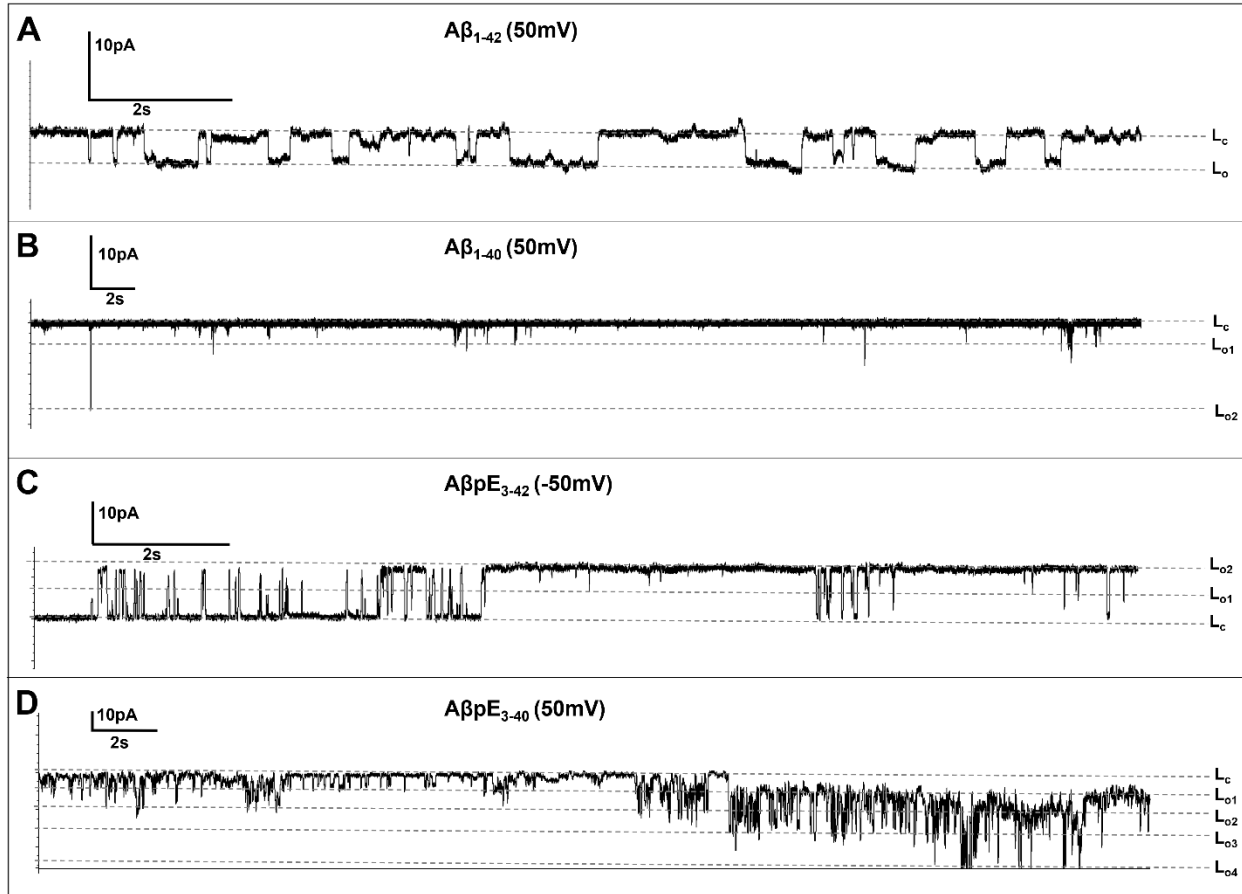
Figure 4.6 - Electrophysiological recordings of $A\beta_{1-42}$ (A), $A\beta_{1-40}$ (B), $A\beta pE_{3-42}$ (C), and $A\beta pE_{3-40}$ (D) in shorter time scale to reveal the single channel conductance behaviors. Discrete conductance levels have been marked with notation Lc, i.e., closed state, and L_{o1}, L_{o2}, …, corresponding to multiple open state levels. These levels have been assigned to include the maximum number of points at a particular conductance level. In all cases except panel C ($A\beta pE_{3-42}$), the hold voltage was +50 mV. For $A\beta pE_{3-42}$, -50 mV was chosen as the step-like conductance activity was more distinguishable compared to the +50 mV trace.

$A\beta pE_{3-42}$ showed regular switching between discrete states L_c and L_{o2} (~300 pS) while also transitioning to a more seldom intermediate states L_{o1} (~150 pS) (Figure 4.6C). This peptide showed relatively fast kinetics of transitions between states in the beginning of the trace

followed by periods of very long (> 1 s) open state dwell time, resembling the behavior of $A\beta_{1-42}$. $A\beta pE_{3-40}$ displayed a complex behavior, i.e., twitching between at least 4 open states (L_{o1} through L_{o4}) with conductance values of approximately 200 pS, 400 pS, 640 pS and 1040 pS respectively (Figure 4.6D). In contrast to the remaining three peptides, $A\beta pE_{3-40}$ showed continuously transitioning events with relatively fast kinetics.

4.4.3 Channel Blocking by Zn^{2+} Ions. As many ion channels of biological importance are modulated by Zn^{2+} ions, which has high affinity for the side chains of certain amino acids (Asp, Glu, His, Cys). The direct modulatory activity of zinc toward ion channel activity and the ability of Zn^{2+} to block $A\beta$ channels has been studied [59][65]. At +100 mV hold voltage, $A\beta_{1-42}$ induced current of ~65 pA, followed by single channel activity (Figure 4.7A). After first addition of 10 mM $ZnCl_2$, the single channel activity persisted for roughly 40 s, then ceased as the membrane switched to a lower macro conductance level. The current did not fully subside even after a second addition of 10 mM $ZnCl_2$, although most of the flickering activity stopped. This data means that Zn^{2+} does exert an inhibitory effect on $A\beta_{1-42}$ channels but a fraction of ion-conducting structures remain active, consistent with a heterogeneous assembly of $A\beta_{1-42}$ molecules in the membrane.

$A\beta_{1-40}$ showed the characteristic burst-like activity, which ceased ~30 min after addition of 10 mM $ZnCl_2$, followed by an unusual behavior of the current, i.e., appearance of long-lived current flickers (or closely spaced short bursts) in addition to infrequent single bursts. In the end of the trace, the current vanished, hence no more $ZnCl_2$ was added (Figure 4.7B).
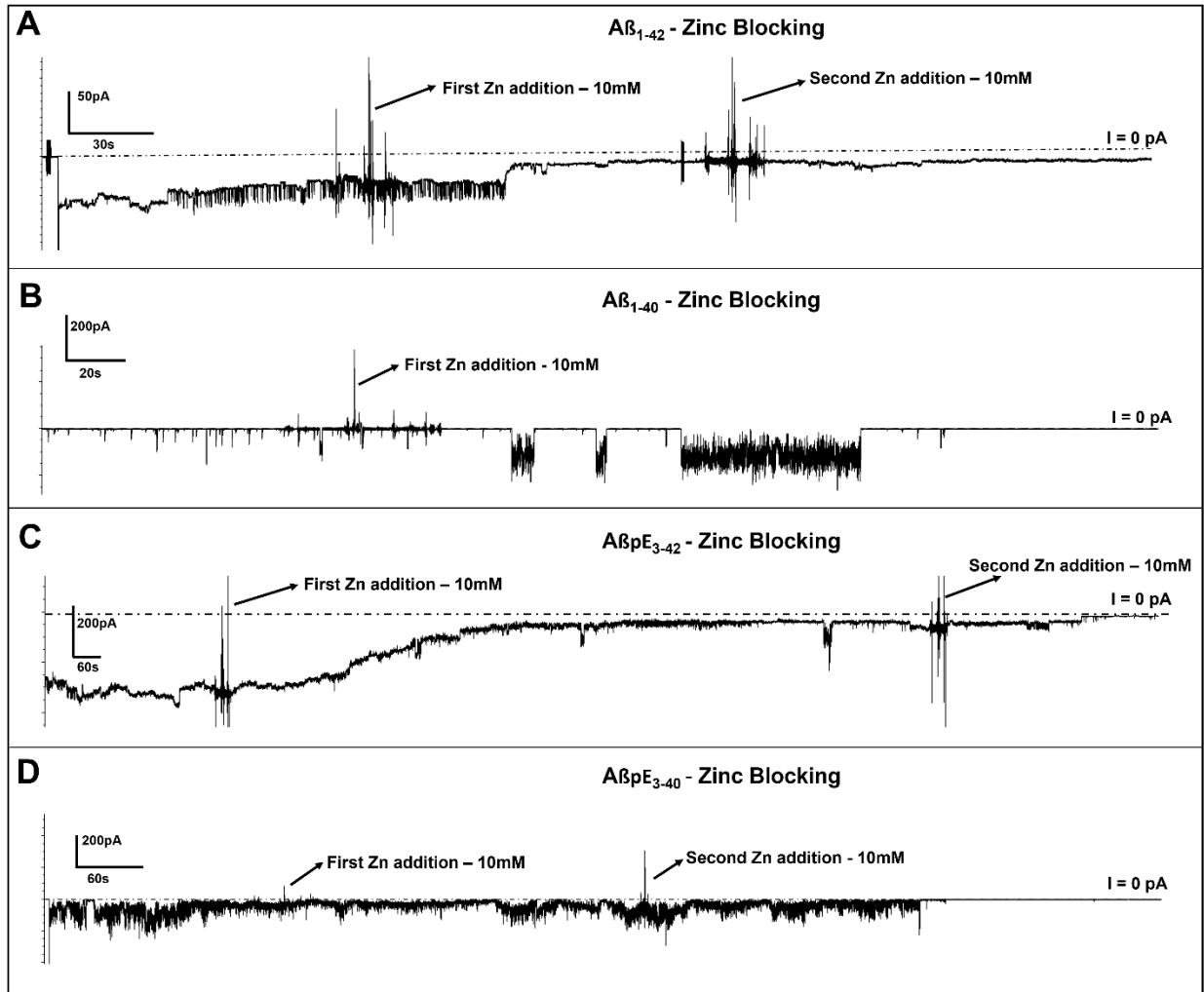
Figure 4.7 - Ion channel blocking activity by Zn2+ ions. Electrophysiological current traces of the peptides at +100 mV hold potential (Aβ$_{1-42}$ (A), Aβ$_{1-40}$ (B), AβpE$_{3-42}$ (C) and AβpE$_{3-40}$ (D)) with 10 mM ZnCl$_2$ added to the trans chamber. In all cases except for Aβ$_{1-40}$ ZnCl$_2$ was added twice, marked by arrows.

AβpE$_{3-42}$ showed jump to a macro conductance level via cooperative opening of multiple channels. The first addition of ZnCl$_2$ drastically reduced the conductance from the initial macro conductance level which did not subside completely. Following a second addition of ZnCl$_2$, the activity persisted for ~120 s and then stopped, reaching a level very close to the baseline (Figure 4.7C). AβpE$_{3-40}$ showed continuous, high frequency burst-like activity (Figure 4.7D). The first 10

mM $ZnCl_2$ addition reduced the amplitude of the spikes, but higher conductance resumed after ~3 min. Approximately 4 min after second addition of $ZnCl_2$, the current reached the zero level.

4.4.4 Peptide Structure from Circular Dichroism (CD): Significant differences between the channel forming activities of the four Aβ peptides are likely associated with their distinct structural features and modes of interactions with lipid membranes. These characteristics were analyzed by biophysical methods. The secondary structure of the peptides without and with lipid vesicles was probed by far-UV CD. Because peptide samples with lipid vesicles were studied before and after extrusion through 100 nm pore-size filters to obtain unilamellar vesicles with defined size, lipid-free peptide sample were also studied before and after extrusion. Spectra of $Aβ_{1-42}$ displayed a deep minimum at 217-218 nm irrespective of extrusion, indicating β-sheet structure [174] (Figure 4.8A). Extruded samples with lipid showed a weaker minimum at 216 nm and a shoulder around 209 nm, suggesting an α/β-type structure. (Unextruded samples with lipid generated spectra with excessive noise due to strong light scattering by vesicles and therefore are not shown.) $Aβ_{1-40}$ generated minima around 217 and 199 nm before extrusion, implying β-sheet and unordered structures (Figure 4.8D). A single minimum at 217 nm after extrusion with approximately same intensity suggests removal of the unordered fraction. In contrast to $Aβ_{1-42}$, the presence of lipid caused formation of unordered, rather than a-helical, structure in $Aβ_{1-40}$. Spectra of $AβpE_{3-42}$ and $AβpE_{3-40}$ showed weaker and red-shifted np* transitions (219-222 nm) before and after extrusion (Figure 4.8G, J). In lipid vesicles, spectra of these peptides exhibited an additional feature around 208 nm, indicating α-helix formation.
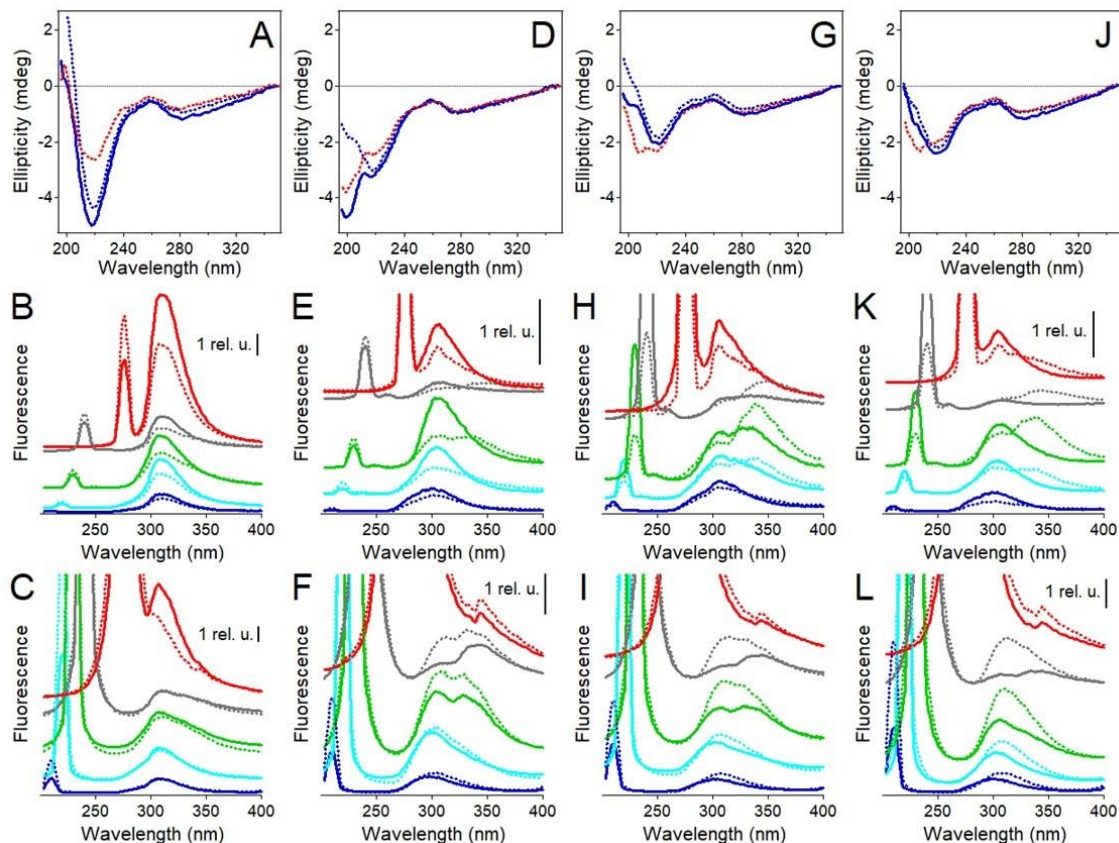
Figure 4.8 - CD and fluorescence spectra of Aβ$_{1-42}$ (A, B, C), Aβ$_{1-40}$ (D, E, F), AβpE$_{3-42}$ (G, H, I), and AβpE$_{3-40}$ (J, K, L). In CD spectra (upper row), blue and red lines correspond to the absence and presence of lipid vesicles, respectively (60 mol % POPC, 30 mol % POPG, 10 mol % cholesterol). For fluorescence data, the middle row presents spectra in the absence of lipid and the lower row shows data in the presence of lipid vesicles. The excitation was at 210 nm (blue), 220 nm (cyan), 230 nm (green), 240 nm (grey), and 275 nm (red). In all cases, dotted lines indicate that the samples have been extruded through 100 nm pore-size polycarbonate membranes. Peptide and total lipid (when present) concentrations were 20 mM and 1 mM, respectively, the buffer was 25 mM NaCl + 25 mM Na,K-phosphate, pH 7.2, and the temperature was 20°C.

Thus, Aβ$_{1-42}$ forms a well-defined β-sheet structure, followed by the pyroglutamylated peptides, while Aβ$_{1-40}$ tends to be more unordered. In all cases except Aβ$_{1-40}$, the presence of membranes appears to induce partial α-helical structure. Together with the channel data, these results indicate a correlation between β-sheet propensity and step-like channel forming potency of the peptides.

In the near-UV region, the CD spectra displayed a negative band at 278-282 nm, which is the induced CD signal due to the S$_0$→S$_1$ (ground to first excited singlet state) transition in the

106

aromatic amino acid side chains [175]. This CD band did not depend on the presence of lipid. However, fluorescence spectroscopy revealed interesting structural features of the peptides, described in the next section.

4.4.5 Structural Features from Fluorescence Spectroscopy. As described in Figure 4.9, excitation of $A\beta_{1-42}$ at wavelength (l_{ex}) varying from 200 nm to 380 nm results in two effects, Rayleigh scattering at l_{ex} and fluorescence at two regions of l_{ex}, i.e. 220-230 nm and 260-280 nm, due to $S_0\rightarrow S_2$ and $S_0\rightarrow S_1$ transitions, respectively. $A\beta_{1-42}$ produced strong fluorescence at 307-310 nm with l_{ex} varying between 210 nm and 275 nm before and after extrusion through 100 nm pore-size filters (Figure 4.8B). Similar emission wavelengths following $S_0\rightarrow S_2$ and $S_0\rightarrow S_1$ excitations indicate $S_2\rightarrow S_1$ internal conversion and emission from a low vibrational energy state of S_1 in both cases. $A\beta_{1-40}$ displayed weaker and blue-shifted fluorescence (301-307 nm), and the blue shift was stronger at shorter l_{ex} (Figure. 4.8E). These features suggest that Phe contributes to fluorescence more than in case of $A\beta_{1-42}$ because Tyr of $A\beta_{1-40}$ is exposed to and quenched by the buffer [176]. For the extruded samples of $A\beta_{1-40}$, an interesting effect has been detected. At l_{ex} = 230 nm, the emission band was split into peaks around 306 and 340 nm, and with l_{ex} = 240 nm the new, red-shifted component extended to larger wavelengths. The red-shifted component of Tyr emission can be rationalized in terms of a specific solvent effect, i.e., strong H-bonding of the phenolic OH group to a base such as HPO_4^{2-} and, possibly, deprotonation. Extrusion rendered a large fraction of the Tyr of $A\beta_{1-40}$ exposed to the buffer, resulting in red-shifted emission. The lack of such splitting in case of $A\beta_{1-42}$ indicates this peptide forms a more compact, solvent-protected β-sheet structure before and after extrusion.

Spectra of AβpE$_{3-42}$ showed still weaker fluorescence, suggesting more quenching by the buffer (Figure. 4.8H). A stronger solvent exposure resulted in appearance of the red-shifted component around 340 nm (for l_{ex} = 220 nm and 230 nm) or 350 nm (for l_{ex} = 240 nm) in addition to the lower-wavelength component at 306-310 nm, and the effect was more pronounced for the extruded samples. AβpE$_{3-40}$ generated one emission band at 300-308 nm before extrusion and split bands after extrusion, with a red-shifter component at 333-342 nm (Figure 4.8K). The absence of the red-shifted emission at l_{ex} = 275 nm indicates that the S$_0$→S$_1$ transition is less solvent-sensitive than the S$_0$→S$_2$ transition because their dipoles are oriented across and along the phenolic ring, respectively, the latter involving the polar hydroxyl group [176]. These data indicate that a) splitting of Tyr fluorescence can be used to assess solvent exposure, and hence the compactness of the tertiary fold, of proteins, b) fluorescence of solvent-exposed and protected fractions can be excited selectively, and c) the Tyr residue is most solvent-exposed in AβpE$_{3-42}$ and most solvent-protected in Aβ$_{1-42}$, the other two peptides showing intermediate solvent exposure of Tyr.

The presence of lipid vesicles resulted in much stronger Rayleigh scattering (Figure. 4.8C, F, I, L). Fluorescence spectra of Aβ$_{1-42}$ did not undergo splitting (Figure. 4.8C), as in the absence of lipid, indicating a compact tertiary fold. In the case of Aβ$_{1-40}$, the emission was split at l_{ex} = 230 nm and 240 nm both before and after extrusion (a red-shifted component at 330-344 nm in addition to one at 304-313 nm) (Figure 4.8F). This means a solvent-exposed Tyr of Aβ$_{1-40}$ even in the presence of vesicles. The poor membrane insertion ability of Aβ$_{1-40}$ is consistent with its less efficient channel forming activity, as discussed above. A solvent-accessible structure in the presence of lipid before and after extrusion was also exhibited by AβpE$_{3-42}$, although in this case

the red-shifted component was less intense and was absent at l_{ex} = 220 nm (Figure. 4.8I), suggesting partial membrane insertion. Spectra of AβpE3-40 in the presence of lipid did not show splitting, especially for the extruded samples (Figure. 4.8L), implying a more efficient protection from the solvent by the membranes. The fluorescence of Aβ1-40, AβpE3-42, and AβpE3-40 with excitation at 275 nm was obscured by strong Rayleigh scattering; the feature around 344 nm is most likely the resonance-Raman scattering peak (Figure 4.8F, I, L). This underscores the usefulness of using a lower wavelength excitation as it not only clears the spectral window of Tyr emission but also reveals the degree of solvent exposure of the fluorophore.

The intriguing effect of Tyr emission splitting raises the question whether the solvent effect is unique to a phosphate buffer. This question was addressed by experiments using Tris-HCl buffer and no buffer at all. In Tris buffer, Aβ1-42 produced a single emission band at 306-313 nm with l_{ex} = 220-275 nm, before and after extrusion (Figure. 4.10A). Spectra of extruded Aβ1-40 displayed split emission with l_{ex} = 220-240 nm, with a red-shifted component at 336-338 nm (Fig. 4.10C). Splitting also occurred for unextruded and extruded AβpE3-42, although with a smaller red-shift effect (e.g., at l_{ex} = 220 nm, the red-shifted component was at 325 nm in Tris buffer vs. 340 nm in phosphate buffer, cf. Figure. 4.8H and Figure 4.10E). Spectra of AβpE3-40 were not split in Tris buffer (Figure. 4.10G). Thus, the Tyr emission splitting is not unique to the phosphate, but the effect is stronger in phosphate than in Tris buffer. Conceivably, Tris can weaken the OH bond of Tyr side chain by H-bonding with both hydrogen and oxygen atoms by its hydroxyl and amino groups but to a lesser extent than HPO_4^{2-}.
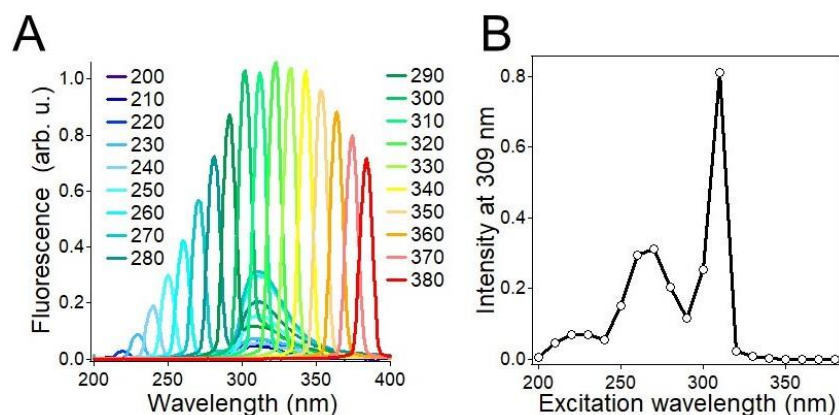
Figure 4.9 - (A): Fluorescence spectra of Ab1-42 in buffer (25 mM NaCl + 25 mM Na,K-phosphate, pH 7.2) with incident light of 200 – 380 nm, as indicated. (B): Emission intensity at 309 nm as a function of the incident light wavelength. Temperature was 20°C. These spectroscopic features reflect the fact that the total extinction of the incident light is due to absorption and scattering, and that in a certain spectral region, absorption results in fluorescence. Although there is only one Tyr (position 10) and three Phe residues (positions 4, 19, 20) in the peptide, the fluorescence is dominated by Tyr due to its larger quantum yield [164]. The spectra display Rayleigh scattering at each excitation wavelength (l_{ex}), as well as Tyr fluorescence around 309 nm when $l_{ex} \leq 290$ nm. Data of panel B show two regions of l_{ex} that produce maximum Tyr fluorescence, i.e., 220-230 nm and 260-280 nm, which are the pp* transitions from the ground stat to the second and first excited singlet states, i.e., $S_0 \rightarrow S_2$ and $S_0 \rightarrow S_1$, respectively (also known as ^1L_a and ^1L_b transitions) [175][176]. (The peak around 310 nm is due to scattered light, not fluorescence.) In the absence of absorption, i.e. above 300 nm, Rayleigh scattering is proportional to l^{-4} and decreases with increasing l whereas below 300 nm absorption dominates and consequently scattering decreases with decreasing l, as seen in panel A.

The presence of lipid membranes did not cause significant changes in fluorescence spectra (Figure. 4.10B, D, F, H), except that the spectra of extruded AβpE$_{3-40}$ showed splitting (Figure. 10H), indicating more solvent-exposed Tyr of this peptide. CD spectra of all four peptides in Tris buffer were similar to those in phosphate buffer (cf. Figure. 4.8 upper row and Figure. 4.11), indicating no secondary structural differences, as expected.

Splitting of Tyr emission also occurred in an unbuffered solution of 25 mM NaCl, although with a smaller red-shift effect. For example, for AβpE$_{3-42}$, at l_{ex} = 230 nm the red-shifted component was located at 338-340 nm in phosphate and Tris buffers and at 327-336 nm in the unbuffered NaCl solution. Also, the intensity of the red-shifted component for the extruded

peptide was much stronger in phosphate buffer than in Tris buffer and in the unbuffered solution.

These data suggest that the splitting of Tyr fluorescence is caused by the solvent and is stronger

when strong H-bonding acceptors and donors are present in the buffer.
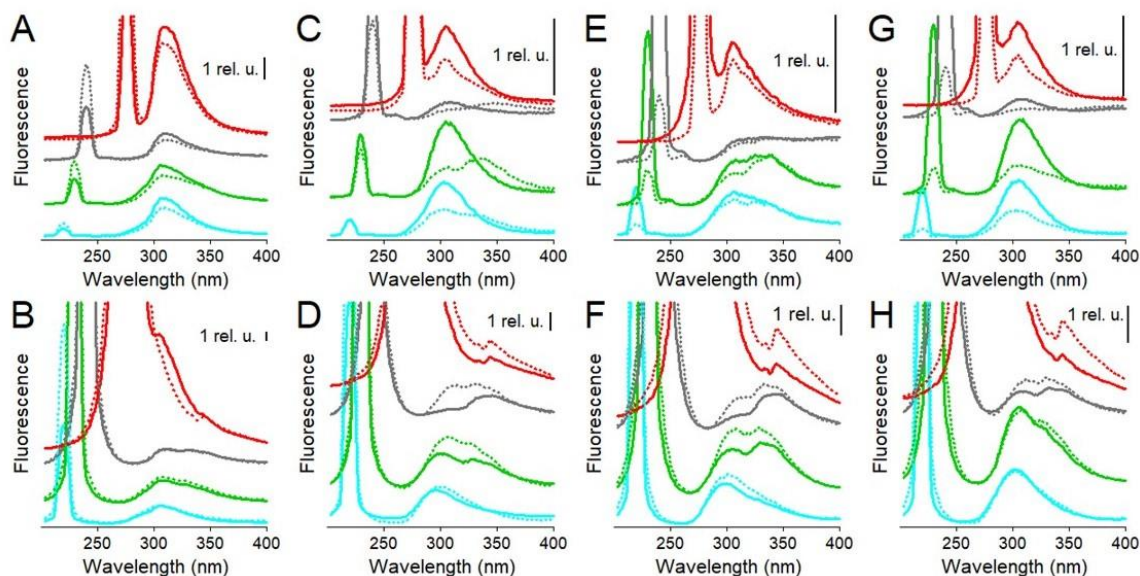
Figure 4.10 - Fluorescence spectra of Aβ1-42 (A, B), Aβ1-40 (C, D), AβpE3-42 (E, F), and AβpE3-40 (G, H) free in buffer (upper row) and in the presence of lipid vesicles (60 mol % POPC, 30 mol % POPG, 10 mol % cholesterol) (lower row). The excitation was at 220 nm (cyan), 230 nm (green), 240 nm (grey), and 275 nm (red). Dotted lines indicate that the samples have been extruded through 100 nm pore-size polycarbonate membranes. Peptide and total lipid (when present) concentrations were 20 mM and 1 mM, respectively, the buffer was 25 mM NaCl + 25 mM Tris-HCl, pH 7.2, and the temperature was 20°C

The structural features of the peptides have been assessed in additional experiments at

37°C to ensure those features are maintained at a physiological temperature. CD spectra showed

slightly more β-sheet content for Aβ$_{1-42}$ at 37°C. Aβ$_{1-40}$ formed β-sheet structure in buffer and the

presence of vesicles caused unordered structure, consistent with the peptide's behavior at 20°C.

AβpE$_{3-42}$ and AβpE$_{3-40}$ without vesicles adopted β-sheet structure with a minimum at 219 nm and

the lipid induced partial α-helix with a shoulder at 207-210 nm similar to data obtained at 20°.
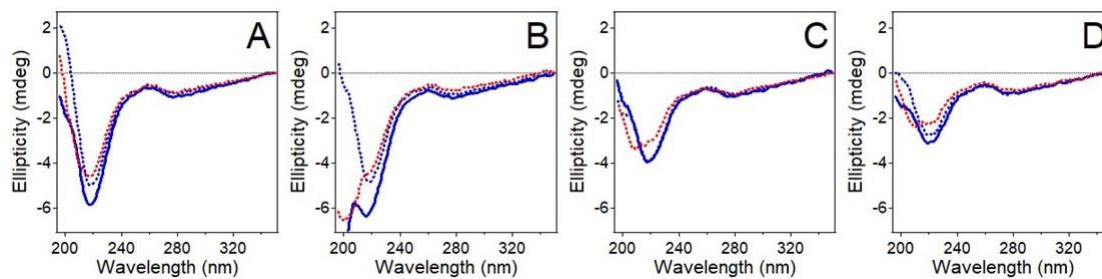
Figure 4.11 - Circular dichroism spectra of Ab1-42 (A), Ab1-40 (B), AbpE3-42 (C), and AbpE3-40 (D) in the absence (blue lines) and presence (red lines) of lipid vesicles composed of 60 mol % POPC, 30 mol % POPG, 10 mol % cholesterol. Dotted lines indicate that the samples have been extruded through 100 nm pore-size polycarbonate membranes. Peptide and total lipid (when present) concentrations were 20 mM and 1 mM, respectively, the buffer was 25 mM NaCl + 25 mM Tris-HCl, pH 7.2, and the temperature was 20°C.

The florescence spectra of the extruded peptides at 37°C were similar to those at 20°C as well. Spectra of Aβ_{1-42} were not split, those of Aβ_{1-40} were split at l_{ex} = 230 and 240 nm and the presence of lipid did not prevent it. The pyroglutamylated peptides produced split spectra at l_{ex} = 220-240 nm, with the red-shifted component in the 332-352 nm region, and lipid vesicles protected these peptides from the solvent reflected in weakening or elimination the red-shifted component.

Overall, fluorescence and CD data indicate that Aβ_{1-42} forms tightly packed β-sheet structure and in membranes acquires fraction of α-helix. Aβ_{1-40} forms less stable and more solvent-exposed β-sheet structure, and the vesicles induce partially unordered structure without protecting from solvent, indicating its poor ability to insert into the membranes. AβpE$_{3-42}$ and AβpE$_{3-40}$ form β-sheet structure in buffer and solvent-protected α/β structure in membranes, indicating efficient membrane insertion. Thus, a correlation is established between the β-sheet propensity, membrane insertion, and channel forming capability of the four Aβ peptides.

112

4.4.6 Structure and Orientation of the Peptides in Membranes from Polarized ATR-FTIR Spectroscopy. Polarized ATR-FTIR spectroscopy was used to gain information on the secondary structure of the peptides reconstituted in lipid multilayers and the orientation relative to the membrane. Figure 4.12 shows the ATR-FTIR spectra of all four peptides at parallel and perpendicular polarizations of the incident light along with the spectral components, as well as the dichroic spectra, in the lipid carbonyl stretching and the peptides' amide I regions. The lipid carbonyl group stretching vibration generates an absorbance band with two components at 1742 cm^{-1} and 1728 cm^{-1}, where the higher and lower wavenumber components correspond to dehydrated and hydrated C=O groups; H-bonding with water weakens the C=O covalent bond and thereby decreases the vibrational frequency.

Significant differences have been detected between the secondary structures of the peptides in supported membranes. $A\beta_{1-42}$ displayed ~46% β-sheet and ~19% α-helix structures, the rest of the peptide being in turn or irregular conformation (Table 1). In contrast, $A\beta_{1-40}$ mostly adopted turn or irregular conformation (68%) with only ~17% β-sheet and ~15% α-helix. The pyroglutamylated peptides had 27-35% β-sheet and 21-25% α-helix. In reality, a fraction of turns is located between β-strands and should be counted as part of the β-sheet structure. The pyroglutamylated peptides also displayed an additional amide I component in the 1666-1663 cm^{-1} region, which has been assigned to α_{II}-helix, i.e. a helical structure with tilted amide plane and with weaker helical H-bonding [177].
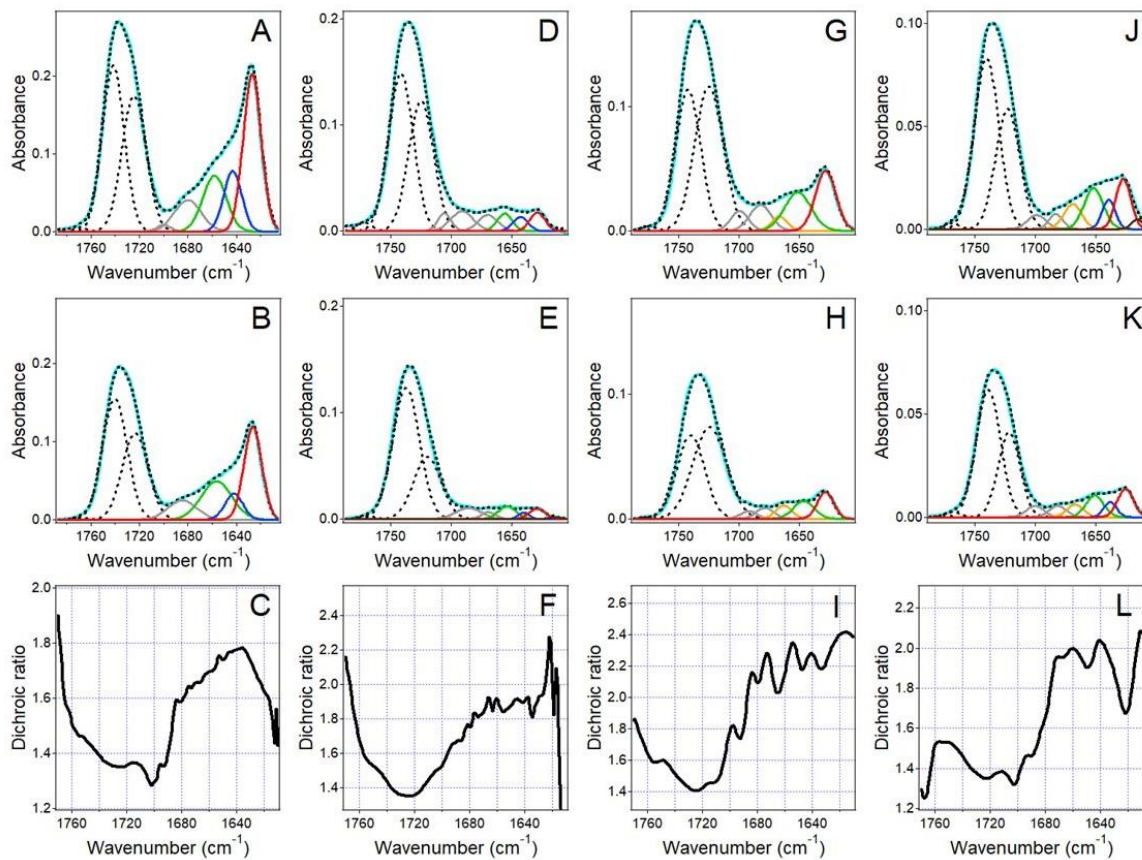
Figure 4.12 - ATR-FTIR spectra of Aβ$_{1-42}$ (A, B), Aβ$_{1-40}$ (D, E), AβpE$_{3-42}$ (G, H), and AβpE$_{3-40}$ (J, K) reconstituted in lipid multilayers composed of 60 mol % POPC, 30 mol % POPG, and 10 mol % cholesterol, hydrated by a D$_2$O-based buffer (25 mM NaCl, 25 mM Na, K-phosphate, pD 7.2), at parallel (first row) and perpendicular (second row) polarizations of the incident light. The measured spectrum is shown in solid line colored cyan, and the fitted curve is shown as black dotted line. Spectral components in lipid carbonyl and peptide amide I regions are presented as follows: lipid carbonyl components: black dashed lines; turn structures: grey; α$_{II}$-helix: orange; α-helix: green; unordered: blue; β-sheet: red; side chains: brown. Panels C, F, I, L show the dichroic spectra, i.e., the ratio of spectra at ∥ and ⊥ polarizations, for Aβ$_{1-42}$, Aβ$_{1-40}$, AβpE$_{3-42}$, and AβpE$_{3-40}$, respectively.

This α$_{II}$-helical structure constituted around 9-12% (3.5-4.6 amino acid residues), i.e. about one helical turn likely located at the edges of the regular α-helix. These results are consistent with CD data (Figure. 4.8A, D, G, J, and Figure 4.11), indicating an ordered, mostly β-sheet structure of Aβ$_{1-42}$, mostly unordered (or turn) conformation of Aβ$_{1-40}$, and α/β structure of AβpE$_{3-42}$ and AβpE$_{3-42}$ in lipid membranes.

114

Notably, the amide I intensity of Aβ$_{1-40}$ relative to that of the lipid C=O band is much weaker compared to Aβ$_{1-42}$ (Figure. 4.12 A, B vs. D, E), indicating that a significant part of Aβ$_{1-40}$ is washed away during injection of the buffer owing to its more hydrophilic nature. AβpE$_{3-42}$ and AβpE$_{3-40}$ have intermediate amide I intensities. This is consistent with fluorescence data showing a most efficient membrane insertion and solvent protection for Aβ$_{1-42}$ and more solvent exposure for Aβ$_{1-40}$ and the pyroglutamylated peptides (Figures. 4.8, 4.10).

Table 4.1 : Amide I wavenumbers (n), fractions (*f*), and numbers of amino acid residues (*N*) for α-helix, β-sheet, turn (*t*), and unordered (r) structures derived from ATR-FTIR spectra.

	Aβ$_{1-42}$	Aβ$_{1-40}$	AβpE$_{3-42}$	AβpE$_{3-40}$
ν_α (cm^{-1})	1659-1657[a]	1656-1654	1651-1646 1666-1663[b]	1652-1651 1668-1666[b]
f_α	0.194±0.0236	0.153±0.0170	0.254±0.0548 0.088±0.0401[b]	0.212±0.0396 0.121±0.0421[b]
N_α	8.15±0.992	6.15±0.680	10.16±2.193 3.52±1.606[b]	8.06±1.504 4.61±1.600[b]
ν_β (cm^{-1})	1627	1629	1628	1627-1625
f_β	0.459±0.0367	0.170±0.0190	0.351±0.0521	0.270±0.0419
N_β	19.26±1.541	6.80±0.760	14.04±2.0846	10.27±1.591
ν_t (cm^{-1})	1700-1678	1705-1669	1699-1678	1700-1681
f_t	0.159±0.0151	0.537±0.0551	0.242±0.0549	0.221±0.0405
N_t	6.68±0.632	21.5±2.204	9.69±2.197	8.37±1.539
ν_ρ (cm^{-1})	1643-1642	1642-1640	1641-137	1639-1637
f_ρ	0.188±0.0150	0.140±0.0525	0.065±0.0596	0.176±0.0809
N_ρ	7.90±0.626	5.60±2.100	2.60±2.383	6.70±3.0747

The orientation of β-strands of membrane-embedded peptides with respect to the membrane normal varied between 30 and 40 degrees (Table 2), similar to the respective angle of mitochondrial and bacterial porins, which form β-barrel structure [178] [179] . AβpE$_{3-42}$ showed the largest tilt of β-strands, i.e. ~38 degrees, which is still in the range of strand tilts of β-barrel porins and may indicate a wider pore formed by this peptide as the pore radius is inversely

proportional to cos(β). The α-helices were tilted obliquely at 50-65 degrees relative to the membrane normal.

Table 4.2: Dichroic ratios and orientational angle for β-sheet and β-helical components of the peptides in lipid membranes.

	R_β	β (°)		R_α	θ (°)
		$\gamma = 0°$	$\gamma = 20°$		
Aβ$_{1-42}$	1.681±0.081	30.9±1.1	30.0±1.4	1.701±0.0765	65.3±3.3
Aβ$_{1-40}$	1.974±0.186	34.8±2.2	34.7±2.67	1.855±0.092	59.4±3.1
AβpE$_{3-42}$	2.234±0.138	37.8±1.4	38.3±1.71	2.221±0.073 2.112±0.0696[a)]	48.9±1.8 51.7±1.8 [a)]
AβpE$_{3-40}$	1.754±0.124	32.0±1.8	31.3±2.19	1.919±0.086 1.963±0.130 [a]	57.3±2.7 56.0±3.9 [a)]

4.4.7 Morphology of Aβ Peptides in Lipid Membranes from AFM. The morphological features of the four Aβ peptides without and with reconstitution in lipid membranes were probed by AFM. First, peptides freshly suspended in aqueous buffer and incubated under fibrillization conditions (24 hours, 37°C) were studied. All freshly suspended peptides showed a distribution of monomers and oligomers in the height range of 1-5 nm (Figure 4.13A, B, C and D – 0hr panel). Aβ$_{1-42}$ showed a uniform distribution of monomers and oligomers in the height range 1-3 nm (section profile below Figure 4.13A) while the pyroglutamylated pEAβ$_{3-42}$ shows increased amounts of larger diameter, possibly higher ordered oligomeric structures (section profile below Figure 4.13C)[66] [180]. Similar behavior was observed among Aβ$_{1-40}$ and the pyroglutamylated variant pEAβ$_{3-40}$, wherein the former exhibits structures whose heights are distributed across 1-3nm and the former displays structures mostly in the 3-5nm range.
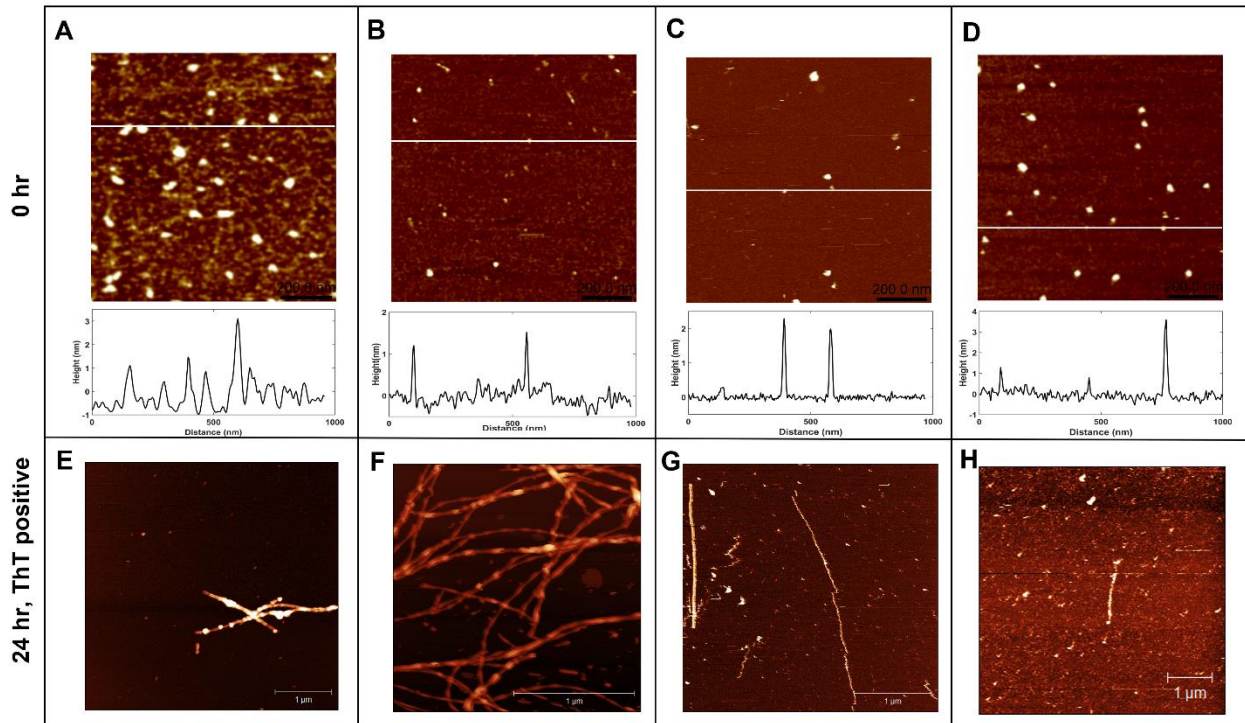
Figure 4.13 - AFM height images of Aβ$_{1-42}$ (A, E), Aβ$_{1-40}$ (B, F), AβpE$_{3-42}$ (C, G), and AβpE$_{3-40}$, (D, H) deposited on mica immediately after suspension in buffer (upper row) and incubated at 37°C for 24 h to induce fibrillogenesis (lower row). For panels A, B, C, D, the scan size is 1 um × 1 um, and the z-scale range is 0–5 nm. The white horizontal lines represent the cross-sections through the image corresponding to section profiles shown below respective images. E: scan size 5 μm × 5 μm, z-scale 0–19 nm; F: scan size 2 μm × 2 μm, z-scale 0–38 nm; G: scan size 3 μm × 3 μm, z-scale 0–6nm; H: scan size 5 μm × 5 μm, z-scale 0–6nm)

Under fibrillogenesis conditions, Aβ$_{1-42}$ and Aβ$_{1-40}$ showed highly dense, entangled fibrous structures (Figure. 14.13E, F – 24hr, ThT positive panel). In contrast, the pyroglutamylated peptides showed a very sparse distribution of individual fibrils without entanglement (Figure 4.13G, H – 24hr, ThT positive panel). Even though all peptides showed a positive thioflavin-T signal (data not shown), the fibril distribution for the pyroglutamylated variants was not easily visualized as compared to the unmodified peptides and some higher order, large-sized oligomers could be observed, which may indicate incomplete fibril elongation and additionally their propensity to be in lower to intermediate order oligomeric β-sheet structures.
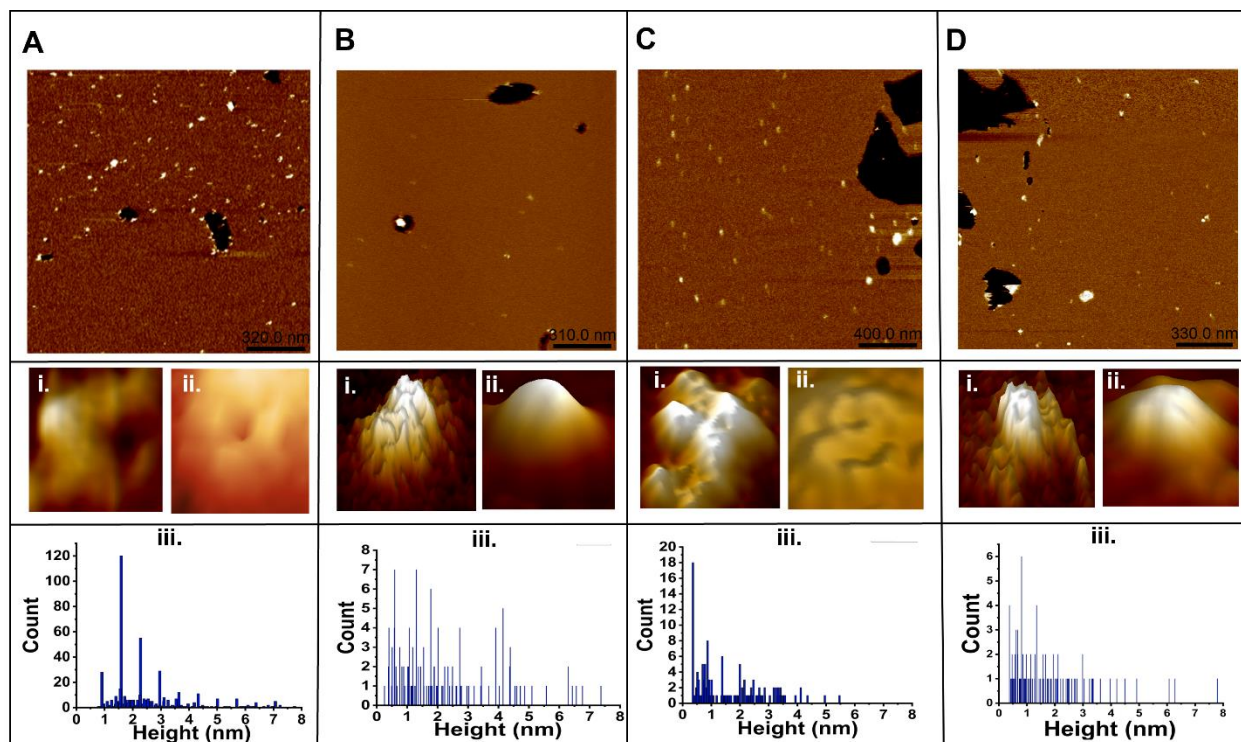
Figure 4.14 - AFM Height images of the Aβ peptides reconstituted in POPC:POPG:Chol (6:3:1 mole ratio) at 1:1000 or 1:500 (peptide:lipid, molar ratio) A: Aβ1-42 (A i., ii.: close up 3D view of ion channel/pore-like structures formed by Aβ1-42; scan size = 20 nm X 20nm , z-scale = 0–2nm. A iii.: Particle height histogram of peptide protruding over the lipid bilayer, combined from 5 separate images). B: Aβ$_{1-40}$ (C i., ii.: close up 3D view of ion channel/pore-like structures formed by Aβ$_{1-40}$; scan size = 30 nm × 30 nm, z-scale = 0–2nm. B iii.: Particle height histogram, combined from 5 separate images). C: AβpE$_{3-42}$ (C i., ii.: close up 3D view of ion channel/pore-like structures formed by AβpE$_{3-42}$; scan size = 30 nm × 30 nm, z-scale = 0–2nm. C iii.: Particle height histogram, combined from 5 separate images). D: AβpE$_{3-40}$ (D i., ii.: close up 3D view of ion channel/pore-like structures formed by AβpE$_{3-40}$; scan sizes = 20 nm × 20 nm, z-scale = 0–2nm. A iii.: Particle height histogram, combined from 5 separate images).

Next, the morphological features of the peptides reconstituted in lipid membranes supported on mica were studied. In all cases, the image analysis showed two populations of peptide oligomers, one protruding from the membrane 0.5–1.5 nm above the bilayer surface, assigned to membrane-inserted structures, and the other exceeding 1.5 nm, assigned to a membrane-adsorbed or partially membrane inserted peptide pool [153] (Figure 4.14, histogram panels for each peptide indicated by iii). Among the membrane inserted fractions, a small sub-population exhibited pore or channel like morphology. These structures were better resolved in

case of $A\beta_{1-42}$ and featured annular assemblies composed of 4-6 units with an outer diameter of ~14-16 nm and a central pore of ~1-~2.1nm (Figure. 4.14 A i, ii.)[96]. The other three peptides exhibited oligomeric structures in the same height range. Pore-like morphologies were not identified for $A\beta_{1-40}$ and $A\beta pE_{3-40}$ (Fig. 4.14B i, ii., and D i., ii.), although $A\beta pE_{3-40}$ did exhibit weak subunit like topology in some cases. For $A\beta pE_{3-42}$, annular, pore-like structures were seen with outer diameter from 9 to 15 nm (Fig. 4.14C i., ii). Clusters of pore-like structures were seen for this peptide as well. Overall, apparent pore-like structures were formed more readily by $A\beta_{1-42}$, followed by $A\beta pE_{3-42}$, consistent with the patch clamp data showing regular step-like channel behavior for these two peptides [181].

4.5 Discussion

The structural changes (formation of lactam ring at residue 3) in the pyroglutamate modified peptides makes them relatively more hydrophobic, which may increase their propensity to partition into the lipid bilayer hydrophobic core and form stabilized structures [142]. Voltage clamp electrophysiological experiments indicate that pE modified peptides and the full length $A\beta$ form stable structures in the membrane that display pore like/ion channel like behavior, albeit with different characteristics. Among all the peptides tested, $A\beta_{1-42}$ and its pyroglutamylated counterpart $A\beta pE_{1-42}$ displayed highly stable channel conductance with clearly distinguishable open-close states and conductance levels. Multiple experimental and computational studies have supported the pore/channel formation capabilities of $A\beta_{1-42}$ in planar bilayers and cell membranes alike [58][70][160] [182]. In our studies, we observed that $A\beta_{1-42}$ exhibiting highly consistent electrical activity, with some recordings displaying stable single channel conductance.

Fluorescence spectroscopy, CD spectroscopy and ATR-FTIR spectroscopy all indicate that $A\beta_{1-42}$ displays large content of β-sheet secondary structures in these lipid membranes with high degree of sequestration of hydrophobic amino acid residues into the hydrophobic core of the lipid bilayer. This is consistent with the previously reported behavior of $A\beta_{1-42}$, which has concluded th1at $A\beta_{1-42}$ displays β-sheet enriched structures in lipid membranes [107] [183] [184]. This is also consistent with the MD simulations and models proposed for channel formation capability of $A\beta_{1-42}$ with β-sheet rich strands lining the periphery of the channel walls and stabilize interactions with the hydrophobic core of the bilayer [160] [185] [186]. Parallels have been drawn between porin channels and Aβ channels as porins adapt a β-barrel structure in bilayers with strong electrophysiological activity and the β-strand orientations calculated from dichroic ratios of ATR-FTIR spectra indicate that the angular orientations are in-line with what has been observed for β-barrel porins [166]. In our study, we were able to resolve a tetrameric subunit like morphology with a central pore of diameter ~1 – 2.1nm via AFM imaging. Previous imaging studies (AFM and EM) have also demonstrated pore-like structures with 4-6 subunits and a large degree of structural interconversion among the morphological states [58][66][108][[109] .

In contrast, $A\beta_{1-40}$ displays significantly different characteristics across the board. The channel formation capacity is weak, with mostly intermittent burst like activity observed and no clear single channel conductance was found [181]. CD and ATR-FTIR data indicate that $A\beta_{1-40}$ displays mostly unordered or low degree of α-helical secondary structure content and significantly lower β-sheet content compared to $A\beta_{1-42}$. Another strong conclusion that can be drawn from spectroscopic studies is that $A\beta_{1-40}$ displays a higher degree of hydrophilicity and

lower partitioning into the lipid bilayer core. AFM imaging also revealed that $A\beta_{1-40}$ displays mostly globular protrusions from the surface of the bilayer without clearly resolvable pore like morphologies. Taking these data together, it can be concluded that $A\beta_{1-40}$ does not insert strongly into the membrane and the electrical activity displayed by $A\beta_{1-40}$ could be more of a membrane destabilization mechanism without explicitly forming ion conducting pores. Although some previous reports have indicated the possibility of $A\beta_{1-40}$ forming pores in planar bilayers, recent cell excised membrane patch clamp electrophysiological studies have concluded that structural features of $A\beta_{1-40}$ are not ideally suited to form ion channels in physiological membranes [62][181].

The pyroglutamylated variants $A\beta pE_{3-42}$ and $A\beta pE_{3-40}$ display structural properties which are in between those of $A\beta_{1-42}$ and $A\beta_{1-40}$. Both the pyroglutamylated variants display higher β-sheet content and membrane insertion capabilities compared to $A\beta_{1-40}$. $A\beta pE_{3-42}$ displayed highly stable ionic conductance with single channel behavior clearly apparent in many recordings. Previous reports on the pore/channel formation capacity of $A\beta pE_{3-42}$ in comparison to $A\beta_{1-42}$ reach similar conclusions, with the conductance behavior reported being almost identical to the ones presented here [154][180]. This indicates that the pore formation and electrical activity are highly repeatable across experimental studies and the possibility of similar membrane embedded channel structures existing in comparison to those studies. The ionic conductance characteristics of the $A\beta pE_{3-40}$ displayed more variability with single channel conductance exhibiting switching between multiple conductance levels, which appear to be approximate integer multiples of unitary conductance. AFM imaging reveals clusters of pore-like structures for $A\beta pE_{3-42}$ and $A\beta pE_{3-}$

40. The subunit morphology was weakly resolved through imaging; however, the central pore was not resolvable in both cases, possibly due to AFM tip convolution issues.

The N-terminal segment of Aβ peptides (amino acid residues ~1-14 counting from -NH$_2$ end) is charged and is shown to be disordered in structure. After the proteolytic cleavage of first 2 residues and subsequent formation of a lactam ring on the glutamate residue at position 3, the hydrophobicity of the peptide increases and thus the partitioning of the peptide into the hydrophobic core of the lipid bilayer is energetically favored [173][180]. Our results, through correlative structural, functional, and morphological techniques support this notion. N-terminal truncated and pyroglutamylated peptides make up a significant portion of the proteinaceous amyloid plaques in patients with AD and their relative concentrations increasingly considered to be reliable biomarkers for AD diagnosis [180]. These structural and functional studies offer considerable evidence on the possibility of these peptides forming ion channels in neuronal cell membranes. Therapeutic measures which either avoid the formation of these ion channels (oligomerization inhibitors) or small molecule blockers that can block the ionic conductance behavior of these peptides could be credible avenues in halting the cascade of AD [101].

4.6 Conclusions

In this chapter, we have characterized the structural, morphological, and functional behavior of Aβ$_{1-42}$, Aβ$_{1-40}$ and their pyroglutamylated variants AβpE$_{3-42}$ and AβpE$_{3-40}$ in disease relevant lipid bilayer system using a combination of spectroscopy (Fluorescence, CD and FTIR), AFM imaging and voltage clamp electrophysiology. The relative difference in their characteristics offers a pathway towards effective therapeutics development.

Chapter 4 is in part a manuscript in preparation with *Karkisaval A.G, Balster B., Nguyen A., Abedin F., Tatulian S., and Lal. R.* titled 'Channel forming activities and structural features of unmodified and pyroglutamylated Aβ peptides in lipid membranes'. The dissertation author was the primary author of the manuscript.

Chapter 5

Unfolding of Amyloid-β oligomers via AFM based Single Molecule Force Spectroscopy

5.1 Introduction

The oligomeric organization of Aβ, the intermolecular interactions that are involved in structural transitions of oligomers and the influence of microenvironments have been of particular interest in the current AD landscape [55]. Due to the dynamic nature of these structural transitions and the wide conformational space accessed by oligomeric units (polymorphism), conventional techniques such as XRD, NMR and cryo-EM have not been able to probe the exact structural organization [187]. Added to the complexity of Aβ being a membrane protein/membrane associated protein, sample preparation schemes can significantly affect the oligomerization propensity and pathway of oligomerization. As stated in Chapter 1, section 1.5, it is vital to understand Aβ-membrane interactions, under varying environmental factors to build a phase space of all probable modalities of nanoscale interaction of the peptide. Oligomerization and subsequent aggregation can be tightly linked to a protein's folding energy landscape (Chapter 1, section 1.5, Figure 7) [61]. It is important to consider the fact that a particular oligomeric intermediate could be 'misfolded' and the interactions of this misfolded intermediate could be the origin of cytotoxicity [188]. It has been noted that partial unfolding of an intermediate state has to happen for the peptide/protein to form a critical oligomeric nucleus, which can in turn propagate fibril growth, leading to a cross-β sheet core structure [189] [190]. Hence, probing Aβ

interactions from a protein folding/misfolding standpoint could improve the overall understanding of Aβ oligomer landscape.

Atomic Force Microscopy based Single Molecule Force Spectroscopy (SMFS) is a technique that is uniquely suited to probe biomolecular interactions at a single molecule level. The unprecedented force sensitivity of the technique allows quantifying pico-Newton levels of forces involved in stabilizing biomolecular structures in their native environment [191] [192]. In SMFS, the AFM probe (which can be chemically functionalized with specific molecules) is moved towards the surface containing the biomolecule of interest at a constant velocity. Once the probe is in close proximity to the molecule, a molecular bond can be formed (whose origins can be specific or non-specific in nature) between the biomolecule of interest on the surface and the complementary biomolecule which is immobilized on the probe. After the bond has formed, the AFM probe is retracted at a constant velocity, while the deflection of the cantilever is continuously monitored. As the probe is moved further away from the surface, the mechanical strain experienced by the bond increases and the bond snaps at a particular force which can be precisely monitored. In addition to quantifying rupture force, other biophysical characteristics of the system can also be calculated [193].

Depending on the objective of the experiment, SMFS can be broadly classified into two categories (Figure 5.1): 1) Ligand-Receptor binding quantification (Figure 5.1A), 2) Molecular unfolding of polymer chains [88] (Figure 5.1B). In the first type, the objective is to quantify the force it takes to rupture a molecular bond between a ligand and a receptor, most commonly antibody-antigen interactions in the biological context. In this experiment, the receptor of interest is immobilized on a flat surface or if it's a membrane embedded receptor, it can be

125

reconstituted in a lipid membrane environment. The ligand is commonly bound to the AFM probe using surface chemistry techniques. In some variations of the technique, a ligand can be indirectly bound to the AFM probe via an extensible linker molecule which helps in reducing long-range interactions between the probe and the surface. Then, in a typical experimental session, the AFM probe is brought into contact with the surface containing receptors at a particular velocity, held at the closest distance for 0.5-1s such that a bind forms between the ligand and the receptor, all while continuously monitoring the deflection of the cantilever. In the next step, the AFM probe is retracted at a set reversal velocity and as the distance between the probe and the surface increases, the molecular bond ruptures, and the force at which the bond ruptured can be precisely quantified. As an extension of the technique, the retraction is generally performed at multiple loading rates which helps in gathering information about the bond lifetimes and kinetic constants [194] [195].
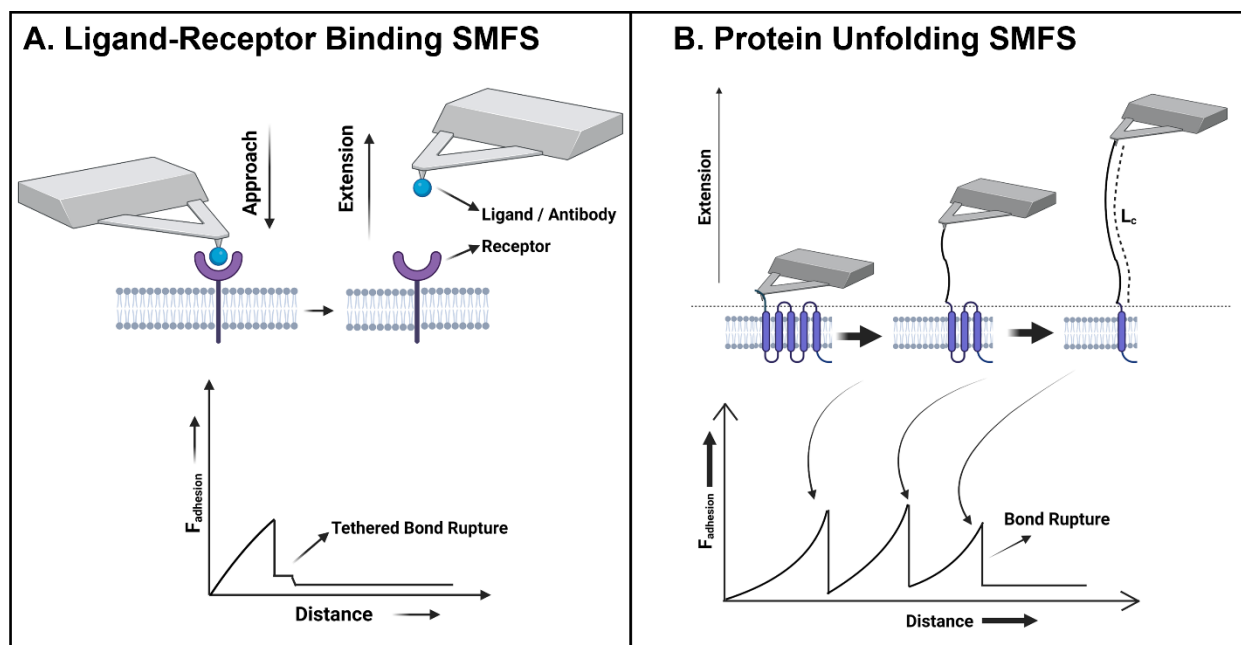
Figure 5.1 - Experimental details and differences in SMFS approaches. A) The first type of experiment wherein a ligand is chemically conjugated to the AFM probe and the receptor is present either on a flat surface or embedded in the lipid bilayer. An approach-retract cycle is shown with the corresponding F-d spectra shown below which displays the tether bond breaking (only the retraction portion of the curve which contains the bond breaking event is shown). B) The second type of SMFS experiment which focuses on unfolding of linear chained molecules. The schematic shows the experimental scheme of sequentially unfolding a multi-domain protein (each cylinder represents a domain/subunit) from a lipid membrane interface. The corresponding F-d spectra is shown below. The entropic stretching of the polymeric domain and complete unfolding of the domain results in the characteristic zig-zag pattern.

The second type of SMFS experiment is performed to understand the unfolding behavior of a polymer chain, most commonly in the case of proteins. The experimental setup is quite similar to the setup mentioned in ligand-receptor SMFS and depending on the situation, both globular proteins and membrane proteins can be unfolded in similar fashion. Typically, the protein of interest is either immobilized onto the surface using molecular tethers or embedded in the lipid membrane such that the protein is in its native 3D conformation [196]. In the case of globular, soluble proteins, a polyprotein construct can be created to increase the repeatability of unfolding behavior [197]. In a routine unfolding experiment, the AFM probe is brought into

contact with the surface (or lipid bilayer) containing the protein and allowed to form a non-specific interaction mediated bond with the N-terminus or C-terminus of the protein. In some situations, the amino acid residues that form the loop connecting two domains of the protein can also attach to the AFM probe [198]. After the bond has formed, the probe is retracted at a constant velocity. With the extension increasing, the intermolecular hydrogen bonds and van der Waals forces that stabilize the 3D structure of the protein are broken and the protein molecule starts unfolding and becomes a linear chain, one amino acid at a time. If the protein is made out of multiple domains (quaternary structure of proteins), then individual domains unfold one after the other as long as a stable bond between the AFM probe and the amino acid residue in contact with the probe can be maintained. In the majority of cases, a characteristic zig-zag force-distance (F-d) spectra can be obtained with the successful unfolding of all domains of the protein, which can be used to identify the type of protein [199] [200] [201]. These types of unfolding experiments provide intimate knowledge about the organization of the protein in a 3D conformation and a wealth of structural data can be generated.

Proteins are polymeric complexes of amino acids and thus the data generated from unfolding SMFS experiments can be analyzed via statistical polymer mechanics models. Under the action of an external mechanical stimuli, the protein polymer chain undergoes entropic stretching until one of the domains is fully unfolded, then a drop in the force can be extended until the force is enough to start unfolding the next connected domain [199] [202]. The part of the chain that is fully unfolded corresponds to the length of the polymer chain held end to end, often called the contour length (L_c). The part of the F-d spectra which displays the characteristic entropic stretching pattern can be fit with Worm-Like Chain (WLC) or Freely Rotating Chain (FRC)

model and a contour length can be extracted [199][200]. In the case of protein molecules, the WLC model has been shown to work more consistently. The force of unfolding a polymer chain is given by equation [203]:

$$F(x) = \frac{k_B T}{l_p} \left(\frac{1}{4} \left(1 - \frac{x}{L_c} \right)^{-2} + \frac{x}{L_C} - \frac{1}{4} \right) \tag{5.1}$$

Where, 'F(x)' is the extension dependent force, k_B is the Boltzmann constant, T is the temperature, l_p is the persistence length of the polymer chain (commonly used value for amino acids is 0.4nm, with monomer length of 0.36nm [204]) , L_c is the contour length, i.e the length of the protein that is unfolded and held in a linear orientation and 'x' is the extension or the distance between the surface and the AFM probe. Once contour lengths are extracted for each of the unfolding peaks in the F-d spectra, the number of amino acids unfolded can be found out with great certainty, assuming reasonable attachment modes (i.e., N-terminus, C-terminus, or loops).

5.2 Materials and Methods

Aβ$_{1-42}$ was purchased from Anaspec Inc (CA). 1-palmitoyl-2-oleoyl-glycero-3-phosphocholine (POPC), 1-palmitoyl-2-oleoyl-sn-glycero-3-phospho-(1'-rac-glycerol) (POPG), 1,2-dioleoyl-sn-glycero-3-phosphocholine (DOPC), 1,2-dipalmitoyl-sn-glycero-3-phosphocholine (DPPC), 1,2-distearoyl-sn-glycero-3-phosphoethanolamine-N-[amino(polyethylene glycol)-2000] (DSPE-PEG(2000) Amine) and Cholesterol were purchased from Avanti Polar Lipids (Alabaster, AL). SNL-10 probes were purchased from Bruker (Billerica, MA). All other chemicals were purchased from Invitrogen or Sigma-Aldrich.

5.2.1 Sample Preparation: The main lipid mixtures used in the study were POPC: POPG: Cholesterol (6:3:1 mol%), DOPC-DPPC (1:1 wt/wt) or DOPC-Cholesterol at varying cholesterol content. In all cases, lipids dissolved in chloroform were measured in the required ratio and dried in glass vials for >6 hours in a vacuum chamber. Dried lipids were then hydrated in a buffer (10mM, 300mM KCl, 2mM $CaCl_2$, pH 7.4) for 30 minutes at room temperature to form large unilamellar vesicles (LUVs). The LUV solution was then bath sonicated for 20 minutes or until the solution was clear to form small unilamellar vesicles (SUVs). $A\beta_{1-42}$ was dissolved in 1% ammonium hydroxide and divided into aliquots and stored at -80°C until used. To the premade vesicle solution, $A\beta_{1-42}$ was added at a final ratio of 100:1 (lipid: protein molar ratio) and incubated at room temperature for 10 minutes and then briefly sonicated for 60-90 seconds to form proteoliposomes. A 10-20ul solution of proteoliposomes were then added to a piece of freshly cleaved mica and incubated for 10 minutes at room temperature. The sample was then rinsed 5x and resuspended in the same buffer.

5.2.2 AFM Imaging and Force Spectroscopy: AFM Imaging and SMFS were carried out on a Multimode V AFM connected to a Nanoscope V controller (Bruker, Billerica, MA). All imaging was carried out either in tapping or peak force tapping (PFQNM) mode using the Nanoscope 9.1 software interface. SNL-10 cantilevers with a spring constant in the range of 0.1-0.3N/m were used for all imaging and spectroscopy studies. The spring constant of the cantilever was calibrated using the thermal noise method before every imaging or SMFS session. As the chances of cantilever contamination can be significant in SMFS experiments, a fresh cantilever was used in between experimental sessions and sometimes even among different samples in the same session. For SMFS experiments, the typical methodology was as follows: We first imaged the

sample to confirm a suitable distribution of proteins on the membrane surface and then selected

a location with high density and lateral distribution of proteins. Once the area was selected, we

used the 'point and shoot' F-d curve collection scheme available in the Nanoscope 9.1 software.

Briefly, a boxed region of interest was selected and converted to discrete points on a square grid.

An F-d curve was collected at each of those points. All F-d curves were collected with 1um/s tip

approach velocity and 500nm/s retraction velocity. In order to increase the probability of the

protein region binding to the probe, a force of ~1nN was applied and held constant for 1-1.5s at

the closest approach point of the probe. This time delay also increases the probability of a non-

specific bond forming between the probe and the molecule of interest. On an average about

3000 F-d curves were collected for each membrane-protein condition. Control F-d curves (lipid

bilayer without proteins in it) were also collected to rule out any effects that arise purely from

bilayers.

5.2.3 SMFS Data Analysis: Each SMFS experiment generates large amounts of data. Due to the

highly stochastic nature of protein bind and unbinding, the percentage of curves actually showing

an unfolding event (full or partial unfolding) tend to be very low (<3% in large sample sizes). In

addition, the contour lengths and force calculated for the unfolding of the same domain (or

segment) of the protein can show wide variability. In order to analyze the curves a semi-

automatic approach was implemented. First, F-d curves showing obvious unfolding events were

manually sorted into 'probable clusters' i.e, curves that display visual resemblance among each

other. After the curves were sorted into these clusters, further analysis of quantifying contour

lengths via WLC fitting, force distribution etc were performed in the FODIS automated

environment. Fodis is an application developed in the Matlab environment which is uniquely built for analysis of large datasets of SMFS experiments [205] [206].

Once the F-d curves were brought into the Fodis environment, a baseline correction operation was performed to discard force offsets caused during F-d collection in the experiment. Next, all curves were smoothed using a shape preserving 3rd order polynomial Savitzky-Golay filter to remove high frequency noise spikes, which also aids in precise fitting of a WLC curve to the force peaks detected [205]. All curves were aligned to the first crossover positive force to maintain homogeneity of WLC model fitting. The WLC model is shown to be suitable for forces below 500pN and thus for WLC fitting and Lc extraction in Fodis, a minimum force threshold of 30pN and a maximum force threshold of 500pN was set. Persistence length of 0.4nm was chosen for all analysis [203][204]. Fodis transforms the F-d curves into F-Lc space representation and determines the optimal Lc from the density of points clustered around a particular Lc [207]. The detection efficiency of the algorithm can be adjusted through force and contour length bin size parameters in the Fodis interface. After all the relevant force peaks of the F-d curves were fit with WLC models, contour length was extracted and expressed in histograms and tile panel layouts for better visualization. All further visualization and display related operations were then carried out in Matlab.

5.2.4 AFM Imaging Data Analysis: AFM images collected during SMFS experiments were analyzed either through Nanoscope Analysis v1.5 (Bruker, Billerica, MA) or Gwyddion SPM analysis software (http://gwyddion.net/ [208]). Briefly, all collected images were line flattened through a 2nd order polynomial filter or median filter. Data are expressed as AFM height images.

5.3 Results and Discussion

5.3.1 SMFS of DOPC-DPPC- Aβ$_{1-42}$

In order to understand the unfolding behavior of Aβ$_{1-42}$ in the presence of lipid membrane we first performed AFM imaging. In the case of DOPC-DPPC (1:1 wt/wt) lipid bilayer a clear phase separation between the DOPC phase and the DPPC phase were observed due to difference in transition temperatures of the lipids (-20°C for DOPC and 41°C for DPPC). This phase separation was apparent in AFM height images where a height difference of ~1 nm could be observed between DOPC and DPPC bilayers (Figure 5.2A ii. and B ii.) [209]. Aβ$_{1-42}$ was found to be embedded in both DOPC and DPPC phases, with more localization of the peptide observed at the phase boundaries. A wide distribution of oligomeric sizes was observed all throughout the imaging area ranging in height from 1 nm to 10 nm above the bilayer plane. Occasionally, small linear fragments of protofibrils/fibrillar aggregates could be seen branching out from a critically aggregated nucleus. These fibrils then grew and elongated on the lipid bilayer (Figure 5.2A i) and B i)) .
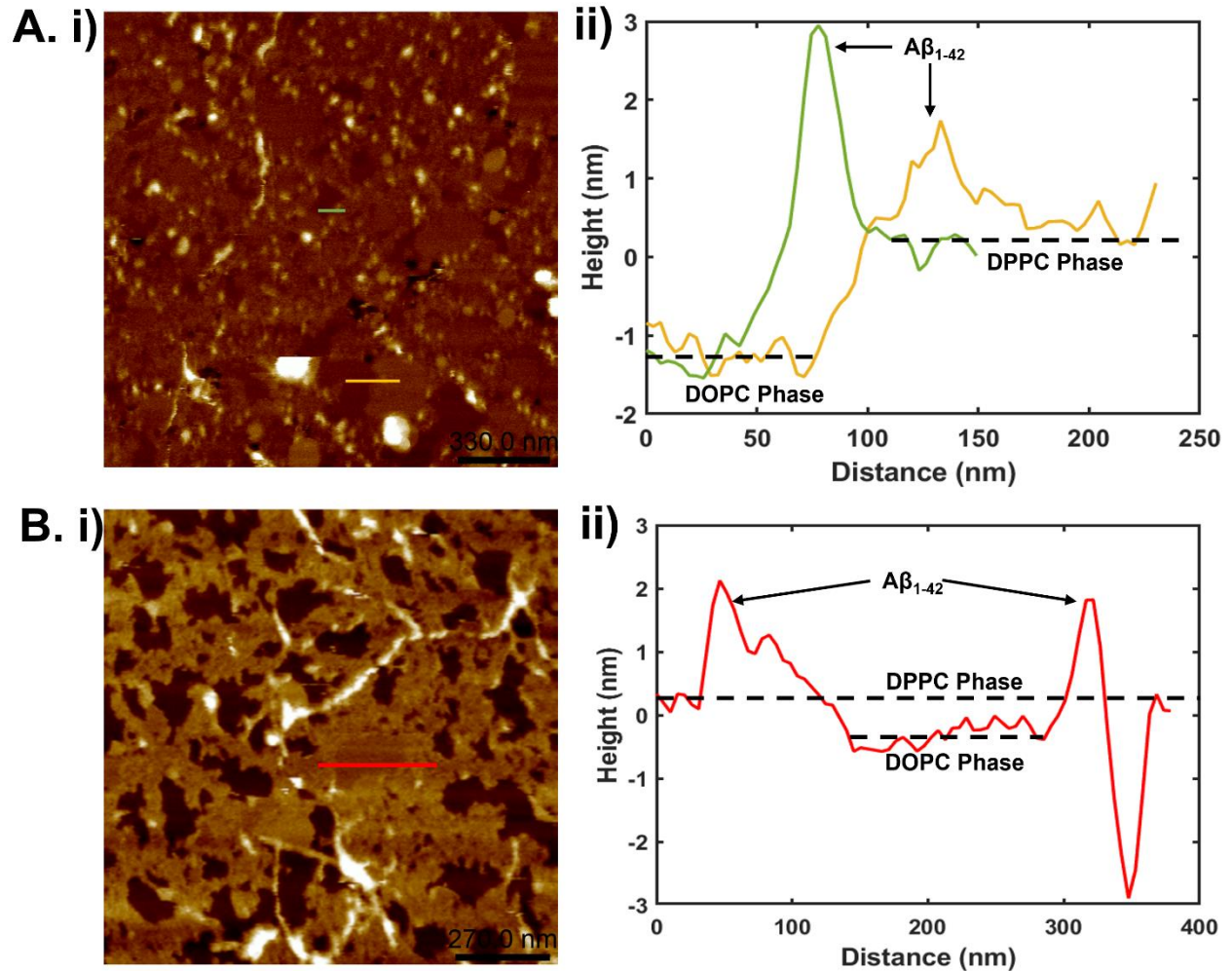
Figure 5.2 - AFM height images of Aβ1-42 reconstituted in DOPC:DPPC (1:1 wt/wt) lipid bilayers at 100:1 (lipid:protein) molar ratio, immobilized on mica. A. i) and B. i) – two separate height images from different samples. Panels ii) in both images correspond to the section height profiles of the lines drawn on their respective height images. The profiles are color coded. Aβ$_{1-42}$ peaks are indicated with arrows in the section plane corresponding to peaks on the profile. In panel A i) short protofibrils can be observed and in panel B i) mature, elongated fibrils can be observed. The heights and locations of the DOPC and DPPC phases are indicated by dashed lines. Scan size for A is 1.7um X 1.7um and B is 1.3um X 1.3um. Z-scale for both images is 0-20nm. The darkest color-coded part of the image corresponds to the mica plane.

After imaging the distribution of Aβ$_{1-42}$ oligomeric structures on the membrane, we performed the SMFS routine and collected F-d spectra over multiple imaging locations. Throughout this analysis, we refer to F-d spectra that show an entropic stretching behavior

followed by a drop in the force (corresponding to bond rupture) as an 'unfolding event'. The adhesive forces are expressed in positive units throughout the study; however, it should be noted that the raw data generated will have opposite sign convention (attractive forces are typically designated negative sign convention in AFM). Typically, in these experiments, majority of the F-d spectra either don't display any interaction between the AFM probe and the surface (F-d spectra with no adhesion force peaks, Figure 5.3A) or show a large adhesion peak (due to long range interaction forces between the AFM probe and the support surface, Figure 5.3B) or show adhesion peaks with tether bond rupture events (no stretching of the peptide chain, but only bond rupture between the AFM probe and the peptide molecule, Figure 5.3C). In all conditions, about ~1% of collected curves show an unfolding signature, however the distribution of these unfolding events are heterogenous in nature (Figure 5.3D). Keeping these various scenarios in mind, we discarded F-d traces which display characteristics shown in Figure 5.3A, B and C (including F-d spectra which have highly unstable baselines, red bounding box in Figure 5.3) and only included F-d traces where a clear entropic stretching followed by bond rupture (characteristic of protein chain unfolding) were seen (Figure 5.3D, green bounding box). Once these data acceptance criteria are met, the remaining F-d spectra were analyzed in the Fodis environment. In a lot of F-d spectra, a big adhesion peak can be found near the tip-sample separation of zero. This corresponds to non-specific adhesion due to long range interactions between the bulk of the probe and the surface [193]. Thus, we set a lower threshold of 10nm on the contour length for the consideration of a peak to be an unfolding peak. Any contour length below 10nm was not considered to be associated to the unfolding process as this would sometimes overlap with the non-specific adhesion peak and complicate the analysis.
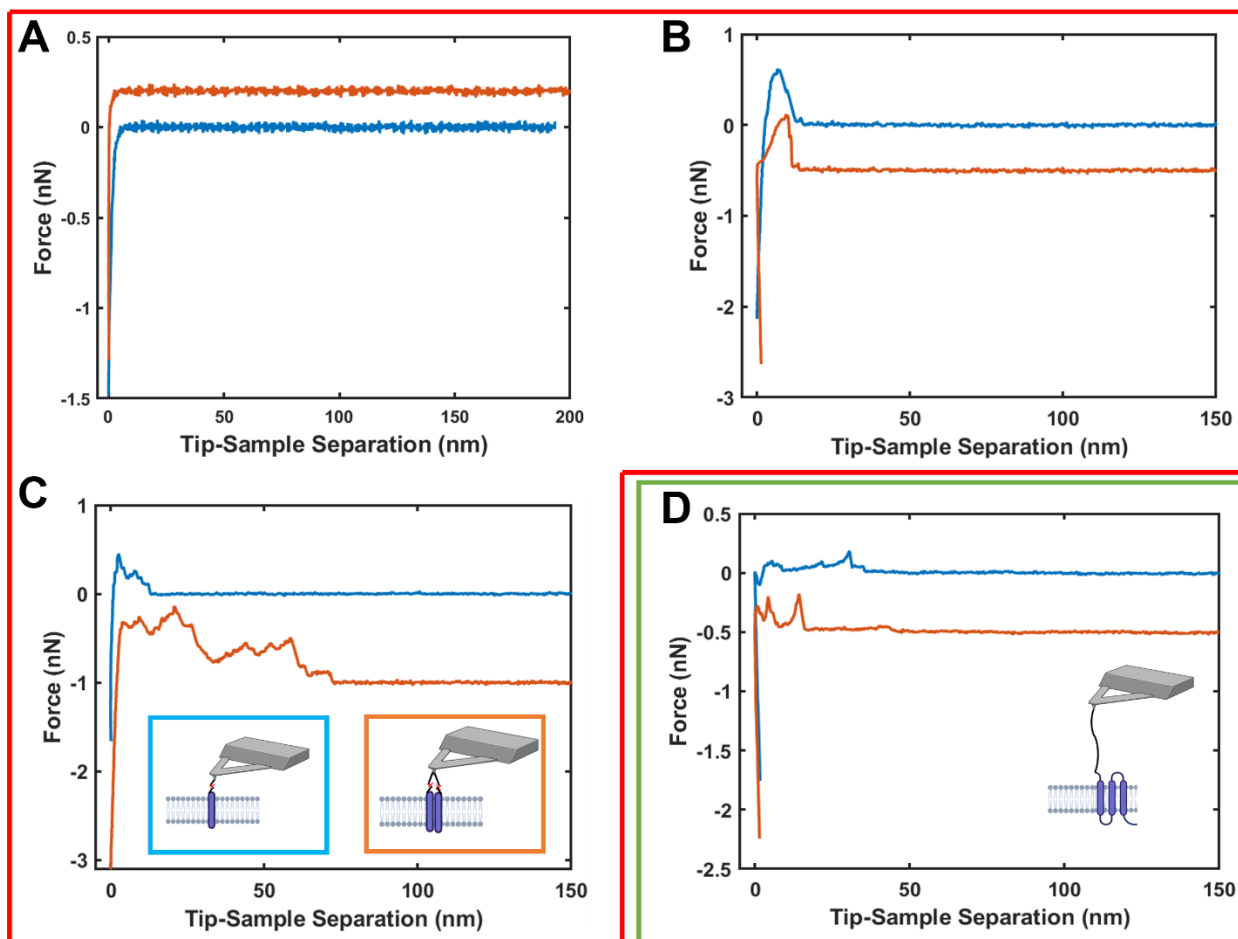
Figure 5.3 - Representative SMFS F-d spectra under different situations and data evaluation criteria. A) F-d spectra when no interaction occurs between the AFM probe and the sample. B) F-d spectra when only long-range adhesive interactions occur between the surface and the probe. C) F-d spectra in a tether bond rupture event – single tether (blue) or multiple tether bond breakage events(orange) with graphical depictions of the respective events shown in insets. D) F-d spectra of protein unfolding events – inset shows graphical display of one possible scenario. The red bounding box drawn for panels A, B and C indicates that these types of datasets are not considered for further evaluation. The green bounding box drawn for panel D represents the F-d spectra that are considered for further analysis.
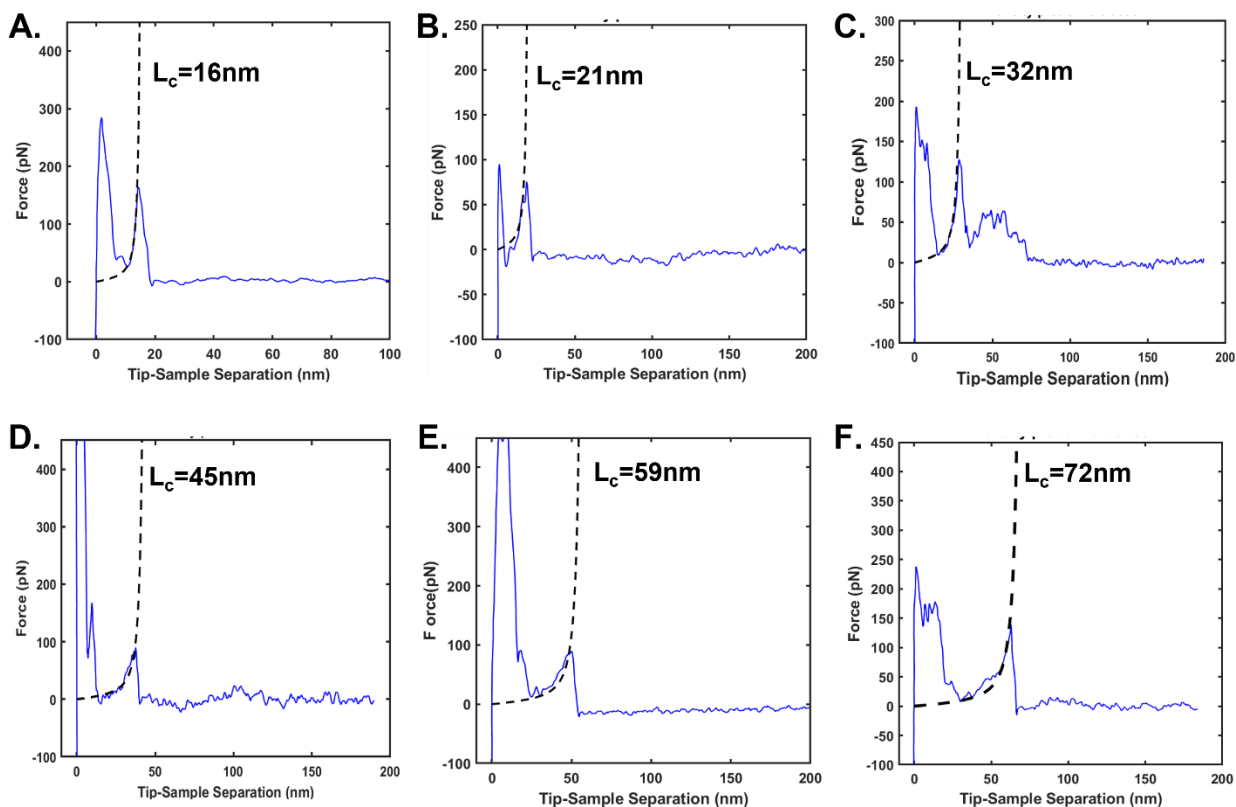
Figure 5.4 - Six representative F-d spectra collected on DOPC-DPPC- Aβ1-42 reconstituted sample displaying single unfolding peak fitted with WLC models. Among the collected data, spectra with single peak were found and pooled together. The contour length (Lc) calculated for each curve is displayed in black dashed lines.

In the Fodis data analysis environment, we split the bulk of the unfolding spectra into 3 main categories – spectra which display one main unfolding peak, spectra displaying two main unfolding peaks and spectra which displayed more than 2 unfolding peaks. For all of these categories we performed WLC model fitting to extract contour lengths (Lc) observed under one set of experimental conditions. Figure 5.4A-F shows the various F-d spectra fit with WLC curves corresponding to their respective contour lengths, which lie in the range of 15nm – 75nm. The contour length is defined as the length traversed over a fully stretched polypeptide chain. From this definition, a contour length can be converted to number of amino acids that have been

unfolded and stretched into a linear configuration from the native 3D configuration of the protein domains. A few studies have shown that amino acid sequence length can be reasonable approximated to 0.36nm/aa [204]. In the case of these spectra which display single unfolding peaks, using the amino acid sequence length, the number of amino acids stretched range from 41 to 208, which in the case of $A\beta_{1-42}$ translates to 1 to 5 monomers. The force at which the bond between the AFM probe and stretched segment of the peptide breaks, called the rupture force, is found to vary between 50-180pN. The amplitude of this force is comparable to the intermolecular forces at the nanoscale that stabilize the secondary or tertiary structure of the protein [210] [211].
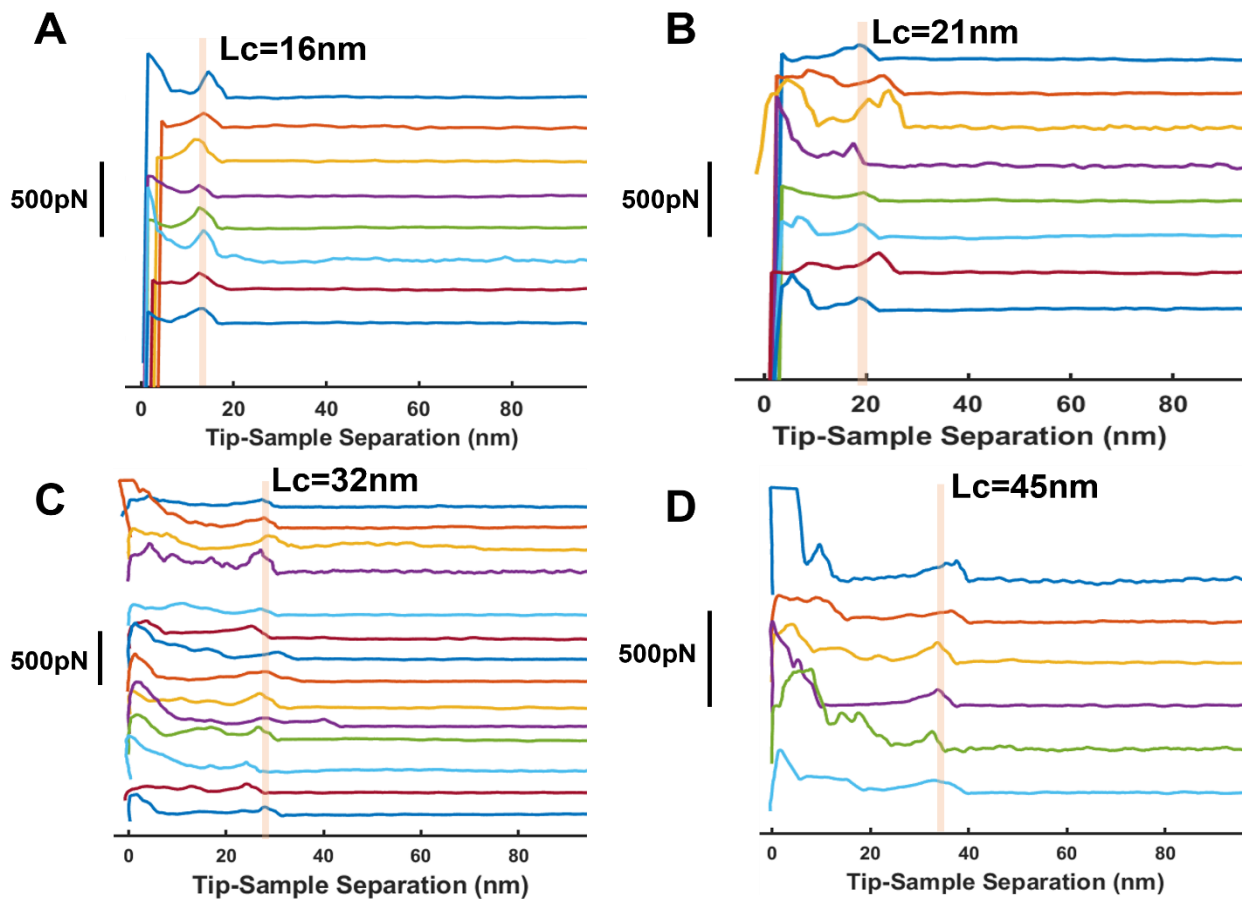
Figure 5.5 - Staggered representation of F-d spectra with dominant single unfolding peaks. In all panels, each color coded trace represents one F-d spectra which can be categorized under a particular contour length. The translucent orange band in each panel is is drawn corresponding to the contour length mentioned next to it A) Lc~=16nm, B) Lc~=21nm, C) Lc~=32nm and D) Lc~=45nm. In all panels, the scale bar to the left represents 500pN force.

Figure 5.5A-D, shows a vertically staggered representation of the F-d spectra with dominant single unfolding peaks. Among all the F-d spectra categorized into single unfolding peaks (n=38), 21% of the spectra display a contour length of ~16nm and ~21nm respectively. 38% of the spectra display contour length of ~32nm. In comparison, contour length of ~45nm and ~72nm are displayed by 15% and 5% respectively. The relative portioning of these single unfolding peak curves into different contour length space indirectly indicates the propensity of following a particular unfolding pathway.
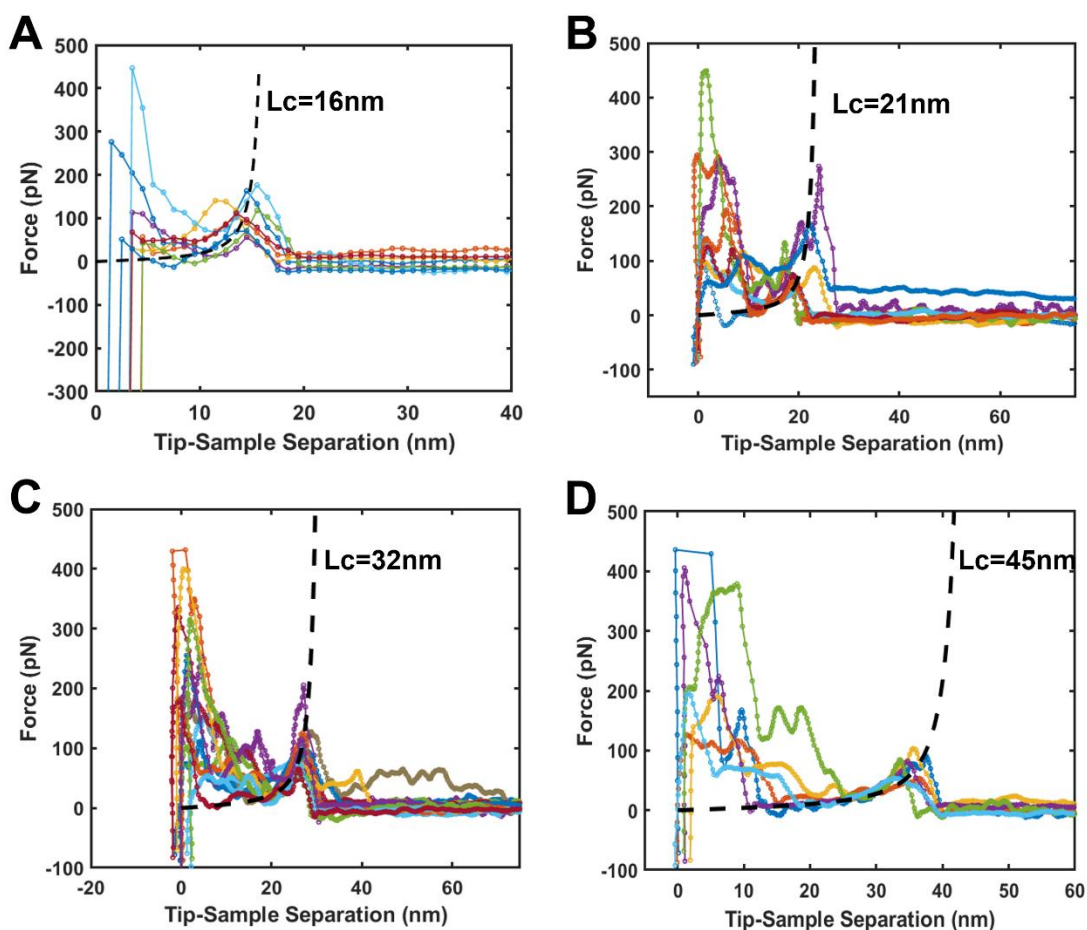
Figure 5.6 - Superimposed representation of the F-d spectra at individual contour lengths. A) Superimposed F-d spectra of curves displaying average contour length of ~16nm (n=8). B) Superimposed F-d spectra of curves displaying average contour length of ~21nm (n=9). C) Superimposed F-d spectra of curves displaying average contour length of ~32nm (n=14) and D) Superimposed F-d spectra of curves displaying average contour length of ~45nm (n=6)

Figure 5.6A-D shows the same spectra in a superimposed fashion wherein the homogeneity of the contour lengths displayed by the curves is more clearly visible in a global fashion. In the case of 16nm contour length (Figure 5.6, A), it can be observed that the force peak is much more cleaner without much interference of the long-range adhesion force peak. This contour length corresponds to ~41 amino acids, which is in good agreement with the argument that this could be a single monomeric unit of an oligomer that's been unfolded. Taking a closer look at the superimposed representation of single unfolding peaks (Figure 5.6C and D), it is evident that some of the unfolding peaks below the respective contour lengths marked on the plot, maybe obscured by the disturbance due to the strong long range adhesion peaks. It is possible that these peaks would represent partial unfolding intermediates of a dimeric association of $A\beta_{1-42}$ oligomers [210].

Dual Unfolding Peaks

The majority of the spectra collected display a single unfolding peak. However, a small subset of the population also displays 2 dominant unfolding peaks as shown in Figure 5.7A, B and C. The F-d spectra under this category showed 2 clear peaks, each peak characterized by an entropic stretching regime with increasing slope of the force, followed by a drop in the force and the process repeats for the next domain of the protein complex. Although the statistical power of these F-d spectra aren't high, their behavior is interesting and is in line with what is observed for spectra with single unfolding peak.

Figure 5.7 - Three characteristic F-d spectra collected on DOPC:DPPC: Aβ$_{1-42}$ reconstituted sample displaying dual unfolding peaks. A) F-d spectra displays 2 prominent unfolding peaks with Lc=21nm and Lc=45nm. The inset shows a magnified view of the first unfolding peak which displays peak-splitting and Lc=24nm WLC model could be fitted to the split peak. B) F-d spectra with 2 prominent peaks with Lc=45nm and Lc=72nm. C) F-d spectra displaying 2 prominent peaks with peak-splitting behavior seen similar to panel A. The extracted Lc were 45nm, 60nm and 75nm (split peak).

In all cases of double unfolding peaks, to a fair degree of approximation, each unfolding peak could be fitted with a WLC model with contour lengths matching the ones observed in single unfolding peak. The contour lengths commonly observed for dual unfolding peaks were 21nm, 45nm (in pairs, Figure 5.7A), 45nm, 72nm (in pairs, Figure 5.7, B) and 45nm, 60nm (Figure 5.7, C). It is interesting to note that these contour lengths are approximately similar (within ±1nm) to the ones observed in single unfolding peaks. This could indicate that in the spectra with dual unfolding peaks, we might be observing the unfolding of two domains (dimeric intermediate is possible too) in a sequential fashion. However, the order in which the domains unfolded would not always be the same and any 2 contour lengths in the range of 15-75nm could occur in pairs.

Another interesting behavior observed in these traces were the peak-splitting effect. In these cases (Figure 5.7 A, C) the slope of the force peak would increase in accordance with WLC model up to a certain contour length and the force would drop by about ~15% - 20% (a visible

dip in the force peak is shown in inset of Figure 5.7A which displays this peak-splitting effect and also in Figure 5.7C). These small dips in the force was followed by more stretching of the unfolded peptide chain and subsequent bond breakage. This effect can be ascribed to partial refolding of a few amino acids in the stretched portion of the peptide [212]. These amino acids acquire an intermediate conformation, which further increases the contour length accessible. In the case of Figure 5.7 A and C, the increase in contour length post peak splitting is ~3nm and ~15nm respectively.

Multiple Unfolding Peaks
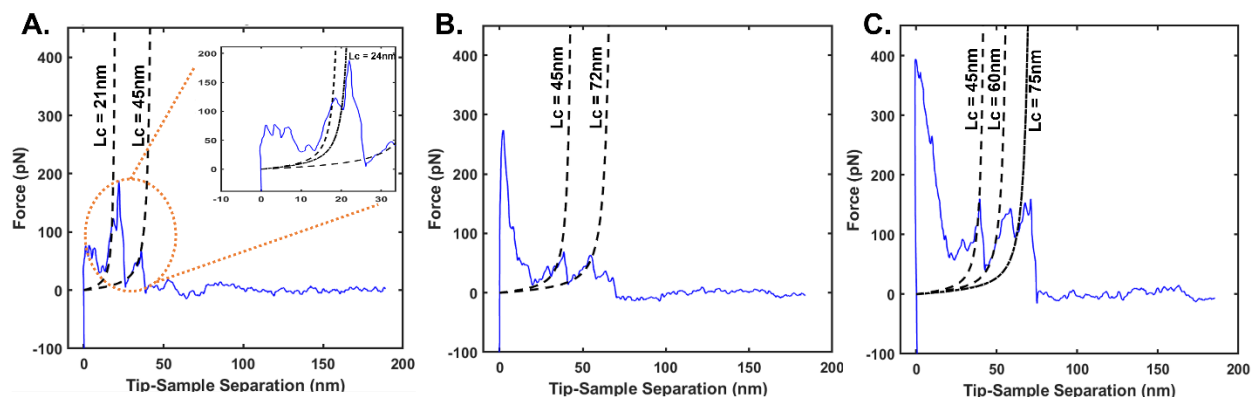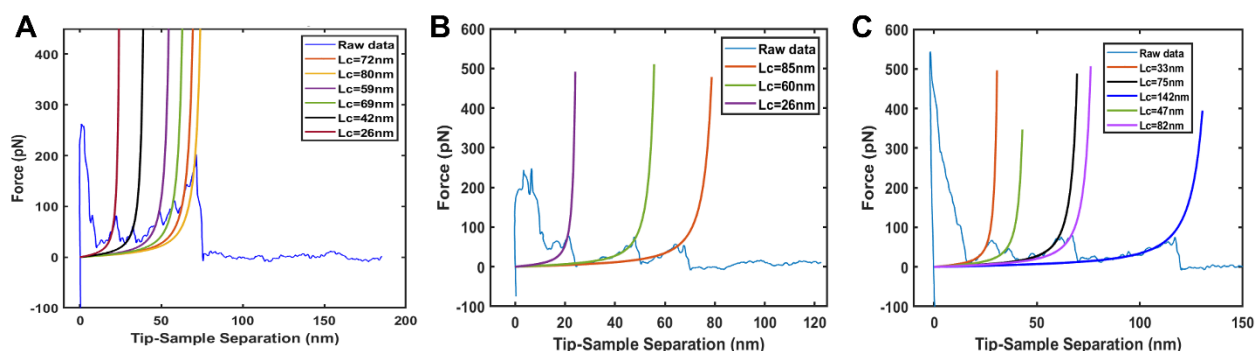

Figure 5.8 - Three characteristic F-d spectra collected on DOPC:DPPC: Aβ1-42 reconstituted sample displaying multiple unfolding peaks with different signatures. A) First type of unfolding spectra with closely spaced multiple peaks fitted with WLC model (Lc = 26nm, , 42nm, 59nm, 69nm, 72nm and 80nm). B) Second main type of F-d spectra with peaks spaced far apart (Lc=26nm, 60nm and 85nm). C) F-d spectra from a subsequent experiment done in similar conditions showing multiple peaks spaced apart with peak splitting (Lc=33nm, 47nm, 75nm, 82nm and 142nm)

In addition to F-d spectra displaying single and double unfolding peaks, we also observed a small portion of the selected curves (~10%) displaying multiple unfolding peaks. The multi-peak behavior is seen mainly as two separate types – multi-peaks in intermediate folding states (Figure 5.8A) and well separated multi-peaks (Figure 5.8B and C). Interestingly, most of the contour lengths found in cases of multi-peaks also match the ones seen in single and dual peaks, with the exception of 85nm and 142nm in Figure 5.8B and C. The type of multiple peak unfolding displayed

in Figure 5.8A was commonly observed, however the position of the peaks were quite heterogenous. In these cases, an intermediate unfolded state is achieved, and the force starts to increase again until a similar peak at a higher contour length is encountered. This effect can be attributed to a change in anchoring point of the unfolding intermediate [212] [213]. Generally, it is assumed that when a particular segment of the protein is being unfolded under a mechanical force, there is an anchor point (could be loop residues connecting domains), until which all amino acid residues are unfolded and the local peak in the force is reached. Once the anchor point is reached, additional force must be applied to the remaining folded portion of the protein and a new anchor point is formed through which the next portion of the unfolding can happen. This behavior happens to be the case in Figure 5.8B and C, where a clear force peak is reached (first anchor point reached) and as the tip-sample distance increases, the next domain is unfolded until the next anchor point is reached. However, in the case of Figure 5.8A, these anchor points seem to dynamically change with the applied force leading to local maxima in the peaks detected [200].

Figure 5.9 - Global representation of detected single unfolding peaks in contour length space. A) and B) Trace number vs contour length (Lc) representation of single peaks detected in in Lc<40nm (A) and >40nm (B) respectively. C) and D) Probability densities of peaks detected in panels A and B respectively, fit with multi-gaussian. E) Rupture Force vs contour length representation of all the peaks single peaks

144

Global Representation

Displaying the detected contour lengths in a global representation (in contour length space) provides some more quantitative information regarding unfolding [207]. Figure 5.9A and B display the contour lengths detected in two separate sessions of analysis wherein Lc<40nm (Figure 5.9A) and Lc>40nm (Figure 5.9B) plotted against the trace numbers corresponding to a particular Lc. Each of the yellow bars indicates the Lc detected for the particular trace. Figure 5.9 C and D show the probability distribution of a particular Lc being detected in the pool of selected curves in panels A and B respectively. This probability distribution was then fit using the automatic multi-Gaussian fitting feature available in Fodis environment [205]. The Gaussian fit is superimposed on the respective probability distributions. The contour length of ~16nm has a probability of 0.31 and the contour length of ~34nm has a probability of 0.61. These data indicate that unfolding of peak near the 32-34nm contour length is highly likely and an average contour length of ~33nm corresponds approximately to ~92 unfolded amino acids. This amino acid number corresponds to a dimeric configuration of Aβ. From Figure 5.9D, contour length of ~57nm has a probability of ~0.67. This contour length corresponds to ~158 amino acids, which is closer to a tetrameric configuration of Aβ. Figure 5.9E shows a combined representation of bond rupture forces detected after WLC fitting, where the rupture force ranges from 50pN to 200pN, with higher concentration in the 50-100pN range.
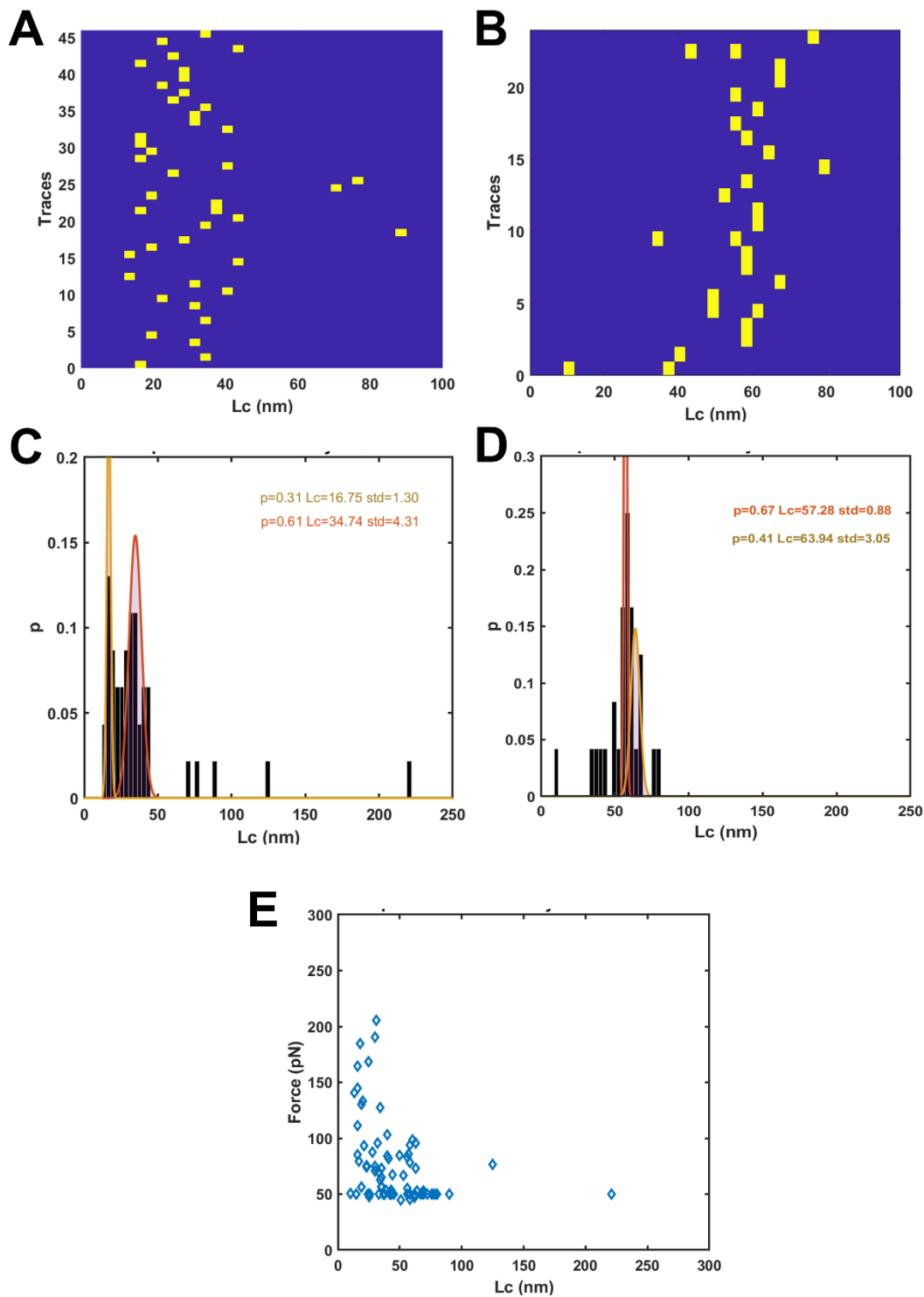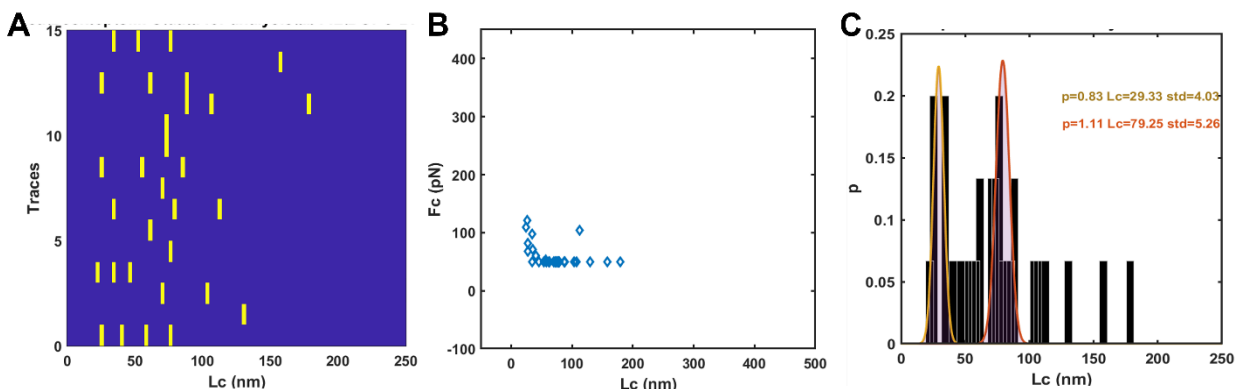
Figure 5.10 - Global representation of detected multiple unfolding peaks in contour length space. A) Trace number vs contour length plot, B) Rupture force vs contour length and C) probability distribution of detected peaks fitted with multi-gaussian

Similar global representation was performed for F-d spectra where multiple peaks were detected through WLC fitting. Figure 5.10A shows the Trace # vs contour length representation with the yellow blocks marking the Lc detected. As its evident, the Lc detected are quite heterogenous and not very concentrated as seen in the previous global representation corresponding to single unfolding peaks (Figure 5.9D). Figure 5.10B and C display the rupture force and the probability density of a particular Lc being detected. It has to be emphasized that because of the low statistical sampling of the dataset, contour lengths other than the ones shown in Figure 5.10C, were unable to be fit by Gaussian curves. Individual F-d spectra representations, however, do display multiple contour lengths for spectra classified under the 'multiple peaks' category.

5.3.3 SMFS of DOPC-Cholesterol (30%) - Aβ$_{1-42}$

In the next phase, we performed similar sets of experiments on Aβ$_{1-42}$ reconstituted in DOPC:Cholesterol (30% mol) bilayers to understand the commonalities and differences in SMFS

behavior and probe any membrane composition specific effects on oligomerization and unfolding. Figure 5.11A shows the height image acquired in one of the imaging areas with the corresponding height profile in Figure 5.11B. The distribution of oligomer heights on the surface of lipid bilayers were similar to the ones observed in DOPC:DPPC bilayers with the height ranging from 1-10nm above the bilayer plane. In some of the locations imaged, we also observed small protofibrillar intermediates forming which eventually grew into mature fibrils (Figure 5.11A, C and D). Hence, these conditions represent the stage in the $A\beta_{1-42}$ lifecycle in which small oligomers form and some oligomeric nuclei start propagating into fibril structures.

Interestingly, it was observed that in some of the regions on the same sample, $A\beta_{1-42}$ oligomers show a 'carpeting effect', wherein surfaces of lipid bilayers appeared to be covered by a film $A\beta_{1-42}$ oligomers (Figure 5.11C and D) [56]. The oligomers appear as regular spherical units loosely connected to each other and a pseudo-ordering effect is visible where these spherical units are assembled in small chain like structures (5-7 oligomeric units), forming a mosaic pattern throughout the imaging area. Figure 5.11C shows one such area where the lower darker parts of the image represent the carpeted $A\beta_{1-42}$ and small protofibrils growing from some these nuclei can be observed as well (brighter portions of the image). We performed SMFS experiments on this area to quantify the unfolding behavior in this membrane environment. Figure 5.11D shows a large area scan of the imaging area after performing the SMFS experiment. The white box overlaid in Figure 5.11D, indicates the area in which SMFS experiment was performed in panel C. From Figure 5.11,D it can be observed that some of the spherical oligomeric units have been completely removed from the interface (empty spots) indicating that oligomeric units were unfolded and pulled out of membrane [213].
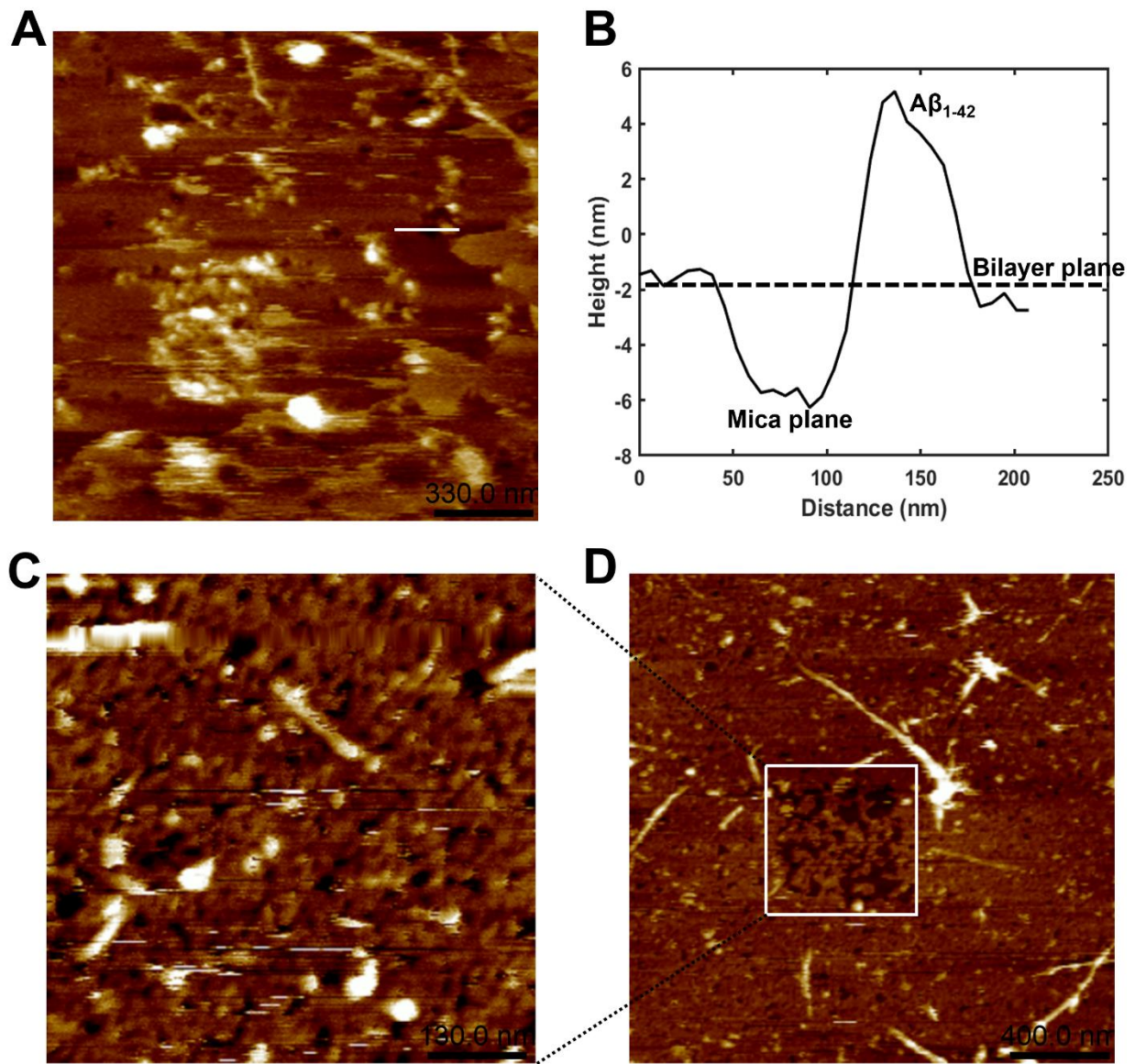
Figure 5.11 - AFM height images of DOPC:Cholesterol (30% mol): Aβ1-42. A) Large area height image of Aβ1-42 embedded in lipid bilayer showing a wide variety of oligomeric structures including small fibrils. B) Section height profile of the white horizontal line drawn in panel A showing the height distribution. C) One of the representative areas chosen to perform SMFS. In this area large patches of Aβ$_{1-42}$ arranged in a carpeted fashion, with fibrils growing and propagating from some oligomeric nuclei. D) A larger area scan collected after the SMFS experiment. The white box inset is the area that was chosen for SMFS in panel C. It can be noted that some of the oligomers have been missing/pulled out completely after SMFS. (Scan size for panel A is 1.5um X 1.5um, panel C is 650nm X 650nm and panel D is 1.7um X 1.7um. Z-scale for A is 0-20nm, C is 0-10nm and D is 0-25nm)

148

For the SMFS experiment, we followed similar analysis methodology as before and classified the collected F-d spectra into categories of single unfolding peak, dual unfolding peak etc. Of all the F-d curves selected for further analysis (after discarding unsuitable F-d spectra) single unfolding peaks were found in high percentage.
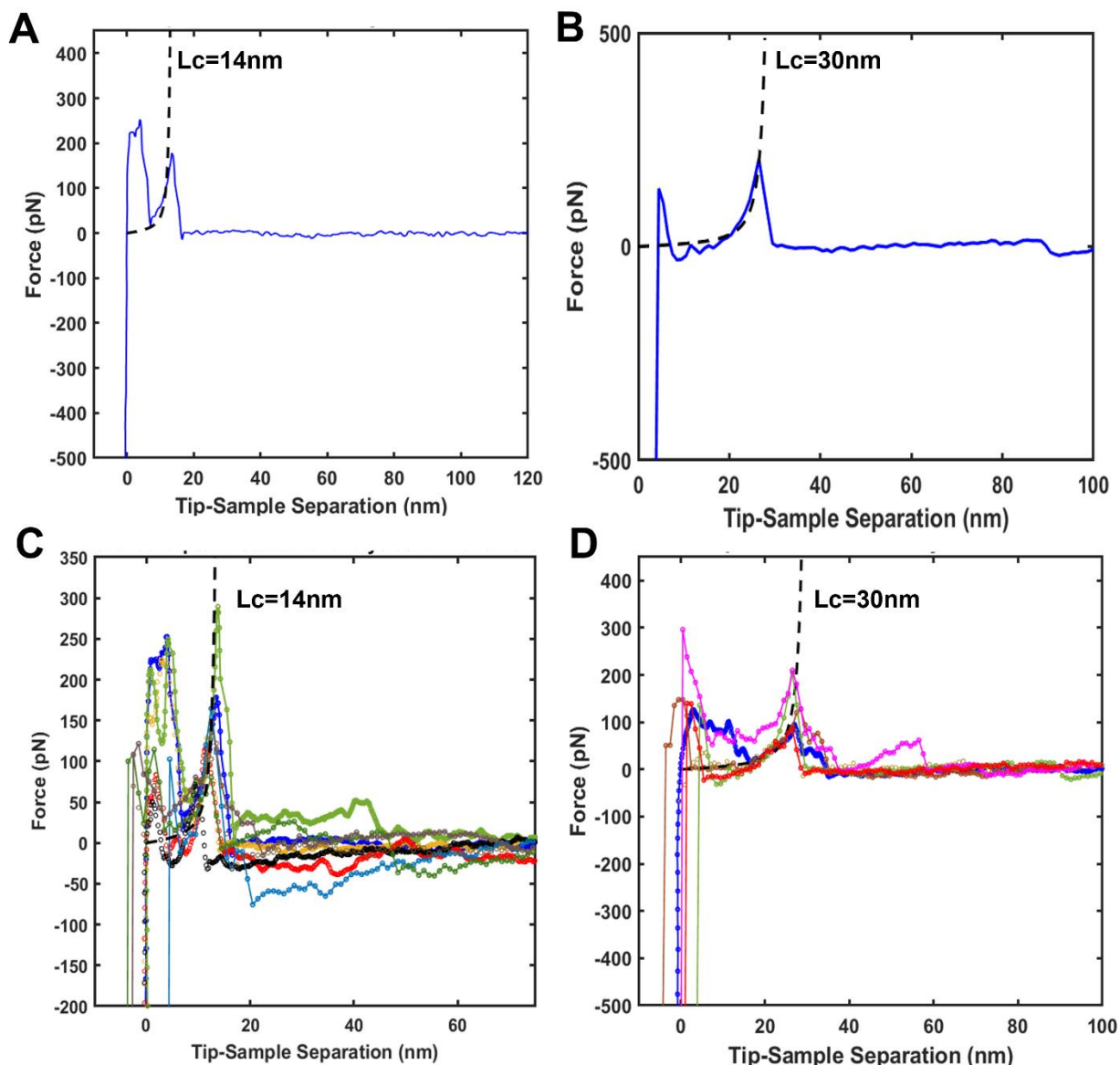
Figure 5.12 - Representative F-d spectra collected on DOPC:Cholesterol (30% mol): Aβ1-42 displaying dominant single unfolding peak. A) F-d spectra with WLC fit (black dashed lines) contour length ~14nm. B) F-d spectra with WLC fit (black dashed lines) contour length
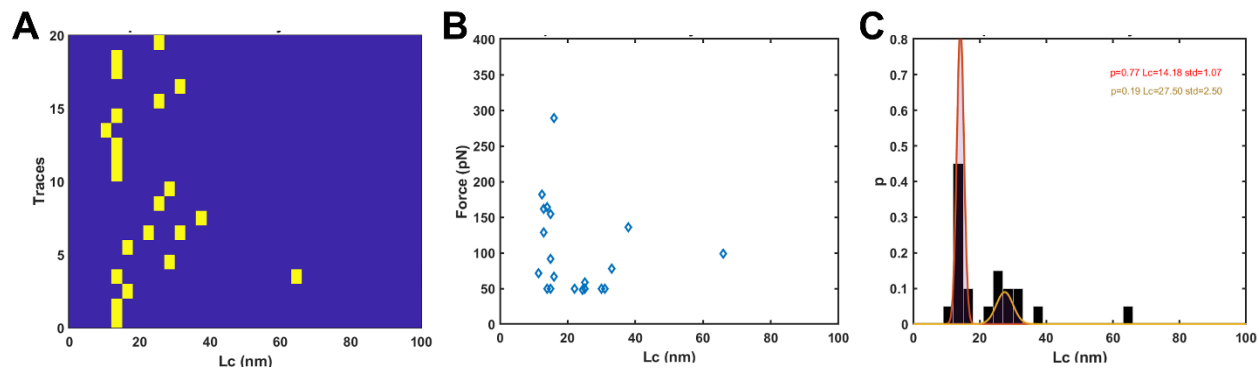
Figure 5.13 - Global representation of detected single unfolding peaks in contour length space. A) Trace number vs contour length plot, B) Rupture force vs contour length and C) probability distribution of detected peaks fitted with multi-gaussian

In the case of DOPC:Chol(30%): $A\beta_{1-42}$ reconstituted system, the curves displaying single unfolding peaks displayed contour lengths of 14nm and 30nm (Figure 5.11A and B, with superimposed F-d spectra of same contour lengths in panels A and B, shown in C and D respectively). These individual contour lengths correspond to approximately ~39 and ~83 amino acids which are in close proximity to monomeric and dimeric units of $A\beta_{1-42}$. Out of the curves categorized under these two contour lengths, roughly 64% of them correspond to Lc of 14nm and the remaining correspond to Lc of 30nm. Global representations in contour length space (Figure 5.13) display two dominant, mean contour lengths of ~14nm and ~28nm (Figure 5.13,C). The rupture force distribution in this case (Figure 5.13B) was found to be more dispersed in the 50pN to 200pN range. The probability of occurrence of 14nm contour length seemed to be higher than the 28nm contour length (p=0.77 vs p=0.19). This indicates that the monomeric subunit unfolding seems to be the most probable pathway of unfolding that occurs universally in almost all samples.

Dual Unfolding Peaks
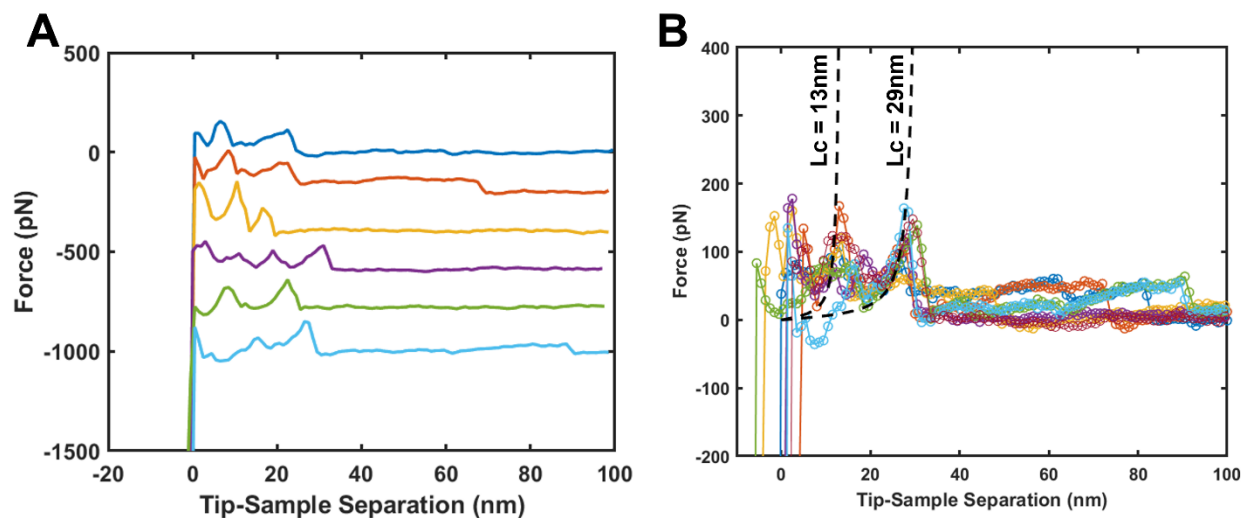
Figure 5.14 - Combined plot representation of F-d spectra displaying dual peaks on DOPC:Chol(30%):Aβ1-42 sample. A) Staggered representation of F-d spectra displaying dominantly dual unfolding peaks. B) Superimposed representation of the same set of F-d spectra with dominant dual peaks, contour length of ~13nm and ~29nm have been marked in the high density regions

Similar to the case of DOPC:DPPC:Aβ$_{1-42}$, the unfolding peaks in DOPC:Chol(30%):Aβ$_{1-42}$ sample showed dual unfolding peaks with contour lengths (~13nm and ~29nm) close to the ones seen in single unfolding peaks (Figure 5.14A and B). These peaks also roughly correspond to single Aβ$_{1-42}$ monomer and dimeric units being unfolded under the action of force.

Multiple Unfolding peaks

In addition to single and double unfolding peaks, a small sub-population of F-d spectra also displayed multiple unfolding peaks (Figure 5.15A, B and C). In all the F-d spectra categorized for this sample, only ~5% of the curves display multi-peak unfolding behavior.
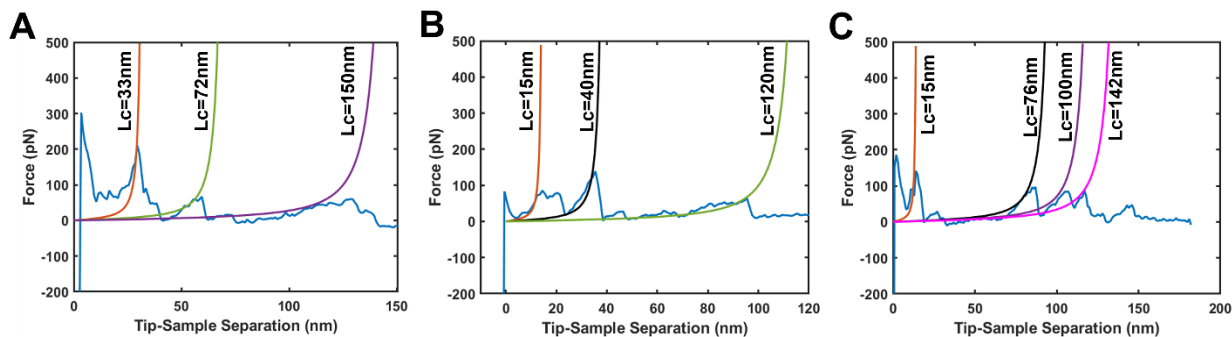
Figure 5.15 - Representative F-d spectra which show multiple peaks in DOPC:Chol(30%):Aβ$_{1-42}$ sample. The corresponding WLC fit and the contour lengths are marked on the detected peaks.

One interesting detail that is different from the DOPC:DPPC:Aβ1-42 sample for the spectra displaying multi peaks is that, for these cases, the WLC curves displayed comparatively weak fitting (Figure 5.15, A(Lc=72nm and 150nm), B(Lc=40nm and Lc=120nm) and C(Lc=76nm, 100nm and Lc=142nm). Contour lengths in these cases ranged from ~15nm to ~150nm, corresponding to ~42 amino acids and ~417 amino acids respectively.

Analyzing the unfolding behavior of proteins offers valuable insights into the 3D organization of the proteins in their native environment. In the AD field, there has been a major problem of trying to pinpoint which exact oligomeric species is responsible for cytotoxic cascade. As such, multiple biochemical techniques have been used to isolate oligomeric fractions in various preparations. The problem, however, in these approaches is the possibility of modification of the protein structure and organization due to harsh chemical treatments used. As Aβ oligomers are known to be highly dynamic and unstable, atomic resolution studies (ssNMR and cryoEM) have proven extremely challenging and the polymorphic nature of Aβ has only exacerbated the situation. Keeping these factors in mind, AFM based single molecule force spectroscopy experiments offer a unique window in exploring the 3D organization of proteins

without any chemical modification and in their native environment [200][201]. Additionally, for membrane proteins which are much harder to crystallize for crystallographic studies, AFM-SMFS maybe ideally suited to probe structural organization.

We analyzed the unfolding behavior of $A\beta_{1-42}$ reconstituted in two different membrane environments; DOPC:DPPC and DOPC:Chol (30%). We found some similarities in the unfolding behavior in these membrane systems. In both cases, F-d spectra displaying single unfolding peak were found to be the highest and the smallest contour length of single unfolding peak seems to be almost the same in both membrane systems (Lc=~15nm in DOPC:DPPC bilayers vs Lc=~14nm in DOPC:Chol (30%) bilayers). This contour length corresponds to amino acid count of ~41-43 which is in excellent agreement with the notion that a monomeric subunit of a 3D structure was unfolded in both cases. In both membrane systems, we also found other contour lengths associated with single unfolding peak behavior. Interestingly, most of the contour lengths found for single peaks were approximate integer multiples of the lowest contour length. This behavior was also observed in F-d spectra which display dual or multiple unfolding peaks, where approximate integer multiples of the lowest contour length were successively unfolded (in both membrane systems). This could hint at the possibility of structural commonalities in 3D organization of Aβ in both membrane systems and also the possibility of traversing similar unfolding pathways under the action of a mechanical force. Unfolding corresponding to monomeric and dimeric units were most commonly seen and this is in line with a previous report of a closely related AFM-SMFS experiment which concluded that dimers maybe the kinetically stabilized structures in Aβ which act as oligomeric nuclei for the propagation of amyloid structures [210][211].

Conventionally, the results from AFM-SMFS unfolding experiments are compared to the available structural models of the proteins to assign the signatures of the F-d spectra to tertiary/quaternary structure organization of proteins [200][201][212]. Unfortunately, in the case of Aβ, no experimental oligomeric structural models are available, which makes F-d spectra peak signature assignment extremely difficult. Additionally, we cannot rule out the possibility of attachment site variability in these experiments without a structural model to refer to [201]. Another factor that should be emphasized is the statistical power of the experiments carried out in this study. Generally, as attachment of the probe to the protein and the complete unfolding of the protein can be stochastic in nature, large number of datasets are needed to make statistical conclusions about the unfolding behavior [201]. As this is a very preliminary study on the feasibility of the approach in quantifying unfolding behavior of Aβ peptides, we only resorted to collecting ~3000 F-d spectra per membrane system, with 1-2% yield in the total number of spectra displaying unfolding behavior. In the future we hope to increase the sample size by at least a factor of 10 to obtain robust statistical information and quantify the unfolding pathways of polymorphic structures of Aβ. Due to the highly powerful and simplistic nature of the approach, we hope to build a robust pipeline and a phase space of all possible unfolding behavior of Aβ in various membrane systems. The information obtained from unfolding experiments can pave the way to the development of better structural models for Aβ oligomers.

5.4 Conclusion

In Chapter 5, we probed the unfolding behavior of Aβ$_{1-42}$ oligomeric structures in lipid bilayers via AFM-SMFS method. Structural similarities in the unfolding intermediates of Aβ were

found in both membrane systems. Further implementation of the approach in mutationally modified Aβ and different membrane environments under varying environmental conditions can offer extremely valuable insight into the 3D organization of Aβ in membrane environments.

Chapter 5, in part, is a manuscript under preparation with Karkisaval A.G; and Lal R. titled 'Single molecule unfolding of Aβ$_{1-42}$ oligomers from lipid bilayers'. The dissertation author was the primary author of the manuscript.

Chapter 6

Design and Implementation of combined Atomic Force Microscopy – Total Internal Reflection Fluorescence Microscope

6.1 Introduction

Membrane-Protein interaction phenomena form the basis of many important biological functions and are also implicated in various disorders. Increasing evidence suggest that in the case of Alzheimer's disease, Parkinson's disease and other neurological disease cascades, interaction and subsequent disturbance of membrane environment are the critical events which begin the progression of the disease. As such, imaging-based approaches have served as critical tools in elevating our understanding of such interactions. Fluorescence microscopy is one such approach which has transformed our understanding of the biological and biophysical world in extreme detail [214]. The versatility of fluorescence labeling methods, availability of a plethora of fluorescence probes that can be used to specifically visualize a particular biomolecule with great fidelity and the ease of use of microscopy instrumentation over the years, offers immense advantage to researchers and allows the collection of a wide variety of information from a single experiment [215]. Compared to other imaging methods such as electron microscopy (Scanning Electron Microscopy, Transmission Electron Microscopy) which offer nanoscale resolution, fluorescence microscopy offers the main advantage of observing biological phenomena in near native conditions, with little disturbance to the biological function and dynamics.

Fluorescence microscopy has evolved rapidly over the years to keep up with the resolution requirements to study nanoscale interactions in both in-vitro and in-vivo settings.

Conventional fluorescence microscopy (also known as widefield fluorescence or epifluorescence microscopy, Figure 6.1a) is highly suited to study cellular and tissue level interactions with unprecedented access to specifically label whole cells or even intracellular organelles. The ease of use and adaptability of the system to study live cell interactions has made this modality of imaging a common tool found in most biological laboratories. The XY resolution (also known as the lateral resolution) is limited to ~200nm and ~500nm in the axial direction (Z-direction) due to light diffraction effects (also known as Abbe Diffraction limit) [216] [217]. Even though these resolution limits were not much of problem when studying biological systems in length scales >500nm, subcellular interactions (such as protein-protein, protein-membrane, other subcellular organelle, and small molecule interactions) which happen at length scales much lesser than 500nm, proved to be extremely challenging to study under conventional fluorescence microscopy methods and additionally the background fluorescence, with poor optical sectioning in thick samples created further problems in achieving high signal to noise ratio measurements. The advent of confocal and multi-photon microscopy have led to overcoming the background fluorescence problem with substantially better signal-to-noise ratio measurements compared to widefield fluorescence in samples thicker than 5um [218] [219] [220].

Recent advances in technology, fluorophore kinetics and image processing have paved the way for a new wave of fluorescence microscopy techniques that have far surpassed the diffraction limit set forth in conventional forms of fluorescence microscopy. These new techniques, collectively called super-resolution fluorescence microscopy (SRM) have enabled roughly an order of magnitude improvement in the lateral and axial resolution compared to conventional methods [221] [222]. The development of SRM techniques have been a

combination of illumination technology engineering and computational methods that improve the spatial localization of fluorescent molecules within the plane of the sample. Illumination engineering approaches mainly involve different forms of structured illumination microscopy (SIM) approaches, where in samples are illuminated by varying phase of light (creating interference stripe patterns) and the collected images are analyzed in frequency domain to reconstruct an image which has high spatial resolution (about a 2-3 fold improvement in resolution, Figure 6.1d and e) [223] [224]. Variants of this technique include interference-based SIM and Point scanning SIM. Light sheet fluorescence microscopy (LSFM) and lattice light sheet are set of techniques which involve illuminating a thin section of the sample (light sheet) and collecting the light emitted in the perpendicular direction (Figure 6.1d). The sample can be successively illuminated at different heights along the z-direction and 3D information can be reconstructed [225] [226]. Another widely used commercial solution to improved resolution is stimulated emission depletion microscopy (STED, Figure 6.1f) where light from 2 independent lasers form a doughnut configuration illumination scheme(formed by modification of pupil plane of the illuminating objective lens) on the sample are successively used to excite an area of the sample (using the first laser) and then selectively deplete the fluorescence of the sample in the area surrounding the center of the first excitation zone (using the 2nd laser), thus effectively limiting the area of emission. This technique is highly effective and has achieved resolutions of ~50-80nm in the lateral direction [227] [228].
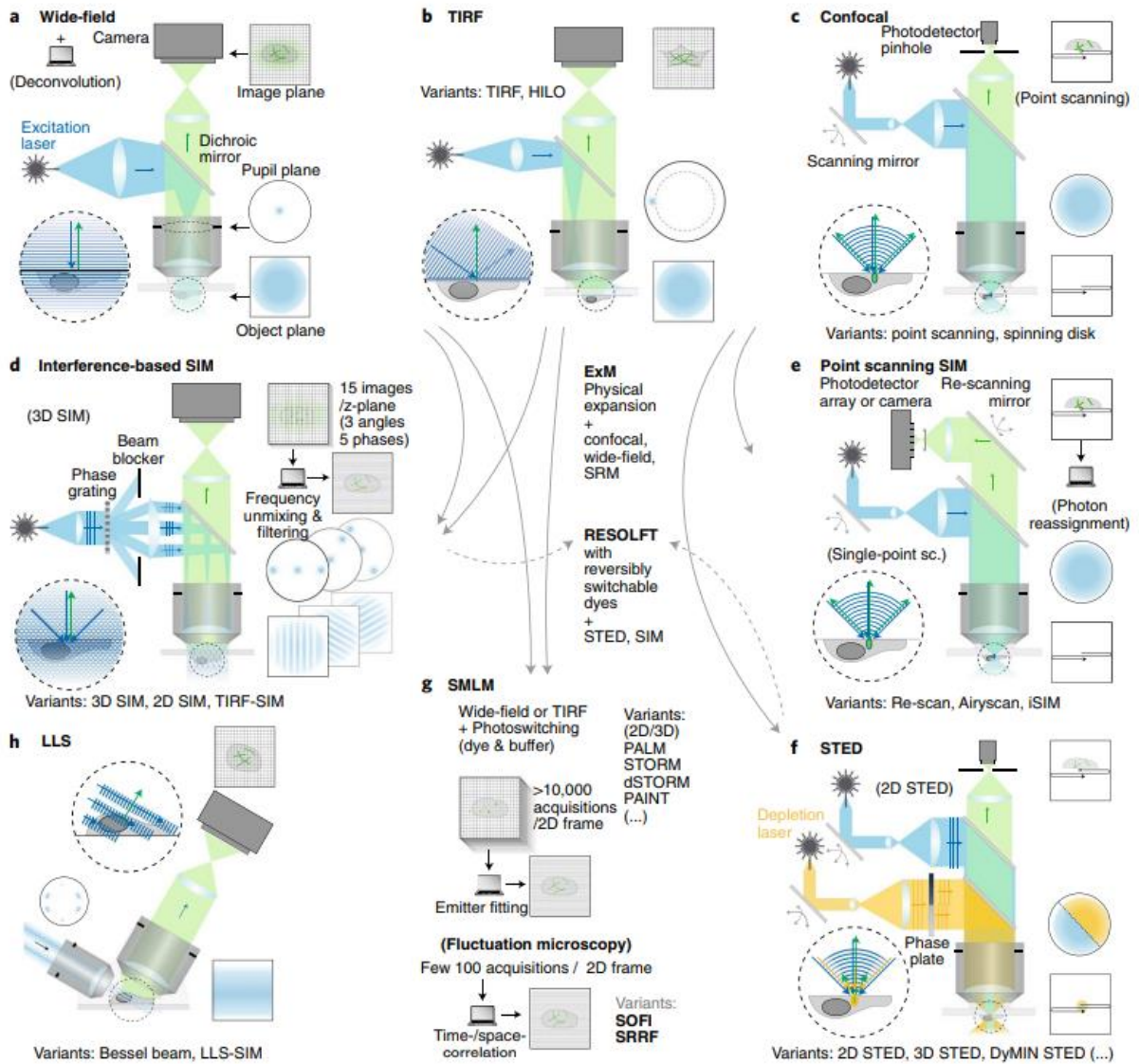
Figure 6.1 - Various schemes of fluorescence microscopy and their respective illumination and light collection schemes: a) Widefield fluorescence microscopy, b) Total Internal Reflection Fluorescence (TIRF), c) Confocal Fluorescence Microscopy, d) Interference-based structural illumination microscopy (SIM), e) Point Scanning structural illumination microscopy, f) Stimulated Emission Depletion Microscopy (STED), g) Single molecule Localization Microscopy techniques (SMLM) and h) Lattice Light sheet microscopy (LLS). The figure also shows interconvertibility between techniques with small to medium modifications to the experimental setup. Figure is adapted from [222] with permission from Springer Nature.

The other major area in the improvement of resolution in microscopy is approaching the resolution problem from a computational standpoint. These techniques, collectively called single molecule localization microscopy (SMLM, Figure 6.1g) aim to localize the location of individual fluorophores on the sample and reconstruct a fluorescence image based on the spatial coordinates of the localizations computed [222]. In these techniques, the fluorescence emitted by the fluorophores are collected in conventional illumination schemes like widefield, TIRF or confocal at high frame rates. The fluorophores used in these techniques and the sample environment enable either random switching or controlled switching on/off of the fluorophores in individual frames. Then, computational algorithms which can calculate the time autocorrelation, radial autocorrelation, brightness gradients etc for each pixel can be used to locate the fluorophore location in the sample with high fidelity. This is done across the time stack of images and a super-resolved image can be reconstructed by superposition of localizations calculated. The most common techniques under this umbrella are Stochastic Optical Reconstruction Microscopy (STORM) [229] [230], Photoactivated Localization Microscopy (PALM) [231] [232] and Points accumulated in Nanoscale Topography (PAINT) [233]etc.

Even though superresolution techniques have revolutionized fluorescence microscopy and the way we look at the biological world, multi-parametric information other than optical information are hard to gather. This has led to the development of combined techniques which merge the functionalities of two different microscopy modalities to gather multi-parametric and multi-dimensional set of information. This has paved the way for the development of 'correlative microscopy' techniques such as integrated fluorescence and electron microscopy, fluorescence microscopy combined with electrophysiology, fluorescence combined with magnetic resonance

imaging etc [234] [235]. As such, the combination of atomic force microscopy and fluorescence microscopy has the capacity of combining the unprecedented z-resolution and superior XY resolution (AFM probe limited) of AFM with high degree of chemical specificity and time resolution of fluorescence studies. Additionally, this combination also uniquely allows nanomechanical probing capacity of AFM to be integrated to a fluorescence system, paving the way for analyzing specific systems with high degree of mechano-biological interplay. Keeping these considerations in mind, we designed and implemented a combined AFM – Total internal reflection fluorescence microscopy system for high spatio-temporal resolution imaging and nanomechanical studies of membrane-protein interaction phenomena.

Total internal reflection (TIR) is the phenomenon in which a beam of light entering the interface between a high refractive index(n_1) material and a low refractive index(n_2) , $n_1 > n_2$, material beyond a certain angle of incidence, gets fully reflected into the medium with high refractive index (Figure 6.2). The angle beyond which TIR occurs is called the critical angle (θ_c) and is dependent on the ratio of refractive indices (n_2/n_1), through Snell's law (Eq 6.1).
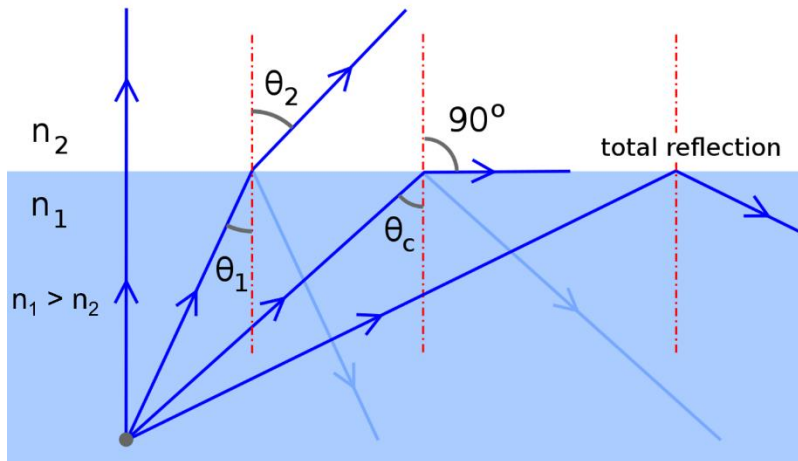
Figure 6.2 - Schematic displaying the principle of Total Internal Reflection (TIR), where θ_1 is the beam incidence angle and θ_2 is the beam transmission angle with respect to the interface normal.

$$\theta_c = \sin^{-1}\left(\frac{n_2}{n_1}\right) \qquad (6.1)$$

The greater the difference in refractive indices of the two optical media at the interface, the smaller the critical angle needed to achieve TIR.

An interesting effect is observed when a light beam total internally reflects from the interface. Due to boundary conditions placed on the propagation of electromagnetic wave through the interface, a small portion of the reflected light penetrates through the interface into the low refractive index medium. This portion of the reflected beam that penetrates into lower index medium is called an evanescent wave or an evanescent field (Figure 6.3). The evanescent wave is a standing wave, and its intensity decreases exponentially from the interface of reflection in the direction of the surface normal.
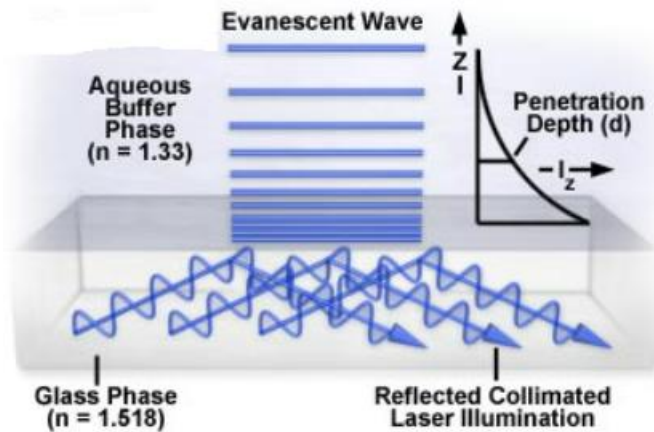
Figure 6.3 - Graphical schematic showing the evanescent wave generation at the interface. Modified from https://www.olympus-lifescience.com/en/microscope)

Due to the exponentially decaying amplitude of the evanescent wave, molecules close to the interface can be selectively excited using the energy provided by the evanescent wave. The evanescent field intensity I(z) and the penetration depth (d) of the evanescent wave is given by the equations (6.2) and (6.3) [236]:

$$I(z) = I(o)e^{\frac{-z}{d}} \tag{6.2}$$

$$d = \frac{\lambda}{4\pi n_1}\left(\frac{sin^2\theta_i}{sin^2\theta_c} - 1\right)^{\frac{-1}{2}} \tag{6.3}$$

Where, I(z) is the z-dependent intensity of the evanescent wave, 'z' is the distance from the interface along the surface normal, 'd' is the penetration depth of the evanescent wave, λ is the wavelength of light, and θ_i and θ_c are the incidence and critical angles respectively.

The phenomenon of TIR and evanescent wave has been exploited in fluorescence imaging, leading to the development of Total internal reflection fluorescence microscopy (TIRFM) where a light beam (usually laser light beam) is reflected off from the interface of a glass-slide or coverslip in contact with aqueous buffer containing the fluorescently labeled sample of interest,

163

generating an evanescent wave that penetrates into the sample (Figure 6.1b). Due to the exponential decay of the evanescent wave intensity, fluorescently labeled structures which are close to the interface can only be excited, thus reducing the bulk fluorescence of the background material. The penetration depth is generally in the 150nm to 300nm range and can be tuned by adjusting the refractive indices of the interfacing mediums and the wavelength of light used [237] [238]. This small penetration depth is really useful in rejecting background light from fluorophores and offers excellent optical sectioning capabilities. Thus, TIRF has emerged to be a highly reliable and relatively simple fluorescence technique for observation of extremely thin samples [237].

Practical implementation of TIRF in microscopy systems can be achieved approximately in 3 configurations, although multiple others are possible. The commercially available solution for TIRF microscopy involves the use of specially designed high numerical aperture objective lenses (NA >1.4). This method (called objective TIRF or o-TIRF, Figure 6.4C) can be used in conjunction with already setup microscopes with modifiable laser illumination. Although, methodologically simple, the objective lenses used for TIRFM are prohibitively expensive and the configuration only allows for an excitation of a small XY area and relatively poor signal to noise ratio. The second possibility is of using a coupling prism through which a beam of light can be reflected (Figure 6.4A). The fluorescently tagged molecules can either be directly immobilized on the surface of the prism and the fluorescence emission can be collected by the microscope objective in normal fashion. Although this method offers good signal to noise ratio, stringent mechanical and sample holding requirement are placed, which makes this design somewhat impractical for universal applications.
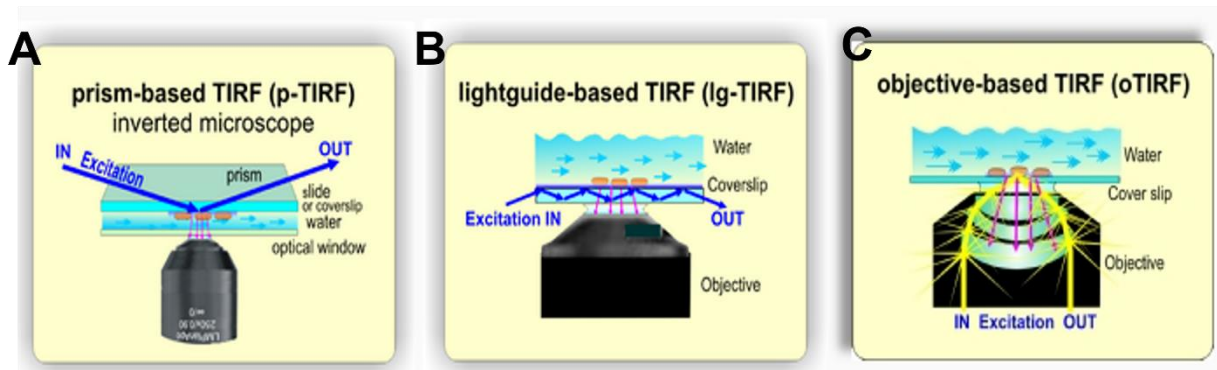
Figure 6.4 - Schematic showing the possible configurations of TIRFM. A) prism-based TIRF, B) light guide based TIRF and C) objective based TIRF (image printed with permission from http://www.tirf-labs.com/tirfmicroscopy.html)

The third configuration is called a light-guide based TIRF system (Figure 6.4B) in which a high refractive index medium coverslip acts as a waveguide or lightguide which allows for transmission of total internally reflected light. All the interfaces at which TIR occurs will have evanescent wave. This configuration is simple to adapt and can be built around already installed microscope configurations. It allows for large area excitation using evanescent waves and can work with multiple sample holding considerations [239].

In our implementation of the combined AFM-TIRF system, we chose to go with the light guide based TIRF approach simply because of the ease of adaptability, AFM access to the sample from the top and overall ease of use of the combined system.

6.2 Design

All the components, subsystems were built around the Olympus IX71 inverted fluorescence microscope. For the AFM, we used a Bruker Bioscope SZ scanner, with its scanner mounting platform. The Bioscope SZ was connected to a Nanoscope IVa AFM controller, running Nanoscope v6.31 software to control all AFM functions. Other than minor cosmetic changes to

accommodate mechanical constraints on the setup, no other modifications were made to the

AFM and used as it is. The basic premise of the combined setup is shown in Figure 6.5. The

majority of the design consisted of optomechanical path design and sample setup subsystems.

Firstly, we split the design process into 3 main aspects – i) laser illumination and optical coupling

subsystem design, ii) sample holding and translating stage design and iii) integration of optics and

AFM.
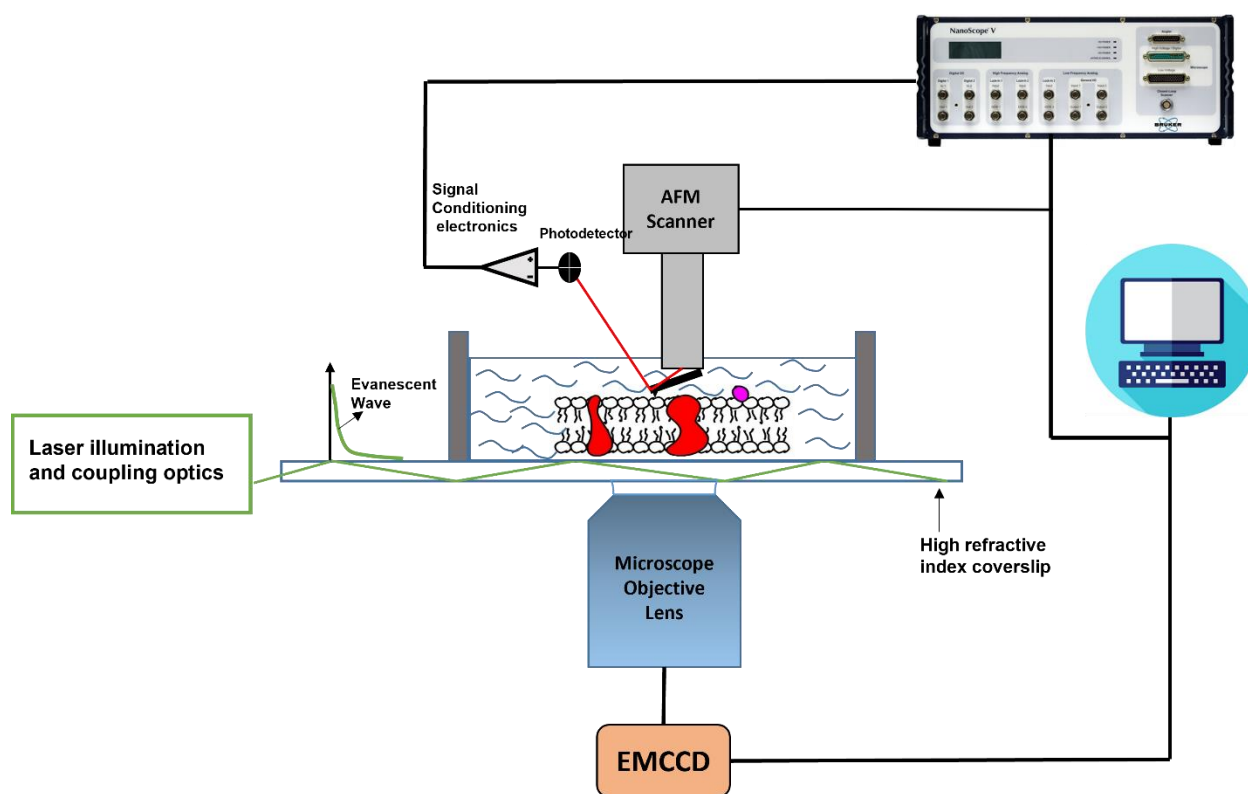
Figure 6.5 - Block diagram level schematic of the combined AFM-TIRF microscope assembly. The AFM machinery is used directly from a Bioscope SZ setup (top portion of the figure). The microscope objective lens, EMCCD (electron-multiplying CCD camera) are part of the Olympus IX71 inverted microscope.

6.2.1 Illumination and optical coupling path subsystem design

In order to work with a wide spectrum of visible wavelength fluorophores, we decided to

work with a wavelength combination optical setup. Briefly, a 450nm laser (1.6W), 532nm laser

(1W) and a 635nm laser (0.5W) were used as main sources of illumination to cover the visible spectrum. Additionally, we also integrated a 458-515nm, 25mW, single mode, Ar-Kr gas laser as a separate illumination pathway, without any additional optics. The coupling scheme of laser output to the optical fiber was similar to the one shown in Figure 6.6, using a 5x objective and U-coupler (Note: the extra Ar-Kr laser path is not shown in the schematic). The beams emanating from each of the lasers were collimated using aspherical collimating lenses.
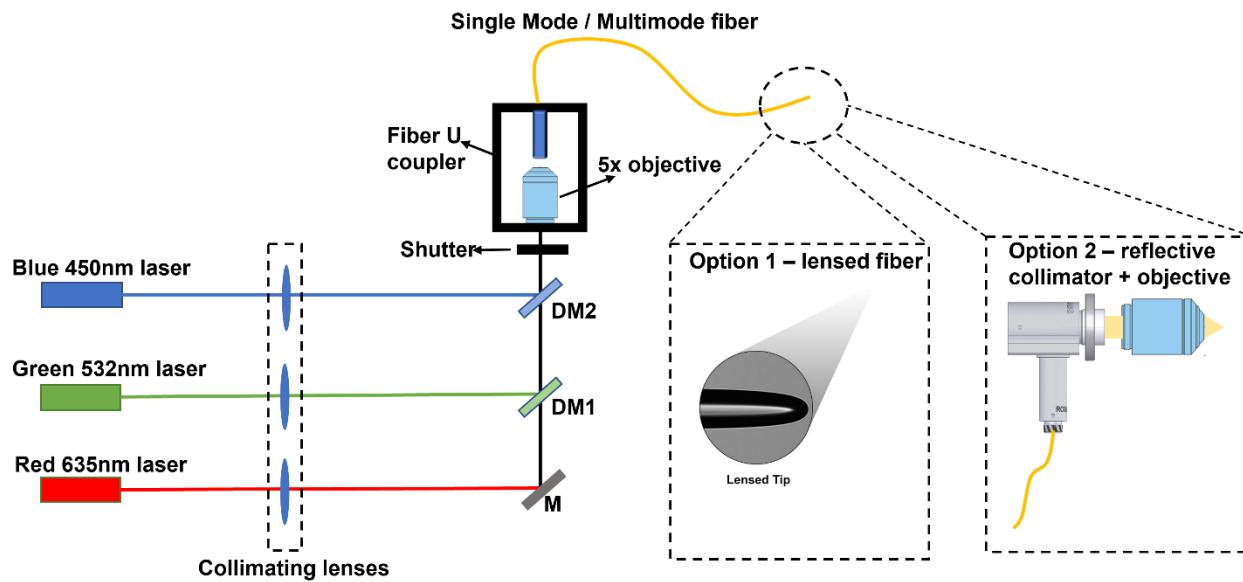
Figure 6.6 - Schematic of the illumination side optical setup. The left side of the figure consists of laser combination setup. The fiber U coupler helps in coupling the combined light beam into a single or multi mode optical fiber using a 5x objective lens. The right side shows 2 approaches used to couple light into the coverslip 1) lensed fiber approach and 2) objective lens based end butt coupling approach. DM refers to dichroic mirrors and M refers to first surface reflecting mirror.

After collimating the beams, the green and blue lasers were reflected from dichroic mirrors DM1 and DM2 and combined with the red laser. The combined collimated beam is then impinged on the aperture of a 5x coupling objective lens mounted on a U-shaped coupler. The combined laser beam is focused by the 5x objective into the aligned core of a single mode fiber or a 50um core multimode fiber. Once the light has been coupled into the optical fiber, then the

167

illumination is coupled to the coverslip/light guide via 2 independent methods – a) lensed fiber-based end facet coupling or b) objective lens based end fire coupling.

a) Lensed-fiber based end facet coupling (Figure 6.6, Option 1)

In this approach, a bare optical fiber with one of its ends formed into a lens shaped structure (Figure 6.6, 'option 1' panel inset) is brought into close proximity with the edge of a coverslip or light guide. The light is coupled into the light guide and undergoes TIR at the interface of high and low refractive index media, thus creating evanescent wave profiles throughout the imaging area [239]. This was achieved by mounting a lensed fiber (Thorlabs LFM1S-1, 0.2 NA) on a 3D printed platform, which was in turn mounted on a XYZ-Translation stage. In order to finely align the lensed fiber adjacent to the light guide (in Z-direction), a micro-stepper motor (Actuonix P8-ST-10) was glued onto the 3D printed mount platform and holds the lensed fiber on top (Figure 6.7).
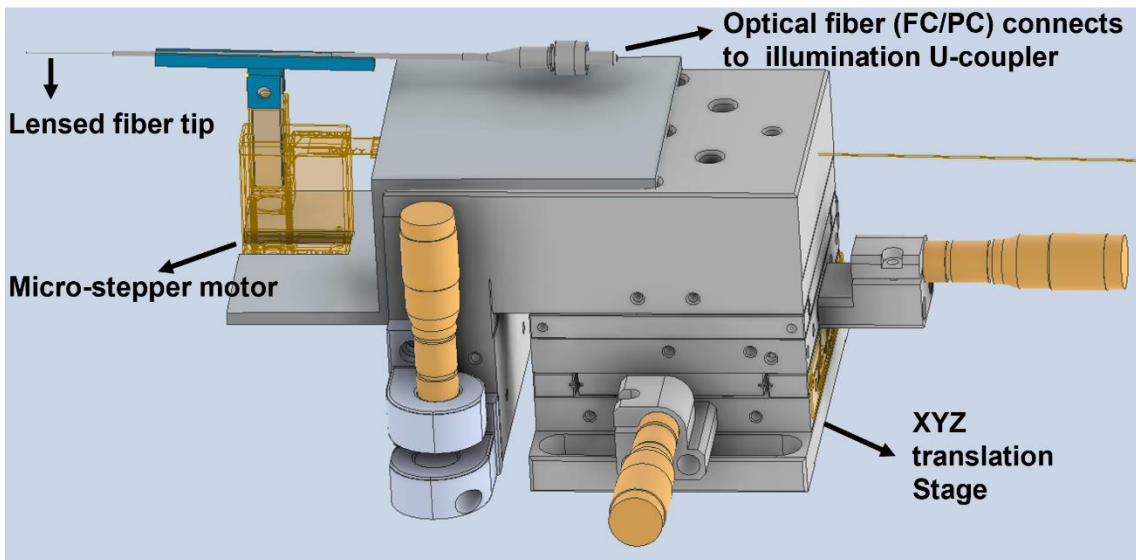
Figure 6.7 - Lensed fiber coupling assembly schematic.

The stepper motor is operated in 165:1 gear ratio mode creating steps of ~1.8um. The lensed fiber tip is brought into close proximity of the coverslip using the stage and stepper motor during alignment.

b) Objective lens based end-fire coupling (Figure 6.6, option 2)

Using similar concept as in (a), we implemented a secondary approach where instead of a lensed fiber, a 40x, 0.65NA objective lens (Olympus UMPlan) was used to couple light into the end facet of the light guide [240]. The optical fiber output from the illumination side U-coupler is connected to a reflective collimator (Thorlabs RC08FC-P01). The reflective collimator and the objective lens are mounted together on a 3D printed mount, which is placed on top of a XYZ translation stage (Figure 6.8).
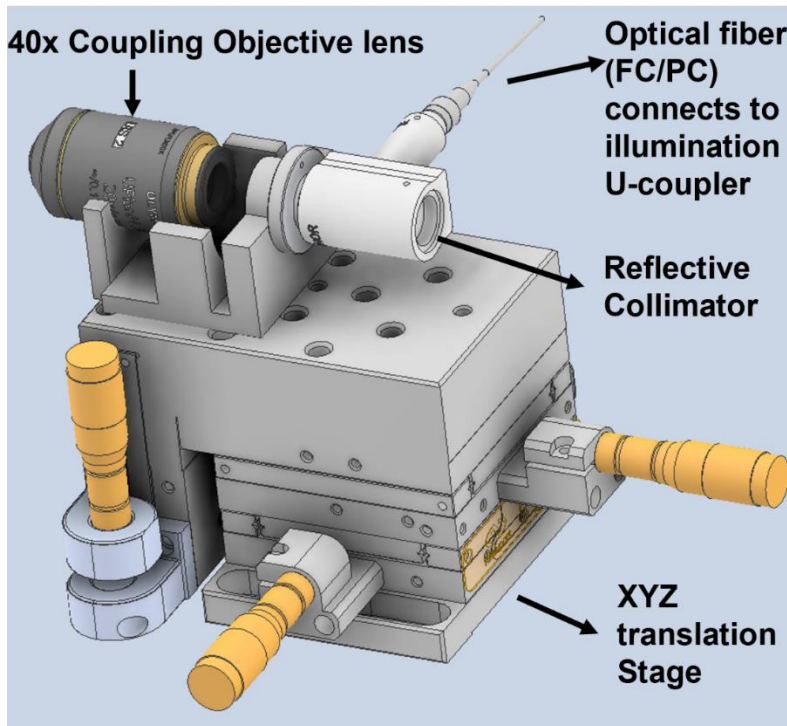
Figure 6.8 - Objective lens-based end fire coupling scheme.

6.2.2 Sample holding stage design

In light guide based TIRF system, the light sources are generally coupled into the light guide/coverslip from the side facet of the light guide structure. In order to achieve this, we fabricated a steel stage whose dimensions are compatible with Olympus IX71 microscope, which has a portion of the stage cut from the right side where the coupling optics assembly can be placed. The other dimensions and structure of the stage followed the mechanical requirements of the AFM scanner mounting platform. A 2-axis XY translation platform was mounted on one side of the stage, on top of which a 3D printed sample holding platform is mounted (Figure 6.9).
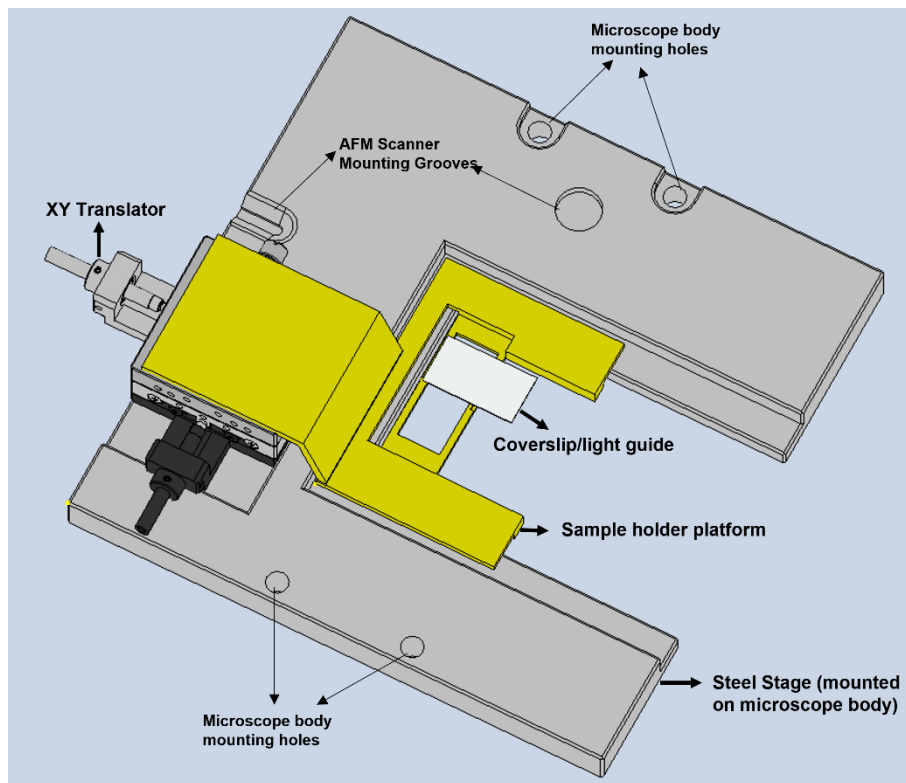
Figure 6.9 - Microscope stage with sample holder assembly

6.2.3 Integration of Optics and AFM

After all the illumination subsystems were built, the stage assembly was mounted on the body of the Olympus IX71 microscope, and the coupling optics were mounted on an aluminum breadboard and fixed next to the microscope as shown in Figure 6.10 (for coupling option 1) and 6.11 (for coupling option 2).
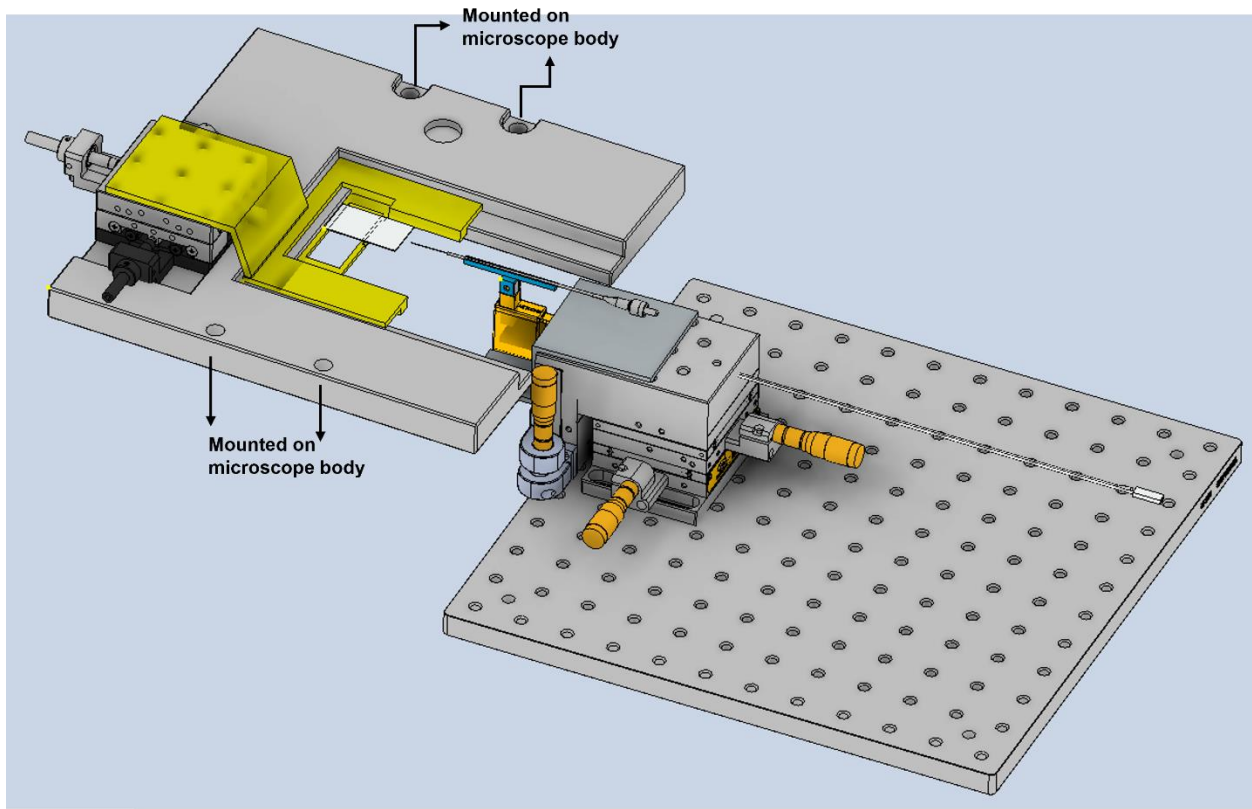
Figure 6.10 - Isometric view of the stage assembly combined with lensed fiber coupling optics assembly.

In both cases, coarse alignment was performed by translating the lensed fiber (or objective) using the XYZ stage and fine alignment (only in case of lensed fiber) was done using microstepping of the stepper motor. The fluorescence signal from the sample was continuously monitored to arrive at the best position of alignment.
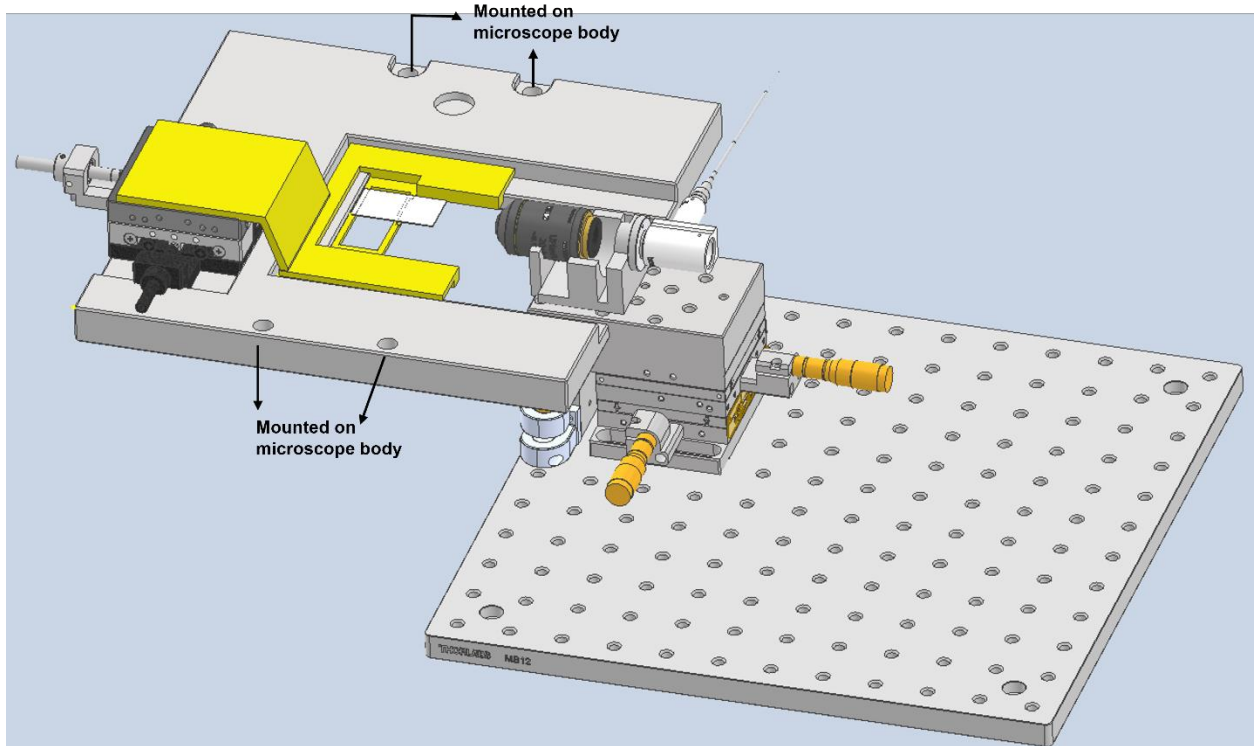
Figure 6.11 - Isometric view of the stage assembly combined with objective lens-based coupling optics assembly.

6.3 Implementation and performance
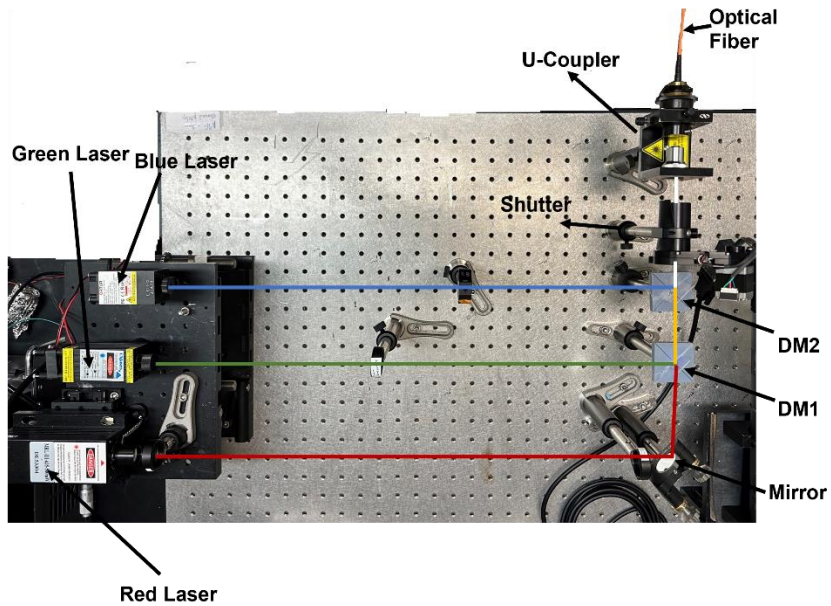
Figure 6.12 - Implementation of laser wavelength combining illumination subsystem.

The hardware level implementation of laser wavelength combination setup is shown in Figure 6.12 (conforming to the design shown in Figure 6.6). The system can also be operated with any of the 3 wavelengths independently.
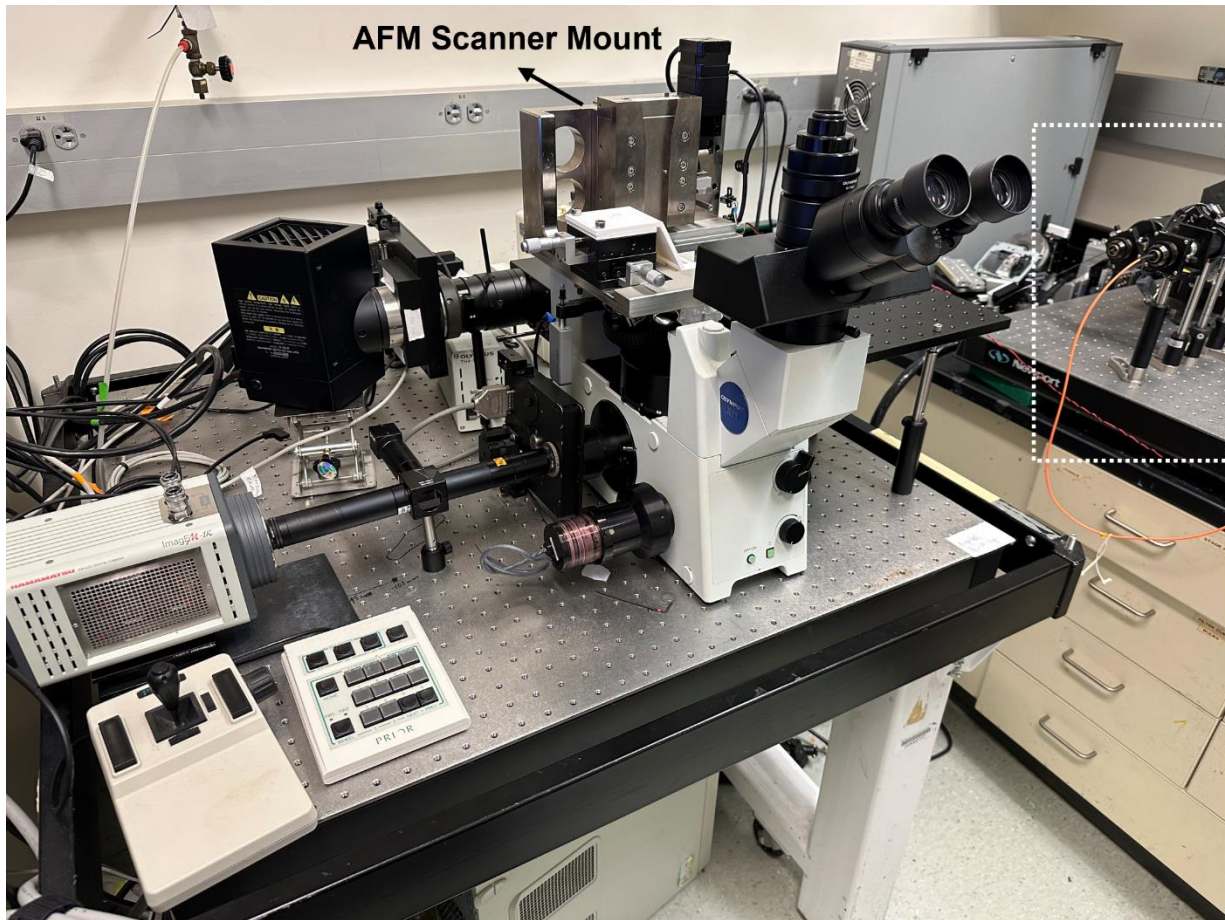
Figure 6.13 - Integrated microscopy setup. The picture displays illumination optics (white box) connected to coupling optics and sample stage and AFM scanner mount fixed on Olympus IX71 inverted fluorescence microscope. To the right of the microscope, the image collection optics consists of a split path between an EMCCD and a CMOS camera.

Figure 6.13 shows the overall integrated microscopy setup with illumination, microscope body, AFM scanner mount and image collection optics. The full setup was placed on a vibration isolation table for reduced acoustic noise coupling. The image collection could be done either via

EMCCD camera (low light conditions) or CMOS camera (for faster frame rates). Most of the collected images shown (further in the document) were collected on the EMCCD camera.
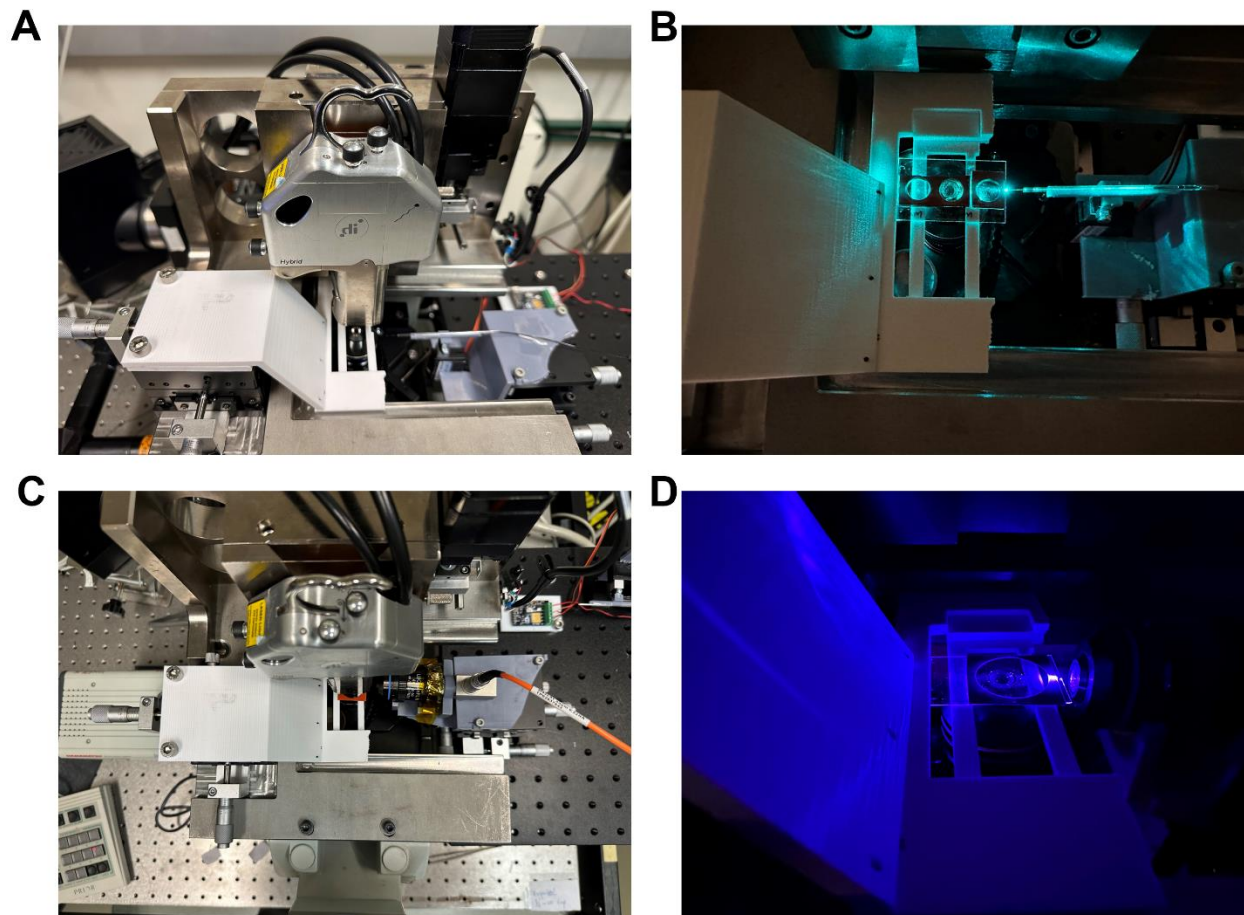
Figure 6.14 - Closeup views of AFM scanner and integrated microscopy setup. A) Combined AFM-TIRF setup with lensed fiber coupling, B) Photograph of the setup shown in A with illumination on, C) Combined AFM-TIRF system with objective lens based coupling and D) Photograph of the setup shown in C with illumination on.

Figure 6.14 shows closeup views of the integrated AFM-TIRF system in both modes of illumination, with 6.14A and B corresponding to lensed fiber-based illumination and Figure 6.14C and D corresponding to objective lens based coupling. The overall setup for both modes of illumination are similar and the modes of illumination can be toggled between either modes by a simple swap of the illumination mounts shown in Figure 6.7 and Figure 6.8 respectively.

6.3.1 TIRF Imaging of fluorescent beads

We first verified the functionality of the TIRF system by imaging 100nm diameter fluorescently labeled polystyrene beads (Tetraspeck beads, Invitrogen) immobilized on high refractive index coverslips made of SF-11 material (R.I = 1.74). A 100x dilution of the beads was drop casted on a freshly cleaned coverslip and dried. The critical angle of TIR for the coverslip-air interface was calculated to be ~35°. The green emission fluorescence (emission λ = 517nm) channel was used for image collection with illumination from the 450nm blue laser. In all cases a 60x water immersion objective was used to collect the generated fluorescence signal.
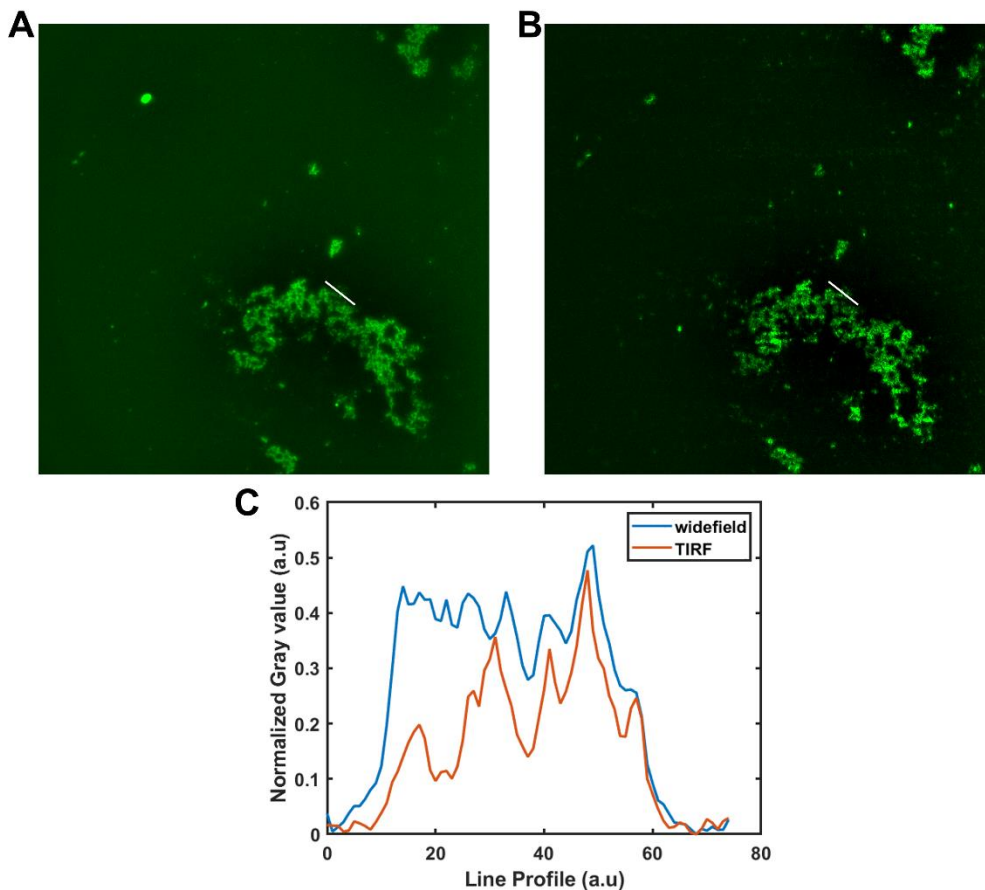
Figure 6.15 - TIRFM imaging of 100nm beads with lensed fiber illumination. A) Widefield fluorescence (excited from integrated Xe lamp), B) TIRFM image of the same area in A, C) Normalized Intensity profiles of the white lines drawn in A and B. Image size = 1024x1024 pixels, 216nm pixel size.

From figure 6.15B, it can be observed that the lensed fiber based TIRF system faithfully

reproduces the arrangement of beads as observed from widefield illumination (Figure 6.15A).

Figure 6.15C shows a section profile of the white line drawn in panel A and B. It is clear that the

background fluorescence in widefield illumination masks some of the features (Figure 6.15C, blue

line) and these features appear with a comparatively higher signal to noise ratio in the TIRFM

image (Figure 6.15C, orange line).
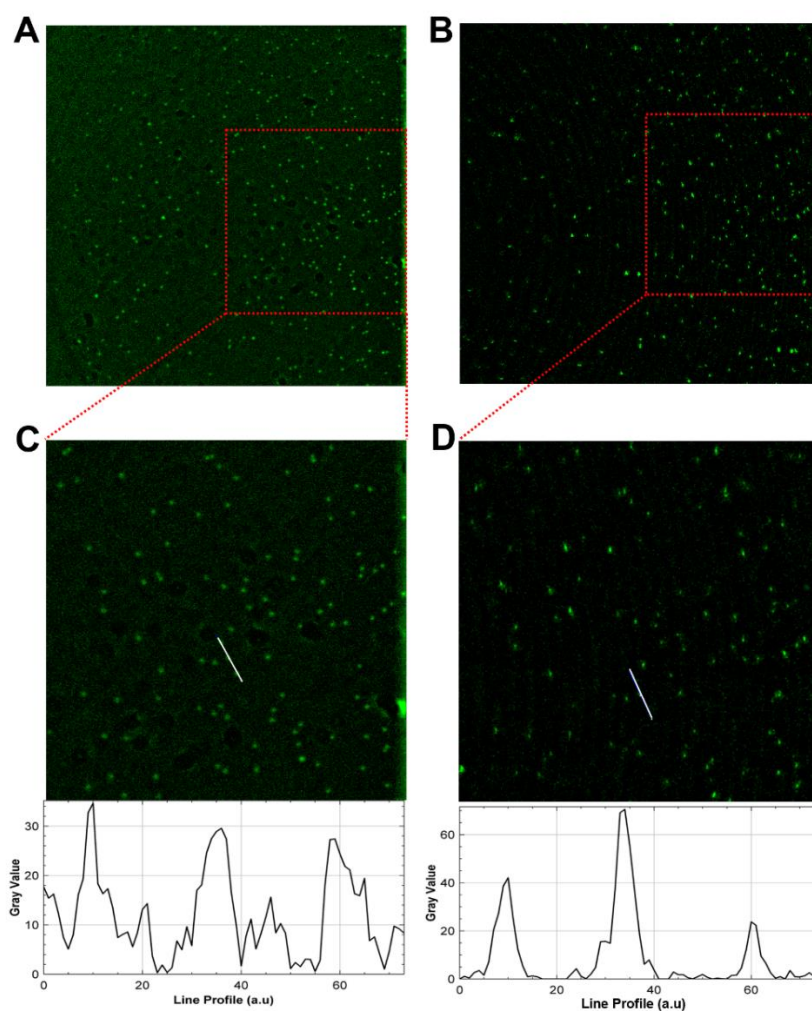
Figure 6.16 - Comparison of widefield and TIRM imaging of 500nm diameter beads in 0.01% FITC solution. A) Widefield image, B) TIRFM image of the same area as in A, C) Zoomed in view of the red box drawn in A, D) Zoomed in view of the corresponding red box drawn in B. In both C and D, the white line is drawn to obtain a intensity section profile, which are shown below each panel. Image size = 1024x1024 pixels, 216nm pixel size.

Figure 6.16 shows fluorescence imaging comparison of widefield and lensed fiber TIRFM approaches for 500nm diameter polystyrene beads immobilized on SF-11 coverslip surface, with 0.01% solution of FITC dye (in 1X PBS) and imaged using the green channel filters (excitation = 450nm and emission = 517nm). Panel A shows the widefield image with significant background pollution visible and panel B, shows the TIRFM image of the same area with comparatively lower background signal. Panels C and D respectively, show a zoomed in view (red boxes) with the intensity profiles (of the white lines) displayed below them. It is quite evident that the signal to noise ratio is reduced in the case of widefield excitation and is substantially higher in the case of TIRF excitation. The figures also display a contrasting difference in the diameter of the structures imaged, with widefield excitation showing almost fully circular beads of 500nm diameter and the TIRF excitation shows the same structures with smaller diameter. This is due to the penetration depth of the evanescent field created under TIRF excitation selectively excites in the region <250nm from the coverslip surface.

6.3.2 TIRF imaging of B103 cells

After validating the TIRF excitation on fluorescent beads, we next imaged B103 neuroblastoma cells fixed on SF-11 coverslips. After the cells were grown on coverslips, they were fixed in 3.5% paraformaldehyde, permeabilized with 0.1% TritonX and subsequently labeled with Alexa488 Phalloidin (Biotium or Invitrogen) stain which targets the actin filaments in the cell cytoskeleton. B103 cells, in general display globular morphology (nucleus region) with neurite growth and elongation. In some areas, growth of the cells can occur in clusters and piled on top of each other.
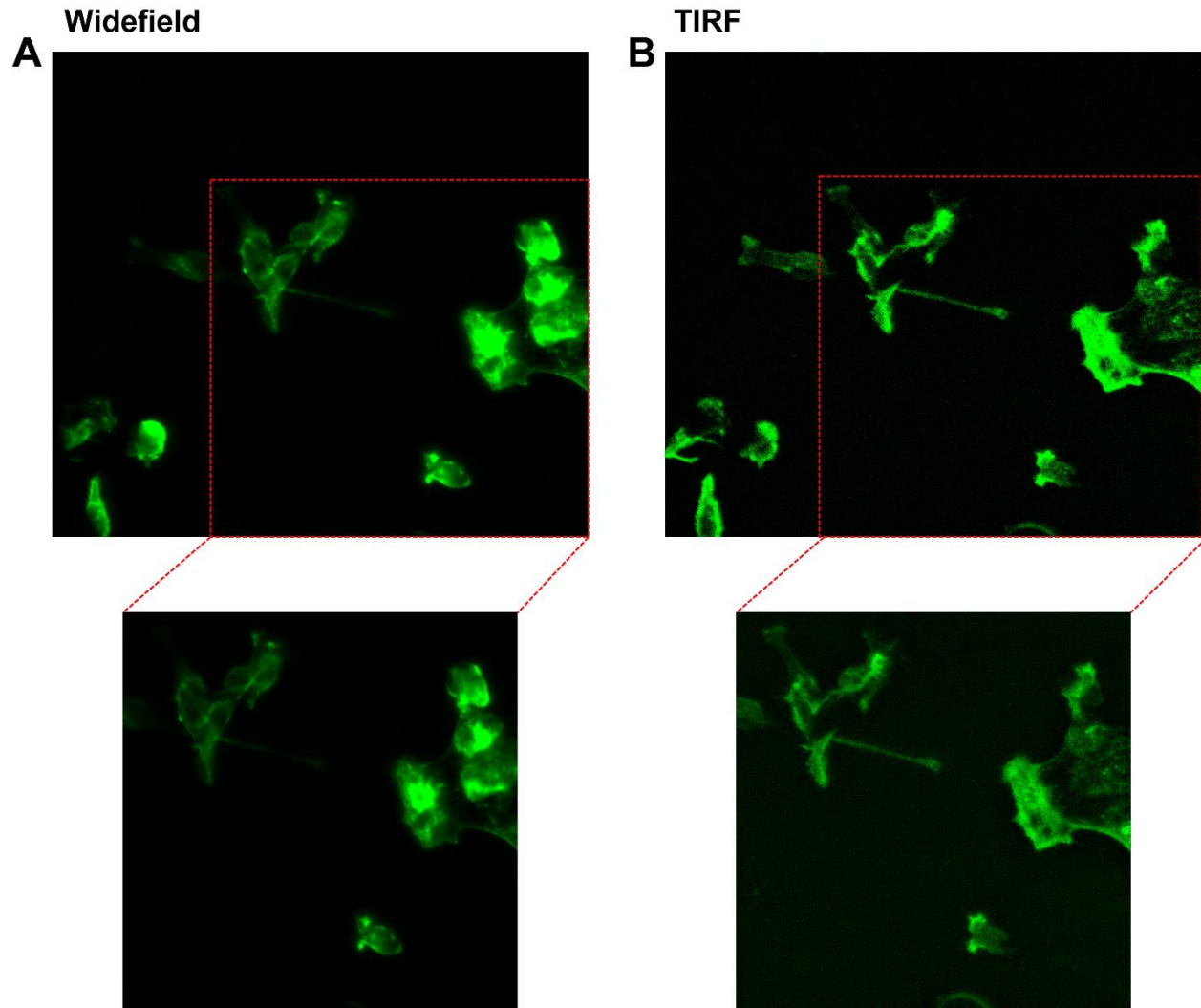
Figure 6.17 - Comparison of Widefield and TIRFM imaging of B103 Neuroblastoma cells. A) Widefield excitation and B) lensed fiber TIRF excitation

Figure 6.17 shows the AF488-Phalloidin channel (green) of B103 cells under widefield and TIRF excitation. From Figure 6.17A and the zoomed in view below (marked in red box), it can be observed that due to high z-dimensions of the cells near the nuclear region, the fluorescence signal is fully overwhelming and cytoskeletal details are not visible. Figure 6.17B and the zoomed in view below (red box) show the same imaging area in A with much higher surface level details. Neurite outgrowth and cytoskeletal features are much more apparent and can be easily distinguished from the corresponding widefield image. In comparison to panel A, the features

are not overwhelmed by the fluorescence signal from other cellular components along the z-direction.

The overall mechanical stability of the system needs to be improved for lower noise in AFM imaging. Currently, due to high degree of acoustic noise coupling, the AFM subsystem can achieve a height noise level of 1.8 - 2nm, which is considerably high for high resolution AFM and combined AFM-TIRF imaging. Conventional optical table vibration isolation methods have been problematic for AFM imaging and more advanced noise isolation methods such as active noise isolation can be applied for greater control over height noise. Once the mechanical noise problem is countered, automated synchronization of pixels generated by AFM and fluorescence imaging can be performed (software level) for improvising localization of the specimen features via both imaging methods. This approach can be useful in the development of combined AFM and super resolution fluorescence in the future.

6.4 Conclusion

In this chapter, we demonstrated the design and development of the AFM-TIRF combined microscopy system. Laser illumination scheme and light coupling via two independent mechanisms (fiber coupling and objective lens coupling) offer a high degree of flexibility and convenience in imaging. The system offers high temporal resolution and specificity via fluorescence imaging and high spatial resolution via AFM imaging. The system is also capable of performing localization based super resolution fluorescence imaging with minor modifications. Future studies of membrane-protein interaction, such as protein diffusion-based oligomerization, real time tracking of amyloid growth in membrane environments with nanomechanical mapping can greatly benefit from the implemented AFM-TIRF imaging system.

Bibliography

[1]   "CDC-Alzheimers,"   [Online].   Available: https://www.cdc.gov/aging/aginginfo/alzheimers.htm#:~:text=Alzheimer's%20disease%20is%20the%20most,thought%2C%20memory%2C%20and%20language.

[2]   "wikipedia - AD," [Online]. Available: https://en.wikipedia.org/wiki/Alzheimer%27s_disease# .

[3]   Keith A. Johnson, , Nick C. Fox, Reisa A. Sperling, William E. Klunk, "Brain Imaging in Alzheimer Disease," *Cold Spring Harbor Perspectives in Medicine,* vol. April, no. 2(4), 2012.

[4]   Zeinab Breijyeh, Rafik Karaman, "Comprehensive Review on Alzheimer's Disease: Causes and Treatment," *Molecules,* vol. 25, no. 5789, 2020.

[5]   "Alz org - what is AD," [Online]. Available: https://www.alz.org/alzheimers-dementia/what-is-alzheimers. [Accessed March 2023].

[6]   "NIA - AD fact sheet," [Online]. Available: https://www.nia.nih.gov/health/alzheimers-disease-fact-sheet. [Accessed March 2023].

[7]   Jefferson W. Kinneya, Shane M. Bemiller, Andrew S. Murtishaw, Amanda M. Leisgang, Arnold M. Salazar, Bruce T. Lamb, "Inflammation as a central mechanism in Alzheimer's disease," *Alzheimer's& Dementia: Translational Research & Clinical Interventions,* vol. 4, pp. 575-590, 2018.

[8]   Christiane Reitz, Ekaterina Rogaeva, Gary W. Beecham, "Late-onset vs nonmendelian early-onset Alzheimer disease A distinction without a difference?," *Neurology Genetics,* vol. 6(5), 2020.

[9]   Paul T Francis, Alan M Palmer, Michael Snape, Gordon K Wilcock, "The cholinergic hypothesis of Alzheimer's disease: a review of progress," *Journal of Neurology Neurosurgery Psychiatry,* vol. 66, pp. 137-147, 1999.

[10]   John Hardy, David Allsop, "Amyloid deposition as the central event in the aetiology of Alzheimer's disease," *Trends in Pharmacological Sciences,* vol. 12, pp. 383-388, 1991.

[11]   Konrad Beyreuther, Colin L. Masters, "Amyloid Precursor Protein (APP) and f3A4 Amyloid in the Etiology of Alzheimer's Disease: Precursor- Product Relationships in the Derangement of Neuronal Function," *Brain Pathology,* vol. 1, pp. 241-251, 1991.

[12]   John A Hardy, Gerald A Higgins, "Alzheimer's Disease: The Amyloid Cascade Hypothesis," *Science,* vol. 256, no. 5054, pp. 184-185, 1992.

[13]   Selkoe, Dennis J, "The molecular Pathology of Alzheimer's Disease," *Neuron,* vol. 6, pp. 487-498, 1991.

[14] Karie N. Dahlgren, Arlene M. Manelli, W. Blaine Stine, Jr., Lorinda K. Baker, Grant A. Krafft, Mary Jo LaDu, "Oligomeric and Fibrillar Species of Amyloid-Beta Peptides Differentially Affect Neuronal Viability," *The journal of biological chemistry,* vol. 277, no. 35, p. 32046–32053, 2002.

[15] Jun Wang, Dennis W. Dickson, John Q. Trojanowski, Virginia M.-Y. Lee, "The Levels of Soluble versus Insoluble Brain Ab Distinguish Alzheimer's Disease from Normal and Pathologic Aging," *Experimental Neurology,* vol. 158, pp. 328-337, 1999.

[16] Kirsten L. Viola, William L. Klein, "Amyloid β oligomers in Alzheimer's disease pathogenesis, treatment, and diagnosis," *Acta Neuropathol,* pp. 183-206, 2015.

[17] M. P. Lambert, A. K. Barlow, B. A. Chromy, C. Edwards ,R.Freed, M. Liosatos, T. E. Morgan,I. Rozovsky,B.Trommer, K.L.Viola, P. Wals, C.Zhang, C. E. Finch, G.A.Krafft, W. L. Klein, "Diffusible, nonfibrillar ligands derived from Ab1– 42 are potentcentral nervous system neurotoxins," *Proc. Natl. Acad. Sci. USA,* vol. 95, pp. 6448-6453, 1998.

[18] Jacques Fantini, Henri Chahinian, Nouara Yahi, *Protein Science,* pp. 1748-1759, 2020.

[19] Erika N. Cline, Ma´ıra Assunc¸ao Bicca, Kirsten L. Viola, William L. Klein, "The Amyloid-beta Oligomer Hypothesis: Beginning of the Third Decade," *Journal of Alzheimer's Disease,* vol. 64, pp. S567-S610, 2018.

[20] Peter T. Nelson, MD, PhD, Irina Alafuzoff, MD, PhD, Eileen H. Bigio, MD, Constantin Bouras, MD,, "Correlation of Alzheimer Disease Neuropathologic Changes With Cognitive Status: A review of the literature," *J Neuropathol Exp Neurol,* vol. 71, no. 5, pp. 362-381, 2012.

[21] C. Duyckaerts, M. Bennecib, Y. Grignon,T. Uchihara, Y. He, F. Piette, J.-J. Hauw, "Modeling the Relation Between Neurofibrillary Tangles and Intellectual Status," *Neurobiology of Aging,* vol. 18, no. 3, pp. 267-273, 1997.

[22] P. Giannakopoulos, F. R. Herrmann, T. Bussière, C. Bouras, E. Kövari, D. P. Perl, J. H. Morrison, G. Gold, P. R. Hof, "Tangle and neuron numbers, but not amyloid load, predict cognitive status in Alzheimer's disease," *Neurology,* vol. 60, no. 9, 2003.

[23] Heiko Braak, Kelly Del Tredici, Neuroanatomy and Pathology of Sporadic Alzheimer's Disease, Springer, 2015.

[24] C.-X. Gong, K. Iqbal, "Hyperphosphorylation of Microtubule-Associated Protein Tau: A Promising Therapeutic Target for Alzheimer Disease," *Current Medicinal Chemistry,* vol. 15, no. 23, pp. 2321-2328, 2008.

[25] Mohandas. E, Rajmohan. V, Raghunath. B, "Neurobiology of Alzheimer's disease," *Indian Journal of Psychiatry,* vol. 51, no. 1, pp. 55-61, 2009.

[26] Lujia Zhou, Joseph McInnes, Keimpe Wierda, Matthew Holt, Abigail G. Herrmann, Rosemary J. Jackson, Yu-Chun Wang, Jef Swerts, Jelle Beyens, Katarzyna Miskiewicz, Sven Vilain, Ilse

Dewachter, Diederik Moechars, Bart De Strooper, Tara L. Spires-Jones, Joris, "Tau association with synaptic vesicles causes presynaptic dysfunction," *Nature Communications,* vol. 8, 2017.

[27] Fuyuki Kametani, Masato Hasegawa, "Reconsideration of Amyloid Hypothesis and Tau Hypothesis in Alzheimer's Disease," *Frontiers in Neuroscience,* vol. 12, 2018.

[28] Jefferson W. Kinneya, Shane M. Bemiller, Andrew S. Murtishaw, Amanda M. Leisgang, Arnold M. Salazar, Bruce T. Lamb, "Inflammation as a central mechanism in Alzheimer's disease," */ Alzheimer's & Dementia: Translational Research & Clinical Interventions,* vol. 4, pp. 575-590, 2018.

[29] Markesbery, William R., "oxidative stress hypothesis in alzheimer's disease," *Free Radical Biology & Medicine,* pp. 134-147, 1997.

[30] Charles E. Seaks, Donna M. Wilcock, "Infectious hypothesis of Alzheimer disease," *PLOS Pathogens,* vol. 16, no. 11, 2020.

[31] Yan Liu, Michel Nguyen, Anne Robert, Bernard Meunier, "Metal Ions in Alzheimer's Disease: A Key Role or Not?," *Acc. Chem. Res,* vol. 52, pp. 2026-2035, 2019.

[32] Fan Liu, Zhuo Zhang, Lin Zhang, Ruo-Ni Meng, Jia Gao, Ming Jin, Ming Li, Xiao-Peng Wang, "Effect of metal ions on Alzheimer's disease," *Brain and Behavior,* vol. 12, 2021.

[33] Guo-fang Chen, Ting-hai Xu, Yan Yan, Yu-ren Zhou, Yi Jiang, Karsten Melcher, H Eric Xu, "Amyloid beta: structure, biology and structure-based therapeutic development," *Acta Pharmacologica Sinica,* pp. 1205-1235, 2017.

[34] Richard J. O'Brien, Philip C. Wong, "Amyloid Precursor Protein Processing and Alzheimer's Disease," *Annu. Rev. Neurosci,* vol. 34, pp. 185-204, 2011.

[35] David S. Knopman, Helene Amieva, Ronald C. Petersen, Gäel Chételat, David M. Holtzman, Bradley T. Hyman, Ralph A. Nixon, David T. Jones, "Alzheimer disease," *NATURE REVIEWS | Disease Primers,* 2021.

[36] Selkoe, Dennis J, "normal and abnormal biology of the beta-amyloid precursor protein," *Ann. Rev. Neurosci,* vol. 17, pp. 489-517, 1994.

[37] Jing Zhao, Xinyue Liu, Weiming Xia, Yingkai Zhang, Chunyu Wang, "Targeting Amyloidogenic Processing of APP in Alzheimer's Disease," *Frontiers in Molecular Neuroscience,* vol. 13, 2020.

[38] Arun K Ghosh, Margherita Brindisi, Jordan Tang, "Developing beta-secretase inhibitors for treatment of Alzheimer's disease," *Journal of Neurochemistry,* vol. 120, pp. 71-83, 2012.

[39] Hamley, I. W., "The Amyloid Beta Peptide: A Chemist's Perspective. Role in Alzheimer's and Fibrillization," *Chemical Reviews,* vol. 112, pp. 5147-5192, 2012.

[40] Alex E. Roher, Jerome Baudry, Michael O. Chaney, Yu-Min Kuo, W. Blaine Stine, Mark R. Emmerling, "Oligomerization and ¢bril assembly of the amyloid-beta protein," *Biochimica et Biophysica Acta,* vol. 1502, pp. 31-43, 2000.

[41] Harald Hampel, John Hardy, Kaj Blennow, Christopher Chen, George Perry, Seung Hyun Kim, Victor L. Villemagne, Paul Aisen, Michele Vendruscolo, Takeshi Iwatsubo, Colin L. Masters, Min Cho, Lars Lannfelt, Jeffrey L. Cummings, Andrea Vergallo, "The Amyloid-β Pathway in Alzheimer's Disease," *Nature Molecular Psychiatry,* vol. 26, pp. 5481-5503, 2021.

[42] Mattias Tornquist, Thomas C. T. Michaels, Kalyani Sanagavarapu, Xiaoting Yang, Georg Meisl, Samuel I. A. Cohen,Tuomas P. J. Knowles, Sara Linse, "Secondary nucleation in amyloid formation," *Chem. Commun,* pp. 8667-8684, 2018.

[43] Riek, Roland, "The Three-Dimensional Structures of Amyloids," *Cold Spring Harb Perspect Biol,* vol. 9, 2017.

[44] Timo Eichner, Sheena E Radford, "A Diversity of Assembly Mechanisms of a Generic Amyloid Fold," *Molecular Cell,* 2011.

[45] Matthew G. Iadanza, Matthew P. Jackson, Eric W. Hewitt, Neil A. Ranson, Sheena E. Radford, "A new era for understanding amyloid structures and disease," *NATure RevIewS | MolEculAR CEll Biology,* vol. 19, 2018.

[46] Ujjayini Ghosh, Kent R. Thurber, Wai-Ming Yau, Robert Tycko, "Molecular structure of a prevalent amyloid-β fibril polymorph from Alzheimer's disease brain tissue," *Proceedings of the National Academy of the Sciences,* vol. 118, 2021.

[47] Jun-Xia Lu, Wei Qiang, Wai-Ming Yau, Charles D. Schwieters, Stephen C. Meredith, Robert Tycko, "Molecular Structure of beta-Amyloid Fibrils in Alzheimer's Disease Brain Tissue," *Cell,* vol. 154, pp. 1257-1268, 2013.

[48] Thorsten Lührs, Christiane Ritter, Marc Adrian, Dominique Riek-Loher, Bernd Bohrmann, Heinz Döbeli, David Schubert, Roland Riek, "3D structure of Alzheimer's amyloid-β(1–42) fibrils," *Proceedings of the National Academy of Sciences,* vol. 102, pp. 17342-17347, 2005.

[49] Lothar Gremer, Daniel Schölzel,Carla Schenk,Elke Reinartz,Jörg Labahn, Raimond B. G. Ravelli, Markus Tusche,Carmen Lopez-Iglesias,Wolfgang Hoyer, Henrike Heise,Dieter Willbold, Gunnar F. Schröder, "Fibril structure of amyloid-b(1–42)by cryo–electron microscopy," *Science,* vol. 358, pp. 116-119, 2017.

[50] Tycko, Robert, "Amyloid Polymorphism: Structural Basis and Neurobiological Relevance," *Neuron,* vol. 86, 2015.

[51] Marcus Fändrich, Jessica Meinhardt, Nikolaus Grigorieff, "Structural polymorphism of Alzheimer Aβ and other amyloid fibrils," *Prion,* pp. 89-93, 2009.

[52] Aneta T. Petkova, Richard D. Leapman, Zhihong Guo, Wai-Ming Yau, Mark P. Mattson, Robert Tycko, "Self-Propagating, Molecular-LevelPolymorphism in Alzheimer'sb-Amyloid Fibrils," *Science,* vol. 307, 2005.

[53] Iryna Benilova, Eric Karran, Bart De Strooper, "The toxic Aβ oligomer and Alzheimer's disease: an emperor in need of clothes," *Nature Neuroscience,* vol. 15, pp. 349-357, 2012.

[54] Sergio T. Ferreira, William L. Klein, "The Abeta oligomer hypothesis for synapse failure and memory loss in Alzheimer's," *Neurobiology of Learning and Memory,* vol. 96, pp. 529-543, 2011.

[55] Masafumi Sakono, Tamotsu Zako, "Amyloid oligomers: formation and toxicity of Aboligomers," *The FEBS Journal,* 2010.

[56] Yao Tian, Ruina Liang, Amit Kumar, Piotr Szwedziak, John H. Viles, "3D-visualization of amyloid-β oligomer interactions with lipid membranes by cryo-electron tomography," *Chemical Science,* no. 20, 2021.

[57] Kenji Sasahara, Kenichi Morigaki, Kyoko Shinya, "Effects of membrane interaction and aggregation of amyloid β-peptide on lipid mobility and membrane domain structure," *Physical Chemistry Chemical Physics,* no. 23, 2013.

[58] Hai Lin, Rajinder Bhatia, Ratneshwar Lal, "Amyloid β protein forms ion channels: implications for Alzheimer's disease pathophysiology," *The FASEB Journal,* 2001.

[59] Nelson Arispe, Eduardo Rojas,Harvey B. Pollard, "Alzheimer disease amyloid-beta protein forms calcium channels in bilayer membranes: Blockade by tromethamine and aluminum," *Proc.Nati.Acad.Sci.USA,* vol. 90, pp. 567-571, 1993.

[60] Heledd H. Jarosz-Griffiths, Elizabeth Noble, Jo V. Rushworth, Nigel M. Hooper, "Amyloid-β Receptors: The Good, the Bad, and the Prion Protein," *Journal of Biological Chemistry,* vol. 291, no. 7, pp. 3174-3183, 2016.

[61] David Balchin, Manajit Hayer-Hartl, F. Ulrich Hartl, "In vivo aspects of protein folding and quality control," *Science,* vol. 353, no. 6294, 2016.

[62] N Arispe, H B Pollard, E Rojas, "Giant multilevel cation channels formed by Alzheimer disease amyloid beta-protein [A beta P-(1-40)] in bilayer membranes.," *Proc. Natl. Acad. Sci. USA,* vol. 90, pp. 10573-10577, 1993.

[63] M. Kawahara, N. Arispe, Y. Kuroda, and E. Rojas, "Alzheimer's Disease Amyloid (8-Protein Forms Zn2+-Sensitive, Cation-Selective Channels Across Excised Membrane Patches from Hypothalamic Neurons," *Biophysical Journal,* vol. 73, pp. 67-75, 1997.

[64] Meng-chin Allison Lin, Bruce L Kagan, "Electrophysiologic properties of channels induced by Aβ25–35 in planar lipid bilayers," *Peptides,* vol. 23, no. 7, pp. 1215-1228, 2002.

[65] Yutaka Hirakura, Wendy W Yiu, Andrew Yamamoto, Bruce L Kagan, "Amyloid peptide channels: blockade by zinc and inhibition by Congo red," *Amyloid,* vol. 7, no. 3, pp. 194-199, 2000.

[66] Arjan Quist, Ivo Doudevski, Hai Lin, Rushana Azimova, Douglas Ng, Blas Frangione, Bruce Kagan, Jorge Ghiso, Ratnesh Lal, "Amyloid ion channels: A common structural link for protein-misfolding disease," *Proc. Natl. Acad. Sci. USA,* vol. 102, pp. 10427-10432, 2005.

[67] Hilal A. Lashuel, Dean Hartley, Benjamin M. Petre, Thomas Walz & Peter T. Lansbury Jr, "Amyloid pores from pathogenic mutations," *Nature,* vol. 418, 2002.

[68] Jang H, Connelly L, Arce FT, Ramachandran S, Kagan BL, Lal R, "Mechanisms for the Insertion of Toxic, Fibril-like β-Amyloid Oligomers into the Membrane," *J Chem Theory Comput,* vol. 9, 2013.

[69] Connelly L, Jang H, Teran Arce F, Ramachandran S, Kagan BL, Nussinov R, Lal R, "Effects of Point Substitutions on the Structure of Toxic Alzheimer's β-Amyloid Channels: Atomic Force Microscopy and Molecular Dynamics Simulations," *Biochemistry,* vol. 51, pp. 3031-3038, 2012.

[70] Connelly L, Jang H, Teran Arce F, Capone R, Kotler SA, Ramachandran S, Kagan BL, Nussinov R, Lal R, "Atomic Force Microscopy and MD Simulations Reveal Pore-Like Structures of All-d-Enantiomer of Alzheimer's β-Amyloid Peptide: Relevance to the Ion Channel Mechanism of AD Pathology," *J Phys Chem B,* vol. 11, pp. 1728-1735, 2012.

[71] E. L. Ilya Levental, "Regulation of membrane protein structure and function by their lipid nano-environment," *Nature Reviews Molecular Cell Biology,* vol. 24, pp. 107-122, 2023.

[72] Elizabeth S. Haswell, Rob Phillips, Douglas C. Rees, "Mechanosensitive channels: what can they do and how do they do it?," *Structure,* vol. 19, pp. 1356-1369, 2012.

[73] Eduardo Perozo, Douglas C Rees , "Structure and mechanism in prokaryotic mechanosensitive channels," *Current Opinion in Structural Biology,* vol. 13, pp. 432-442, 2003.

[74] Avia Rosenhouse-Dantsker,Dolly Mehta, Irena Levitan, "Regulation of Ion Channels by Membrane Lipids," *Comprehensive Physiology,* vol. 2, 2012.

[75] Anna L. Duncan, Wanling Song, Mark S.P. Sansom, "Lipid-Dependent Regulation of Ion Channels and GProtein–Coupled Receptors:Insights from Structures and Simulations," *Annual Review of Pharmacology and Toxicology,* vol. 60, pp. 31-50, 2020.

[76] Linda J. Pike, "Lipid rafts: bringing order to chaos," *Journal of Lipid Research,* vol. 44, pp. 655-667, 2003.

[77] John A. Allen, Robyn A. Halverson-Tamboli & Mark M. Rasenick, "Lipid raft microdomains and neurotransmitter signalling," *Nature Reviews Neuroscience ,* vol. 8, pp. 128-140, 2007.

[78] Pontes B., Monzo P., Gole L., Le Roux A.-L., Kosmalska A.J., Tam Z.Y., Luo W., Kan S., Viasnoff V., Roca-Cusachs P., "Membrane tension controls adhesion positioning at the leading edge of cells," *J Cell Biol.,* vol. 216, pp. 2959-2977, 2017.

[79] Hetmanski J.H.R., de Belly H., Busnelli I., Waring T., Nair R.V., Sokleva V., Dobre O., Cameron A., Gauthier N., Lamaze C., "Membrane tension orchestrates rear retraction in matrix-directed cell migration.," *Dev Cell.,* vol. 51, pp. 460-475, 2019.

[80] Jophin G Joseph, Allen P Liu, "Mechanical Regulation of Endocytosis: New Insights and Recent Advances," *Adv Biosyst,* vol. 4, 2020.

[81] Ewa Sitarskaa, Alba Diz-Muñoz, "Pay attention to membrane tension: Mechanobiology of the cell surface," *Curr Opin Cell Biol.,* vol. 66, pp. 11-18, 2020.

[82] Donald E Ingber , "Mechanobiology and diseases of mechanotransduction," *Ann Med,* vol. 35, pp. 564-577, 2003.

[83] G. Binnig, H. Rohrer, Ch. Gerber, and E. Weibel, "Surface Studies by Scanning Tunneling Microscopy," *Phys. Rev. Lett.,* vol. 49, 1982.

[84] G. Binnig, H. Rohrer, "Scanning tunneling microscopy," *Surface Science,* vol. 126, pp. 236-244, 1983.

[85] G. Binnig, C. F. Quate, and Ch. Gerber, "Atomic Force Microscope," *Phys. Rev. Lett.,* vol. 56, 1986.

[86] A Engel, D J Muller, "Observing single biomolecules at work with the atomic force ¨," *Nature structural biology,* vol. 7, no. 9, pp. 715-718, 2000.

[87] Yves F. Dufrêne, Toshio Ando, Ricardo Garcia, David Alsteens, David Martinez-Martin, Andreas Engel, Christoph Gerber, Daniel J. Müller, "Imaging modes of atomic force microscopy for application in molecular and cell biology," *Nature Nanotechnology,* 2017.

[88] Daniel J. Müller, Andra C. Dumitru, Cristina Lo Giudice, Hermann E. Gaub, Peter Hinterdorfer, Gerhard Hummer, James J. De Yoreo, Yves F. Dufrêne, David Alsteens, "Atomic Force Microscopy-Based Force Spectroscopy and Multiparametric Imaging of Biomolecular and Cellular Systems," *Chem. Rev.,* vol. 121, pp. 11701-11725, 2021.

[89] Thorsten Hugel, Markus Seitz, "The Study of Molecular Interactions by AFM Force Spectroscopy," *Macromol. Rapid Commun.,* vol. 22, pp. 989-1016, 2001.

[90] Richard D. Piner, Jin Zhu, Feng Xu, Seunghun Hong, Chad A. Mirkin, ""Dip-Pen" Nanolithography," *Science,* vol. 283, 1999.

[91] Toshio Ando, Takayuki Uchihashi, Noriyuki Kodera, "High-Speed AFM and Applications to Biomolecular Systems," *Annual Review of Biophysics,* vol. 42, pp. 393-414, 2013.

[92] Peter Markiewicz, M. Cynthia Goh, "Atomic force microscope tip deconvolution using calibration arrays," *Review of Scientific Instruments,* vol. 66, 1995.

[93] Erwin Neher, Bert Sakmann, "Single-channel currents recorded from membrane of denervated frog muscle fibres," *Nature,* vol. 260, pp. 799-802, 1976.

[94] O. P. Hamill, A. Marty, E. Neher, B. Sakmann & F. J. Sigworth, "Improved patch-clamp techniques for high-resolution current recording from cells and cell-free membrane patches," *Pflfigers Arch,* vol. 391, pp. 85-100, 1981.

[95] Zakharian, E., Recording of Ion Channel Activity in Planar Lipid Bilayer Experiments, Springer Science+Business Media, LLC, 2013.

[96] Bert Sakmann, Erwin Neher, Single-Channel Recording, Springer, 1995.

[97] Pankaj D Mehta, Tuula Pirttila, Sangita P Mehta, Eugene A Sersen, Paul S Aisen, Henryk M Wisniewski, "Plasma and Cerebrospinal fluid levels of Amyloid-beta proteins 1-40 and 1-42 in Alzheimer Disease," *Arch Neurol,* vol. 57, 2000.

[98] Martin Tolar, Susan Abushakra, John A. Hey, Anton Porsteinsson & Marwan Sabbagh, "Aducanumab, gantenerumab, BAN2401, and ALZ-801—the first wave of amyloid-targeting drugs for Alzheimer's disease with potential for near term approval," *Alzheimer's Research & Therapy,* vol. 95, 2020.

[99] Li-Kai Huang, Shu-Ping Chao, Chaur-Jong Hu, "Clinical trials of new drugs for Alzheimer disease," *J Biomed Sci.,* vol. 27, 2020.

[100] Jeff Sevigny, Ping Chiao, Thierry Bussière, Paul H. Weinreb, Leslie Williams, Marcel Maier, Omar Quintero-Mon, , Robert H. Scannevin, H. Moore Arnold, Thomas Engber, Yaming Hang, Alvydas Mikulskis, Jan Grimm, Christoph Hock, Roger M. Nitsch & Alfred Sand, "The antibody aducanumab reduces Aβ plaques in Alzheimer's disease," *Nature,* vol. 537, pp. 50-56, 2016.

[101] Hernandez A.M., Urbanke H., Gillman A., Lee J., Ryazanov S., Agbemenyah H.Y., Benito E., Jain G., Kaurani L., Grigorian G., Zweckstetter M, Benz R., Giese A., Schneider A., Korte M., Lal R., Griesinger C., Eichele G., Fischer A, "The diphenylpyrazol compound anle138b blocks Abeta channels and rescues disease phenotypes in a mouse model for amyloid pathology.," *EMBO Molecular Medicine,* vol. 10, pp. 32-47, 2018.

[102] Coralie Di Scala, Nicholas Armstrong, Henri Chahinian, Eric Chabrière, Jacques Fantini, Nouara Yahi, "AmyP53, a Therapeutic Peptide Candidate for the Treatment of Alzheimer's and Parkinson's Disease: Safety, Stability, Pharmacokinetics Parameters and Nose-to Brain Delivery," *Int J Mol Sci,* vol. 23, no. 21, 2022.

[103] Lukasz Goldschmidt, Poh K. Teng, Roland Riek, and David Eisenberg, "Identifying the amylome, proteins capable of forming amyloid-like fibrils," *Proc. Natl. Acad. Sci. USA,* vol. 107, pp. 3487-3492, 2010.

[104] Raimon Sabaté 1, Alba Espargaró, Natalia S de Groot, Juan José Valle-Delgado, Xavier Fernàndez-Busquets, Salvador Ventura, "The role of protein sequence and amino acid composition in amyloid formation: scrambling and backward reading of IAPP amyloid fibrils," *J Mol Biol,* vol. 404, pp. 337-352, 2010.

[105] Devkee M Vadukul, Oyinkansola Gbajumo, Karen E Marshall, Louise C Serpell, "Amyloidogenicity and toxicity of the reverse and scrambled variants of amyloid-β 1-42," *FEBS Lett,* vol. 591, pp. 822-830, 2017.

[106] Ian Walsh, Flavio Seno, Silvio C.E. Tosatto and Antonio Trovato, "PASTA2: An improved server for protein aggregation prediction," *Nucleic Acids Research,* vol. 42, 2014.

[107] Gillman AL, Lee J, Ramachandran S, Capone R, Gonzalez T, Wrasidlo W, Masliah E, Lal R., "Small molecule NPT-440-1 inhibits ionic flux through Aβ1–42 pores: implications for Alzheimer's disease therapeutics," *Nanomedicine: Nanotechnology, Biology, and Medicine.,* 2016.

[108] Joon Lee, Young Hun Kim, Fernando T. Arce, Alan L. Gillman, Hyunbum Jang, Bruce L. Kagan, Ruth Nussinov, Jerry Yang, Ratnesh Lal, "Amyloid β Ion Channels in a Membrane Comprising Brain Total Lipid Extracts," *ACS Chemical Neuroscience,* vol. 8, pp. 1348-1357, 2017.

[109] Ricardo Capone, Steven Blake, Marcela Rincon Restrepo, Jerry Yang, and Michael Mayer, "Designing Nanosensors Based on Charged Derivatives of Gramicidin A," *J. Am. Chem. Soc.,* vol. 129, pp. 9737-9745, 2007.

[110] Kirsten Gade Malmos, Luis M. Blancas-Mejia, Benedikt Weber, Johannes Buchner,Marina Ramirez-Alvarado, Hironobu Naiki, Daniel Otzen, "ThT 101: a primer on the use of thioflavin T to investigate amyloid formation," *AMYLOID,* vol. 24, pp. 1-16, 2017.

[111] Chung-Jung Tsai, Shuo Liang Lin, Haim J. Wolfson, Ruth Nussinov, "Studies of protein-protein interfaces: A statistical analysis of the hydrophobic effect," *Protein Science,* vol. 6, pp. 53-64, 2008.

[112] Lee, Changhoon, "ANS - a versatile fluorescent probe from protein folding study to drug design," *BioWave,* vol. 12, 2010.

[113] Oktay K. Gasymov, Ben J. Glasgow, "proteins, ANS fluorescence: Potential to augment the identification of the external binding sites of," *Biochimica et Biophysica Acta,* vol. 1774, pp. 403-411, 2007.

[114] Vitaly V. Kushnirov, Alexander A. Dergalev, Alexander I. Alexandrov, "Proteinase K resistant cores of prions and amyloids," *Prion,* vol. 14, pp. 11-19, 2020.

[115] Hedstrom, Lizbeth, "Serine Protease Mechanism and Specificity," *Chem. Rev.,* vol. 12, pp. 4501-4524, 2002.

[116] Nelson Arispe, Harvey Pollard, Eduardo Rojas, "Zn2+ interaction with Alzheimer amyloid beta portein calcium channels".

[117] Rajinder Bhatia, Hai Lin, Ratneshwar Lal, "Fresh and globular amyloidbprotein (1– 42) inducesrapid cellular degeneration: evidence for AbPchannel-mediated cellular toxicity," *The FASEB Journal,* pp. 1233-1243, 2000.

[118] Urmi Sengupta, Ashley N. Nilson, Rakez Kayed, "The Role of Amyloid-β Oligomers in Toxicity, Propagation, and Immunotherapy," *EBioMedicine,* vol. 6, pp. 42-49, 2016.

[119] Erwin Cabrera, Paul Mathews, Emiliya Mezhericher, Thomas G Beach, Jingjing Deng, Thomas A Neubert, Agueda Rostagno, Jorge Ghiso, "Aβ truncated species: Implications for brain clearance mechanisms and amyloid plaque deposition," *Biochim Biophys Acta Mol Basis Dis,* vol. 1864, pp. 208-225, 2018.

[120] Laurijssens B, Aujard F, Rahman A., "Animal models of Alzheimer's disease and drug development," *Drug Discov Today Technol,* vol. 10, 2013.

[121] Masters CL, Simms G, Weinman NA, Multhaup G, McDonald BL, Beyreuther K, "Amyloid plaque core protein in Alzheimer disease and Down syndrome," *Proc Natl Acad Sci,* vol. 82, pp. 4245-4249, 1985.

[122] Rostagno A, Holton J, Lashley T, Revesz T, Ghiso J., "Cerebral amyloidosis: amyloid subunits, mutants and phenotypes.," *Cell Mol Life Sci,* vol. 67, pp. 581-600, 2010.

[123] Portelius E, Westman-Brinkmalm A, Zetterberg H, Blennow K., "Determination of β-amyloid peptide signatures in cerebrospinal fluid using immunoprecipitation-mass spectrometry," *J Proteome Res,* vol. 5, pp. 1010-1016, 2006.

[124] Saido TC, Yamao-Harigaya W, Iwatsubo T, Kawashima S., "Amino-and carboxyl-terminal heterogeneity of β-amyloid peptides deposited in human brain," *Neurosci Lett,* vol. 215, pp. 173-176, 1996.

[125] Mar Hernandez-Guillamon, Stephanie Mawhirt, Steven Blais, Joan Montaner, Thomas A. Neubert, Agueda Rostagno, Jorge Ghiso, "Sequential Amyloid-β Degradation by the Matrix Metalloproteases MMP-2 and MMP-9," *J Biol Chem.,* vol. 290, pp. 15078-15091, 2015.

[126] Pantelopulos GA, Straub JE, Thirumalai D, Sugita Y., "Structure of APPC991–99 and implications for role of extra-membrane domains in function and oligomerization," *Biochimica et Biophysica Acta (BBA)-Biomembranes,* vol. 1860, pp. 1698-1708, 2018.

[127] Brenda D Moore, Paramita Chakrabarty, Yona Levites, Tom L Kukar, Ann-Marie Baine, Tina Moroni, Thomas B Ladd, Pritam Das, Dennis W Dickson & Todd E Golde, "Overlapping profiles of Aβ peptides in the Alzheimer's disease and pathological aging brains," *Alzheimer's Research & Therapy volume,* vol. 4, 2012.

[128] Norelle C. Wildburger, Thomas J. Esparza, Richard D. LeDuc, Ryan T. Fellers, Paul M. Thomas, Nigel J. Cairns, Neil L. Kelleher, Randall J. Bateman & David L. Brody, "Diversity of Amyloid-beta Proteoforms in the Alzheimer's Disease Brain," *Scientific Reports,* vol. 7, 2017.

[129] Rostagno A, Neubert TA, Ghiso J, "Unveiling brain Aβ heterogeneity through targeted proteomic analysis," *Amyloid Proteins,* pp. 23-43, 2018.

[130] Farron L McIntee, Patrizia Giannoni, Steven Blais, George Sommer, Thomas A Neubert, Agueda Rostagno, Jorge Ghiso, "In vivo Differential Brain Clearance and Catabolism of Monomeric and Oligomeric Alzheimer's Aβ protein," *Front Aging Neurosci,* vol. 8, 2016.

[131] Wirths O, Zampar S., "Emerging roles of N-and C-terminally truncated Aβ species in Alzheimer's disease," *Expert Opin Ther Targets,* vol. 23, pp. 991-1004, 2019.

[132] Pike CJ, Overman MJ, Cotman CW, "Amino-terminal deletions enhance aggregation of β-amyloid peptides in vitro," *J Biol Chem,* vol. 270, pp. 23895-23898, 1995.

[133] Christina E. Murray, Priya Gami-Patel, Eleni Gkanatsiou, Gunnar Brinkmalm, Erik Portelius, Oliver Wirths, Wendy Heywood, Kaj Blennow, Jorge Ghiso, Janice L. Holton, Kevin Mills, Henrik Zetterberg, Tamas Revesz & Tammaryn Lashley, "The presubiculum is preserved from neurodegenerative changes in Alzheimer's disease," *Acta Neuropathologica Communications,* vol. 6, 2018.

[134] H. Lewis, D. Beher, N. Cookson, A. Oakley, M. Piggott, C. M. Morris, E. Jaros, R. Perry, P. Ince, R. A. Kenny, C. G. Ballard, M. S. Shearman, R. N. Kalaria, "Quantification of Alzheimer pathology in ageing and dementia: age-related accumulation of amyloid-β(42) peptide in vascular dementia," *Neuropathology and Applied Neurobiology,* vol. 32, no. 2, pp. 103-118, 2006.

[135] Di Scala C, Chahinian H, Yahi N, Garmy N, Fantini J, "Interaction of Alzheimer's β-amyloid peptides with cholesterol: mechanistic insights into amyloid pore formation.," *Biochemistry,* vol. 53, pp. 4489-4502, 2014.

[136] Coralie Di Scala, Nouara Yahi, Sonia Boutemeur, Alessandra Flores, Léa Rodriguez, Henri Chahinian & Jacques Fantini, "Common molecular mechanism of amyloid pore formation by Alzheimer's β-amyloid peptide and α-synuclein," *Scientific Reports,* vol. 6, 2016.

[137] K.Yanagisawa, "Role of gangliosides in Alzheimer's disease," *Biochimica et Biophysica Acta (BBA)-Biomembranes,* vol. 1768, pp. 1943-1951, 2007.

[138] Kotler SA, Walsh P, Brender JR, Ramamoorthy A., "Differences between amyloid-β aggregation in solution and on the membrane: insights into elucidation of the mechanistic details of Alzheimer's disease.," *Chem Soc Rev,* vol. 43, pp. 6692-6700, 2014.

[139] Bikash R. Sahoo, Takuya Genjo, Michael Bekier, Sarah J. Cox, Andrea K. Stoddard, Magdalena Ivanova, Kazuma Yasuhara, Carol A. Fierke, Yanzhuang Wang, Ayyalusamy Ramamoorthy, "Alzheimer's amyloid-beta intermediates generated using polymer-nanodiscs," *Chemical Communications,* vol. 54, pp. 12883-12886, 2018.

[140] Bikash Ranjan Sahoo, Takuya Genjo, Sarah J. Cox, Andrea K. Stoddard, G.M. Anantharamaiah, Carol Fierke, Ayyalusamy Ramamoorthy, "Nanodisc-Forming Scaffold Protein Promoted Retardation of Amyloid-Beta Aggregation," *Journal of Molecular Biology,* vol. 430, no. 21, pp. 4230-4244, 2018.

[141] Korshavn KJ, Bhunia A, Limd MH, Ramamoorthy A., "Amyloid-β adopts a conserved, partially folded structure upon binding to zwitterionic lipid bilayers prior to amyloid formation," *Chem Commun (Camb),* vol. 52, pp. 882-885, 2016.

[142] Jessica Nasica-Labouze, Phuong H. Nguyen, Fabio Sterpone, Olivia Berthoumieu, Nicolae-Viorel Buchete, Sébastien Cote, John H. Viles, Tong Zhang, Chunyu Wang, Philippe Derreumaux, "Amyloid β Protein and Alzheimer's Disease: When Computer Simulations Complement Experimental Studies," *Chem. Rev.,* vol. 115, pp. 3518-3563, 2015.

[143] Sciacca MF, Kotler SA, Brender JR, Chen J, Lee D, Ramamoorthy A., "Two-step mechanism of membrane disruption by Aβ through membrane fragmentation and pore formation.," *Biophys J,* vol. 103, pp. 702-710, 2012.

[144] Demuro A, Mina E, Kayed R, Milton SC, Parker I, Glabe CG., "Calcium dysregulation and membrane disruption as a ubiquitous neurotoxic mechanism of soluble amyloid oligomers.," *J Biol Chem,* vol. 280, pp. 17294-17300, 2005.

[145] Demuro A, Smith M, Parker I., "Single-channel Ca2+ imaging implicates Aβ1–42 amyloid pores in Alzheimer's disease pathology," *J Cell Biol,* vol. 195, pp. 515-524, 2011.

[146] Sarah J Cox, Brian Lam, Ajay Prasad, Hannah A Marietta, Nicholas V Stander, Joseph G Joel, Bikash R Sahoo, Fucheng Guo, Andrea K Stoddard, Magdalena I Ivanova, Ayyalusamy Ramamoorthy, "High-Throughput Screening at the Membrane Interface Reveals Inhibitors of Amyloid-β," *Biochemistry,* vol. 59, pp. 2249-2258, 2020.

[147] S Fossati, J Cam, J Meyerson, E Mezhericher, I A Romero, P O Couraud, B B Weksler, J Ghiso, A Rostagno, "Differential activation of mitochondrial apoptotic pathways by vasculotropic amyloid-beta variants in cells composing the cerebral vessel walls," *FASEB J,* vol. 24, pp. 229-241, 2010.

[148] Todd K, Ghiso J, Rostagno A, "Oxidative stress and mitochondriamediated cell death mechanisms triggered by the familial Danish dementia ADan amyloid," *Neurobiol Dis,* vol. 85, pp. 130-143, 2016.

[149] Wei G, Shea J-E., "Effects of solvent on the structure of the Alzheimer amyloid-β (25–35) peptide.," *Biophys J,* vol. 91, pp. 1638-1647, 2006.

[150] Zhang-Haagen B, Biehl R, Nagel-Steger L, Radulescu A, Richter D, Willbold D., "Monomeric amyloid beta peptide in hexafluoroisopropanol detected by small angle neutron scattering.," *PLoS One,* vol. 11, 2016.

[151] Mirzabekov TA, Silberstein AY, Kagan BL., "Use of planar lipid bilayer membranes for rapid screening of membrane active compounds.," *Methods in enzymology.,* pp. 661-674, 1999.

[152] Todd K, Fossati S, Ghiso J, Rostagno A., "Mitochondrial dysfunction induced by a post-translationally modified amyloid linked to a familial mutation in an alternative model of

neurodegeneration.," *Biochimica et Biophysica Acta (BBA)-Molecular Basis of Disease,* vol. 1842, pp. 2457-2467, 2014.

[153] Joon Lee, Alan L. Gillman, Hyunbum Jang, Srinivasan Ramachandran, Bruce L. Kagan, "Role of the fast kinetics of pyroglutamate-modified amyloid-β oligomers in membrane binding and membrane permeability," *Biochemistry,* vol. 53, pp. 4704-4714, 2014.

[154] Alan L Gillman, Hyunbum Jang, Joon Lee, Srinivasan Ramachandran, Bruce L Kagan, Ruth Nussinov, Fernando Teran Arce, "Activity and architecture of pyroglutamate-modified amyloid-β (AβpE3-42) pores," *J Phys Chem B,* vol. 118, pp. 7335-7344, 2014.

[155] Randa Bahadi, Peter V. Farrelly, Bronwyn L. Kenna, Cyril C. Curtain, Colin L. Masters, Roberto Cappai, Kevin J. Barnham, Joseph I. Kourie, "Cu2+-induced modification of the kinetics of Aβ(1-42) channels," *Am J Physiol Cell Physiol,* vol. 285, pp. 873-880, 2003.

[156] Arispe N, Pollard HB, Rojas E., "Zn2+ interaction with Alzheimer amyloid beta protein calcium channels.," *Proc Natl Acad Sci,* vol. 93, pp. 1710-1715, 1996.

[157] Kagan B, Azimov R, Azimova R., "Amyloid peptide channels," *J Membr Biol,* vol. 202, pp. 1-10, 2004.

[158] Hirakura Y, Kagan B., "The role of amyloid peptide channels in Alzheimer and other amyloidoses.," *Einstein Quart J Biol Med,* vol. 16, 2000.

[159] Österlund N, Moons R, Ilag LL, Sobott F, Gräslund A., "Native ion mobility-mass spectrometry reveals the formation of β-barrel shaped amyloid-β hexamers in a membrane-mimicking environment.," *J Am Chem Soc,* vol. 141, pp. 10440-10450, 2019.

[160] Hyunbum Jang, Fernando Teran Arce, Srinivasan Ramachandran, Ricardo Capone, Rushana Azimova, Bruce L Kagan, Ruth Nussinov, Ratnesh Lal, "Truncated beta-amyloid peptide channels provide an alternative mechanism for Alzheimer's Disease and Down syndrome," *Proc Natl Acad Sci U S A,* vol. 107, pp. 6538-6543, 2010.

[161] Arce FT, Jang H, Ramachandran S, Landon PB, Nussinov R, Lal R., "Polymorphism of amyloid β peptide in different environments: implications for membrane insertion and pore formation.," *Soft Matter,* vol. 7, pp. 5267-5273, 2011.

[162] T Mirzabekov, M C Lin, W L Yuan, P J Marshall, M Carman, K Tomaselli, I Lieberburg, B L Kagan, "Channel formation in planar lipid bilayers by a neurotoxic fragment of the beta-amyloid peptide," *Biochem Biophys Res Commun,* vol. 202, pp. 1142-1148, 1994.

[163] Lin MA, Kagan BL., "Electrophysiologic properties of channels induced by Aβ25–35 in planar lipid bilayers," *Peptides,* vol. 23, pp. 1215-1228, 2002.

[164] Hirakura Y, Lin M, Kagan BL., "Alzheimer amyloid Aβ1–42 channels: effects of solvent, pH, and Congo Red.," *J Neurosci Res,* vol. 57, pp. 458-466, 1999.

[165] Jessica L Wittnam 1, Erik Portelius, Henrik Zetterberg, Mikael K Gustavsson, Stephan Schilling, Birgit Koch, Hans-Ulrich Demuth, Kaj Blennow, Oliver Wirths, Thomas A Bayer, "Pyroglutamate amyloid β (Aβ) aggravates behavioral deficits in transgenic amyloid mouse model for Alzheimer disease," *J Biol Chem,* vol. 287, pp. 8154-8162, 2012.

[166] Hardy J, Selkoe DJ., "The amyloid hypothesis of Alzheimer's disease: progress and problems on the road to therapeutics," *Science,* vol. 297, pp. 353-356, 2002.

[167] Rostagno A, Lal R, Ghiso J., "Protein misfolding, aggregation, and fibril formation: common features of cerebral and non-cerebral amyloidosis.," *Neurobiology of Alzheimer's Disease,* vol. 133, 2007.

[168] Ghiso J, Fossati S, Rostagno A., "Amyloidosis associated with cerebral amyloid angiopathy: cell signaling pathways elicited in cerebral endothelial cells," *J Alzheimers Dis,* vol. 42, pp. 167-176, 2014.

[169] Long JM, Holtzman DM., "Alzheimer disease: an update on pathobiology and treatment strategies.," *Cell,* vol. 179, pp. 312-339, 2019.

[170] Goldblatt G, Cilenti L, Matos JO, Lee B, Ciaffone N, Wang QX, Tetard L, Teter K, Tatulian SA. , "Unmodified and pyroglutamylated amyloid β peptides form hypertoxic hetero-oligomers of unique secondary structure.," *FEBS J.,* vol. 284, no. 9, pp. 1355-1369, 2017.

[171] Gunn AP, Wong BX, Johanssen T, Griffith JC, Masters CL, Bush AI, Barnham KJ, Duce JA, Cherny RA., "Amyloid-b peptide Ab3pE-42 induces lipid peroxidation, membrane permeabilization and calcium-influx in neurons.," *J Biol Chem.,* vol. 291, pp. 6134-6145, 2016.

[172] Dunkelmann T, Schemmert S, Honold D, Teichmann K, Butzküven E, Demuth HU, Shah NJ, Langen KJ, Kutzsche J, Willbold D, Willuweit A., "Comprehensive Characterization of the Pyroglutamate Amyloid-β Induced Motor Neurodegenerative Phenotype of TBA2.1 Mice.," *J Alzheimers Dis.,* vol. 63, pp. 115-130, 2018.

[173] Thomas A. Bayer, "Pyroglutamate Aβ cascade as drug target in Alzheimer's disease," *Molecular Psychiatry,* vol. 27, pp. 1880-1885, 2022.

[174] Sreerama N., Woody, R. W, Circular dichroism of peptides and proteins., John Wiley & Sons , 2000.

[175] S. D. Antosiewicz JM, "UV-Vis spectroscopy of tyrosine side-groups in studies of protein structure. Part 1: basic principles and properties of tyrosine chromophore.," *Biophys Rev. ,* vol. 8, pp. 151-161, 2016.

[176] JR., Lakowicz, Principles of Fluorescence Spectroscopy., Kluwer Academic/Plenum Publishers, 1999.

[177] Wang J, El-Sayed MA., "The effect of protein conformation change from alpha(II) to alpha(I) on the bacteriorhodopsin photocycle," *Biophys J.,* vol. 78, pp. 2031-2036, 2000.

[178] Zeth K, Thein M., "Porins in prokaryotes and eukaryotes: common themes and variations," *Biochem J.,* vol. 431, pp. 13-22, 2010.

[179] D. M. Tibor Páli, "Tilt, Twist, and Coiling in β-Barrel Membrane Proteins: Relation to Infrared Dichroism," *Biophysical Journal,* vol. 80, pp. 2789-2797, 2001.

[180] Lee J, Gillman AL , Jang H , Ramachandran S, . Kagan BL, Nussinov R, Arce FT. , "Role of Fast Kinetics of Pyroglutamate Modified Amyloid-β Oligomers in Membrane Binding and Membrane Permeability.," *Biochemistry,* 2014.

[181] David C Bode , Mark D Baker, John H Viles, "Ion Channel Formation by Amyloid-β42 Oligomers but Not Amyloid-β40 in Cellular Membranes," *J Biol Chem,* vol. 292, pp. 1404-1413, 2017.

[182] Capone R, Quiroz FG, Prangkio P, Saluja I, Sauer AM, Bautista MR, Turner RS, Yang J, Mayer M., "Amyloid beta- induced ion flux in artificial lipid bilayers and neuronal cells: resolving a controversy.," *Neurotoxicity Research,* vol. 16, pp. 1-13, 2009.

[183] Bruce L Kagan, Jyothi Thundimadathil, "Amyloid peptide pores and the beta sheet conformation," *Adv Exp Med Biol,* vol. 677, pp. 150-167, 2010.

[184] Abhijith G Karkisaval, Agueda Rostagno, Rustam Azimov, Deependra K Ban, Jorge Ghiso,Bruce L. Kagan, Ratnesh Lal, "Ion channel formation by N-terminally truncated Aβ (4–42): relevance for the pathogenesis of Alzheimer's disease," *Nanomedicine: Nanotechnology, Biology, and Medicine,* vol. 29, 2020.

[185] Durrell, S.R., Guy, H.R., Arispe, N., Rojas, E., Pollard, H.B., "Theoretical models of the ion channel structure of amyloid-b protein," *Biophys. J.,* vol. 67, p. 2137–2145, 1994.

[186] Shafrir Y, Durell S, Arispe N, Guy HR, "Models of membrane-bound Alzheimer's Abeta peptide assemblies.," *Proteins,* vol. 78, pp. 3473-3487, 2010.

[187] "Mara Zielinski, Christine Röder, Gunnar F. Schröder," *Journal of Biological Chemistry,* vol. 297, 2021.

[188] Yuri L. Lyubchenko , "Amyloid misfolding, aggregation, and the early onset of protein deposition diseases: insights from AFM experiments and computational analyses," *AIMS Molecular Science,* vol. 2, pp. 190-210, 2015.

[189] Martino Calamai, Fabrizio Chiti, Christopher M. Dobson, "Amyloid Fibril Formation Can Proceed from Different Conformations of a Partially Unfolded Protein," *Biophys J.,* vol. 89, pp. 4201-4210, 2005.

[190] Victoria J. McParland, Neil M. Kad, Arnout P. Kalverda, Anthony Brown, Patricia Kirwin-Jones, Michael G. Hunter, Margaret Sunde, and Sheena E. Radford, "Partially Unfolded States of β2-Microglobulin and Amyloid Formation in Vitro," *Biochemistry,* vol. 39, pp. 8735-8746, 2000.

[191] Thorsten Hugel, Markus Seitz, "The Study of Molecular Interactions by AFM Force Spectroscopy," *Macromol. Rapid Commun,* vol. 22, 2001.

[192] Jordanka Zlatanova, Stuart M. Lindsay, Sanford H. Leuba, "Single molecule force spectroscopy in biology using the atomic force microscope," *Progress in Biophysics & Molecular Biology,* vol. 74, pp. 37-61, 2000.

[193] Hans-Ju¨rgen Butt, Brunero Cappella, Michael Kappl, "Force measurements with the atomic force microscope: Technique, interpretation and applications," *Surface Science Reports ,* vol. 59, pp. 1-152, 2005.

[194] Fangzhou Xia, Kamal Youcef-Toumi, "Review: Advanced Atomic Force Microscopy Modes for Biomedical Research," *Biosensors ,* vol. 12, 2022.

[195] Hauke Clausen-Schaumann, Markus Seitz, Rupert Krautbauer, Hermann E Gaub, "Force spectroscopy with single bio-molecules," *Current Opinion in Chemical Biology,* vol. 4, pp. 524-530, 2000.

[196] Thomas E. Fisher, Andres F. Oberhauser, Mariano Carrion-Vazquez, Piotr E. Marszalek, Julio M. Fernandez, "The study of protein mechanics with the atomic force microscope," *TIBS,* vol. 24, 1999.

[197] Elias M. Puchner, Gereon Franzen, Mathias Gautel, Hermann E. Gaub, "Comparing Proteins by Their Unfolding Pattern," *Biophysical Journal,* vol. 95, pp. 426-434, 2008.

[198] Elias M Puchner, Hermann E Gaub, "Force and function: probing proteins with AFM-based force spectroscopy," *Current Opinion in Structural Biology,* vol. 19, pp. 605-614, 2009.

[199] Megan L Hughes, Lorna Dougan, "The physics of pulling polyproteins: a review of single molecule force spectroscopy using the AFM to study protein unfolding," *Reports on Progress in Physics,* vol. 79, 2016.

[200] Johannes Thoma, K. Tanuj Sapra, and Daniel J. Muller, "Single-Molecule Force Spectroscopy of Transmembrane Beta-Barrel Proteins," *Annual Review of Analytical Chemistry,* vol. 11, pp. 375-395, 2018.

[201] Nicola Galvanetto, Zhongjie Ye, Arin Marchesi, Simone Mortal, Sourav Maity, Alessandro Laio, Vincent Torre, "Unfolding and identification of membrane proteins in situ," *eLife,* vol. 11, 2022.

[202] Andreas Janshoff, Marcus Neitzert, York Oberdorf, Harald Fuchs, "Force Spectroscopy of Molecular Systems - Single Molecule Spectroscopy of Polymers and biomolecules," *Angew. Chem. Int. Ed.,* vol. 39, pp. 3212-3237, 2000.

[203] C. Bustamante, J. F. Marko, E. D. Siggia, S. Smith, "Entropic Elasticity of λ-Phage DNA," *Science,* vol. 265, pp. 1599-1600, 1994.

[204] Matthias Rief, Mathias Gautel, Filipp Oesterhelt, Julio M. Fernandez and Hermann E. Gaub, "Reversible Unfolding of Individual Titin Immunoglobulin Domains by AFM," *Science,* vol. 276, pp. 1109-1112, 1997.

[205] Nicola Galvanetto, Andrea Perissinotto, Andrea Pedroni, Vincent Torre, "Fodis: Software for Protein Unfolding Analysis," *Biophysical Journal,* vol. 114, pp. 1264-1266, 2018.

[206] Nina I. Ilieva, Nicola Galvanetto, Michele Allegra, Marco Brucale, Alessandro Laio, "Automatic classification of single-molecule force spectroscopy traces from heterogeneous samples," *Bioinformatics,* vol. 36, pp. 5014-5020, 2020.

[207] Elias M. Puchner, Gereon Franzen, Mathias Gautel, Hermann E. Gaub, "Comparing Proteins by Their Unfolding Pattern," *Biophysical Journal,* vol. 95, pp. 426-434, 2008.

[208] David Nečas, Petr Klapetek, "Gwyddion: an open-source software for SPM data analysis," *Cent. Eur. J. Phys. ,* vol. 10, pp. 181-188, 2012.

[209] Joaquim T. Marquês, Rodrigo F. M. de Almeida, Ana S. Viana, "Biomimetic membrane rafts stably supported on unmodified gold," *Soft Matter,* vol. 8, pp. 2007-2016, 2012.

[210] Zhengjian Lv, Robin Roychaudhuri, Margaret M. Condron, David B. Teplow, Yuri L. Lyubchenko, "Mechanism of amyloid beta protein dimerization determined using single-molecule AFM force spectroscopy," *Scientific Reports,* Vols. 3, 2880, 2013.

[211] Junping Yu, Julia Warnke, Yuri L. Lyubchenko, "Nanoprobing of α-synuclein misfolding and aggregation with atomic force microscopy," *Nanomedicine: Nanotechnology, Biology and Medicine,* vol. 7, pp. 146-152, 2011.

[212] Max Kessler, Kay E. Gottschalk, Harald Janovjak, Daniel J. Muller, Hermann E. Gaub, "Bacteriorhodopsin Folds into the Membrane against an External Force," *Journal of Molecular Biology,* vol. 357, pp. 644-654, 2006.

[213] F. Oesterhelt, D. Oesterhelt, M. Pfeiffer, A. Engel, H. E. Gaub, D. J. Muller, "Unfolding Pathways of Individual Bacteriorhodopsins," *Science,* vol. 288, pp. 143-146, 2000.

[214] Malte Renz, "Fluorescence Microscopy - A Historical and Technical Perspective," *Cytometry Part A,* vol. 83, pp. 767-779, 2013.

[215] Michael J. Sanderson, Ian Smith, Ian Parker, Martin D. Bootman, "Fluorescence Microscopy," *Cold Spring Harb Protoc;,* 2014.

[216] Daniel Evanko , "Primer: fluorescence imaging under the diffraction limit," *Nature Methods,* vol. 6, 2009.

[217] JOLIEN S. VERDAASDONK, ANDREW D. STEPHENS, JULIAN HAASE, KERRY BLOOM, "Bending the Rules: Widefield Microscopy and the Abbe Limit of Resolution," *Journal of Cellular Physiology,* vol. 229, pp. 132-138, 2014.

[218] Adaobi Nwaneshiudu, Christiane Kuschal, Fernanda H. Sakamoto, R. Rox Anderson, Kathryn Schwarzenberger, Roger C. Young, "Introduction to Confocal Microscopy," *Journal of Investigative Dermatology,* vol. 132, 2012.

[219] Stephen W. Paddock, Confocal Microscopy, SpringerLink, 1999.

[220] Fritjof Helmchen, Winfried Denk, "Deep tissue two-photon microscopy," *Nature Methods,* vol. 2, pp. 932-940, 2005.

[221] BONNIE O. LEUNG , KENG C. CHOU, "Review of SuperResolution Fluorescence Microscopy for Biology," *Applied Spectroscopy,* vol. 65, 2011.

[222] Lothar Schermelleh, Alexia Ferrand, Thomas Huser, Christian Eggeling, Markus Sauer, Oliver Biehlmaier, Gregor P. C. Drummen, "Super-resolution microscopy demystified," *Nature Cell Biology,* vol. 21, pp. 72-84, 2019.

[223] Yicong Wu, Hari Shroff , "Faster, sharper, and deeper: structured illumination microscopy for biological imaging," *Nature Methods,* vol. 15, pp. 1011-1019, 2018.

[224] Ying Ma, Kai Wen, Min Liu, Juanjuan Zheng, Kaiqin Chu, Zachary J Smith, Lixin Liu, Peng Gao, "Recent advances in structured illumination microscopy," *Journal of Physics: Photonics,* vol. 3, 2021.

[225] Rory M Power, Jan Huisken, "A guide to light-sheet fluorescence microscopy for multiscale imaging," *Nature Methods,* vol. 14, pp. 360-373, 2017.

[226] Peter A. Santi, "Light Sheet Fluorescence Microscopy: A Review," *Journal of Histochemistry & Cytochemistry,* vol. 59, pp. 129-138, 2011.

[227] Katrin I Willig, Benjamin Harke, Rebecca Medda & Stefan W Hell, "STED microscopy with continuous wave beams," *Nature Methods,* vol. 4, pp. 915-918, 2007.

[228] Eva Rittweger, Kyu Young Han, Scott E. Irvine, Christian Eggeling & Stefan W. Hell, "STED microscopy reveals crystal colour centres with nanometric resolution," *Nature Photonics,* vol. 3, pp. 144-147, 2009.

[229] Sebastian van de Linde, Anna Löschberger, Teresa Klein, Meike Heidbreder, Steve Wolter, Mike Heilemann & Markus Sauer, "Direct stochastic optical reconstruction microscopy with standard fluorescent probes," *Nature Protocols,* vol. 6, pp. 991-1009, 2011.

[230] Johnny Tam, David Merino, "Stochastic optical reconstruction microscopy (STORM) in comparison with stimulated emission depletion(STED) and other imaging methods," *Journal of Neurochemistry,* vol. 135, pp. 643-658, 2015.

[231] Ricardo Henriques, Caron Griffiths, E. Hesper Rego, Musa M. Mhlanga, "PALM and STORM: Unlocking Live-Cell Super-Resolution," *Biopolymers,* vol. 95, pp. 322-331, 2011.

[232] ERIC BETZIG, GEORGE H. PATTERSON, RACHID SOUGRAT, O. WOLF LINDWASSER, SCOTT OLENYCH, JUAN S. BONIFACINO, MICHAEL W. DAVIDSON, JENNIFER LIPPINCOTT-SCHWARTZ, AND HARALD F. HESS, "Imaging Intracellular Fluorescent Proteins at Nanometer Resolution," *Science,* vol. 313, pp. 1642-1645, 2006.

[233] Joerg Schnitzbauer, Maximilian T Strauss, Thomas Schlichthaerle, Florian Schueder & Ralf Jungmann, "Super-resolution microscopy with DNA-PAINT," *Nature Protocols,* vol. 12, pp. 1198-1228, 2017.

[234] Jeffrey Caplan, Marc Niethammer, Russell M Taylor II, Kirk J Czymmek , "The power of correlative microscopy: multi-modal, multi-scale, multi-dimensional," *Current Opinion in Structural Biology,* vol. 21, pp. 686-693, 2011.

[235] Pascal de Boer, Jacob P Hoogenboom & Ben N G Giepmans, "Correlated light and electron microscopy: ultrastructure lights up!," *Nature Methods,* vol. 12, pp. 503-513, 2015.

[236] Daniel Axelrod, "Chapter 9 Total Internal Reflection Fluorescence Microscopy," *Methods in Cell Biology,* vol. 30, pp. 245-270, 1989.

[237] Daniel Axelrod, "Total internal reflection fluorescence microscopy in cell biology," *Methods in Enzymology,* vol. 361, pp. 1-33, 2003.

[238] Daniel Axelrod, "Cell-substrate contacts illuminated by total internal reflection fluorescence.," *Journal of Cell Biology,* vol. 89, pp. 141-145, 1981.

[239] David A. Coucheron, Øystein I. Helle, Cristina I. Øie, Firehun T. Dullo, Balpreet S. Ahluwalia, "Chip Based Nanoscopy: Towards Integration and High-throughput Imaging," *Proc. of SPIE ,* vol. 10350, 2017.

[240] Ida S. Opstad, Florian Ströhl, Marcus Fantham, Colin Hockings, Oliver Vanderpoorten, Francesca W. van Tartwijk, Julie Qiaojin Lin, Jean-Claude Tinguely, Firehun T. Dullo, Gabriele S. Kaminski-Schierle, Balpreet S. Ahluwalia, Clemens F. Kaminski, "A waveguide imaging platform for live-cell TIRF imaging of neurons over large fields of view," *Journal of Biophotonics,* vol. 13, 2020.